RADIAL AND LONGITUDINAL PROPAGATION OF FLUX JUMPS IN TYPE II SUPERCONDUCTING CYLINDERS IN AXIAL FIELDS

Jean F. Bussiere

Dissertation submitted to the Faculty of the Graduate School
of the University of Ottawa in partial fulfillment
of the requirements for the degree
Doctor of Philosophy

1973

ACKNOWLEDGEMENTS

It is a pleasure indeed to acknowledge the help received from Professor Marcel A. R. LeBlanc. The daily conversations with him made this work a pleasant and memorable experience.

Thanks are also due to the professors of the Department of Physics and the members of the Superconductivity group for helpful discussions.

I also wish to thank Miss L. T. Sawyer for her cooperation in typing this thesis and Miss S. L. Kwan for her assistance in preparing the numerous drawings.

A most deserving thanks is due to my wife Maria for her encouragement and understanding throughout the period of this work.

Finally, the financial support of the NRC and the Government of Ontario was much appreciated.

A B S T R A C T

Two aspects of the dynamics of flux jumps in cylinders of type II superconductors in axial fields are investigated, the radial collapse of flux and the longitudinal propagation of this collapse.

In part I we develop a model which describes the evolution with time and in space of the radial collapse of flux in type II superconductors. Although we restrict ourselves to adiabatic conditions and to the case where the critical current density J_c is independent of field, the model can easily be extended to include more realistic and complicated features of the real situation. Using this model, which is essentially based on a flux diffusion equation for type II superconductors coupled to a heat equation we are able to calculate sequences of profiles of magnetic field, temperature and power dissipation density during flux jumps in type II superconductors. The model also enables us to predict the magnitude, duration and other features of flux jumps which can be readily compared with observations.

The role played by the initial magnetization $\langle 4\pi M \rangle$, average magnetic induction $\langle B \rangle$ and initial field profile on the kinetics of flux jumps are investigated theoretically for cylinders with physical parameters corresponding to NbTi. Comparison with experimental results gives both good qualitative and quantitative agreement for the rate of

collapse of flux.

In part II we present experimental measurements of the longitudinal propagation of flux jumps in type II superconducting cylinders. We show that this process is controlled by electromagnetic coupling and is entirely determined by the characteristics of radial flux collapse. Velocities ranging between $\sim 10^4$ and 10^6 cm/sec are reported for samples of NbTi, NbZr, Vanadium and Niobium. Changes in velocity with initial magnetization $\langle 4\pi M\rangle$, average magnetic induction $\langle B\rangle$, field profile, normal state resistivity, transport current, bath temperature and diameter are investigated. The variations of velocity are found to be consistent with the characteristics of radial flux collapse deduced from our calculations.

TABLE OF CONTENTS

ACKNOWLEDGEMENTS		i
ABSTRACT		ii
INTRODUCTION		1
EXPERIMENTAL		6

PART I

THE KINETICS OF RADIAL FLUX COLLAPSE IN TYPE II SUPERCONDUCTORS IN AXIAL FIELDS

CHAPTER I	DISCUSSION AND INTRODUCTION		16
CHAPTER II	THE DIFFUSION OF FLUX IN NORMAL CONDUCTORS		
	I	INTRODUCTION	24
	II	SLAB OF FINITE WIDTH	25
	III	CYLINDER IN A LONGITUDINAL FIELD	31
	IV	CONCLUSION	34
CHAPTER III	PENETRATION OF FLUX IN A TYPE II SUPERCONDUCTORS DURING A FLUX JUMP: THEORETICAL CONSIDERATIONS		
	I	INTRODUCTION	35

	II	RELATION BETWEEN ELECTRIC FIELD AND CURRENT DENSITY IN A TYPE II SUPERCONDUCTOR	37
	III	FLUX PENETRATION IN A TYPE II SUPERCONDUCTING SLAB	41
		a) Initial Conditions	41
		b) Diffusion equation	43
		c) Method of solution	46
	IV	SUPERCONDUCTING CYLINDER IN AN AXIAL FIELD	52
		a) Initial conditions	52
		b) Fundamental equations and method of solution	54
	V	SCALING LAWS FOR SLAB AND CYLINDER	58
		a) Dimensionless equations	58
		b) Scaling laws for flux, field and time	62
		c) Scaling laws for $\partial\phi/\partial t$ and power	63
CHAPTER IV		RADIAL COLLAPSE OF FLUX IN TYPE II SUPERCONDUCTING CYLINDERS: THEORETICAL CALCULATIONS	
	I.	INTRODUCTION	64
	II	VALUES OF CONSTANTS AND ASSUMPTIONS USED IN THE CALCULATIONS	65
		a) Critical Temperature and Field	65
		b) Critical Current Density	66
		c) Specific heat	67
		d) Flux-flow resistivity	67
		e) Perturbation	69

	III	EFFECT OF MAGNETIZATION $<4\pi M>$ ON RADIAL COLLAPSE OF FLUX IN NbTi CYLINDERS	69
		a) Introduction	69
		b) Time of Collapse as a function of $<4\pi M>$	70
		c) Shape of the Voltage pulses $\partial\phi/\partial t$ vs time	75
		d) Field, Temperature and Power Dissipation profiles during a flux jump	79
	IV	EFFECT OF INITIAL FIELD PROFILE	90
		a) Introduction	90
		b) Time of radial collapse as a function of initial field profile	91
		c) Shape of the voltage pulses $\partial\phi/\partial t$ vs t.	98
		d) Field, Temperature and Power Dissipation Profiles.	100
	V	EFFECT OF THE AVERAGE MAGNETIC INDUCTION $<B>$ ON RADIAL COLLAPSE OF FLUX	112
		a) Introduction	112
		b) Effect of $<B>$ on τ_R and τ_t	113
	VI	RADIUS OF FIELD PENETRATION AS A FUNCTION OF TIME	116
	VII	CONCLUSION	118
CHAPTER V		RADIAL COLLAPSE OF FLUX IN A NbTi CYLINDER: EXPERIMENTAL RESULTS AND COMPARISON WITH THEORY	
	I	INTRODUCTION	122
	II	EXPERIMENTAL AND THEORETICAL VALUES OF τ_R	123

	III	SEQUENCES OF PROFILES OF FIELD, TEMPERATURE AND POWER DISSIPATION DURING FLUX JUMPS IN NbTi-3	128
	IV	EXPERIMENTAL AND THEORETICAL VOLTAGE PULSES: $\partial\phi/\partial t$ vs t	135
		a) Theoretical Pulse Shapes	135
		b) Experimental Pulse Shapes	139
	V	CONCLUSION	142
CHAPTER VI	RELATION BETWEEN PURELY RADIAL COLLAPSE OF FLUX IN A CYLINDER AND RADIAL COLLAPSE OBSERVED DURING LONGITUDINAL PROPAGATION		
	I	INTRODUCTION	145
	II	VALUES OF τ_R MEASURED FOR PURELY RADIAL COLLAPSE OF FLUX AND FOR LONGITUDINAL PROPAGATION IN NbTi-3	146
	III	VALUES OF τ_R MEASURED FOR LONGITUDINAL FLUX JUMPS IN NbTi-2, NbZr-1, V-2 AND NbTi-4	148
	IV	CONCLUSION	154

PART II

THE LONGITUDINAL PROPAGATION OF FLUX JUMPS ALONG TYPE II SUPERCONDUCTING CYLINDERS IN AXIAL FIELDS

CHAPTER VII	INTRODUCTION TO PART II		157
CHAPTER VIII	THERMAL VS ELECTROMAGNETIC PROPAGATION		
	I	INTRODUCTION	160
	II	VELOCITY WITH NO MAGNETIC MOMENT	162
	III	VELOCITY WITH A MAGNETIC MOMENT PRESENT	164
		a) Bath Temperature $T_b = 4.2^oK$	165
		b) Bath Temperature $T_b = 2.46^oK$	168
	IV	CONCLUSION	171
CHAPTER IX	LONGITUDINAL VELOCITY AS A FUNCTION OF MAGNETIZATION $<4\pi M>$		
	I	INTRODUCTION	174
	II	VELOCITY VS $<4\pi M>$ IN NbTi	176
		a) Samples NbTi-1 and NbTi-2	176
		b) Sample NbTi-3	199
		c) NbTi-4	199
	III	VELOCITY VS $<4\pi M>$ IN NbZr	204
		a) NbZr-1	204
		b) NbZr-2	210

IV	VELOCITY VS <$4\pi M$> IN NIOBIUM	212
V	VELOCITY VS <$4\pi M$> IN VANADIUM	216
	a) V-1	216
	b) V-2	219
V	CONCLUSION	224

CHAPTER X STRUCTURE OF FLUX JUMPS AND ASYMMETRICAL FLUX PENETRATION DURING LONGITUDINAL PROPAGATION

I	INTRODUCTION	225
II	SHAPE OF VOLTAGE PULSES OBSERVED DURING LONGITUDINAL PROPAGATION	227
III	DISCUSSION AND CONCLUSION	234

CHAPTER XI RELATION BETWEEN THE RATE OF RADIAL FLUX COLLAPSE AND THE VELOCITY OF LONGITUDINAL PROPAGATION

I	INTRODUCTION	238
II	RELATION BETWEEN LONGITUDINAL VELOCITY V AND τ_R FOR FLUX JUMPS TRIGGERED ALONG A GIVEN MAGNETIZATION CURVE	240
	a) Experimental Results	240
	b) Discussion	249
III	RELATION BETWEEN V AND τ_R FOR FLUX JUMPS OF CONSTANT MAGNETIZATION TRIGGERED IN DIFFERENT FIELDS	253
	a) Experimental Results	255
	b) Discussion	255
IV	CONCLUSION	262

CHAPTER XII	VARIATION OF THE LONGITUDINAL VELOCITY WITH EXTERNAL FIELD AND NORMAL STATE RESISTIVITY		
	I	INTRODUCTION	265
	II	VELOCITY AS A FUNCTION OF EXTERNAL FIELD H	267
		a) NbTi-4	267
		b) NbZr-1 and NbTi-2	267
		c) Discussion	269
	III	EFFECT OF NORMAL STATE RESISTIVITY	276
	IV	CONCLUSION	278
CHAPTER XIII	EFFECT OF A TRANSPORT CURRENT ON THE LONGITUDINAL VELOCITY OF PROPAGATION OF FLUX JUMPS		
	I	INTRODUCTION	280
	II	EXPERIMENTAL RESULTS AND DISCUSSION	280
	III	CONCLUSION	288
CHAPTER XIV	EFFECT OF BATH TEMPERATURE ON THE LONGITUDINAL VELOCITY OF PROPAGATION OF FLUX JUMPS		
	I	INTRODUCTION	290
	II	EXPERIMENTAL RESULTS	291
		a) NbZr-1	291
		b) NbTi-2	297
		c) V-1	305
	III	DISCUSSION AND CONCLUSION	307

CHAPTER XV EFFECT OF DIAMETER ON LONGITUDINAL VELOCITY OF PROPAGATION OF FLUX JUMPS

I INTRODUCTION 308

II EXPERIMENTAL RESULTS 309

a) Vanadium 309

b) NbTi 309

c) NbZr 310

III DISCUSSION AND CONCLUSION 315

CONCLUSION 317

APPENDICES

APPENDIX A DIFFUSION OF FIELD IN A NORMAL SLAB WHERE THE INITIAL FIELD PROFILE IS LINEAR: EXACT SOLUTION 321

APPENDIX B PENETRATION OF FLUX IN A SUPERCONDUCTING SLAB: NUMERICAL METHOD OF SOLUTION 325

APPENDIX C PENETRATION OF FLUX IN A SUPERCONDUCTING CYLINDER: METHOD OF SOLUTION 340

I ANALOG EQUATIONS 340

a) Case Where the Field Has Initially Penetrated to the Center of the Cylinder. 344

b) Case Where the Field Has Not Initially Penetrated to the Center of the Cylinder 346

	II COMPUTER PROGRAM	349
	a) Definition of Symbols	349
	b) Definition and Use of Parameter K(I)	352
	c) Programme Listing	355
APPENDIX D	THOMAS ALGORITHM FOR A TRIDIAGONAL MATRIX	366
APPENDIX E	VALIDITY OF CORRECTION $\delta\Phi$ USED FOR THE NUMERICAL SOLUTION OF THE FLUX DIFFUSION EQUATION	368
REFERENCES		372

INTRODUCTION

The isothermal critical state model (Bean 64) adequately describes the penetration (or exit) of flux from hard type II superconductors as an external field is varied slowly. According to this model, a hard type II superconductor can be characterized by a critical current density $J_c(H,T)$ which depends on temperature T and on the local magnetic field H, and any emf, however small, will induce the full critical current density to flow locally in the superconductor. Therefore in the regions which experienced a change in magnetic induction (hence an emf), a persistent current density is flowing whose magnitude corresponds to the saturation or limiting value J_c and whose direction is determined by the Faraday-Lenz law of induction. The relation between field and current is given by the Maxwell equation:

$$\text{curl } H = \frac{4\pi}{10} J_c$$

which in the case of a cylinder in an axial field takes the form:

$$\frac{\partial H}{\partial r} = 0, \quad \pm \frac{4\pi}{10} J_c$$

This model adequately reproduces the hysteritic magnetization curves observed in hard type II superconductors. The model leads to magnetic field profiles inside a superconductor which depend on the way in which the field is applied, i.e. on "magnetic history". The field profiles are therefore irreversible and as a consequence states of minimum magnetic energy are not usually obtained. This is a direct consequence of the fact that in a hard type II superconductor flux is not free to move. Flux in type II superconductors has been shown to exist in the form of quantized vortices as predicted by Abrikosov (Abrikosov 57) and observed experimentally by Trauble and Essmann (Trauble 68). In "hard" type II superconductors these vortices are strongly pinned by lattice defects, impurities, imperfections, grain boundaries, etc. A strong pinning of these vortices leads to high critical current densities and also to very irreversible magnetic behaviour. If we consider a cylinder of high critical current density along which we apply a magnetic field, then, as the field is increased, persistent currents are induced, causing a magnetic moment to appear in the cylinder. For cylinders of large diameter and/or large critical current density, this magnetic moment (the excess or deficit of flux) can become very large. The magnetic energy of the cylinder will therefore be correspondingly large, in some cases leading to states of energy much greater than that required to restore the normal state.

As a consequence, the specimen is in a state of unstable equilibrium and if sufficiently perturbed may revert completely to the normal state as the persistent currents collapse. This is observed experimentally as a sudden decrease in magnetization and a rise in the temperature of the superconductor. Although all states corresponding to higher total energies than the normal state will collapse if sufficiently perturbed, other states with magnetic profiles yielding lower energies may also be unstable even if perturbed by an infinitesimal amount and a partial decay of the persistent currents can occur for these states.

On the basis of the critical state model, it is possible to derive a necessary condition for the stability of a given profile. Swartz and Bean (Swartz 68) have obtained an expression for the field below which no "flux jump" or instability can occur in an infinite slab under adiabatic conditions. This field is given by:

$$H_{fj} = \{ -\pi^3 c\ J_c / (\frac{\partial J_c}{\partial T}) \}^{\frac{1}{2}}$$

where c is the specific heat per unit volume, J_c the critical current density (assumed independent of magnetic field in their derivation), and $\partial J_c/\partial T$ is the change in critical current density with temperature. The criterion for stability has also been studied by a large number of workers for different thermal and magnetic conditions (Hancox 65, Wipf 67, Hart 68, Yamafuji 69, Chikaba 70, Ogasawara 70, Boyer 72, Yasukochi 72).

Using their "adiabatic critical state model" Swartz and Bean (Swartz 68) were able to calculate the final field and temperature profile after a flux jump under adiabatic conditions for an infinite slab. Their model however, is not easily extended to finite geometries and does not predict the time of duration of flux jumps or intermediate field profiles between the initial and the final states. An understanding of the kinetic behaviour of flux jumps is of importance since stabilization involves a dynamic balance between heat and flux diffusion.

In this thesis, we present two aspects of the dynamics of flux jumps in cylinders of type II superconductors in axial fields, the radial collapse of flux and the longitudinal propagation of this collapse.

In part I, we develop a model which describes the evolution with time and in space of the radial collapse of flux in type II superconductors. Although we restrict ourselves to adiabatic conditions and to the case where J_c is independent of field, the model can easily be extended to include more realistic and complicated features of the real situation as well as effects due to the presence of a normal metal at the surface of the superconductor. Using this model, which is essentially based on a diffusion equation for type II superconductors coupled to a heat equation, we are able to calculate field and temperature profiles, power dissipation and time of duration of flux jumps in type II superconductors. The model also predicts final temperature and field profiles for finite geometries. Comparison with experimental results in NbTi cylinders gives both good qualitative and quantitative agreement for the rate of collapse of flux.

In part II, we present experimental measurements of the longitudinal velocity of propagation of flux jumps in cylinders of type II superconductors. We show that this process is controlled by electromagnetic coupling and is intimately related to the behaviour of the radial collapse of flux. Although at present we have no theory to predict the absolute value of the longitudinal velocity (which is observed to vary between $\sim 10^4$ to 10^6 cm/s) we are able to explain qualitatively, in terms of the characteristics of radial collapse of flux, the relative changes in velocity with magnetic history in a given conductor and the ratio of the velocities for conductors of different materials and geometries.

E X P E R I M E N T A L

I. SAMPLE PREPARATION AND DESCRIPTION

The samples consisted of solid cylinders, wires and one hollow cylinder. Their dimensions, resistivity at the critical temperature $\rho_n(T_c)$, resistivity ratio at low temperature ρ_{300^oK}/ρ_{T_c}, origin and description are listed in Table I. The composition, critical temperature and specific heat of the materials from which these samples are made are listed in Table II. The specific heat of the superconducting state was taken to be $C_s = \gamma \frac{H}{H_{c2}(T)} T + \alpha T^n$ where γT is the electronic specific heat of the normal state and α and n are constants which are adjusted to fit the available experimental measurements. The enthalpy is defined as:

$$\text{enthalpy} = \int_{T_b}^{T_c} C_s(T)dT$$

where T_b is the bath or initial temperature, $C_s(T)$ the superconducting specific heat and T_c the critical temperature. In Table II, T_b was taken to be 2.5^oK for Vanadium and 4.2^oK for the other materials.

Table I

Sample	Diameter (cm)	$\rho_n(T_c)$ ($\mu\Omega$-cm)	ρ_{300}/ρ_{T_c}	Sample Description
Nb	.051	0.8	40	Cold drawn wire, Fansteel Metallurgical Corp.
V-1	.051	1.7	9	Cold drawn wire, Materials Research Corp.
V-2	.077	1.7	10	Cold drawn wire, Materials Research Corp.
NbZr-1	.051	25		Cold rolled wire, Wah Chang Corp.
NbZr-2	.310	25		Cold rolled rod with deep cracks, Supercon.
NbTi-1	.0254	56	1.6	T48 B magnet wire with copper cladding removed, Supercon.
NbTi-2	.0482	56	1.6	T48 B magnet wire with copper cladding removed, Supercon.
NbTi-3	.1905	65		Rod machined from cold-rolled T48 material, Supercon.
NbTi-4	.175 ext. .138 int.	65		Hollow cylinder machined from cold rolled T48 material, Supercon.

Table II

Material	Composition	T_c (^oK)	Specific heat*				Enthalpy (mJ/cm^3)
			α ($J/M.^3deg^{n+1}$)	β ($J/M.^3deg^4$)	γ ($10^3 J/M.^3deg^2$)	n	
Nb	99.9% pure	9.2 a)	34.3 e)	12.7 e)	0.69 e)	3 e)	60
V	99.9% pure	5.2 b)	155 b)	42 b)	1.18 b)	3 b)	31 †
NbZr	$Nb_{.75}Zr_{.25}$	10.8 c)	7.56 g)	16.7 g)	1.57 g)	3.8 g)	130
NbTi	$Nb_{.36}Ti_{.64}$	9.5 d)	38.16 h)	14.4 h)	1.05 h)	3.19 h)	105

* $C_s = \gamma T + \beta T^3$, $C_n = \frac{H}{H_{c2}(T)} \gamma T + \alpha T^n$; † $T_b = 2.5^oK$

a) Leupold 64 b) Radebaugh 66a c) Neuringer 66 d) estimated from compilation of M. S. Lubell 69, 72

e) Ferreira de Silva 66 f) Radebaugh 66b g) El Bindari 63 h) Zbasnik 69.

Each sample was first surrounded by a non-inductively wound heater made of No. 38 B & S enameled manganin wire. This heater was used to raise the temperature of the superconductor above T_c before the start of any measurement. Two or three small detector coils made of the same manganin wire and wound in series approximately 2 cm apart on the main heater were used to measure the longitudinal velocity. A small detector coil was also wound near the center of the sample and used to determine the time of radial flux penetration. The number of turns for each detector coil varied from 5 to 15. Small heaters of 10Ω nominal resistance and approximately 15 turns were then wound directly on the superconductor at each end of the main heater. These were used to trigger flux jumps from either end of the sample (see figure 1) Two voltage probes were attached to the superconductor at each end of the heater to measure the normal state resistivity and to monitor the voltage along the superconductor during a flux jump when a transport current was present.

To ensure rigidity, the samples were then encapsulated in a pyrex tube filled with epoxy. In the case of wires studied with a transport current flowing, the free ends were sandwiched between indium foils and copper blocks. The contact resistance achieved in this arrangement was of the order of one micro ohm per contact.

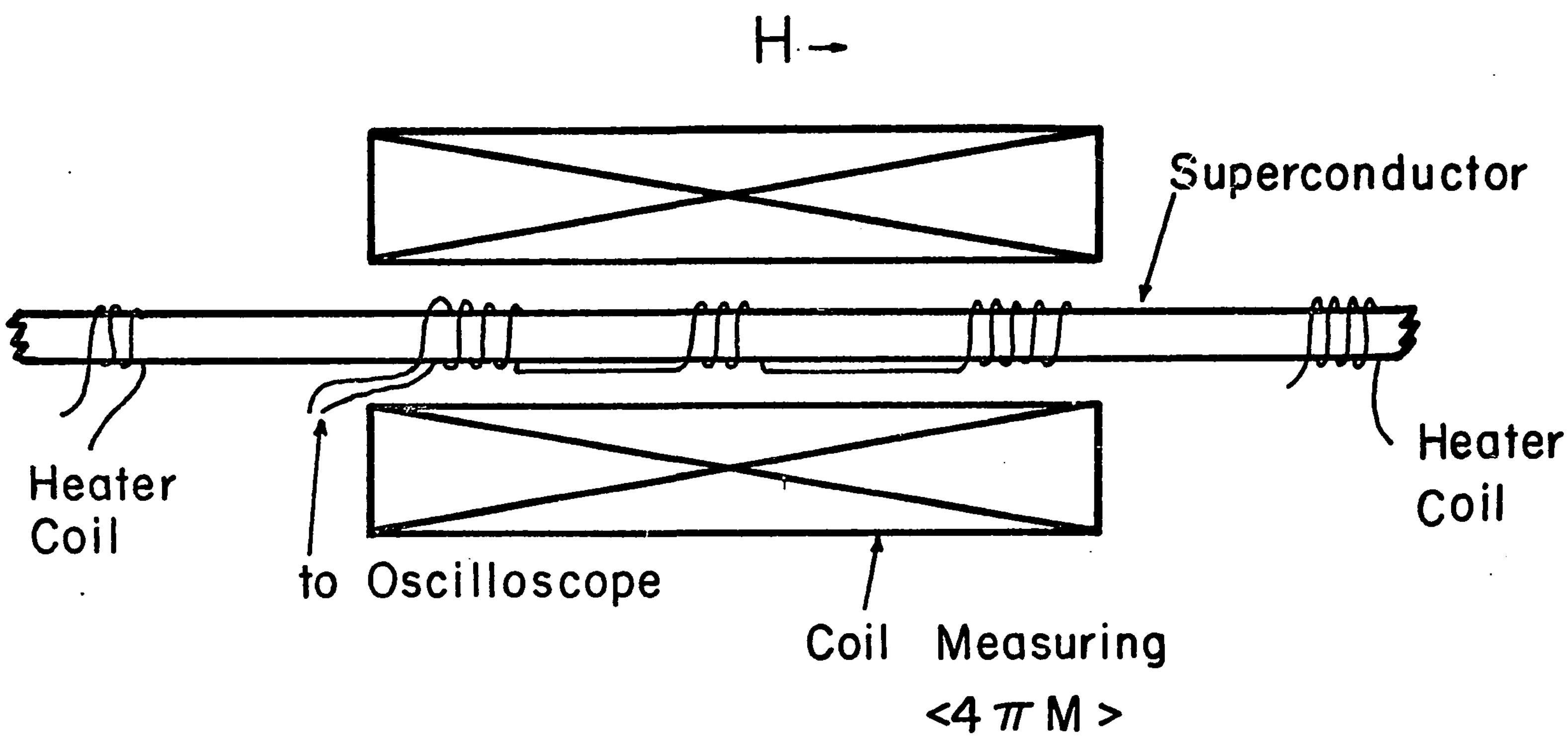

Fig. 1: Schematic of sample, heater and detector coils.

II. METHOD OF MEASUREMENT

The samples were placed in a home-made NbTi solenoid 17 cm long with 3.8 cm bore and capable of producing 35 kG. The magnetic field was always applied along the sample axis (figure 1).

A large pick-up coil made of two concentric oppositely wound coils adjusted so that no net signal is produced in a changing uniform axial field was used to measure the magnetization of the superconducting samples (figure 1). The output of this coil was fed through an electronic integrator to the Y axis of an X-Y recorder, the X axis being driven by a signal proportional to the current in the solenoid. For all measurements, the external field, initial and final magnetization were monitored on the X-Y recorder.

a) Longitudinal Propagation

Longitudinal propagation of flux jumps was triggered by applying a pulse of approximately 12 volts amplitude and 20 μsec duration (with 1 μsec rise-time) to either of the two small heater coils (see figure 1). The pulsing circuit is described in section III. The pulse was also used to trigger the oscilloscope after a given delay obtained from an Ortec 416 A Gate and Delay Generator modified to give a maximum delay of 1.1 msec.

The oscilloscope trace corresponding to the detector coils wound in series was photographed with a Polaroid camera and the velocity of propagation deduced from the trace.

b) Time of Radial Flux Collapse

Radial collapse of flux was triggered by applying a step of current to a small coil made of No. 38 B & S enameled copper wire and wound directly on the sample, main heater and detector coil assembly. The pulsing circuit is described in section III. The rise-time of the pulse was $\sim$ 5 μsec and the field step $\sim$ 300 gauss. The radial time of flux collapse was measured on a dual-beam oscilloscope using simultaneously both detector coils wound in series along the superconductor and a single coil wound near the center of the sample. The similarity and time sequence of the two signals ensured that purely radial collapse had been triggered and that no longitudinal propagation was occurring. The voltage traces obtained from these coils were photographed and the time of radial collapse determined as the width at 1/e of the full height of the voltage peaks.

III. VARIABLE TIME PULSE CIRCUIT

The purpose of this circuit is to provide a high current pulse having a rise-time of the order of one microsecond and variable length. The circuit (figure 2) consists of a monostable multivibrator MS2 which gives a negative pulse whose time of duration depends on the setting of a rotary switch SW1 and a capacitor C5. This pulse is then inverted using transistors Q2 and Q3 and amplified with a Darlington current amplifier Q4-Q6. Switch SW3 is normally closed and with R5 and C3 forms a time constant network to provide a large degree of immunity from the contact bounce and noise of SW3 which could also cause multiple pulsing of the output. Approximately 25 ms after SW3 is pressed, the monostable multivibrator MS1 is triggerred. MS2 is triggered from the leading edge of MS1. The network R2, Z1 and C1 forms a voltage regulator.

The different positions of the rotary switch SW3 provide pulses of lengths varying between 10 μsec and 100 μsec. With external resistors this time can be lengthened and with an infinite resistance a step of current is obtained. The rise-time was generally of the order of 1 μsec, and the maximum current, approximately 5 amps.

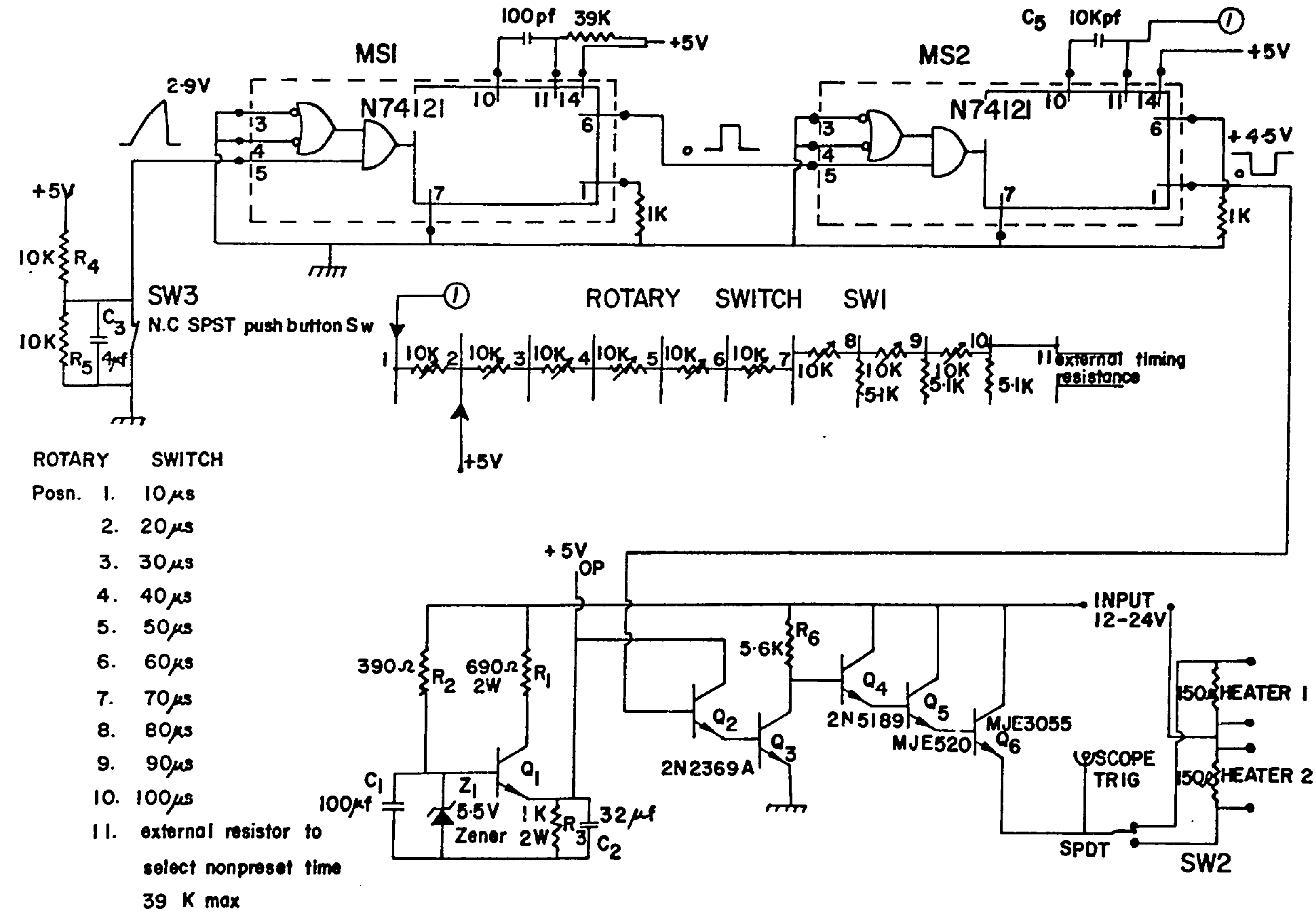

Fig. 2 : Schematic of variable time pulse circuit.

PART I

THE KINETICS OF RADIAL FLUX COLLAPSE IN TYPE II SUPERCONDUCTORS IN AXIAL FIELDS

CHAPTER I

DISCUSSION AND INTRODUCTION

The first aspect of the kinetics of flux jumps to be analysed in this thesis is the radial collapse of flux in cylinders of hard type II superconductors in axial fields.

The kinetic penetration of flux which occurs in a type I superconductor when the field is larger than critical has been the subject of both theoretical and experimental investigations. In a type I superconductor flux penetration occurs only in regions where the magnetic field is greater than critical. If the demagnetizing factor is zero the sudden application of an external magnetic field greater than critical causes a normal-superconducting boundary to be formed initially near the surface of the superconductor. Since in this situation the boundary is stable with respect to distortions, the penetration of flux which occurs as this boundary penetrates the conductor can be readily analysed theoretically. The case of an infinite slab has been solved by Pippard and Lifshitz (Pippard 50, Lifshitz 50), neglecting thermal effects. In this case, as a field greater than critical is applied parallel to the surface of the slab, a thin layer at the surface makes a transition into the normal state so that the normal-superconducting boundary is parallel to the surface and moves into the interior of the metal as the normal state expands. As this boundary advances magnetic flux progressively fills the normal region and as the induced currents in this region decay the field strength near and behind the advancing boundary grows above H_c. The velocity is found by assuming that the boundary moves at such a rate that the field strength next to it attains the critical value H_c as the currents induced in the normal region decay. Solutions have also been obtained taking into account the heat produced by the eddy currents in the normal metal (Ittner 58, Duijvestinjn 59) and the results agree with experiments on hollow cylinders with thin walls (Ittner 58).

Experiments have also been performed on solid cylinders (Faber 53, Chopra 59). In this case only approximate analytic solutions of the theoretical problem have been obtained (Pippard 50, Swihart 63).

When the demagnetizing factor is non-zero, the sample undergoes a transition to the intermediate state unless $H > H_c$. It is found that the normal-superconducting interface may be subject to dynamic instabilities which often generate migrating flux tubes (Faber 58). Nelgecting these effects, one can obtain the total time of transition from simple energy balance arguments (Faber 54, 55). The experimental results for discs in perpendicular fields are in reasonable agreement with this analysis (DeSorbo 64, 65, Baird 64, Laeng 71). Recently, experiments have also been performed in thin films (Huebener 72).

The dynamics of flux penetration in type II superconductors during flux jumps has received scant attention. DeSorbo, using the Faraday rotation technique, was able to observe visually the flux profiles in cold rolled niobium before and after flux jumps (DeSorbo 64). With a similar technique, but using a very fast camera, Wertheimer and Gilchrist (Wertheimer 67) and Harrison et al. (Harrison 72) were able to observe the evolution of these flux profiles with time in discs of type II metals and alloys. The speed of flux penetration was found (Wertheimer 67) to increase with decreasing specimen thickness and increasing normal state resistivity. This behaviour was explained in terms of speed limitation by eddy currents. In their theoretical analysis, Wertheimer and Gilchrist made the crude over-simplifying assumption however that the critical current density drops instantaneously to a value much lower than the initial value, corresponding to a temperature rise which is instantaneous in time. The assumption is also made that the field varies linearly in space within the disc at all times. The specific heat, a basic factor affecting the stability of type II superconductors and the rate of flux penetration does not appear in their equations. As a consequence this theoretical analysis does not distinguish between stable and unstable magnetic configurations.

The basic difference in the phenomenon of flux penetration in type I and type II superconductors can be summarized as follows:

i) In type II superconductors persistent currents can flow throughout the volume or bulk that is superconducting before any disturbance occurs. For this reason one can no longer visualize a sharp travelling boundary across which a discontinuous change in flux and change of phase occurs. In fact, a flux jump can occur without any part of the superconductor ever undergoing a transition to the normal state.

ii) Another complication arises from the possibility of irreversible macroscopic currents flowing in both the superconducting and the normal volume. Dissipation of energy and hence changes in temperature can now occur in both types of regions. Dissipation of energy is encountered in the superconducting volume because the change of flux gives rise to the phenomenon of "flux-flow resistivity" (Kim 65).

iii) The magnitude of the flux-flow resistivity changes continuously from zero to the normal state value inside the superconductor as flux penetration occurs. We can therefore no longer assume a discontinuous change in resistivity at a normal-superconducting phase boundary.

iv) Finally, the liberation of stored magnetic energy during flux jumps can be considerable and generate significant variations of temperature with time and position. As a consequence, the temperature dependence of several quantities must be taken into consideration. In type I superconductors the increase in temperature is not significant and leads to a slight decrease in the critical field H_c. In type II superconductors an increase in temperature will also lead to a decrease in the critical fields H_{c1} and H_{c2} but also produce a change in flux-flow resistivity and a change in the critical current density. Therefore, as the temperature increases in the type II superconductor both the ability of the superconductor to carry a current without resistance and the rate of decay of these currents is affected. Finally, the dependance of the heat capacity on temperature, particularly in the superconducting volume, must be taken into account for a realistic description of the events.

In summary, the kinetics of flux jumping in type II superconductors must therefore be described by considering the interplay of flux penetration and heat generation which determine the extent and speed of flux penetration. A thermal perturbation applied to a type II superconductor causes a reduction of the critical current density J_c which in turn leads to a penetration of flux. This flux penetration produces a further rise in temperature and therefore a further decrease in J_c, and so on. Since the temperature rise depends on specific heat and thermal conductivity, these two quantities play an important role in the mechanism of penetration of flux. The degree of stability of the superconducting state will also depend on $\partial J_c/\partial T$. If $\partial J_c/\partial T$ is zero or positive, the superconductor will be stable against thermal perturbations, since it is the fact that the critical current density decreases with temperature which allows the flux configuration to collapse. A correct and realistic model describing the kinetics of flux jumping must therefore take into account the complex interplay between flux penetration and heat generation.

In part I of this thesis we derive and present detailed applications of a diffusion equation for the penetration of flux in type II superconductors. This diffusion equation is similar to the diffusion equation describing the penetration of field and change in flux in normal metals but takes into account the fact that a superconductor can support a certain critical current density without resistance.

To provide a simple framework with which the complex phenomenon of flux penetration in type II superconductors can be compared, we present in chapter II characteristics of flux penetration in slabs and cylinders of normal material. The manner of flux penetration will tend towards this limit in circumstances where the amount of stored magnetic energy in a superconductor is much larger than its enthalpy.

In chapter III we set up the diffusion equations applicable to the description of flux penetration in cylinders and slabs of type II superconductors. The basic equations from which the diffusion equations are obtained are essentially Faraday's law of induction, Ampere's law, and an empirical relation between the electric field and the current density in type II superconductors. Since the diffusion equation presents a "discontinuity" (see appendix B and C) and must be solved simultaneously with a heat equation to describe the flux jumping process, only numerical solutions can be obtained. The method of solution is described in chapter III. In chapter IV, we present theoretical calculations of the rate of radial flux collapse, of the sequence of field and temperature profiles, and of the rate and distribution of power dissipation during flux jumps in NbTi cylinders for different initial magnetizations, field profiles and average magnetic inductions. In chapter V we systematically compare the experimental and theoretical rate of radial flux collapse for flux jumps triggered along the magnetization curve for a sample of NbTi. We also compare the experimental and theoretical voltage pulses and present theoretical calculations of the field profiles, temperature and power dissipation for two physically distinct flux jumps triggered along this same magnetization curve.

In chapter VI we show that the time of radial collapse of flux in cylinders of type II superconductors is related to the "radial" collapse of flux observed locally on the cylinder during longitudinal propagation of flux jumps along the cylinder.

CHAPTER II

THE DIFFUSION OF FLUX IN NORMAL CONDUCTORS

I. INTRODUCTION

Before analysing the kinetics of flux penetration during flux jumps in type II superconductors (chapter III) we present in this chapter the fundamental characteristics of flux diffusion in normal conductors. We consider two basic simple geometries: a slab of finite width and a cylinder in a parallel field for which the initial field profile is triangular. Such a field and current distribution is a good approximation to the situation frequently encountered in type II superconductors. We assume, however, that at time zero all the currents causing this field profile become resistive. This is a useful simple situation which could be artifically produced in a variety of ways, for instance by applying a large heat pulse with an intense radiation source. Such a situation also corresponds to the limit where the stored magnetic energy in a superconductor is so large compared to the enthalpy that after a time short compared to the total time of flux collapse, enough heat has been produced to make the entire conductor normal.

In sections II and III we show for a slab and cylinder respectively how the flux and magnetic field profiles change as a function of time for the particular case of a triangular initial field profile.

II. SLAB OF FINITE WIDTH

We consider a slab of width 2a in the x-direction and extending inifinitely in the y-z plane (see figure 2.1). The slab, initially assumed to be superconducting, is first cooled in the presence of a magnetic field $-H_o$ and the field then brought to zero. We assume for simplicity, that the density of the induced persistent currents is uniform as in the Bean model (Bean 64) and that $-H_o$ was sufficiently large that persistent currents were induced over the entire width of the slab when the external field was removed. In other words, initially the entire slab is in a critical state of constant current density.

The origin of the x coordinates is taken in the middle of the slab. We assume that at time zero the critical current density drops to zero and hence flux "stored" in the slab starts to disappear.

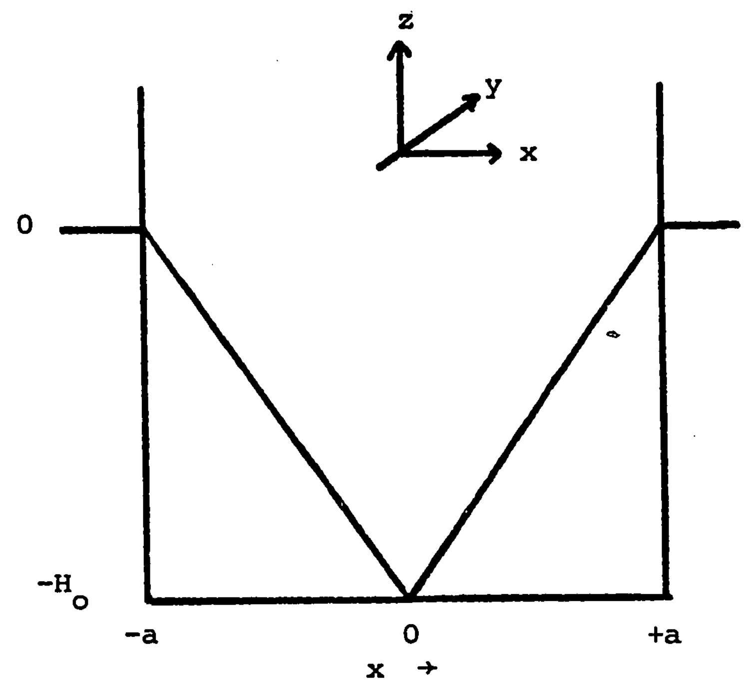

Fig. 2.1

To describe the change in flux, current density and field profile, we use the following equations:

$$\oint \vec{E}.d\vec{\ell} = 10^{-8} \frac{\partial}{\partial t} \oiint H(x).ds \qquad 2\text{-}1$$

$$\vec{E} = \rho_n \vec{J} \qquad 2\text{-}2$$

$$\text{curl } H = \frac{\partial H}{\partial x} = \frac{4\pi}{10} J \qquad 2\text{-}3$$

where $\vec{E}$ is electric field, $H(x)$ is the magnetic field at point x, ρ_n is the normal state resistivity, and $\vec{J}$ is the current density.

Equations 2-1 to 2-3 are Faraday's law of induction in integral form, Ohm's law, and Ampere's law respectively. Equation 2-1 gives the induced electric field due to flux change, whereas equation 2-2 relates this electric field to the current density J and normal state restivity ρ_n in the conductor. To integrate the left hand side of 2-1 we choose a rectangular path in the x-y plane enclosing an area from x = 0 to an arbitrary distance x inside the slab and of length ℓ in the y direction.

For this path equation 2-1 reads:

$$E.\ell = 10^{-8} \frac{\partial}{\partial t}\{ \int_o^x H(x)dx\}. \ \ell$$

or

$$E(x) = 10^{-8} \frac{\partial}{\partial t} \int_o^x H(x)dx \qquad 2\text{-}4$$

We then rewrite 2-3 as:

$$J(x) = \frac{10}{4\pi} \frac{\partial H}{\partial x} \qquad 2\text{-}5$$

and therefore 2-2 becomes:

$$E(x) = \frac{10\rho_n}{4\pi} \left(\frac{\partial H}{\partial x}\right) \qquad 2\text{-}6$$

Equating 2-6 and 2-4 we obtain:

$$\frac{10\rho_n}{4\pi} \frac{\partial H}{\partial x} = 10^{-8} \frac{\partial}{\partial t} \int_o^x H(x)dx$$

Differentiating with respect to x and rearranging yields:

$$\frac{\partial H}{\partial t} = \kappa \frac{\partial^2 H}{\partial x^2} \qquad \text{2-7}$$

where $\kappa = 10^9 \rho_n/4\pi$ is known as the magnetic diffusivity.

Solutions to equation 2-7 are well known. An identical equation is encountered in the study of heat diffusion (Carslaw 59).

A solution to 2-7 may be written as:

$$H(x,t) = \sum_{n=0}^{\infty} e^{-\kappa A_n^2 t} P_n \cos A_n x \qquad \text{2-8}$$

where A_n and P_n are constants and are adjusted to satisfy the boundary conditions. The detailed derivation of the explicit solution for the initial conditions shown in figure 2.1 and the case where ρ_n is a constant (at time t > 0) is given in appendix A. The final result for the evolution of the magnetic field at a depth x with time reads as follows:

$$H(x,t) = \frac{-8H_o}{\pi^2} \sum_{\text{odd } n} \frac{\cos\left(\frac{n\pi}{2a}\right)x}{n^2} e^{-\kappa\left(\frac{n\pi}{2a}\right)^2 t} \qquad \text{2-9}$$

and the total flux threading the slab $\phi(a,t)$ as a function of time is given by the infinite sum:

$$\phi(a,t) = \frac{-32H_o a}{\pi^3} \{ e^{-\kappa(\frac{\pi}{2a})^2 t} - \frac{1}{3^3} e^{-(\frac{3\pi}{2a})^2 t}$$

$$+ \frac{1}{5^3} e^{-\kappa(\frac{5\pi}{2a})^2 t} + \ldots \} \qquad 2\text{-}10$$

Clearly equation 2-10 consists of an infinite sum of exponential terms where the time constants $\tau_n = [\kappa(\frac{n\pi}{2a})^2]^{-1}$ in the series decrease rapidly (as n^2). Further, the amplitude of each of these terms decreases as $1/n^3$. After an interval of time comparable to the largest time constant $\tau_1 = [\frac{4a^2}{\kappa\pi^2}]$ only the first term in the series will contribute since all other terms will become negligible (Bean 69). We can therefore approximate 2-10 by the first term in the series:

$$\phi(a,t) \simeq \frac{-32H_o a}{\pi^3} e^{-t/\tau_n} \qquad 2\text{-}11$$

where

$$\tau_n = \frac{4a^2}{\kappa\pi^2} \simeq \frac{5.093a^2 \times 10^{-9}}{\rho_n} \text{ sec} \qquad 2\text{-}12$$

Figure 2.2 presents a succession of magnetic field distributions H(x) with time. The magnetic field is expressed in units of H_o and the time in units of τ_n. The initial profile is that shown in figure 2.1.

Here we have treated the case of a triangular initial field

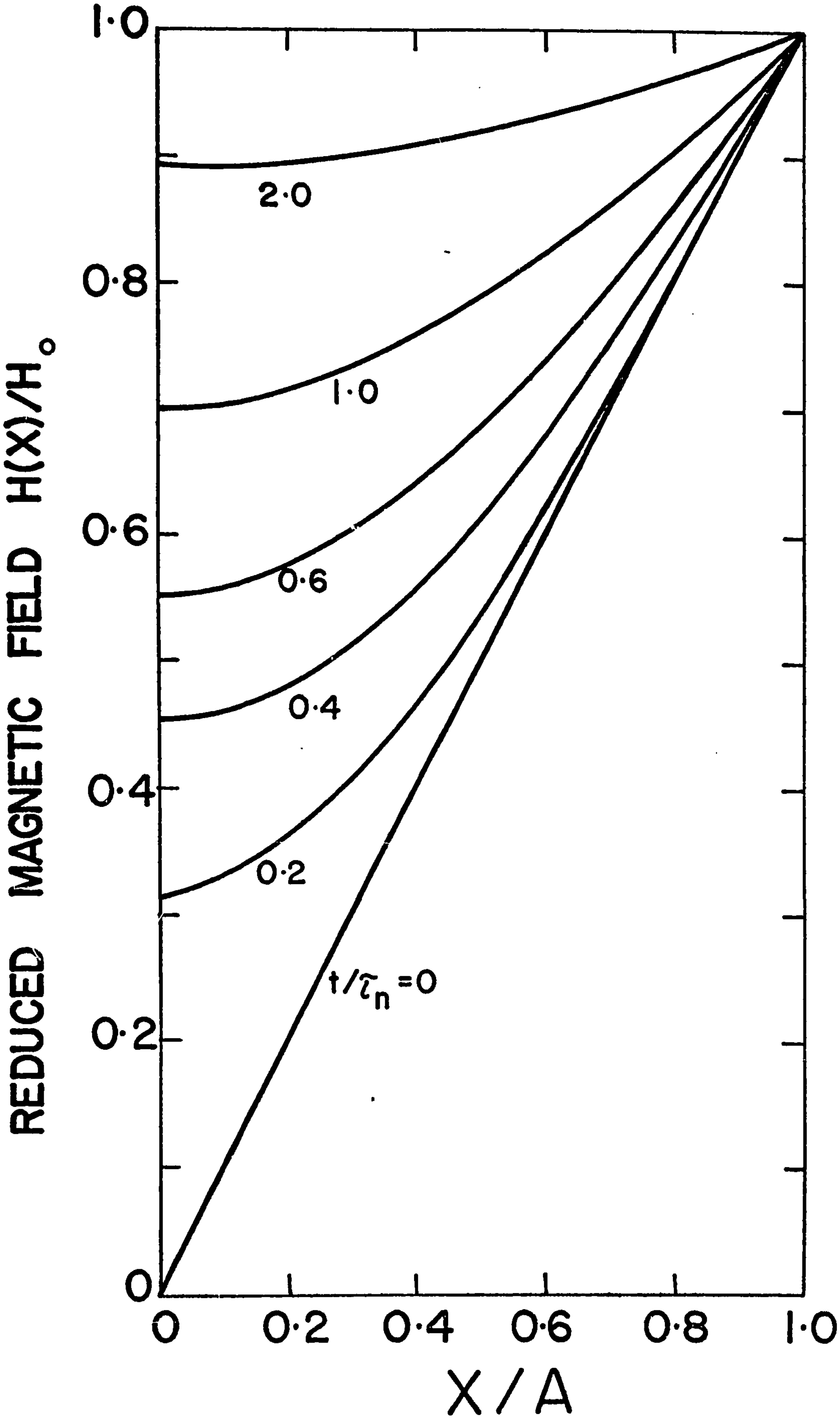

Fig. 2.2: Reduced magnetic field profiles in a normal slab at different reduced time levels t/τ_n. The initial field profile is linear.

profile. Exact solutions have also been obtained for other initial profiles (Carslaw 59). The solutions are of the same type as that presented above. The dominating time constant for these solutions is also the same as that given by equation 2-12.

III. CYLINDER IN A LONGITUDINAL FIELD

In section II we have shown that for a normal slab of finite width the penetration (or exit) of flux and the change in field as a function of time can be described by an infinite sum of exponentials having decreasing time constants and amplitudes. Solutions for the case of an infinite cylinder in an axial field are very similar to solutions for the slab. In this case, however, the trigonometric functions are replaced by Bessel functions (Carslaw 59). Again it is a good approximation to retain only the first term in the expansion and thus to approximate the evolution of flux as a function of time by a single exponential:

$$\phi \simeq \phi_o e^{-t/\tau_n} \qquad 2\text{-}13$$

where the value of τ_n for a cylinder is (Bean 59):

$$\tau_n = \frac{2.17a^2 \times 10^{-9}}{\rho_n} \text{ sec} \qquad 2\text{-}14$$

where a is the radius of the cylinder in cm, and ρ_n is the normal state resistivity in Ω-cm.

Again, equation 2-31 is a good approximation for any initial field profile and the time constant is independent of the initial field profile and also of the magnitude of the initial flux ϕ_o. If we compare the time constants τ_n for the slab of half width a and a cylinder of radius a we obtain the following ratio for the dominant time constants:

$$\frac{\tau_{slab}}{\tau_{cyl.}} \simeq 2$$

Figure 2.3 shows a sequence of field profiles for a cylinder in an axial field where again the initial field profile is taken as triangular, i.e. uniform current density over the entire radius. Again, the magnetic field is normalized to H_o and the time is expressed in units of τ_n. We note that using dimensionless parameters for field and time the field profiles are almost identical in the two cases.

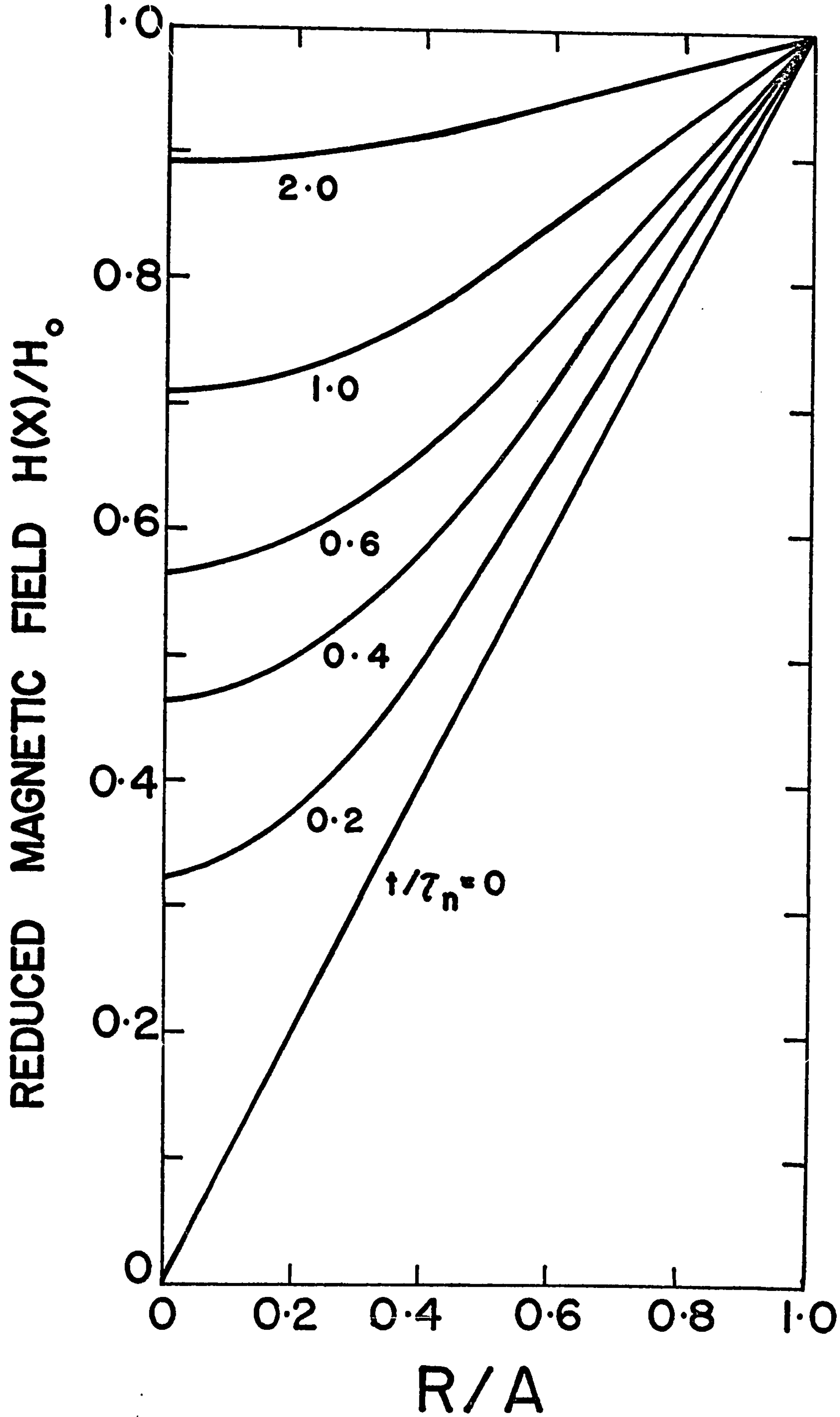

Fig. 2.3: Sequences of magnetic field profiles in a normal cylinder (reduced units). The initial field profile $t/\tau_n = 0$ is linear.

IV. CONCLUSION

In this chapter we have shown that the change in flux in a normal conductor can be described with an infinite sum of exponentials where the time constants in the series decrease rapidly. The coefficients of these terms depend on the initial field profile in the conductor whereas the time constants are independent of profile. After a time which is short compared to the largest time constant but appreciable compared to the other time constants all but the first term can be neglected. This leads to an approximation with a unique time constant independent of field profile. The flux as a function of time can therefore be approximately described with a single exponential:

$$\phi = \phi_o e^{-t/\tau}$$

where τ depends only on the geometry and resistivity of the conductor.

It will be shown in chapter III that the flux change in a superconductor during a flux jump can also be characterized with the aid of a time constant. The value of this time constant however will be shown to depend on numerous quantities, e.g. the initial field profile, the magnitude of the trapped flux, the heat capacity, thermal conductivity, and resistivity. Further the latter three quantities are known to be complicated functions of temperature and magnetic field.

CHAPTER III

PENETRATION OF FLUX IN A TYPE II SUPERCONDUCTOR DURING A FLUX JUMP: THEOETICAL CONSIDERATIONS

I. INTRODUCTION

In chapter II we have shown that flux in a conductor in the normal state decays exponentially with a time constant dependent on geometry and normal state resistivity. In this chapter we consider the change in flux that occurs in a superconductor following a small thermal perturbation applied to a small fraction of its volume at the surface. In a type II superconductor the decay of flux is governed by the ability of the superconductor to carry a current without resistance and therefore depends both on the initial field and current profile and on the critical current density $J_c(T)$. As flux changes occur in a superconducting material, an electric field is induced and joule heating occurs. This joule heating produces a rise in temperature and therefore a decrease in the critical current density J_c. For a flux jump to occur the decrease in J_c due to a small perturbation must be sufficient to cause a macroscopic penetration of flux. This change in magnetic field intensity generates a decrease in J_c

and hence a further change in flux, and so on. The rate of flux penetration will therefore depend on the following; the specific heat C(T), the critical current density $J_c(T)$ and $\partial J_c/\partial T$, factors which are known to affect the stability of a type II superconductor (chapter I), (J_c and $\partial J_c/\partial T$ are field and temperature dependent). Although we can also expect the thermal conductivity and heat transfer to the bath to affect the penetration of flux in a superconductor we will in the following analysis neglect these contributions and therefore assume that flux penetration occurs in a time short compared to the time for heat diffusion.

To solve the problem of flux penetration in a normal conductor we have used (chapter II) Faraday's law of induction, Ampere's law relating current density to the magnetic field, as well as Ohm's law which relates the electric field to the current density in a normal conductor. In the case of a type II superconductor, Faraday's law and Ampere's law are still applicable. Ohm's law, however, can no longer be used to describe the relation between current density and electric field since it does not take into account the possibility of super or resistanceless currents. In section II we exploit an empirical relation relating electric field and current density in type II superconductors. Using this equation instead of Ohm's law we obtain in section III and IV diffusion equations for the flux ϕ in a superconducting slab and cylinder respectively. Since these equations cannot be readily solved analytically we also present in these sections the numerical solution method we developed. Expressing these diffusion equations in terms of dimensionless parameters we present in section V various scaling laws applicable to slabs or cylinders of different widths and diameters. Several results of our calculations with these equations for cylinder geometry will be presented in chapter IV.

II. RELATION BETWEEN ELECTRIC FIELD AND CURRENT DENSITY IN A TYPE II SUPERCONDUCTOR

When a current I is introduced along a flat sheet of a type II superconducting material immersed in a magnetic field which is perpendicular to the surface of the sheet no detectable voltage appears until I exceeds a certain critical current I_c. When the current exceeds I_c however a voltage appears which initially grows rapidly and then becomes linear in I. A typical experimental result is shown in figure 3.1 A linear increase in voltage with increasing current is consistent with the concept of "flux flow" where the viscosity for vortex displacement is independent of velocity (Kim 69). Various explanations have been put forward to account for the initial curved region. Anderson has discussed this in terms of a thermally activated

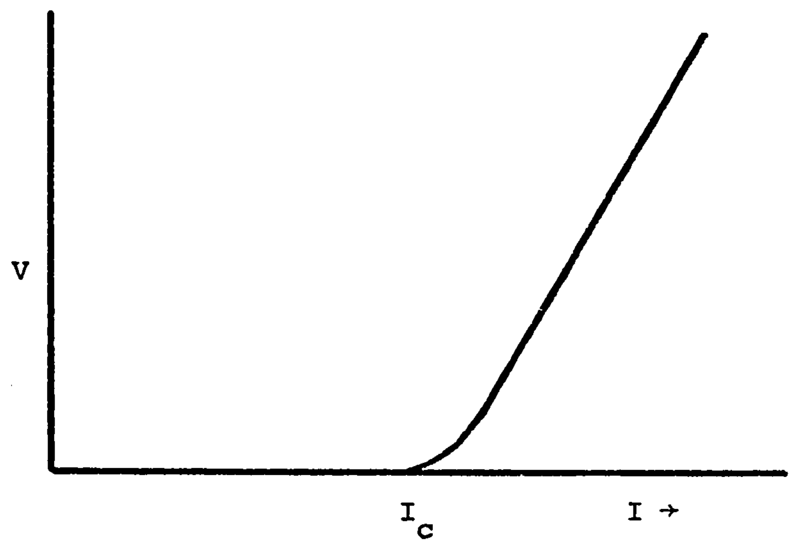

figure 3.1

flux creep mechanism (Anderson 64). Farrell has attributed this to a non-linear effect of the Lorentz force (Farrell 66). The non-linear behaviour may in many cases, however, arise from variations of the critical current along the length of the sample. Jones et al. (Jones 67) have measured the voltage as a function of current I at seven different points along a rod of a tantalum-niobium alloy. Their results indicate that the non-linear region corresponds to a range of current

$$I_c^{min} < I < I_c^{max}$$

where I_c^{max} and I_c^{min} are the minimum and maximum critical currents observed for the segments of the sample. Since they observed only a slight non-linearity when the voltage was measured over small segments of the rod, they conclude that the curved region arises mainly from a superposition of linear V vs I curves with different slopes and thresholds for the different segments along the length of the sample.

They therefore conclude that for a homogeneous sample where the pinning force density is uniform throughout the material, the following relation between electric field E and current density J is valid:

$$E = \begin{cases} 0 & \text{for } J < J_c \\ \rho_f(H,T)\,[J - J_c] & \text{for } J \geqslant J_c \end{cases} \qquad 3\text{-}1$$

where $\rho_f(H,T)$ is denoted as "flux flow resistivity" and is determined from the linear region of the observed voltage variation with current. We note that both ρ_f and J_c will depend on temperature and magnetic field. Values of ρ_f have been measured by Kim and co-workers on NbTa alloys as a function of temperature and external field (Kim 65, 69). Their results indicate that at low temperatures the dependence of ρ_f on H approximately follows the empirical relation:

$$\rho_f/\rho_n = H/H_{c20} \qquad 3\text{-}2$$

where ρ_n is the normal state resistivity and H_{c20} is the critical field extrapolated to absolute zero of temperature. As the field and/or the temperature are increased this linear relation becomes a poor approximation. Further:

$$\rho_f/\rho_n \rightarrow 1 \quad \text{as} \begin{cases} T \rightarrow T_c \\ \text{and/or} \\ H \rightarrow H_{c2}(T) \end{cases} \qquad 3\text{-}3$$

Since during a flux jump the temperature may reach values comparable to and can even exceed T_c we need to use a simple expression for ρ_f in our analysis which adequately describes the observed behaviour and reduces to 3.2 and 3.3 in the limit where $T \rightarrow 0$ and $T \rightarrow T_c$. The following expression satisfies both of these limits and is in good qualitative agreement with experimental measurements (Kim 65, Gilchrist 70):

$$\frac{\rho_f}{\rho_n} = \frac{H}{H_{c20}} + \left(\frac{H}{H_{c2}} - \frac{H}{H_{c20}}\right) \exp\left(\frac{H - H_{c2}}{\lambda}\right) \qquad 3\text{-}4$$

where λ is an adjustable parameter.

III. FLUX PENETRATION IN A TYPE II SUPERCONDUCTING SLAB:

a) Initial Conditions (Time Zero):

We consider a superconducting slab of width 2a extending infinitely in the y-z plane (see figure 3.2). The slab is first cooled in the presence of a magnetic field H_o applied in the z-direction. With the slab in the superconducting state the external field is subsequently increased slowly (hence isothermally) to a final value H_{ex}. For simplicity, the critical current density J_c is assumed to be independent of field over the range between H_o and H_{ex} and to decrease linearly with temperature:

$$J_c = J_o \left[1 - T/T_c(H)\right] \qquad 3\text{-}5$$

The constant J_o is chosen to correspond to the critical current density of the material in the range of field under study. Equation 3-5 is a simple but satisfactory approximation applicable to hard type II superconductors (Hampshire 69, Crow 72). The value of $T_c(H)$ for the material is taken to be the critical temperature in the external field H_{ex} or a certain average field $\langle B \rangle$. Again, for simplicity, the critical temperature T_c was assumed to decrease linearly with magnetic field in the following manner:

$$T_c(H) = T_c(H = 0) \quad [1 - \frac{H}{H_{c20T}}] \qquad 3\text{-}6$$

where H_{c20T} is a field chosen using the values for T_c at $H = 0$ and of H_{c2} at 4.2^oK from the literature. The linear approximation 3.6 is generally valid in the range of temperature $T/T_c > 0.5$ (Babiskin 65, Ferreira de silva 66).

The initial isothermal field penetration corresponds to the Bean critical state model (Bean 64), the slope $\partial H/\partial x$ being given by the Maxwell equation:

$$\frac{\partial H}{\partial x} = \frac{4\pi}{10} J_c \qquad 3\text{-}7$$

The magnetic field penetrates the slab linearly to a distance x_z and is equal to H_o from this point to the center of the slab.

For simplicity we first consider the case where $H_o = 0$ and write the equations for the right hand side of the slab. The value of the local field $H(x)$ at a point x inside the slab is then given by:

$$H(x) = \begin{cases} 0 & \text{for} \quad x < x_z \\ \frac{H_{ex}}{(a - x_z)} (x - x_z) & \text{for } x_z \leqslant x \leqslant a \end{cases} \qquad 3\text{-}8$$

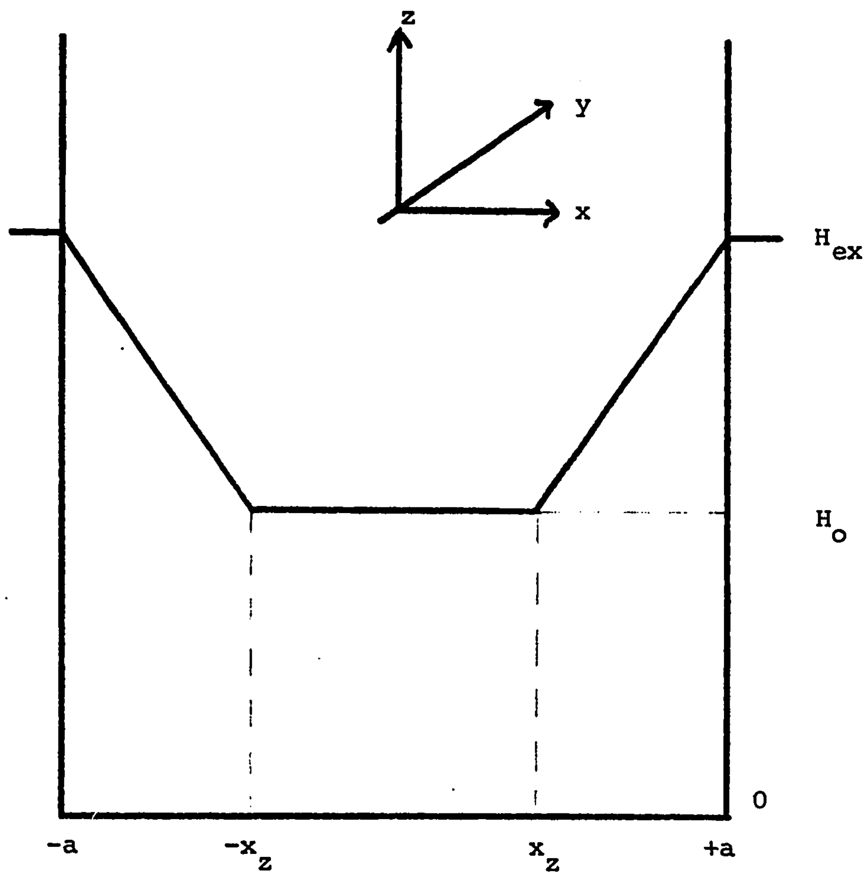

figure 3.2

b) Diffusion Equation:

To obtain a diffusion equation for the magnetic flux we first write the following equations:

$$\oint \vec{E}.\vec{d\ell} = 10^{-8} \frac{\partial}{\partial t} \iint \vec{H}.\vec{ds} \qquad 3\text{-}9$$

$$\frac{\partial H}{\partial x} = \frac{4\pi}{10} J(T) \tag{3-10}$$

$$E(x) = \begin{cases} 0 & \text{for } J < J_c \\ \rho_f(H,T)\left[J - J_c(T)\right] & \text{for } J \geqslant J_c \end{cases} \tag{3-11}$$

where 3-9 is Faraday's law in integral form, 3-10 is Ampere's law for our infinite slab geometry and 3-11 is an empirical relation between electric field and current density in a superconductor discussed earlier in section II. The value of $\rho_f(H,T)$ is given by equation 3-4.

Equation 3-9 can be rewritten as:

$$E(x) = 10^{-8} \frac{\partial \phi(x)}{\partial t} \tag{3-12}$$

where

$$\phi(x) = \int_0^x H(x)\,dx \tag{3-13}$$

Introducing 3-11 in 3-12 and using 3-10 we get for $J > J_c$:

$$\rho_f \left[\frac{10}{4\pi}\frac{\partial H}{\partial x} - J_c(T)\right] = 10^{-8} \frac{\partial \phi}{\partial t} \tag{3-14}$$

Noting that:

$$H(x) = \frac{\partial \phi}{\partial x} \tag{3-15}$$

and $$\frac{\partial H}{\partial x} = \frac{\partial^2 \phi}{\partial x^2} , \qquad 3\text{-}16$$

equation 3-14 is expressed with the flux ϕ as the dependent variable:

$$\frac{\partial^2 \phi}{\partial x^2} - \frac{4\pi}{10} J_c(T) = \frac{4\pi \times 10^{-9}}{\rho_f} \frac{\partial \phi}{\partial t} \qquad 3\text{-}17$$

$$(J \geqslant J_c)$$

Equation 3-17 is a diffusion equation which is valid in the regions of the superconductor where $J \geqslant J_c$. In the regions where no current is circulating initially, the isothermal critical state model is still valid. Since the temperature T is influenced by the rate of penetration of flux in the slab we need a second equation relating T and ϕ to analyze the situation. The Joulean power dissipation due to penetration of flux is given by $\vec{E}.\vec{J}$ Assuming adiabatic conditions we may write:

$$C(T)\frac{\partial T}{\partial t} = \vec{E}.\vec{J} \qquad 3\text{-}18$$

where C(T) is the specific heat per unit volume. Expressing E and J in terms of the flux ϕ we obtain:

$$C(T)\frac{\partial T}{\partial t} = \frac{10^{-7}}{4\pi} \frac{\partial \phi}{\partial t} \cdot \frac{\partial^2 \phi}{\partial x^2} \qquad 3\text{-}19$$

The diffusion of flux in a type II superconducting slab is therefore governed by equations 3-17 and 3-19, and the simultaneous solution of these equations will yield $\phi(x)$, $H(x)$, $T(x)$ and $E.J(x)$ as a function of time.

Before proceeding further in the solution of these equations we note that equation 3-17 is valid only in regions where $J \geqslant J_c$. It does not apply to the region of the superconductor where flux has not yet penetrated (i.e. in the region where $J = 0$). Consequently the equation is valid over the entire slab only in the case where the field has initially penetrated the entire slab ($x_z = 0$).

c) Method of Solution:

The equations to be solved are:

$$\frac{\partial^2\phi}{\partial x^2} - \frac{4\pi}{10} J_c(T) = \frac{4\pi \times 10^{-9}}{\rho_f} \frac{\partial\phi}{\partial t} \qquad \text{3-20}$$

for $J \geqslant J_c$

and

$$C(T)\frac{\partial T}{\partial t} = \frac{10^{-7}}{4\pi} \frac{\partial\phi}{\partial t} \frac{\partial^2\phi}{\partial x^2} \qquad \text{3-21}$$

These equations are subject to the following boundary conditions:

i) at time $t = 0$:

$$H(x) = \begin{cases} 0 & \text{for } x < x_z \\ \dfrac{H_{ex}}{2(a - x_z)} (x - x_z)^2 & \text{for } x_z \leqslant x \leqslant a \end{cases} \qquad \text{3-22a}$$

$$T(x) = \begin{cases} T_b & \text{for } 0 < x < x_t \\ T_b + \delta T & \text{for } x_t \leqslant x \leqslant a \end{cases} \qquad \text{3-22b}$$

ii) at times $t \geqslant 0$:

$$\phi(0) = 0 \qquad \text{3-23a}$$

$$H(a) = H_{ex}$$

$$\text{or} \quad \left(\frac{\partial \phi}{\partial x}\right)_{x=a} = H_{ex} \qquad \text{3-23b}$$

In equation 3-22b we have introduced a temperature perturbation δT in the region of the slab extending from x_t to the surface, where x_t

is treated as an adjustable parameter and

$$(a - x_t) << (a - x_z).$$

To obtain solutions to equation 3-20 which apply regardless of the initial depth of penetration of the field we must analyze the case where the field initially has not penetrated to the center of the slab. As stated earlier, in these cases equation 3-20 is valid initially only in the region $x > x_z$.

<u>Case where $x_z \neq 0$:</u>

In the case where the field has not initially penetrated to the center of the slab the field profiles at a certain time t and t + δt will be approximately as shown schematically in figure 3.3. At time t the field penetrates to a distance x_z while at time t + δt the field has penetrated to a distance x_z' where $x_z' \leqslant x_z$.

At time t equation 3-20 is valid over the range $x_z \leqslant x \leqslant a$ since at that time J = 0 for $x < x_z$. We must therefore, after the thermal perturbation 3-22b has been applied, solve equation 3-20 over the range $x_z \leqslant x \leqslant a$ where x_z decrease with time as flux penetrates deeper into the sample. The boundary condition $\phi(0) = 0$ therefore cannot be used for the time intervals t and t + δt. From

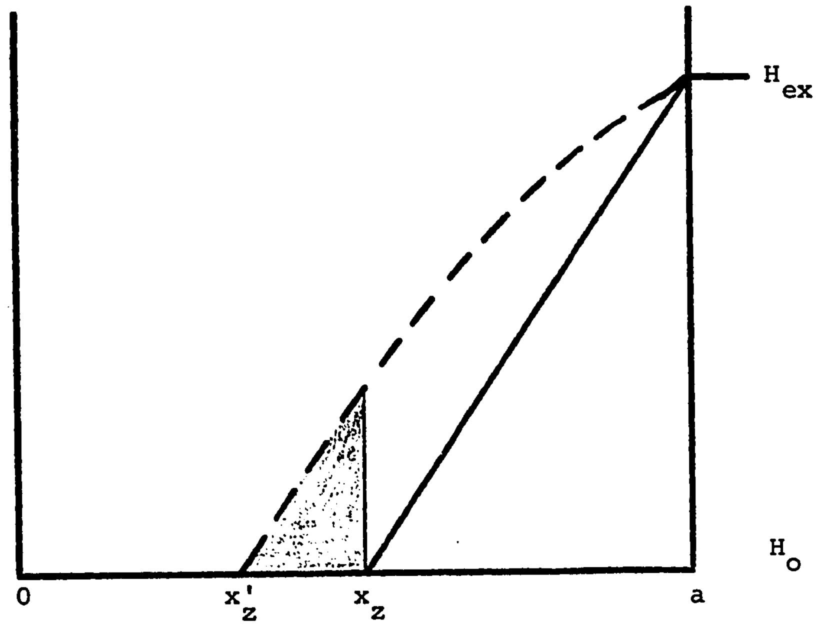

figure 3.3

inspection of figure 3.2 and the previous remarks the reader can appreciate that at point $x = 0$ equation 3-20 is not applicable. We must therefore establish an appropriate boundary condition for the migrating region x_z.

At time level t we have

$$\phi(x_z)_t = 0$$

while at time level $t + \delta t$ this is no longer valid since:

$$\phi(x_z)_{t + \delta t} \geqslant 0$$

To solve for the flux $\phi(x)$ at time level $t + \delta t$ we therefore impose the following artifical albeit reasonable, and temporary boundary condition :

$$\phi_t(x_z) = \phi_{t+\delta t}(x_z) = 0 \qquad 3\text{-}24$$

This boundary condition assumes that initially the flux is constant and equal to zero at point x_z during the interval of time δt between t and $t + \delta t$. This amounts to assuming that any flux crossing the plane $x = x_z$ (shown as the shaded area in figure 3.3) does not influence the distribution of flux on the right hand side of $x = x_z$ and that the electric field at the plane x_z is zero. Although this is a poor approximation when the interval δt is large it is shown in appendix E that the relative contribution due to flux crossing plane x_z becomes negligible in the limit of small time intervals. Equation 3-20 is solved using the artifical boundary condition 3-24 and the ensuing values for the flux $\phi_{t+\delta t}(x)$ and field $H_{t+\delta t}(x)$ are obtained at time level $t + \delta t$ for $x > x_z$. Although the flux $\phi_{t+\delta t}(x_z)$ was initially chosen to be zero at time level $t + \delta t$ the field at this point and time is now no longer equal to zero. We now extrapolate the field configuration to a distance x_z' (see figure 3.3). The shaded area in figure 3.3 is estimated using this extrapolation. This correction to the flux at x_z is then introduced in order to establish a more accurate value for the flux in the entire region between x_z and the surface at time level $t + \delta t$. Taking these corrected values we next compute the temperature profile at this time level.

We have considered several ways of extrapolating the field profile in the region $x < x_z$ at time $(t + \delta t)$:

i) The slope $\partial H/\partial x$ may be taken to be:

$$\frac{\partial H}{\partial x} = \frac{4\pi}{10} J_c(T_b)$$

This simply assumes that the current density flowing in the region $x < x_z$ is equal to the critical current density characteristic of the bath temperature. Since the penetration of flux to the left of x_z gives rise only to a small temperature rise, this approximation should be reasonably accurate.

ii) The approximation which we have used assumes that the slope $\partial H/\partial x$ varies linearly between three grid points situated to the right of x_z. This approximation is discussed in more detail in appendix B.

Using this type of extrapolation the flux at every point $x > x_z$ is then corrected by an amount $\delta\phi = \phi_{t + \delta t}(x_z)$, thus correcting a posteriori the effect of the flux crossing plane x_z. These corrected values of the flux at time $t + \delta t$ are then used to calculate the temperature at this time level.

The numerical methods used to solve 3.20 and 3.21 simultaneously are given in appendix B.

IV SUPERCONDUCTING CYLINDER IN AN AXIAL FIELD

a) Initial Conditions

We consider a superconducting cylinder of radius a extending infinitely in the z direction. The cylinder is first cooled in the presence of a field H_o applied in the z direction and the field subsequently increased to a final value H_{ex} with the cylinder in the superconducting state. We assume a temperature and field dependence of the critical current density J_c and the critical temperature T_c identical to that in the case of the slab, namely:

$$J_c(T) = J_o \left[1 - T/T_c(H)\right] \qquad 3\text{-}26$$

$$T_c(H) = T_c(H = 0) \left[1 - H/H_{c20T}\right] \qquad 3\text{-}27$$

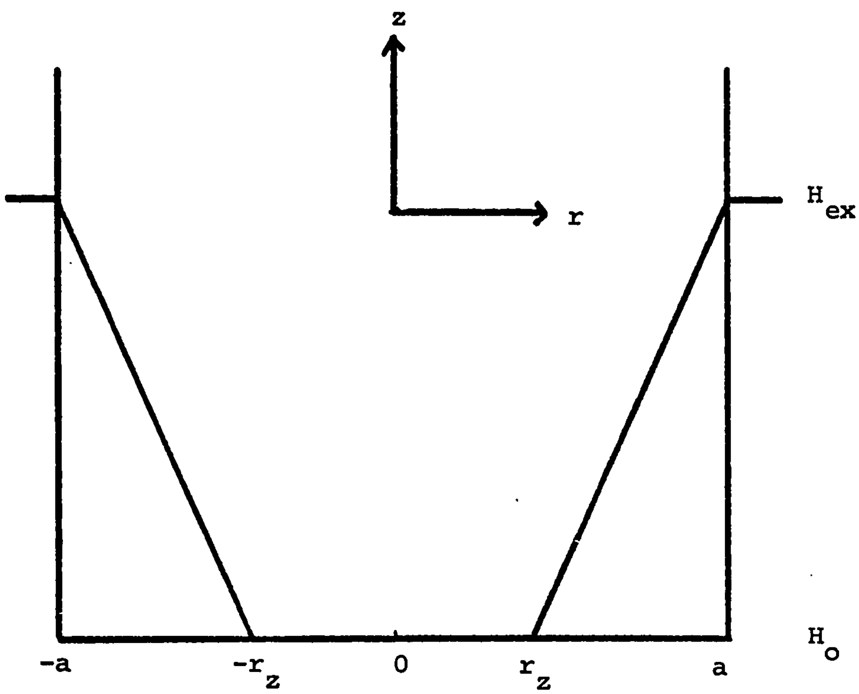

figure 3.4

The field penetration in the cylinder is given by Maxwell's equation which in this case takes the form:

$$\frac{\partial H}{\partial r} = 0 \qquad \text{or} \quad \frac{4\pi}{10} J_c \qquad \text{3-28}$$

and yields a triangular field profile as shown in figure 3.4:

$$H(r) = \begin{cases} 0 & r < r_z \\ \frac{H_{ex}}{(a-r_z)} \left[r - r_z \right] & r_z \leq r \leq a \end{cases} \qquad \text{3-29}$$

where we have assumed $H_o = 0$ for simplicity.

Defining $\phi(r)$, the flux at a given radius r, as

$$\phi(r) = 2\pi \int_o^r H(r) r dr \qquad 3\text{-}30$$

the initial flux (at time zero) is given by:

$$\phi(r) = \begin{cases} 0 & r < r_z \\ \dfrac{2\pi H_{ex}}{6(a - r_z)} \left[2r^3 + r_z^3 - 3r^2 r_z\right] & \text{for } r_z \leqslant r \leqslant a \end{cases} \qquad 3\text{-}31$$

b) Fundamental Equations and Method of Solution:

As in the case of the slab we write the following equations:

$$\int \vec{E}.d\vec{\ell} = 10^{-8} \frac{\partial\phi}{\partial t} \qquad 3\text{-}32$$

where

$$\phi(r) = 2\pi \int_o^r H(r) r dr \qquad 3\text{-}33$$

$$\vec{E} = \begin{cases} 0 & J < J_c \\ \rho_f(H,T)\,[J - J_c] & \text{for } J \geqslant J_c \end{cases} \qquad 3\text{-}34$$

$$\frac{\partial H}{\partial r} = \frac{4\pi}{10} J_c \qquad (\text{for } r > r_z) \qquad 3\text{-}35$$

The value of ρ_f is given by equation 3-4. From 3.32 we obtain:

$$2\pi r\, E(r) = 10^{-8} \frac{\partial \phi}{\partial t} \qquad 3\text{-}36$$

and from 3-33 we obtain:

$$H(r) = \frac{1}{2\pi r} \left(\frac{\partial \phi}{\partial r}\right) \qquad 3\text{-}37$$

which upon differentiation leads to:

$$\frac{\partial H}{\partial r} = \frac{1}{2\pi r} \left[\frac{\partial^2 \phi}{\partial r^2} - \frac{1}{r} \frac{\partial \phi}{\partial r} \right] \qquad 3\text{-}38$$

Combining 3-34, 3-35 and 3-38 yields an equation with the flux as the dependent variable:

$$\frac{\partial^2 \phi}{\partial r^2} - \frac{1}{r} \frac{\partial \phi}{\partial r} - \frac{8\pi^2}{10} r\, J_c(T) = \frac{4\pi \times 10^{-9}}{\rho_f} \frac{\partial \phi}{\partial t} \qquad 3\text{-}39$$

Again we assume adiabatic conditions and obtain the following equation for the temperature:

$$\vec{E}.\vec{J} = C(T)\frac{\partial T}{\partial t}$$

which can be rewritten

$$C(T)\frac{\partial T}{\partial t} = \frac{10^{-7}}{8\pi^2 r}\left(\frac{\partial \phi}{\partial t}\right)\left(\frac{\partial H}{\partial r}\right) \qquad \text{3-40}$$

Equations 3-39 and 3-40 are subject to the following boundary conditions:

a) at time t = 0:

$$\phi(r) = \begin{cases} 0 & r < r_z \\ \dfrac{2\pi H_{ex}}{6(a - r_z)}\left[2r^3 + r_z^3 - 3r^2 r_z\right] & \text{for } r_z \leqslant r \leqslant a \end{cases} \qquad \text{3-41}$$

$$T(r) = \begin{cases} T_b & \text{for} \quad r < r_t \\ T_b + \delta T & \text{for} \quad r_t \leqslant r \leqslant a \end{cases} \qquad \text{3-42}$$

where r_t and δT are adjustable parameters.

b) at times $t \geqslant 0$:

$$\phi(0) = 0$$

$$H(a) = H_{ex}$$

or $\qquad$ 3-43

$$\frac{1}{2\pi a}\left(\frac{\partial\phi}{\partial r}\right)_{r=a} = H_{ex}$$

Again we have introduced an initial temperature perturbation of magnitude δT in a region of the cylinder extending from r_t to the surface.

Equations 3-39 and 3-40 are solved numerically as shown in appendix C. For the case where the field has not initially penetrated to the center of the cylinder equation 3-39 is valid only in those regions where $J \geqslant J_c$ and the technique described for treating this problem in the case of the slab is exploited once more. The analog equations and computer program are described in appendix C.

V SCALING LAWS FOR SLAB AND CYLINDER

It was shown in appendix B and C that the equations governing flux penetration in a slab and cylinder can be expressed in terms of dimensionless parameters. Using these dimensionless parameters we can deduce scaling laws applicable to both slab and cylinder. Since these laws are the same for a slab and a cylinder we will derive them below for the case of the cylinder only.

a) Dimensionless equations

Dimensionless equations describing the reduced flux Φ and reduced temperature θ as a function of time and position have been derived in appendix C for the case of the cylinder. These are:

$$\frac{\partial^2\Phi}{\partial\eta^2} - \frac{1}{\eta}\frac{\partial\Phi}{\partial\eta} - K\eta[1-\theta] = L(\theta)\frac{\partial\Phi}{\partial\xi} \qquad 3\text{-}44$$

$$\frac{\partial\theta}{\partial\xi} = \frac{1}{[G_1\theta + G_2\theta^n]}\left[\frac{\partial\Phi}{\partial\xi}\right]\left[\frac{1}{\eta}\right]\left[\frac{\partial H}{\partial\eta}\right] \qquad 3.45$$

where

$$\Phi = \phi/\phi_o\,, \qquad \phi_o = \pi a^2 H_{ex}$$

$$\eta = r/a, \qquad \xi = t/\tau_n, \qquad \tau_n = 2.17a^2 \times 10^{-9}/\rho_n$$

$$H(\eta) = H(r)/H_{ex}$$

$$G_1 = \frac{4\pi H_o}{H_{c2o}} \gamma\, T_{ch}^2 \;/\; [10^{-7}\, \phi_o^2/a^2]$$

$$G_2 = 4\pi\alpha\, T_{ch}^{n+1} \;/\; [10^{-7}\, \phi_o^2/a^2\,]$$

$$K = \frac{4\pi}{10}\, a^2 J_o/\phi_o$$

$$L(\theta) = 4\pi a^2 \times 10^{-9}/\,(\rho_f \tau_n)$$

The solution of 3-44 and 3-45 depends uniquely on the boundary conditions. The values of the dimensionless variables Φ and θ therefore depend only on the boundary conditions, and on the values of G_1, G_2, K and L. Since the constants G_1 and G_2 depend on the specific heat and equation 3-44 depends on the power n appearing in the expression for the specific heat we will restrict ourselves to the scaling laws valid for a superconductor of a given material with specific characteristics and therefore for which γ, T_c, α and n are fixed. We then look for the scaling laws applicable for cylinders of different radii of this material. For the values of G_1 and G_2 to be constant as the radius of the cylinder varies the ratio $\phi_o H_{ex}/a^2$ must be constant. As a consequence we must take the value of H_{ex} as fixed for the various cylinders.

The constant K may be rewritten as:

$$K = \frac{8\pi}{10} \; a \; J_o/H_{ex} \qquad 3\text{-}46$$

Using Maxwell's equation curl $H = \frac{4\pi}{10} J_c$ the value J_o can be rewritten as:

$$J_o = \frac{H_{ex}}{[\frac{4\pi}{10}]\,[1 - \theta_b]\,[a - r_z]}$$

where θ_b and r_z are the reduced bath temperature and the radius of field penetration respectively. Using this value of J_o is 3-46, we obtain:

$$K = \frac{2}{(1 - \eta_z)(1 - \theta_b)}$$

The value of K depends therefore only on the initial reduced radius of penetration η_z and the reduced bath temperature θ_b.

The value of $L(\theta)$ can be rewritten as:

$$L(\theta) = 2.17 \times 4\pi \,/(\rho_f/\rho_n)$$

where the value of ρ_f/ρ_n depends on the temperature θ and on the average field H in the cylinder, and is independent of the radius a. Since the boundary conditions are independent of the radius a and depend only on the initial reduced field profile the solutions to equations 3-44 and 3-45 are identical for cylinders of different radii provided the external field is kept fixed and the reduced radii of penetration η_z are the same. This is shown schematically in figure 3.5 for two cylinders of radii a and b and radii of penetration r_1 and r_2. The condition to be satisfied in this case is:

$$\frac{r_1}{a} = \frac{r_2}{b}$$

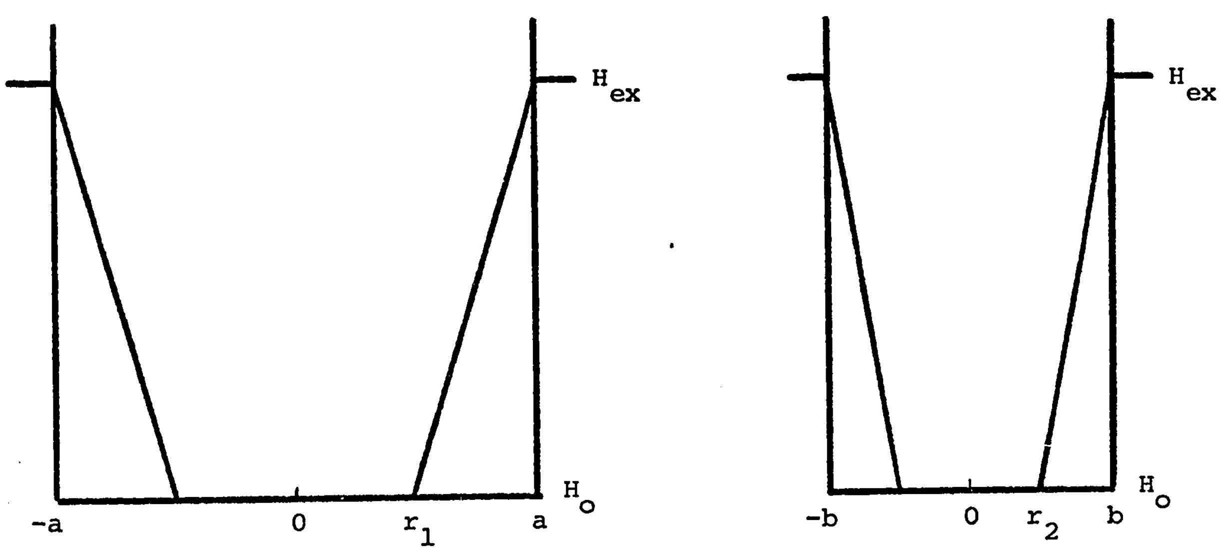

figure 3.5

The scaling law summarized in figure 3.5 means that solutions to equations 3-44 and 3-45 are identical as long as the initial profiles of field are identical in terms of the dimensionless radius η and as long as the external field, as well as bath temperatures are the same. In other words, using the Bean approximation of an initially uniform critical current density we obtain solutions which are size independent. We also note that these size independent solutions correspond to cylinders for which magnetization curves are identical. This implies that a direct comparison between a large and a small cylinder requires that the value of J_c be larger in the smaller cylinder (see figure 3.5).

b) <u>Scaling Laws for Flux, Field and Time</u>:

Since the solutions of equations 3-44 and 3-45 are identical for the two cylinders and field profiles shown in figure 3.5 the values of Φ and θ will be identical for these two cylinders at a given value of the reduced time ξ. The absolute value of the flux ϕ will however be proportional to the square of the radius

$$\phi \propto a^2$$

The magnetic field H at a given value of the reduced radius η and time ξ will be independent of the radius a.

The absolute time will be proportional to the radius squared

$$t \propto a^2$$

c) Scaling Laws for $\partial\phi/\partial t$ and Power

Since both the values of the flux ϕ and time t are proportional to the square of the radius a^2 the value of $\partial\phi/\partial t$ will be independent of radius at a given value of the reduced time ξ.

The power at a given time is given by:

$$E.J = \frac{10^{-8}\ H_{ex}^2}{\left(\frac{8\pi}{10}\right)^2 \tau_n} \quad \frac{\partial\Phi}{\partial\xi} \cdot \frac{1}{\eta} \ \frac{\partial H}{\partial\eta}$$

and is therefore inversely proportional to the radius squared at a given value of the reduced time ξ:

$$P(\eta,\ \xi) \propto\ 1/a^2$$

CHAPTER IV

RADIAL COLLAPSE OF FLUX IN TYPE II SUPERCONDUCTING CYLINDERS: THEORETICAL CALCULATIONS

I. INTRODUCTION

In this chapter we present results of theoretical calculations for the speed of radial flux collapse, power dissipation, temperature and field distributions during flux jumps in $Nb_{.36}Ti_{.64}$ cylinders subject to different initial conditions. The calculations are based on the equations and method of solution developed in chapter III.

In section II of this chapter, we present a summary of the assumptions and the values of the different parameters used in the calculations. The role of the initial magnetic moment $<4\pi M>$ on the kinetics of flux jumps is investigated in section III. We calculate the speed of radial flux collapse, field, power dissipation, and temperature profiles as a function of time for flux jumps corresponding to different initial magnetizations and therefore different stored magnetic energies. The results are found to depend strongly on $<4\pi M>$. In section IV we study the influence of the initial field profile for several constant values of magnetization and a constant average magnetic induction. The initial configuration of the field profile is found to affect strongly the kinetics of flux jumping as well as the size of flux jumps. Steep profiles of flux are shown to lead to very small but rapid rearrangements of flux near the surface of the cylinder. The effect of the average magnetic induction <B> on the time of radial collapse is treated in section V. In section VI we present the results of calculations of the radius of field penetration as a function of time.

II. VALUES OF CONSTANTS AND ASSUMPTIONS USED IN THE CALCULATIONS

The calculations presented in this chapter pertain specifically to $Nb_{.36}Ti_{.64}$ cylinders. Some of the properties of this material such as critical temperature, normal state resistivity, and specific heat are listed in tables I and II. We summarize below the simplifying assumptions we have used in the calculations for the variation of critical field and of critical current density with temperature. We also give the expression used for the flux flow resistivity and describe the perturbation used in the calculations.

a) Critical Temperature and Field:

The critical field H_{c2} was assumed to decrease linearly with temperature:

$$H_{c2}(T) = H_{c20T} \left[1 - T/T_c(H)\right]$$

where H_{c20T} is an adjustable parameter chosen to be equal to 215 kG hence leading to the observed value of 120 kG for H_{c2} at $4.2^{o}K$. Rearranging the above expression, we obtain a linear decrease of the critical temperature T_c with field H:

$$T_c(H) = 9.5^{o}K \; (1 - H/H_{c20T})$$

where the critical temperature in zero field was chosen to correspond to the observed value of $9.5^{o}K$ (see table II). The value of H in the above expression for $T_c(H)$ was set equal to $\langle B \rangle$, the initial average magnetic induction.

b) Critical Current Density:

The critical current density was also assumed to decrease linearly with temperature. Further we take J_c as independent of any local variations of magnetic induction within the sample but as determined by the average value of the magnetic induction:

$$J_c(T) = J_o[\,1 - T/T_c(\langle B \rangle)\,]$$

The first assumption is in good agreement with measurements of J_c as a function of temperature in a Nb - 44 wt% Ti alloy (Hampshire 69). The value of J_o is adjusted so as to give the required magnetization for a specified field profile.

c) Specific Heat:

The specific heat in the superconducting state was taken to the described by the relation

$$C_s(T) = \frac{\langle B \rangle}{H_{c2}} \gamma T + \alpha T^n$$

where γ, α and n are given in table II. $\langle B \rangle$ is the average magnetic induction in the sample.

d) Flux-flow Resistivity:

Since no measurements exist for the flux-flow resistivity of NbTi, the following empirical relation found to be valid for several materials was used:

$$\rho_f/\rho_n = \begin{cases} \dfrac{H}{H_{c20}} + \left(\dfrac{H}{H_{c2}} - \dfrac{H}{H_{c20}}\right) \exp\left(\dfrac{H-H_{c2}}{10\text{kG}}\right) & \text{for } H < H_{c2} \\ 1 & \text{for } H \geqslant H_{c2} \end{cases} \qquad 4.1$$

In this expression H was set equal to $\langle B \rangle$ the initial average magnetic induction in the sample. H_{c2} is the critical field dependent on the local temperature in the sample. H_{c20} is the critical field at absolute zero and was set equal to 150 kG. Curves of ρ_f/ρ_n for the above expression are shown in figure 4.1, and are in good qualitative agreement with experimental measurements in NbTa (Kim 65) and Nb (Gilchrist 70).

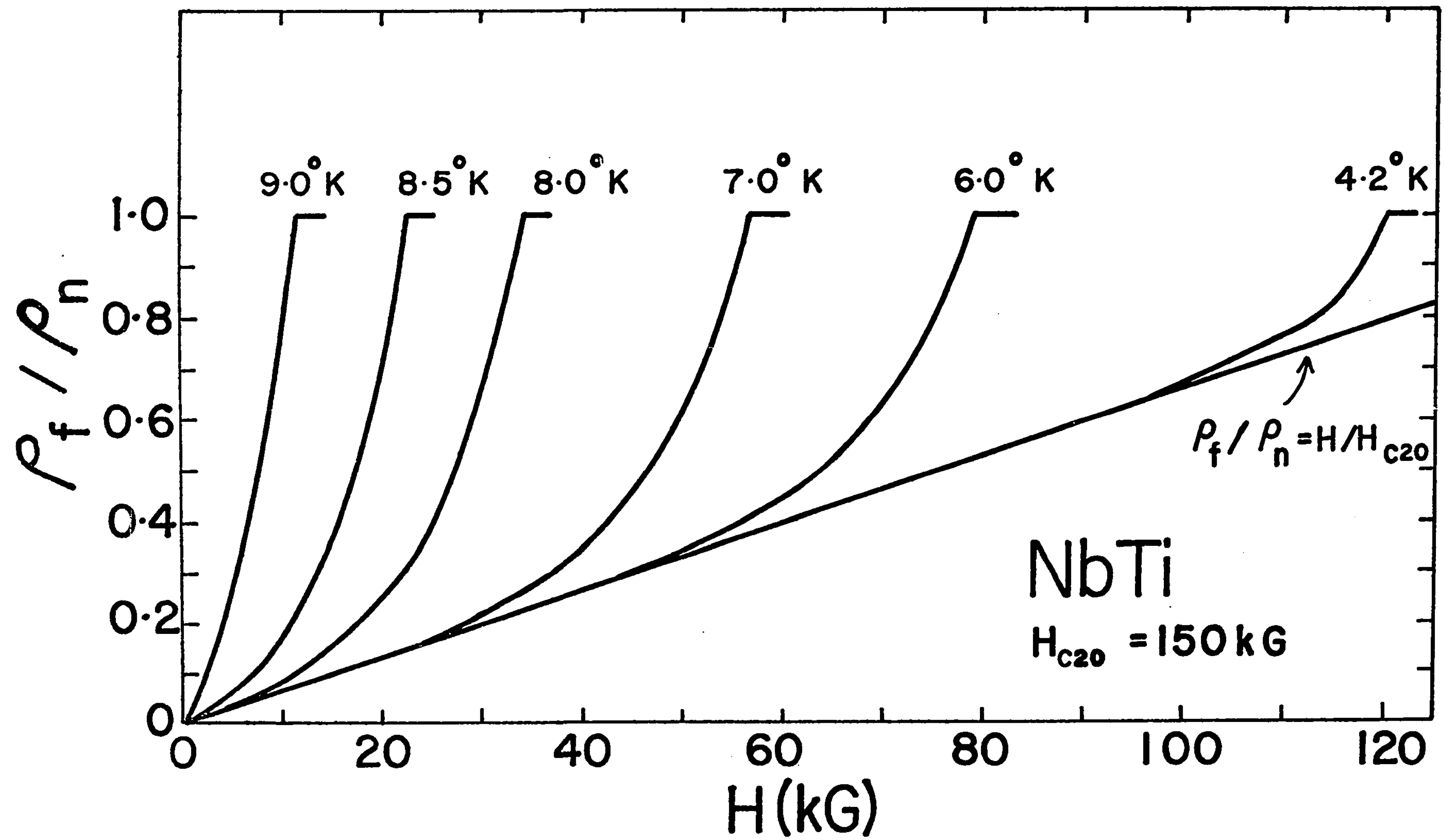

Fig. 4.1: Curves of flux flow resistivity in NbTi obtained from equation 4-1.

e) Perturbation

The perturbation used to initiate flux jumps in our calculations was a thermal pulse causing a temperature rise at time zero equal to 1% of the bath temperature and extending from the surface of the cylinder to a depth equal to 1% of the radius of the cylinder.

III. EFFECT OF MAGNETIZATION $\langle 4\pi M \rangle$ ON RADIAL COLLAPSE OF FLUX IN NbTi CYLINDERS.

a) Introduction:

In this section we present results of calculations of the effect of magnetization $\langle 4\pi M \rangle$ on the time of radial collapse of flux, and on the sequences of profiles of field, temperature and power density for flux jumps occurring in NbTi cylinders. We consider the special case where the field has initially penetrated to the center of the cylinder and where the average magnetic induction $\langle B \rangle$ is held constant and taken equal to 10.0 kG.

In these calculations the field appearing in the expressions for the flux flow resistivity, critical temperature and specific heat was taken to be constant during the flux jumps and set equal to $\langle B \rangle$ everywhere inside the cylinder. We have therefore neglected effects due to changes in resistivity, critical temperature and specific heat with local variations in magnetic field inside the sample. We note that this approximation is valid when $<B> \gg <4\pi M>$.

To characterize the average time of radial collapse, we arbitrarily selected a time interval τ_R which we call the relaxation time and define as the width of the curve $\frac{\partial\phi}{\partial t}$ vs time at 1/e of the maximum height. The total time of duration of flux jumps was characterized by the time τ_t defined as the time required for the value of $\partial\phi/\partial t$ to decrease to 20% of its maximum value.

b) Time of Collapse as a function of $<4\pi M>$:

Figures 4.2 and 4.3 show respectively the total time τ_t and the relaxation time τ_R of radial collapse of flux in NbTi cylinders, as a function of initial magnetization $<4\pi M>$. These values are expressed as ratios of the normal state relaxation time τ_n and are therefore applicable to cylinders of any diameter. We note in these two curves that for small values of $<4\pi M>$ in the region 1.5 kG the values of τ_R and τ_t are very large. These quantities vary approximately as $1/<4\pi M>$ for $<4\pi M>$ smaller than $\sim$ 3.5 kG. For values of $<4\pi M>$ between 3.5 kG and 4.5 kG the reduced relaxation time τ_R/τ_n decreases very rapidly, and then tends more slowly towards 1 for $<4\pi M>$greater than 5 kG. The total time τ_t behaves similarly but decreases more gradually.

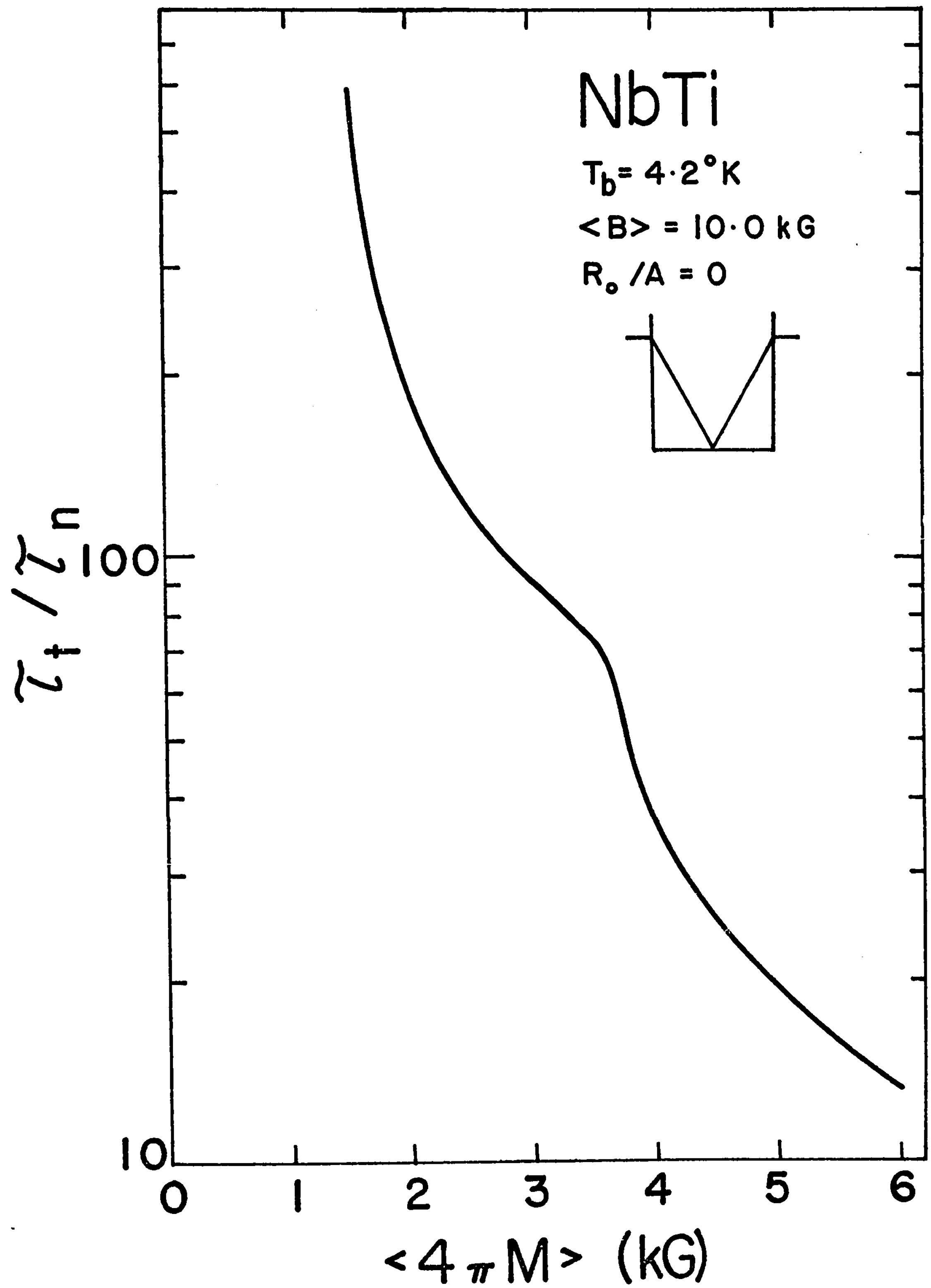

Fig. 4.2: Total time of duration of flux jumps as a function of <4πM> for NbTi cylinders.

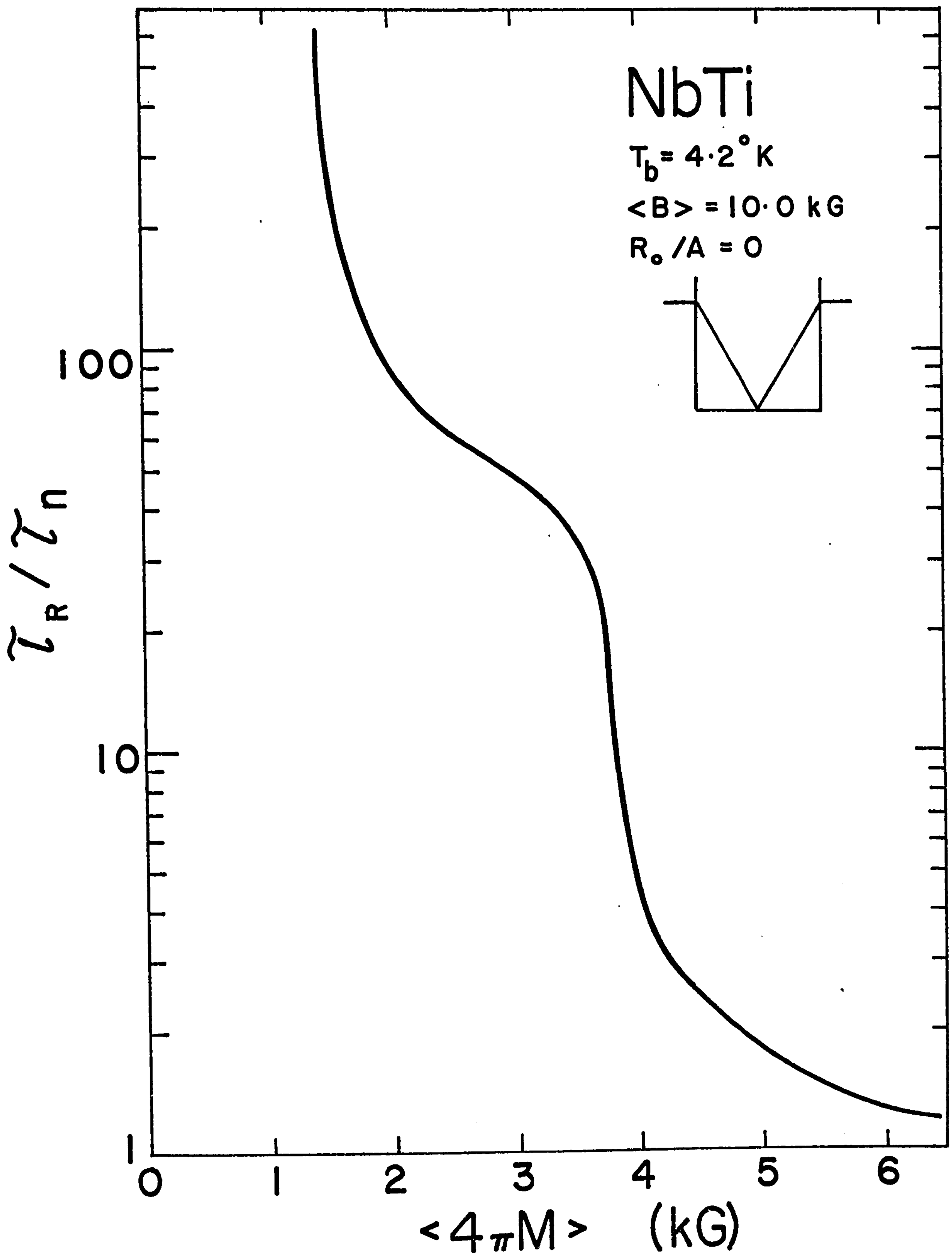

Fig. 4.3: Relaxation time τ_R of flux jumps as a function of <4πM> for NbTi cylinders.

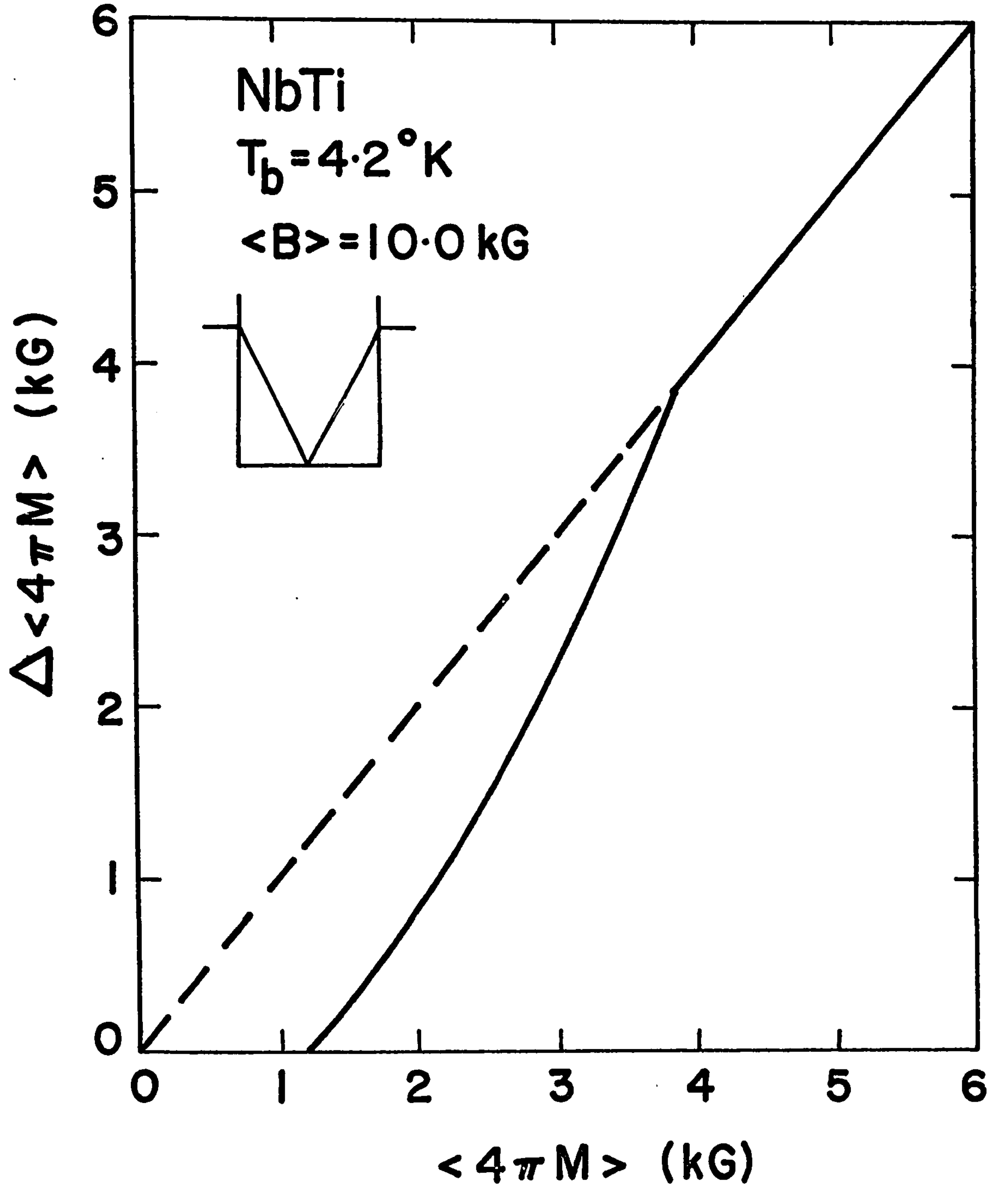

Fig. 4.4: Size of flux jumps Δ<4πM> as a function of initial magnetization <4πM> in NbTi cylinders. The average induction <B> is 10.0 kG and the initial field profile corresponds to full penetration of field.

The decrease in magnetization which occurred during the flux jumps is shown in figure 4.4 (solid line). We note that for $<4\pi M> < 1.3$ kG no flux jumps are encountered. As $<4\pi M>$ is increased beyond this threshold the flux jumps increase rapidly in size. When $<4\pi M> \sim 2.5$ kG, the drop in magnetization during the flux jump is $\sim 50\%$. For $<4\pi M> > 4$ kG the flux jumps are all complete and $\Delta<4\pi M> = <4\pi M>$.

The large values of τ_R and τ_t shown in figures 4.2 and 4.3 for $<4\pi M> \sim 1.4$ kG therefore correspond to very small flux jumps near the limit of stability. When $<4\pi M> < 3$ kG the temperatures reached in the superconductor during the flux jumps are lower than $\sim 8^{o}K$ (see section d) and lead therefore only to an insignificant rise in flux flow resistivity for an ambient field H of 10 kG (see figure 4.1). Accordingly, the small change in flux flow resistivity cannot account for the appreciable and rapid change in τ_t and τ_R in the range $1.4 \text{ kG} < <4\pi M> < 3$ kG. The behaviour of τ_t and τ_R in this region is difficult to explain qualitatively since it appears to be linked to several interdependent factors; namely the stability of the profiles, the peak value of $\partial\phi/\partial t$ and the extent of the flux collapse.

The more rapid drop of τ_R and τ_t which occurs when $<4\pi M> > 3.5$ kG can however be attributed to a large increase in flux flow resistivity during the event. In these circumstances, temperatures in excess of $8^{o}K$ are reached during the flux jumps (see section d).

For large magnetizations we expect that both τ_t and τ_R will tend to a definite limit of the order of τ_n. This limit corresponds to an instantaneous increase in the flux flow resistivity to the normal state value (and a corresponding decrease in J_c) at the onset of the flux collapse. Wee see in figures 4.2 and 4.3 that this limit is approached when $<4\pi M> \sim 6$ kG.

c) <u>Shape of the Voltage Pulses $\partial\phi/\partial t$ vs time</u>:

Figures 4.5 and 4.6 show the calculated voltage pulses $\partial\phi/\partial t$ vs t detected by a pick-up coil of one turn at the surface of a NbTi cylinder during flux jumps corresponding to several values of the initial magnetization $<4\pi M>$. We note that the height of these pulses, which varies between $\sim 4 \times 10^{-3}$ volts for $<4\pi M> = 1.75$ kG and ~ 2 volts for $<4\pi M> = 5.0$ kG, depends strongly on the initial magnetization.

The shape of the pulses also depends on $<4\pi M>$. For small values of $<4\pi M>$ (figure 4.5) the pulses are regular in shape. For magnetizations equal to or greater than 3.5 kG (figure 4.6), however, a structure appears in the pulses. In these instances the value of $\partial\phi/\partial t$ increases rather slowly at first and then increases sharply to a maximum value before dropping rapidly to zero. This change in pulse shape as the initial magnetization is increased can be understood

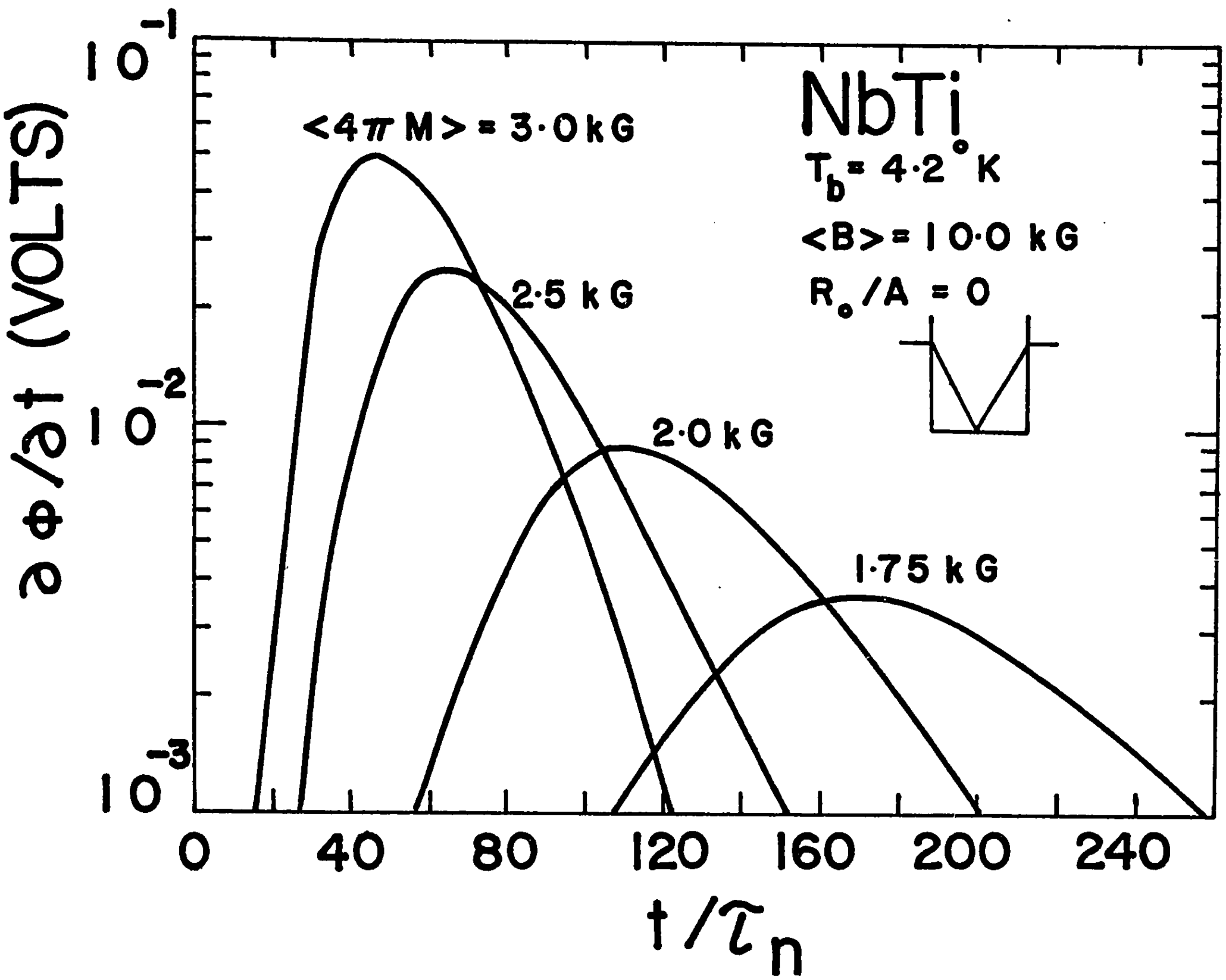

Fig. 4.5: Calculated voltage pulses $\partial\phi/\partial t$ vs t/τ_n seen by a pick-up coil of one turn surrounding a NbTi cylinder during flux jumps with initial magnetizations of 1.75 kG, 2.0 kG, 2.5 kG and 3.0 kG.

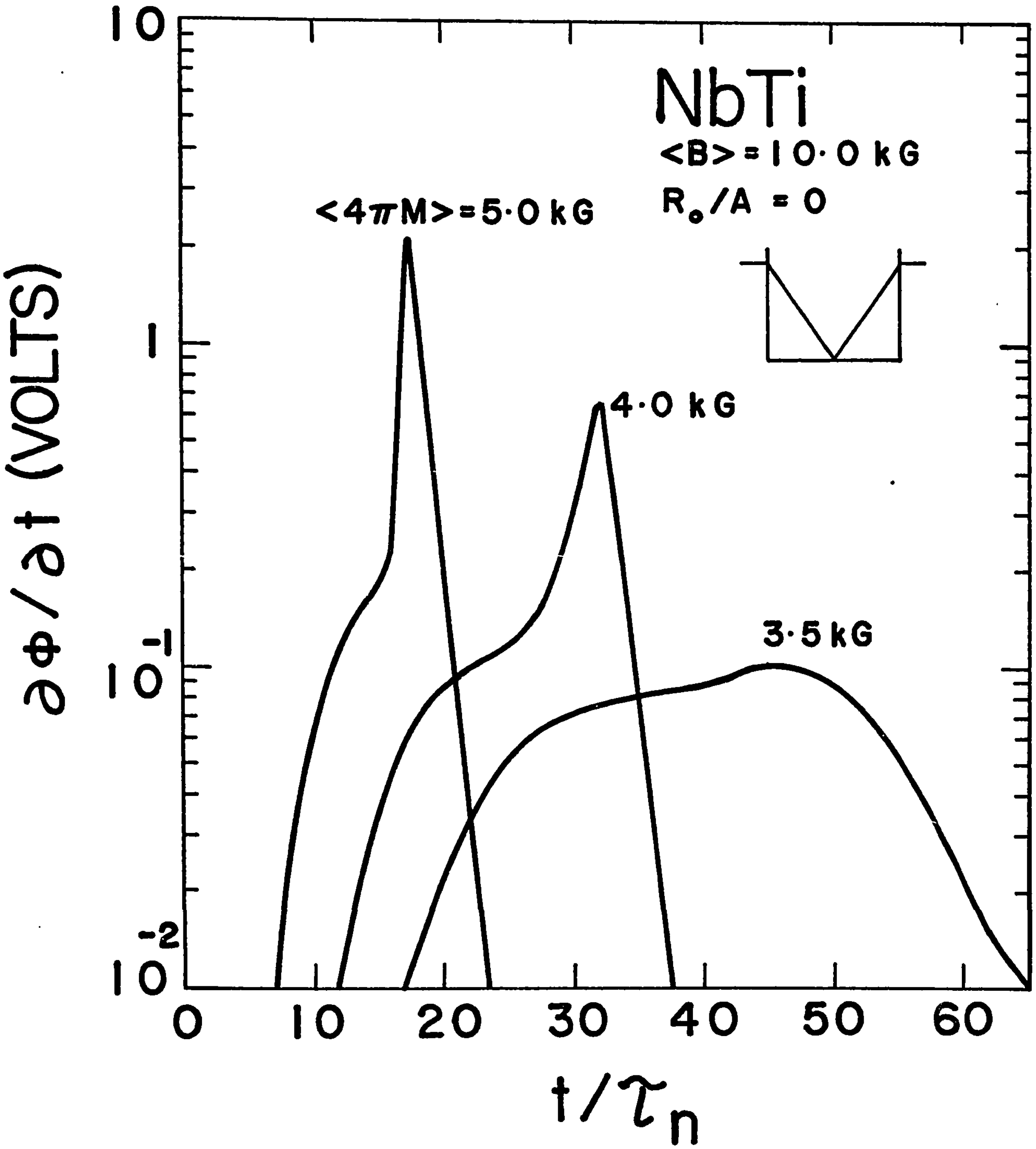

Fig. 4.6: Calculated voltage pulses $\partial\phi/\partial t$ vs. t/τ_n detected by a pick-up coil of one turn surrounding a NbTi cylinder during flux jumps with initial magnetizations of 3.5 kG, 4.0 kG and 5.0 kG.

qualitatively in terms of the variation of flux flow resistivity with temperature. In figure 4.1 we note that for a field of 10 kG the value of ρ_f/ρ_n is almost constant for all temperatures lower than $\sim 8^{\circ}K$ and increases rapidly towards unity when temperatures greater than $\sim 8^{\circ}K$ are reached. At the beginning of the flux jumps described above the flux flow resistivity is therefore of the order of $\langle B\rangle/H_{c2}\cdot\rho_n \sim 0.067\rho_n$. If the flux jump is small and only leads to temperatures less than $\sim 8^{\circ}K$ the effective resistivity remains approximately constant during the jump. This feature is responsible for the regular voltage pulses shown in figure 4.5. If, however, temperatures in excess of $\sim 8^{\circ}K$ are attained in some regions of the sample during the flux jump, the effective resistivity in those regions will then quickly approach ρ_n and the magnitude of $\partial\phi/\partial t$ will consequently increase rapidly (see figure 4.6). The flux will thereafter decay with a time constant of the order of τ_n. The sudden increase in flux flow resistivity above a threshold temperature is therefore responsible for the structure in the voltage pulses appearing in figure 4.6.

Another important feature of the pulses shown in figures 4.5 and 4.6 is that the peak value of $\partial\phi/\partial t$ occurs at a time which depends on $\langle 4\pi M\rangle$. The time for the avalanche to reach a maximum is longer for small initial magnetizations. The peak value occurs at $t/\tau_n \sim 180$ for $\langle 4\pi M\rangle = 1.75$ kG and at $t/\tau_n \sim 18$ for $\langle 4\pi M\rangle = 5$ kG.

d) Field, Temperature and Power Dissipation Profiles During a Flux Jump

To illustrate characteristics of flux jumps for different initial magnetizations we present in this section calculated values of the field, temperature and power dissipation as a function of radial position at different times for flux jumps of three different magnetizations. The field and temperature profiles are presented in terms of reduced parameters and are therefore applicable to cylinders of arbitrary diameter. The power dissipation density is inversely proportional to A^2 and is therefore presented for a cylinder of fixed radius, chosen to be equal to 0.1 cm.

i) $\langle 4\pi M\rangle = 2.0$ kG

Figures 4.7, 4.8 and 4.9 show respectively the field, temperature and power dissipation at different times for an initial magnetization of 2 kG. In this case only a small amount of flux penetrated the cylinder during the flux jump (see figure 4.7) giving rise to a maximum temperature of $\sim 6.2^\circ$K (see figure 4.8). The power dissipation is seen in figure 4.9 to peak for values of $R/A \sim 0.7$ and to reach a maximum value after a time $t/\tau_n \sim 100$, and therefore just before the maximum value of $\partial\phi/\partial t$ is reached (see figure 4.5).

ii) $\langle 4\pi M\rangle = 3.0$ kG:

Figures 4.10, 4.11 and 4.12 show sequences of field, temperature and power dissipation profiles for an initial magnetization of 3.0 kG. In this case the flux jump is greater because of the larger stored magnetic energy. The field profiles (figure 4.10) however show the same features as in the previous case. The final temperature in this case is of the order of 8°K near the surface of

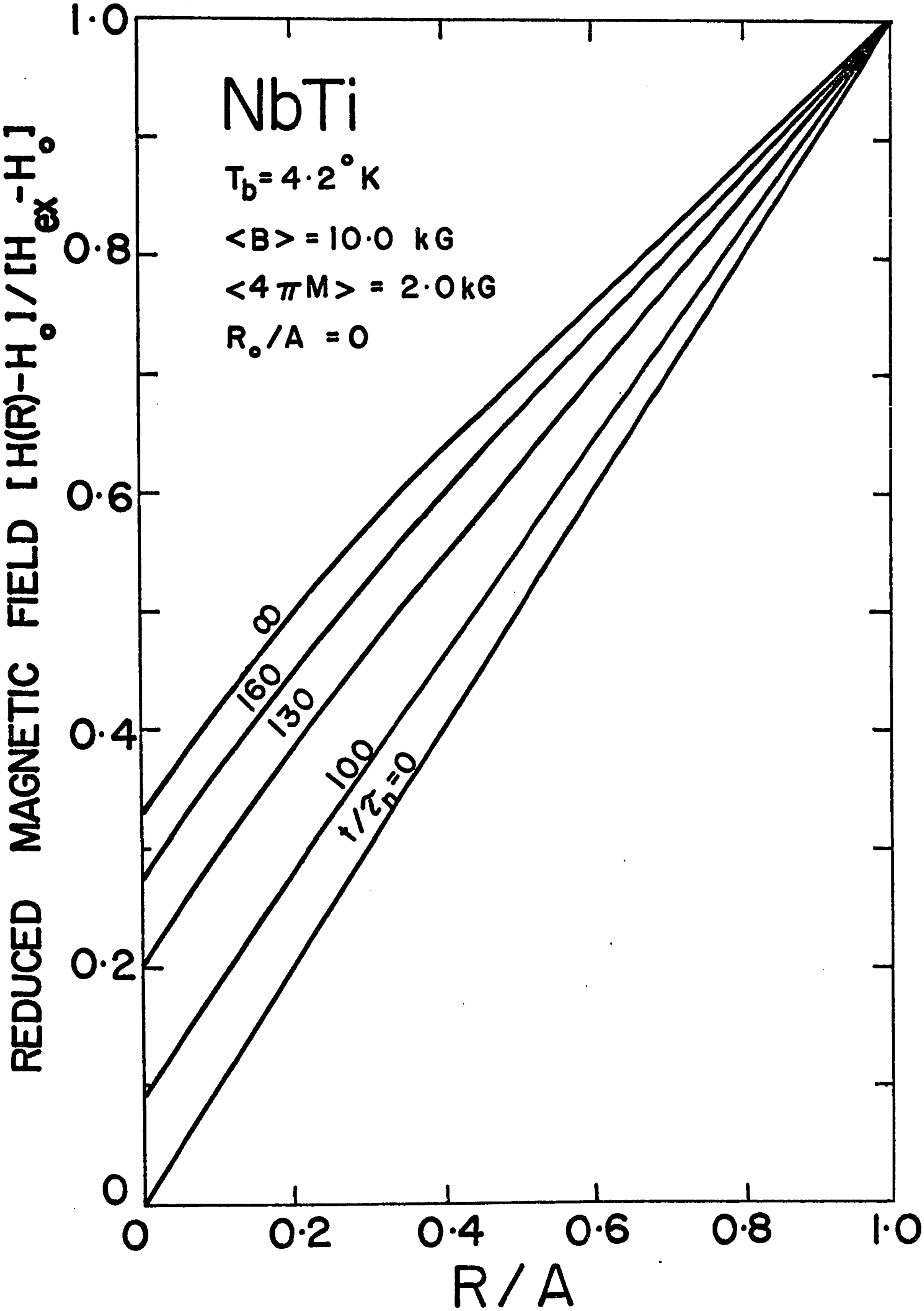

Fig. 4.7: Sequences of magnetic field profiles in a NbTi cylinder during a flux jump when $<4\pi M>$ = 2.0 kG, $R_o/A = 0$

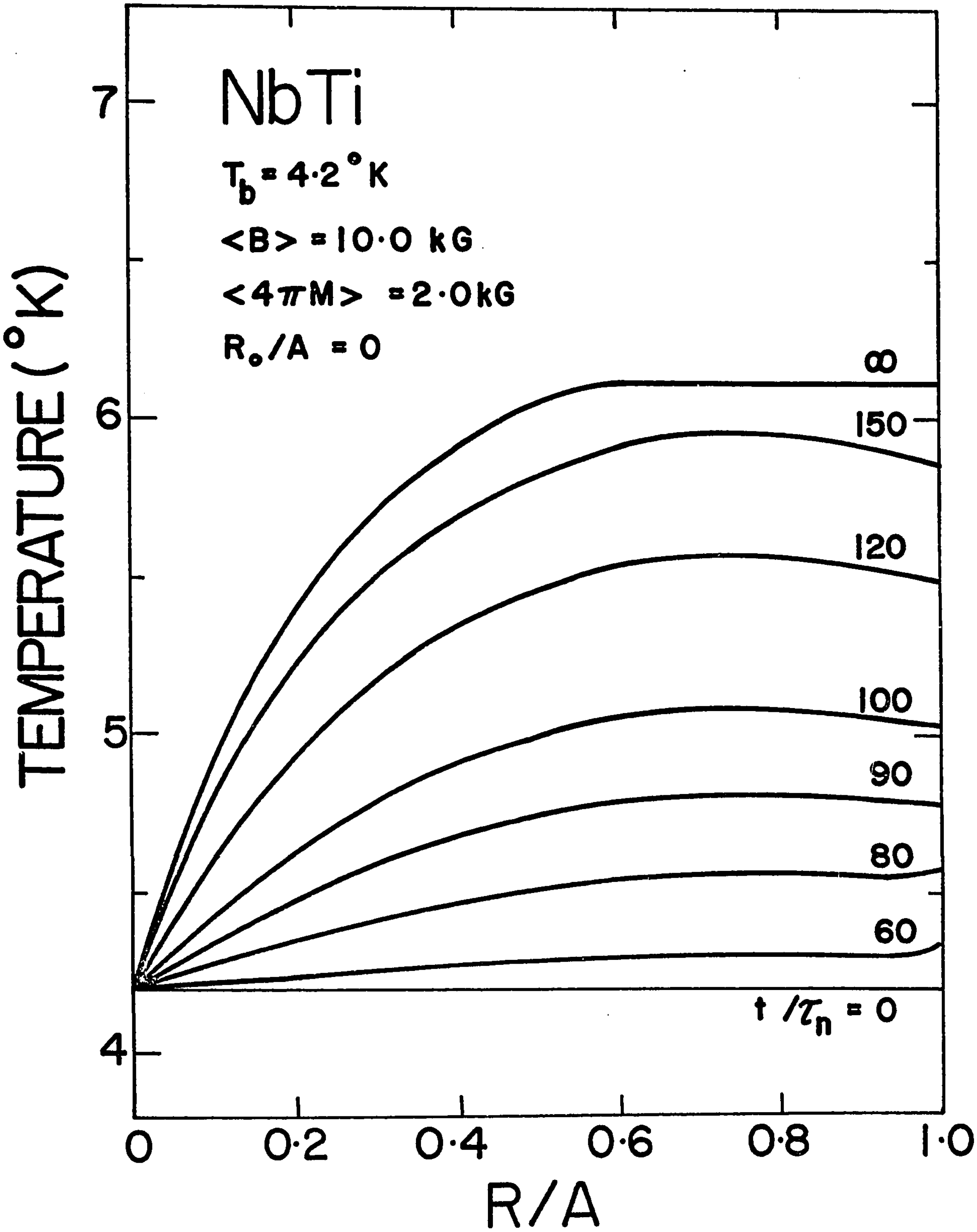

Fig. 4.8: Sequences of temperature distributions in a NbTi cylinder during a flux jump when <4πM> = 2.0 kG, $R_o/A = 0$.

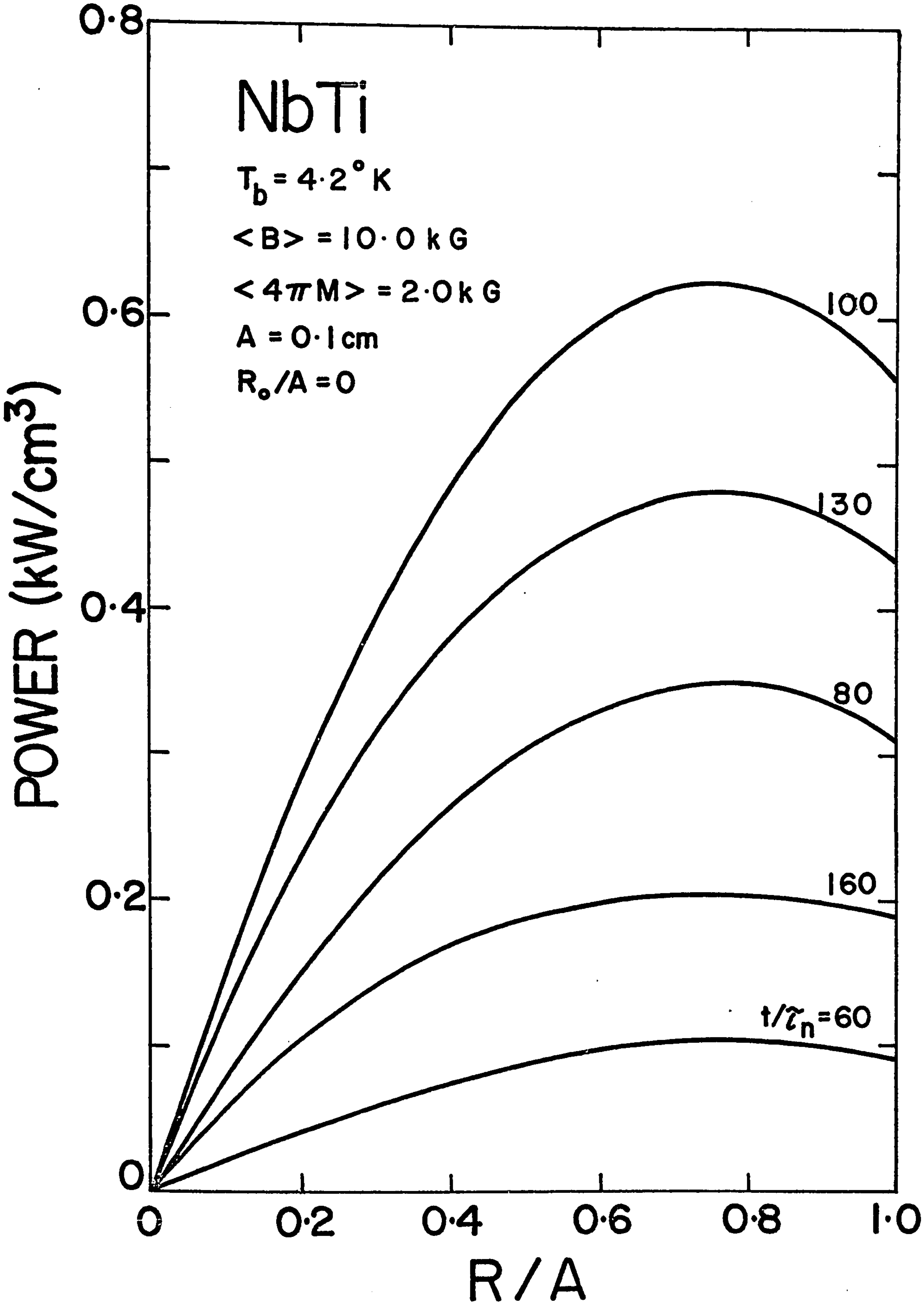

Fig. 4.9: Sequences of power dissipation density in a NbTi cylinder of 0.1 cm radius when $<4\pi M>$ = 2.0 kG, $R_o/A = 0$

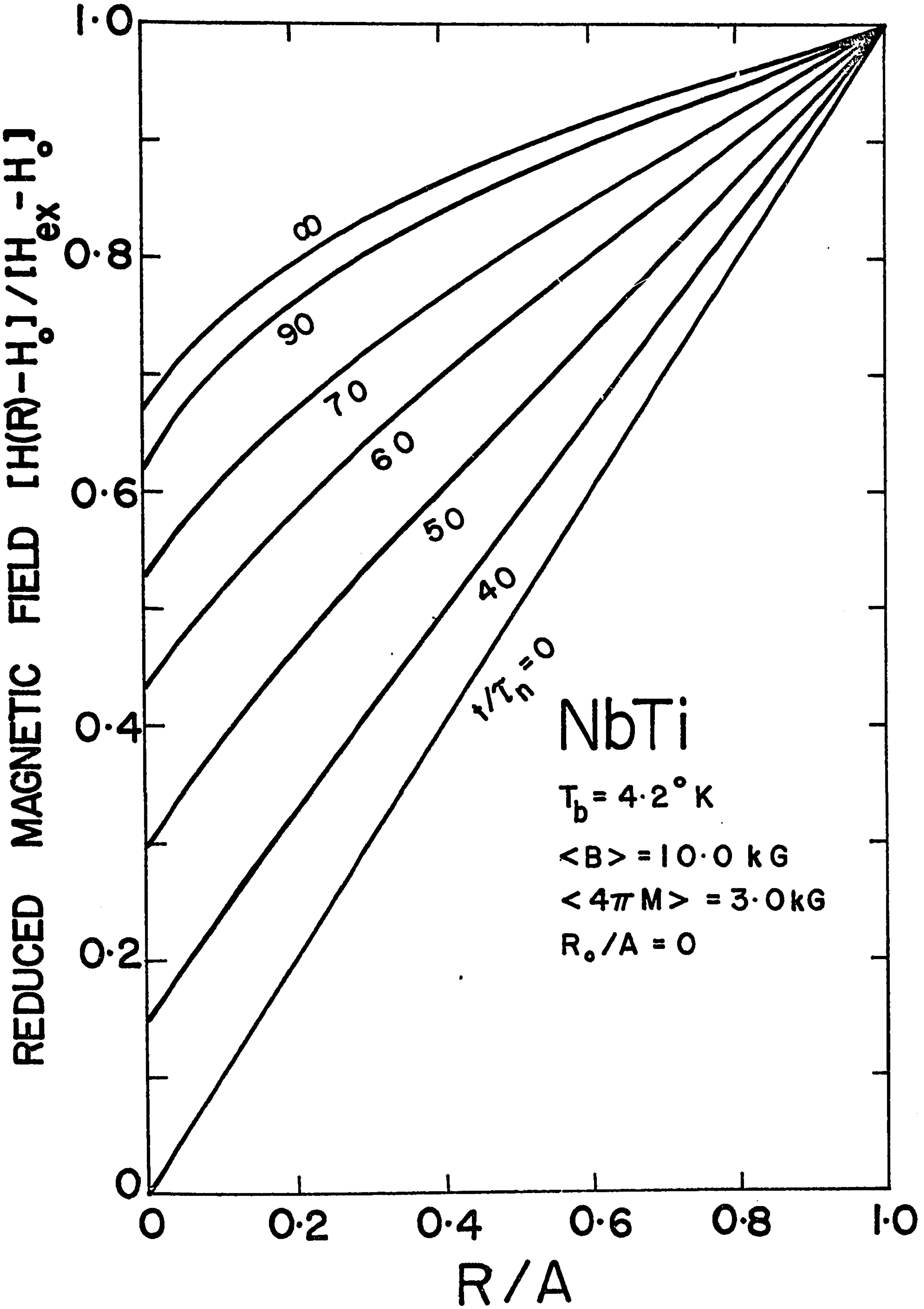

Fig. 4.10: Sequences of magnetic field distributions in a NbTi cylinder during a flux jump when <4πM> = 3.0 kG, R_o/ A = 0

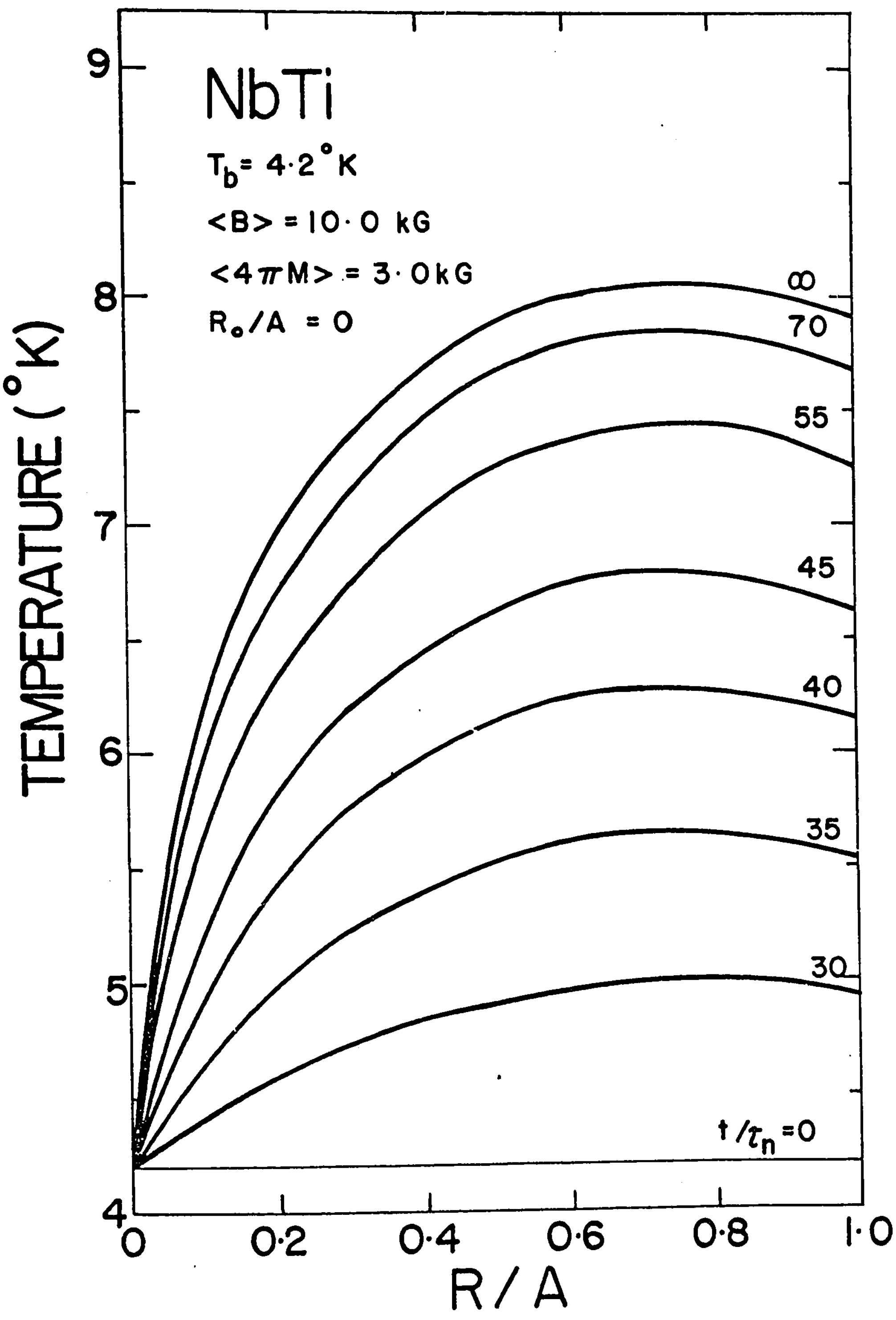

Fig. 4.11: Sequences of temperature distributions in a NbTi cylinder during a flux jump when <4πM> = 3.0 kG, R_o/A = 0.

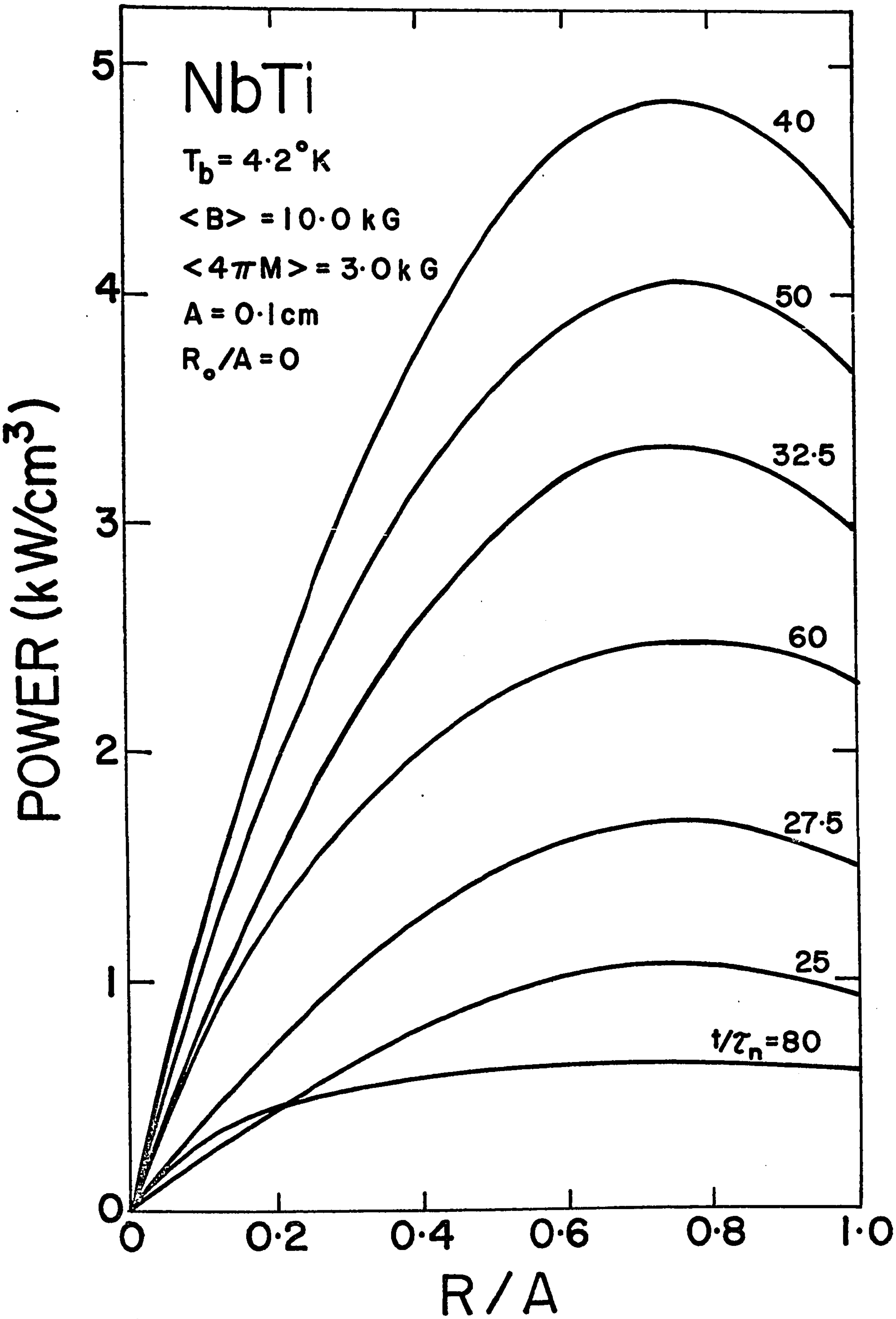

Fig. 4.12: Sequences of power dissipation density in a NbTi cylinder of 0.1 cm radius when <4πM> = 3.0 kG, $R_o/A = 0$

the cylinder (figure 4.11) and the power dissipation reached a maximum value of $\sim$ 5 kW/cm^3, almost an order of magnitude greater than for a magnetization of 2 kG.

iii) $\langle 4\pi M \rangle$ = 4.0 kG:

Figure 4.13 shows the sequence of field profiles during a flux jump for an initial magnetization of 4.0 kG. In this case, the flux jump is nearly complete. During the initial part of the flux jump, the field profiles are regular in shape and similar to that shown in figure 4.10 where the initial magnetization was 3 kG. For t/τ_n equal to, or greater than 32, the slope $\partial H/\partial r$ (hence, the current density) increases rapidly near R/A $\sim$ 0.2. This change in shape of the field profiles is associated with the large values of $\partial\phi/\partial t$ occurring in this time region and shown in figure 4.6. In figure 4.14, we note that this change in field profile corresponds to the attainment of temperatures of the order of 9°K near the surface of the cylinder. The change in the field profiles is therefore due to a sudden increase in flux flow resistivity which occurs when temperatures of the order of 8°K to 9°K are reached near the surface of the cylinder. This increase of resistivity causes a rapid collapse of flux near the surface of the cylinder. This collapse induces large currents deeper into the cylinder, thus distorting the field profiles.

The power dissipation during this flux jump (figure 4.15) is seen to peak initially in the region R/A $\sim$ 0.75, as in the previous

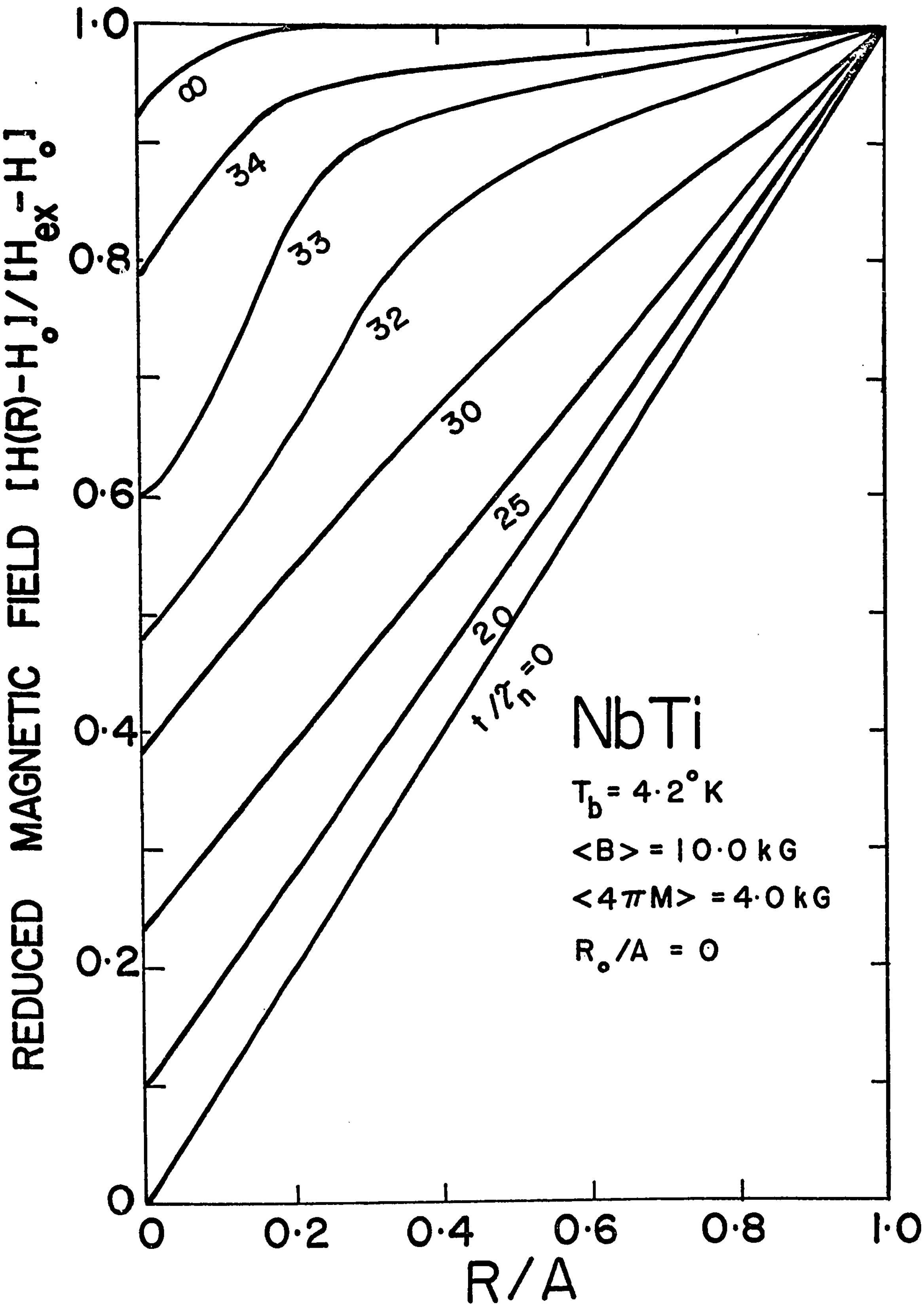

Fig. 4.13: Sequences of magnetic field profiles in a NbTi cylinder during a flux jump when $<4\pi M> = 4.0$ kG, $R_o/A = 0$.

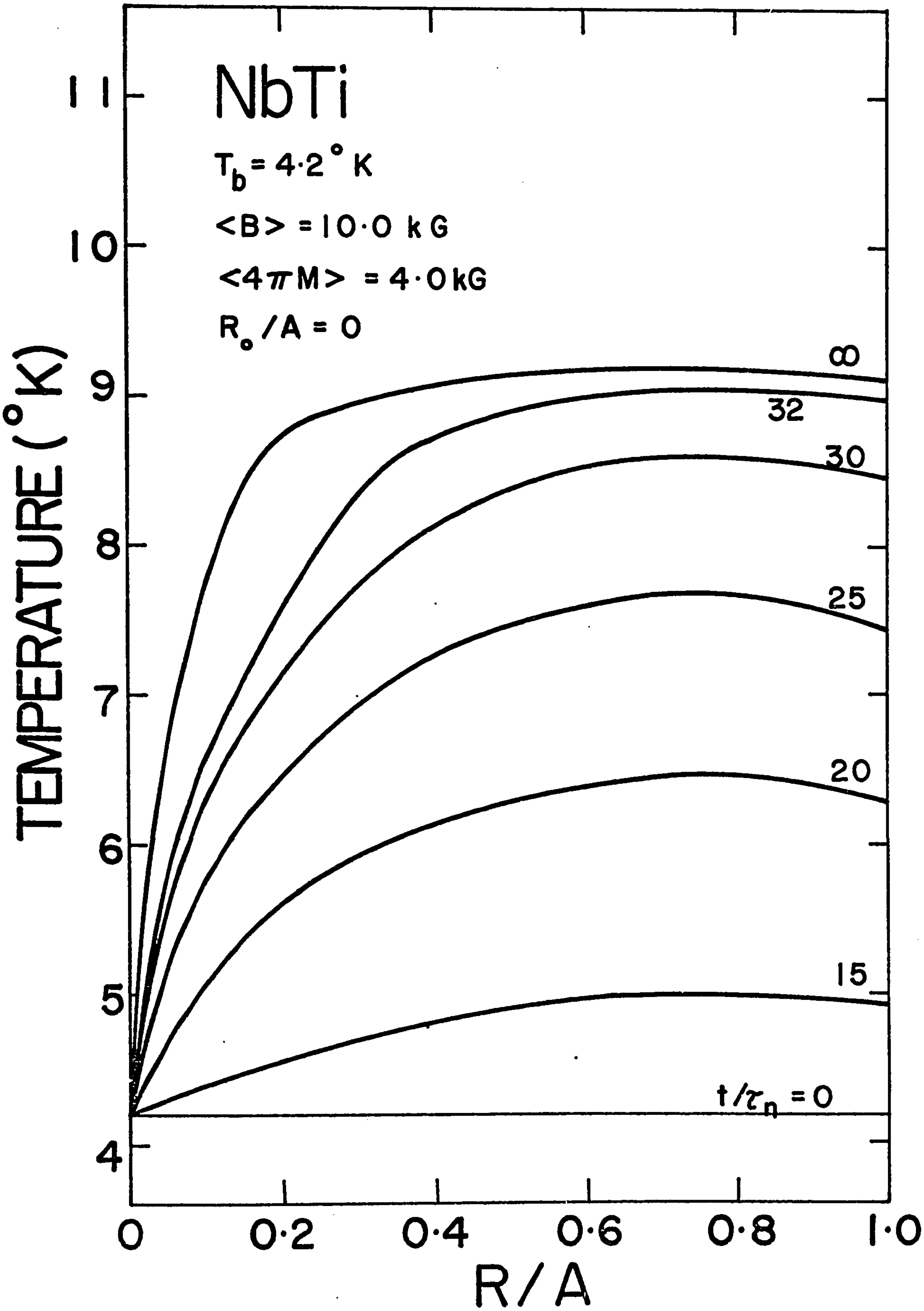

Fig. 4.14: Sequences of temperature distributions in a NbTi cylinder during a flux jump when $<4\pi M> = 4.0$ kG, $R_o/A = 0$.

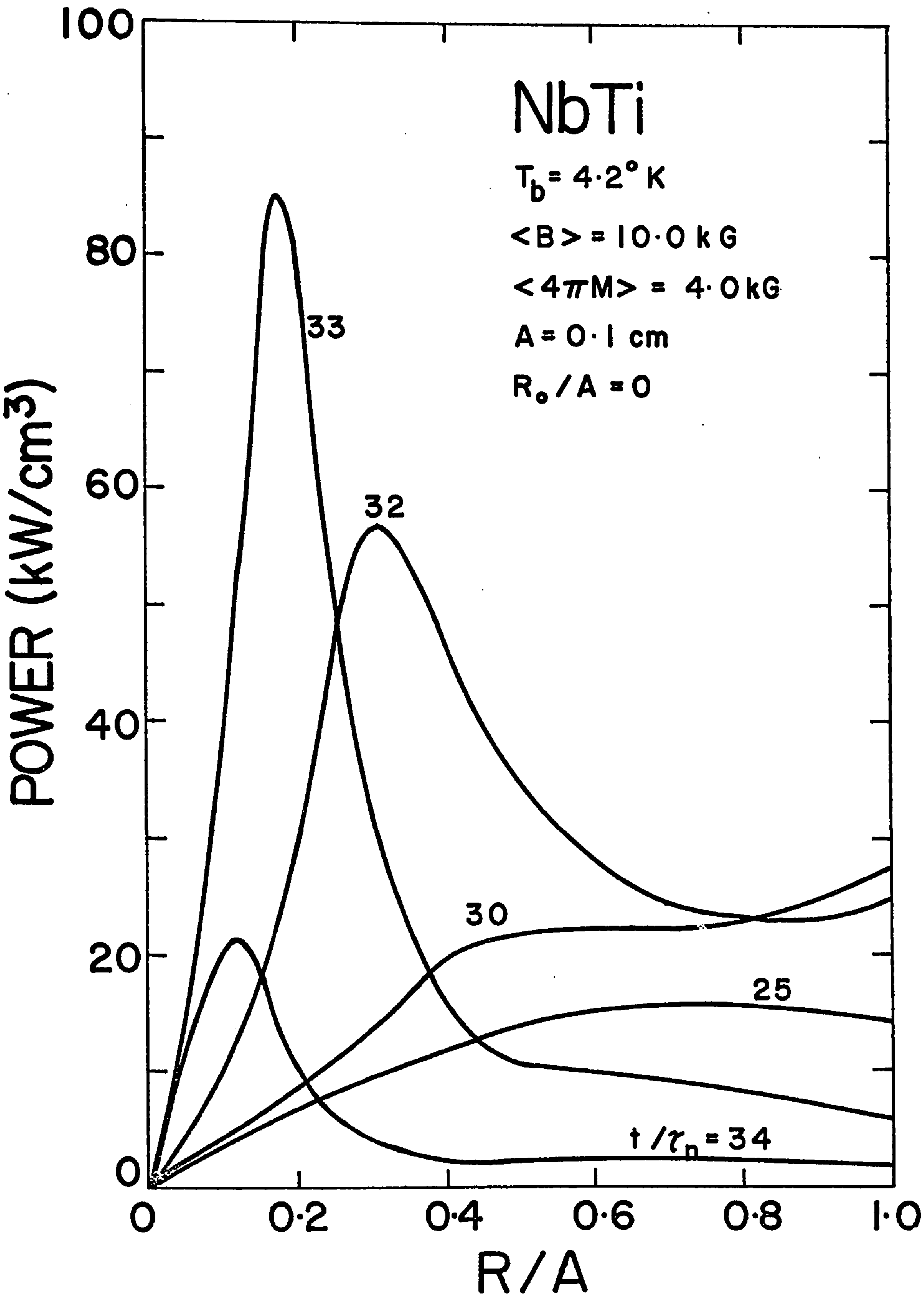

Fig. 4.15: Sequences of power dissipation density in a NbTi cylinder of 0.1 cm radius during a flux jump when $<4\pi M>$ = 4.0 kG, $R_o/A = 0$.

cases. Subsequently, as the flux profiles become distorted, the power dissipation peaks at smaller and smaller radii as time progresses. The maximum value of power in this case is approximately an order of magnitude greater than encountered earlier with $<4\pi M> = 3$ kG.

IV EFFECT OF INITIAL FIELD PROFILE:

a) Introduction:

In the previous section we have shown that the initial magnetizationn$<4\pi M>$ is a dominant factor affecting the collapse of flux in a type II superconductor, and that the time of collapse of flux decreases rapidly with increasing $<4\pi M>$. We considered, however, only situations where the field had initially penetrated to the center of the cylinder. In this section we show that, for a constant magnetization, the initial profile of field, and therefore the critical current density also affects the time of collapse of flux as well as the size of the flux jumps. To distinguish these profiles we have characterized them by the reduced depth of field penetration R_o/A where A is the radius of the cylinder and R_o is the radius to which the field has initially penetrated. We note that $\partial H/\partial r = 0$, hence no currents are initially circulating in the volume between $r = 0$ and

$r = R_o$ of the cylinder. The results we present in this section were calculated for an average induction <B> of 2 kG and a bath temperature $T_b = 4.2^oK$.

b) Time of Radial Collapse as a Function of Initial Field Profile:

The total time of flux collapse τ_t and the relaxation time τ_R are shown respectively in figures 4.16 and 4.17 as a function of R_o/A for three values of the initial magnetization $<4\pi M>$. The field profiles corresponding to $R_o/A = 0$ and $R_o/A \sim 0.9$ are shown schematically in these figures. For all three values of $<4\pi M>$ the total time τ_t (figure 4.16) is seen to first increase slowly with R_o/A until a maximum value is reached, and then to decrease rapidly for $R_o/A > 0.8$. For $<4\pi M> = 3.5$ kG the behaviour of the relaxation time τ_R (figure 4.17) is similar to the total time τ_t. For $<4\pi M>$ equal to 4 kG and 4.5 kG, however, the initial rise in τ_R with R_o/A is very rapid and is again followed by a rapid decrease near $R_o/A \sim 0.8$. The difference in behaviour of τ_R and τ_t versus R_o/A will be shown in subsection d) to be associated with changes in the shape of the corresponding voltage peaks.

The initial increase in τ_R and τ_t with R_o/A can be understood qualitatively in terms of the stored magnetic energy corresponding to different values of R_o/A. Although the initial average magnetization $<4\pi M>$ is fixed for any given curve in figures 4.16 and

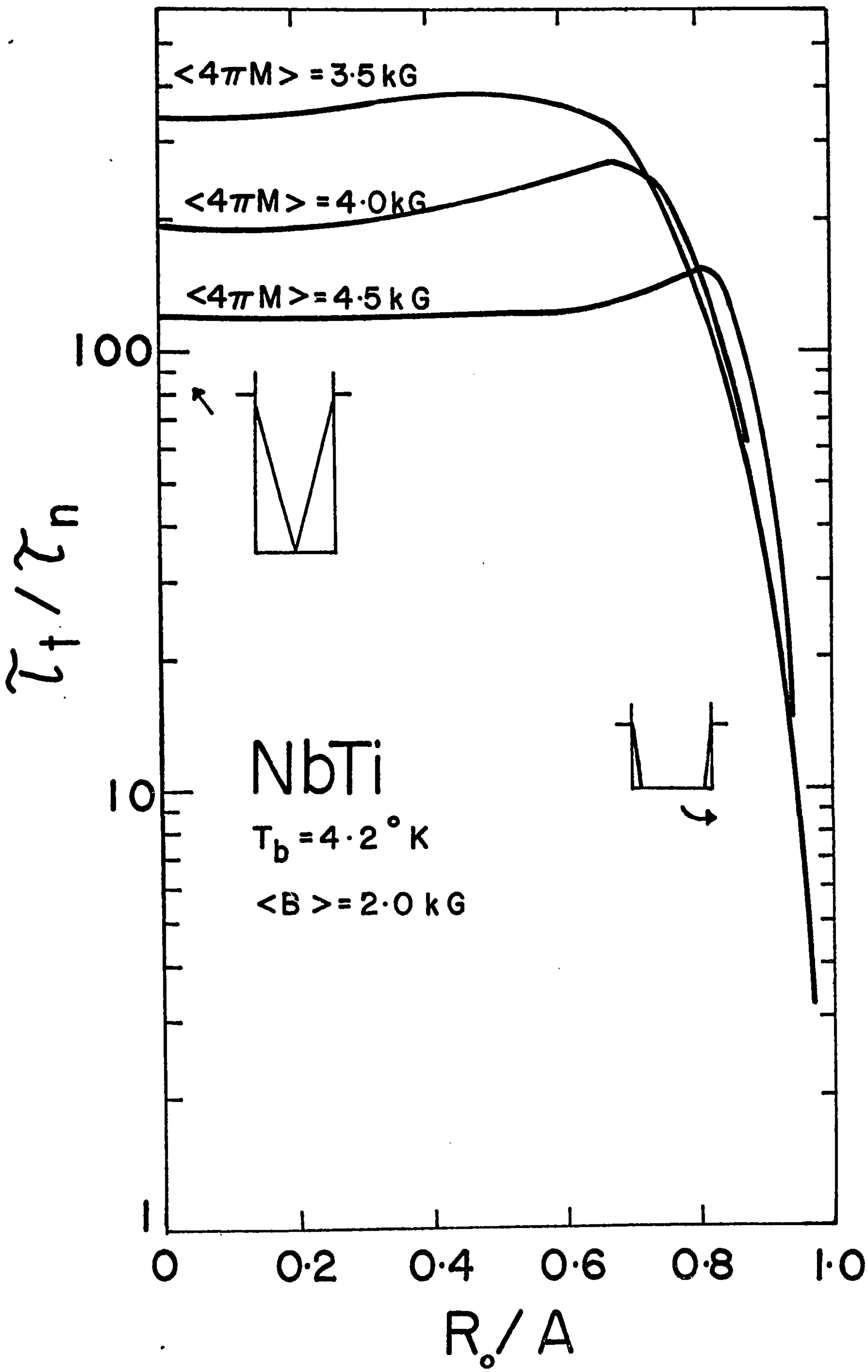

Fig. 4.16: Total time of duration of flux jumps τ_t as a function of initial radius of field penetration R_o/A when $<4\pi M>$ = 3.5 kG, 4.0 kG and 4.5 kG.

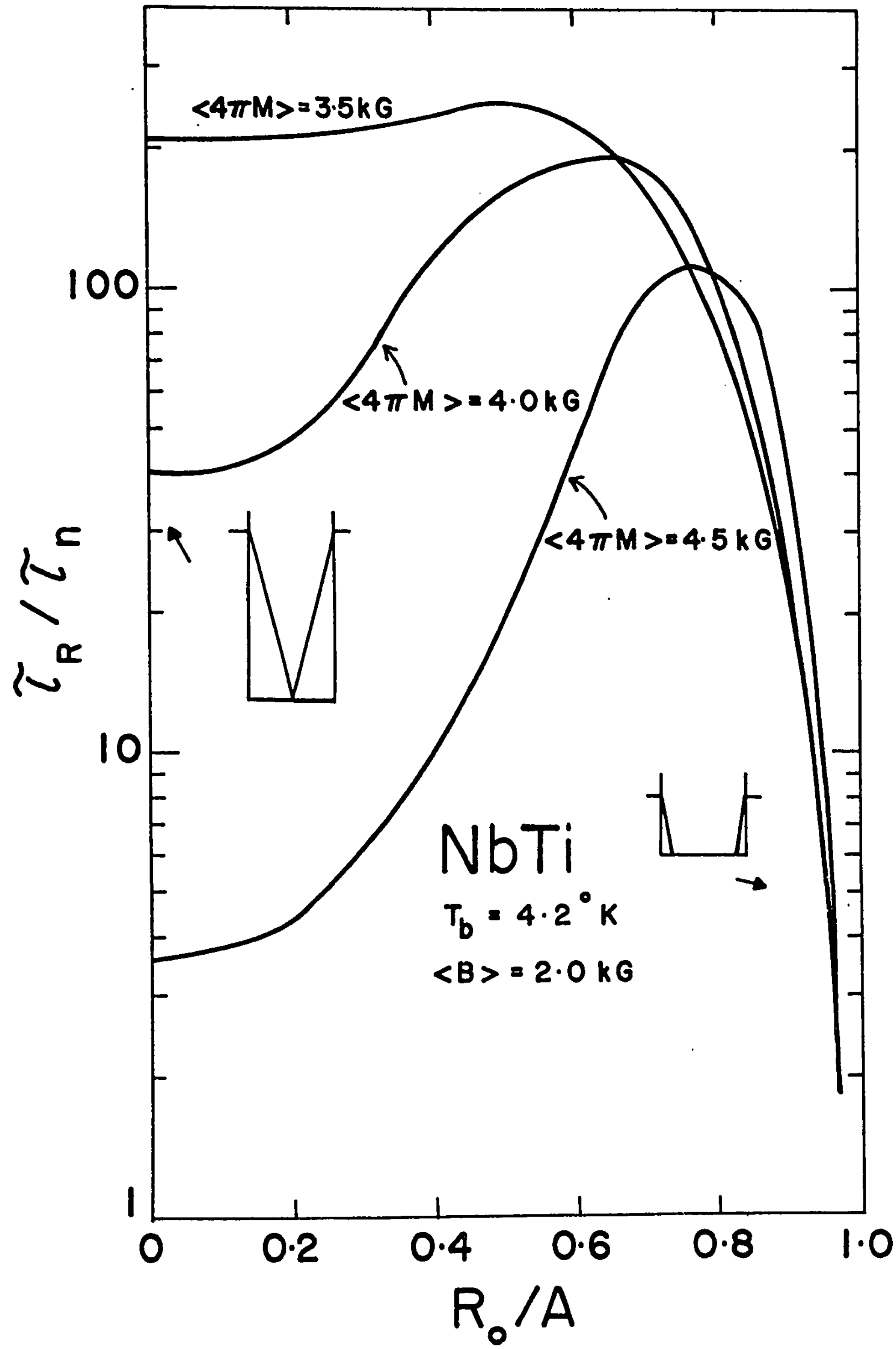

Fig. 4.17: Relaxation time τ_R as a function of the initial radius of field penetration R_o/A in NbTi cylinders when initially <4πM> = 3.5 kG, 4.0 kG and 4.5 kG.

4.17, the magnetic energy decreases monotonically with increasing R_o/A. If $R_o/A = 1$, then the field inside the cylinder is initially uniform and the magnetic energy $E_m = <4\pi M>^2/8\pi$. When $R_o/A = 0$ however, the field profile is triangular and corresponds to an energy of $E_m \sim <4\pi M>^2/6\pi$. This decrease is stored energy with increasing R_o/A is seen from figure 4.18 to be accompanied by a small initial rate of decrease of the size of flux jumps $\Delta<4\pi M>$ with R_o/A (where $\Delta<4\pi M>$ is the drop in magnetization occuring during the flux jump). This initial slow decrease in $\Delta<4\pi M>$ is however followed by a rapid decrease for large values of R_o/A. This rapid decrease cannot be attributed to the decrease in stored energy since the latter tends to level off at a constant value as $R_o/A \to 1$. We account for the rapid decrease in $\Delta<4\pi M>$ and in the time constants τ_t and τ_R for $R_o/A \to 1$ in the following way. Firstly, we note that a decrease in flux jump size with increasing field gradient is expected from semi-quantitative consideration of figure 4.19. In this figure, the profile $R_o/A = 0$ corresponds to an external field H_1 (profile #1, solid line), and profile $R_o/A = 1$ to an external field H_3 which is three times smaller than H_1. The latter profile corresponds to an infinite critical current density flowing at the surface of the cylinder. An intermediate profile corresponding to $R_o/A \sim 0.85$ and external field H_2 is also shown in the figure (profile#2, solid line). The magnetic moment and average magnetization $<4\pi M>$ are the same for these three profiles. For each of the two fields H_1 and H_2 we have also drawn a second profile (dashed line) corresponding to a decrease in J_c

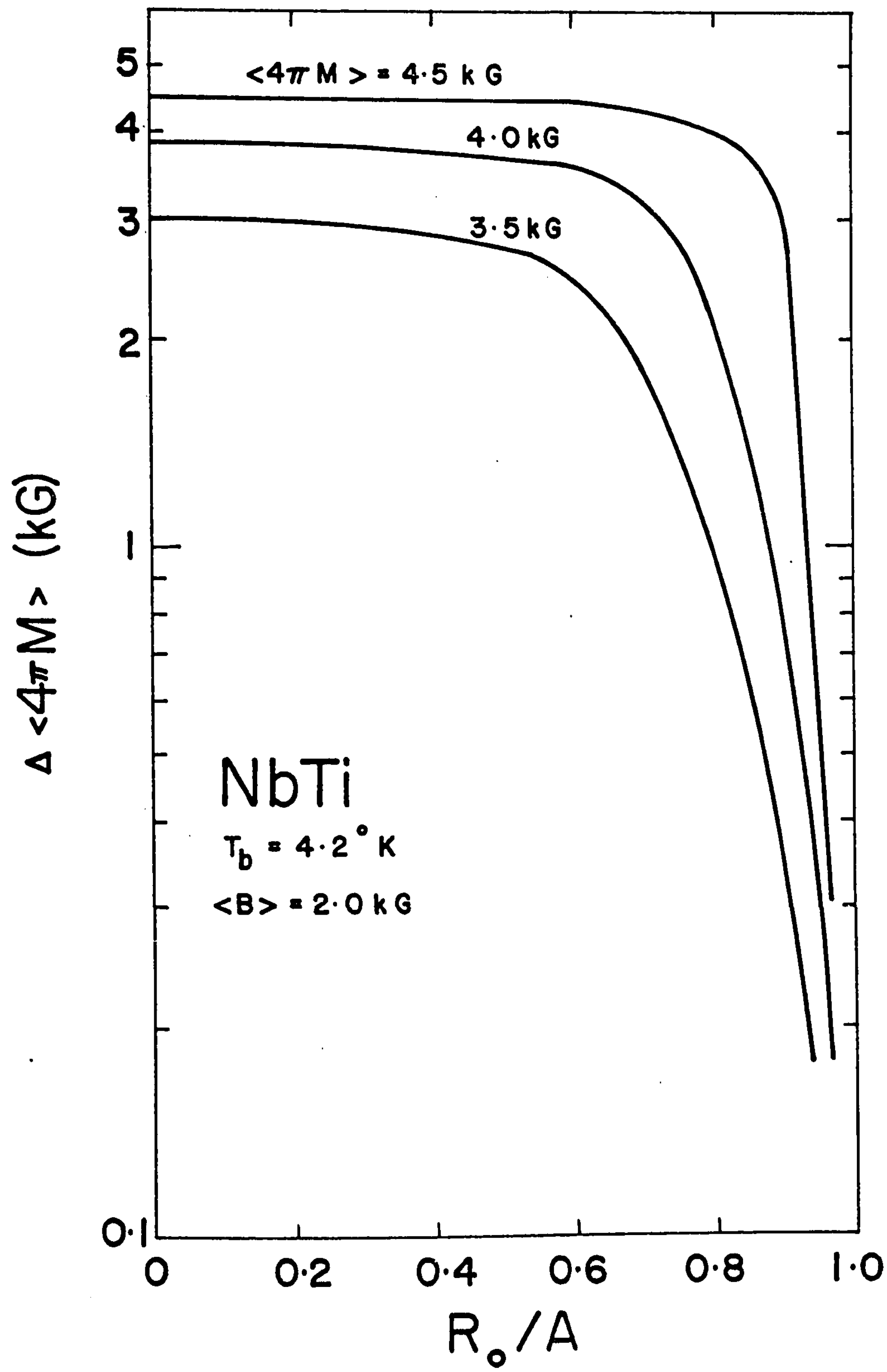

Fig. 4.18: Size of flux jumps $\Delta\langle 4\pi M\rangle$ as a function of the initial radius of field penetration R_o/A in NbTi cylinders when initially $\langle 4\pi M\rangle$ = 3.5 kG, 4.0 kG and 4.5 kG.

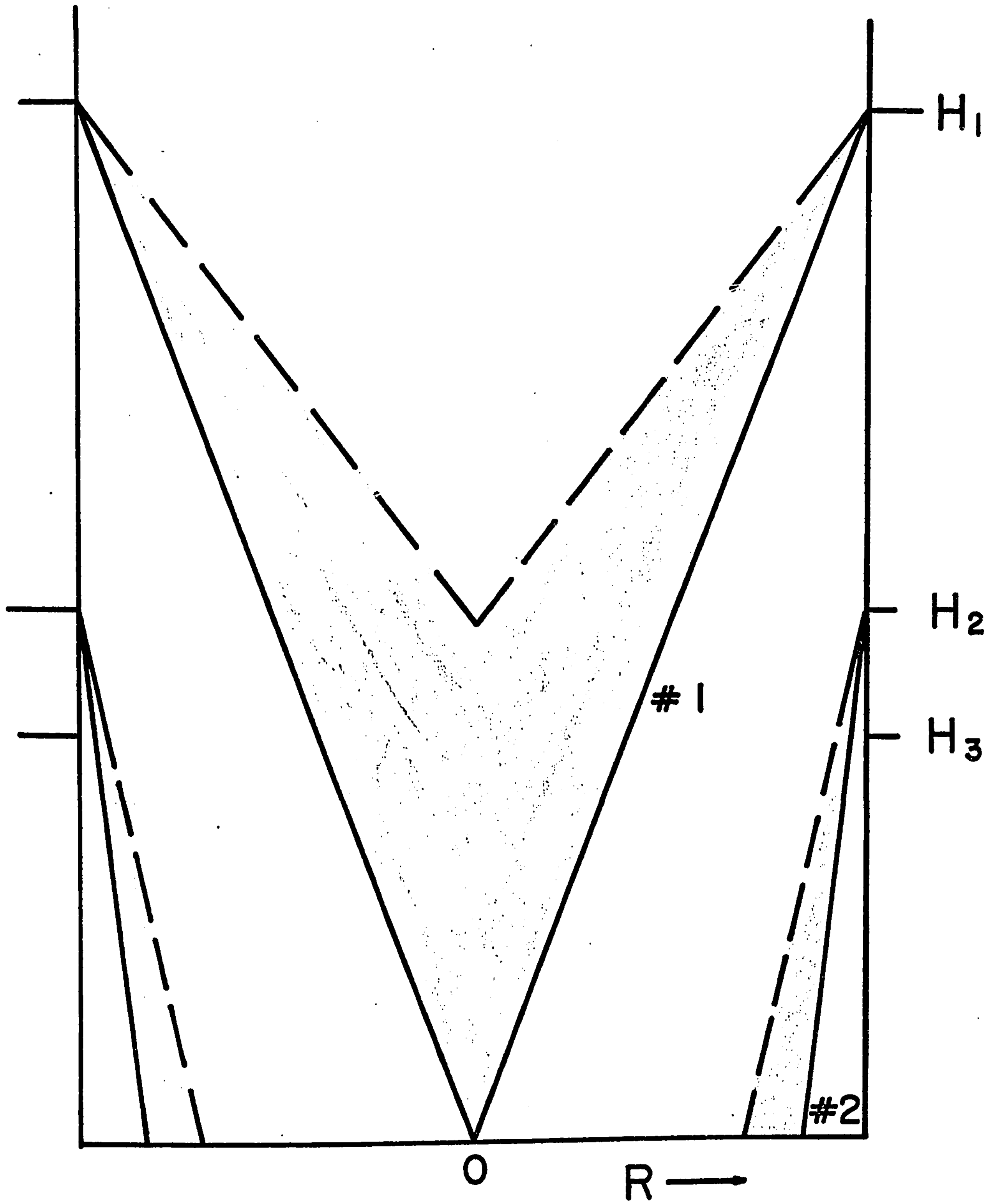

Fig. 4.19: Schematic representation of the effect of field profile on the size of flux jumps.

of a factor of two. The two dashed lines therefore correspond to critical states, hence stable profiles at some common elevated temperature. The shaded areas represent the flux released by the same fractional decrease in the critical current density or the same uniform temperature rise for the two initial situations. It is obvious from this figure that a given temperature rise causes a larger flux penetration for profile #1 than for the steeper profile #2.

Thus, a small thermal perturbation applied to profile H_1 will cause a large penetration of flux leading to an appreciable temperature rise and hence to further flux penetration, etc. As a consequence in this case (if $<4\pi M>$ is appreciable), we expect $\Delta<4\pi M>$ to approach $<4\pi M>$. A perturbation applied to profile H_2 leads to a much smaller flux penetration and therefore to a smaller temperature rise. We then expect a reduction in the size of the flux jump. In the limit of an infinitely steep profile, such as that corresponding to H_3, we expect the size of the flux jump to be infinitesimal. Steep profiles, however, correspond to high current densities flowing in the superconductor and will therefore lead for a given value of $\partial\phi/\partial t$ to a high power dissipation density. Therefore, when the initial field gradient is steep although a small amount of energy is liberated by a small flux jump this energy is liberated quickly and over a small fraction of the volume. Sequences of power dissipation profiles for different initial field profiles will be shown below in subsection e).

In summary, the duration τ_t and τ_R of flux jumps initially increases with R_o/A because the stored energy and the energy released during the events($\Delta\langle 4\pi M\rangle \sim \langle 4\pi M\rangle$ in these instances) decrease with increasing R_o/A. For R_o/A approaching unity, the time required for the flux collapse is progressively shorter because, although a decreasing fraction of the stored energy is released during the jump, this energy is dissipated at a large rate in a small volume. The rate of dissipation is high because the initial current density is large.

c) Shape of Voltages Pulses $\partial\phi/\partial t$ vs t

In figure 4.20, we have plotted, for different values of R_o/A and a constant magnetization of 4.0 kG, calculated curves of the voltage $\partial\phi/\partial t$ vs reduced time t/τ_n detected during a flux jump by a pick-up coil of one turn surrounding the cylinder. These pulses were used to determine the theoretical values of τ_t and τ_R shown in figures 4.16 and 4.17 for $\langle 4\pi M\rangle$ = 4.0 kG. We note in figure 4.20 that the shape of the voltage pulses depends on the initial field profile. The time for $\partial\phi/\partial t$ to attain a maximum decreases monotonically with increasing R_o/A, and therefore with increasing critical current density. For steep field profiles, the main avalanche of flux occurs

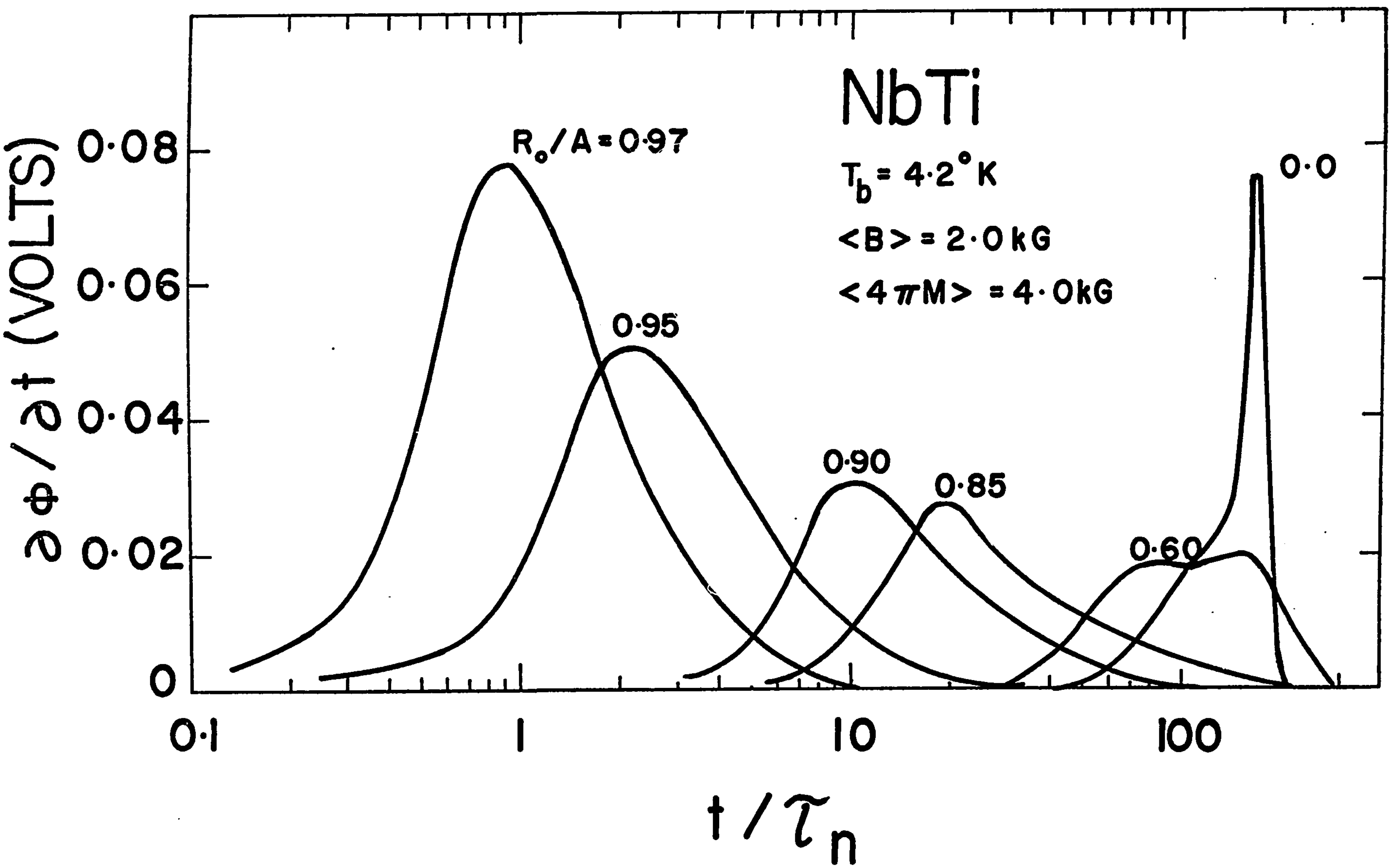

Fig. 4.20: Calculated voltage pulses $\partial\phi/\partial t$ vs t/τ_n detected by a pick-up coil of one turn during flux jumps in a NbTi cylinder when $\langle 4\pi M \rangle = 4.0$ kG. The steepness of the initial field profile if characterized by R_o/A.

very rapidly after the perturbation. For profiles with smaller values of R_o/A the main avalanche of flux appears only after a relatively long delay. For values of R_o/A equal to or close to zero, the initial slow rise in $\partial\phi/\partial t$ is followed by a rapid rise. The appearance of this structure was explained in section III(c) as due to a sharp rise in resistivity which occurs when temperatures close to $T_c(H)$ are reached in the cylinder during the flux jump. This sharp peak in $\partial\phi/\partial t$ is obtained only for average magnetizations greater than $\sim$ 3.5 kG, (section III(c), figure 4.6). The occurrence of this sharp peak in $\partial\phi/\partial t$ causes a large reduction in the relaxation time τ_R but does not affect noticeably the total time of the flux jump τ_t. Since this sharp peak is not encountered for magnetizations of $\sim$ 3.5 kG (see figure 4.6), the behaviour of τ_R in these instances does not differ very much from the behaviour of τ_t (see figures 4.16 and 4.17). For greater magnetization, however, the occurrence of this sharp voltage peak causes the value of τ_R to decrease rapidly with decreasing value of R_o/A (see figures 4.17 & 4.20) and accounts for the difference in behaviour of τ_R and τ_t with R_o/A.

d) Field, Temperature and Power Dissipation Profiles:

In this section, we present sequences of distributions of field, temperature, and power dissipation for three flux jumps corresponding to three different values of R_o/A but to a constant magnetization $\langle 4\pi M\rangle = 4.0$ kG.

i) $R_o/A = 0.0$

Figure 4.21 shows a sequence of field profiles for $R_o/A = 0$. These profiles are very similar to those shown earlier for the same initial magnetization and initial field profile but for an average induction <B> of 10.0 kG (see figure 4.13). In this case, however, the flux jump is slightly smaller because of the larger enthalpy encountered at lower fields. Figure 4.22 shows the temperature distribution at different times. Again, the temperature profiles are similar to those shown in figure 4.14 but were reached at later times because of the lower magnetic induction <B> used in this calculation. The power dissipation is shown in figure 4.23. The profiles are similar to those shown in figure 4.15 but are approximately an order of magnitude smaller because of the lower magnetic induction <B>.

ii) $R_o/A = 0.6$

Figure 4.24 shows sequences of field profiles for $R_o/A = 0.6$. In this case, the flux jump is smaller than for $R_o/A = 0$ and the field profiles are regular in shape. The temperature distributions during this flux jump are given in figure 4.25. In this case the final temperatures are smaller than for $R_o/A = 0$. The rise in temperature near the surface, however, occurs at a faster rate, corresponding to the larger power dissipation (figure 4.26) produced near the surface at these times. The power dissipation for this flux jump is seen to initially peak near the surface of the cylinder, and at later times to

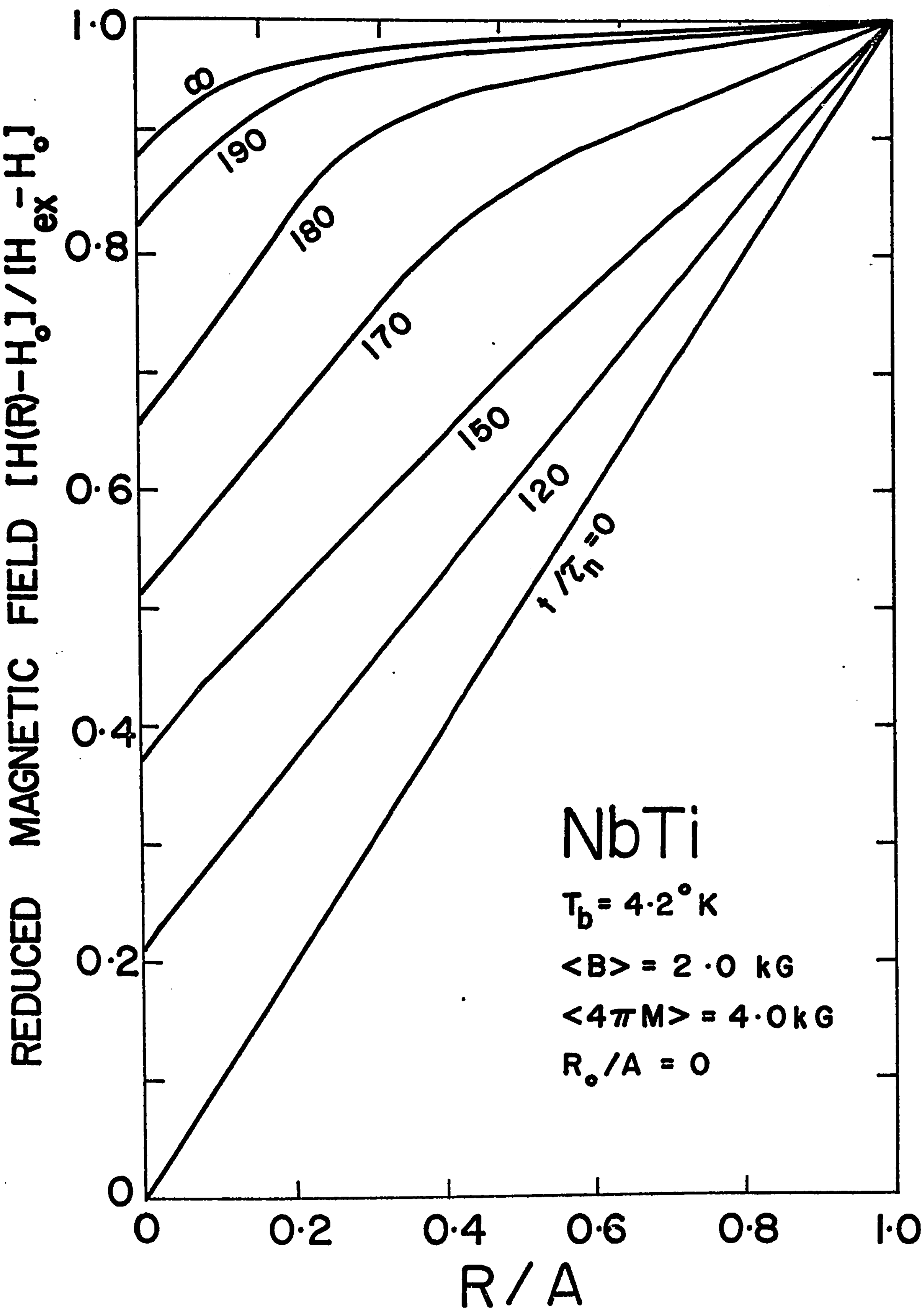

Fig. 4.21: Sequences of magnetic field profiles in a NbTi cylinder during a flux jump when $<4\pi M> = 4.0$ kG, $R_o/A = 0$.

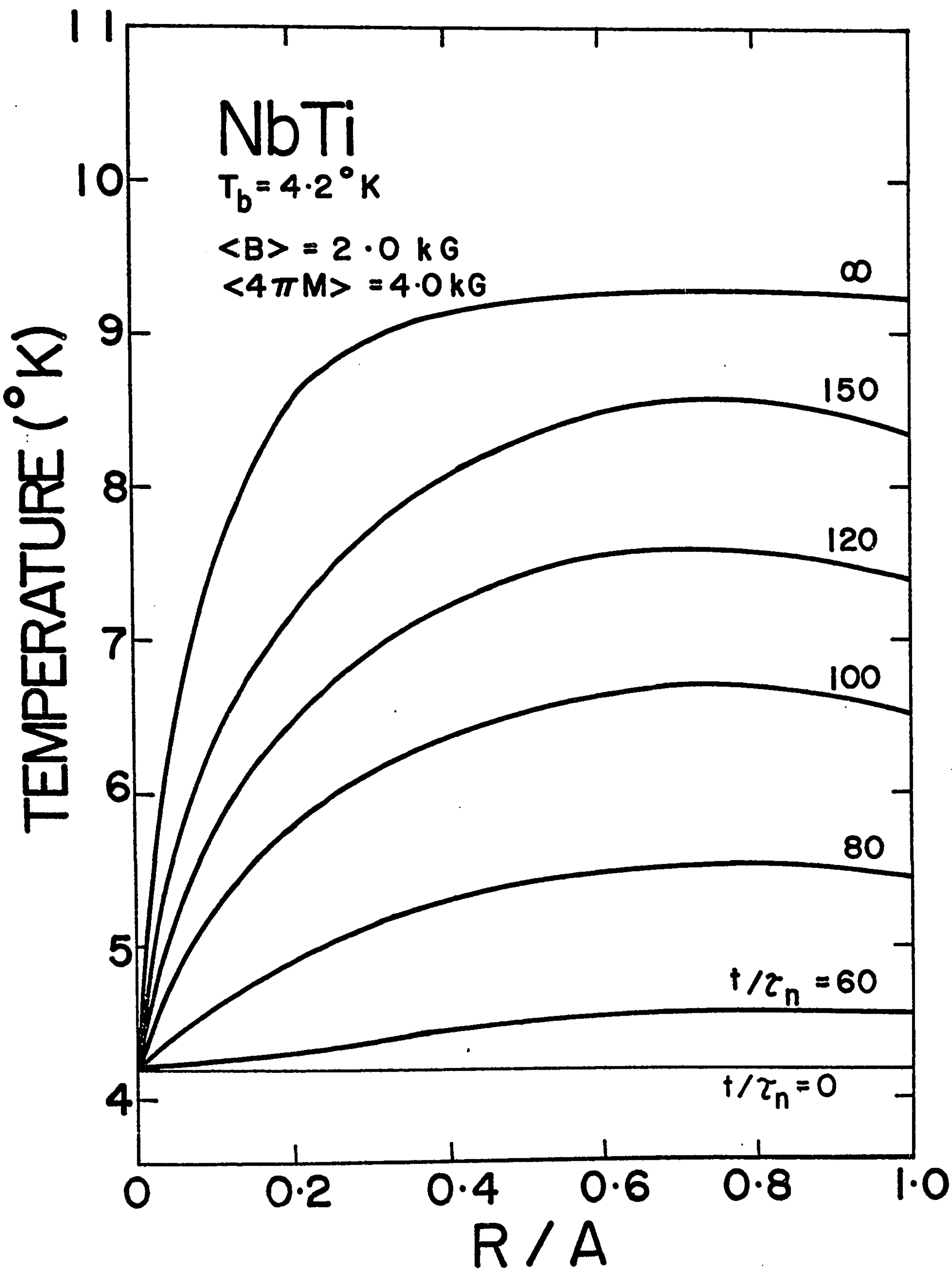

Fig. 4.22: Sequences of temperature distributions in a NbTi cylinder during a flux jump when <4πM> = 4.0 kG, $R_o/A = 0$.

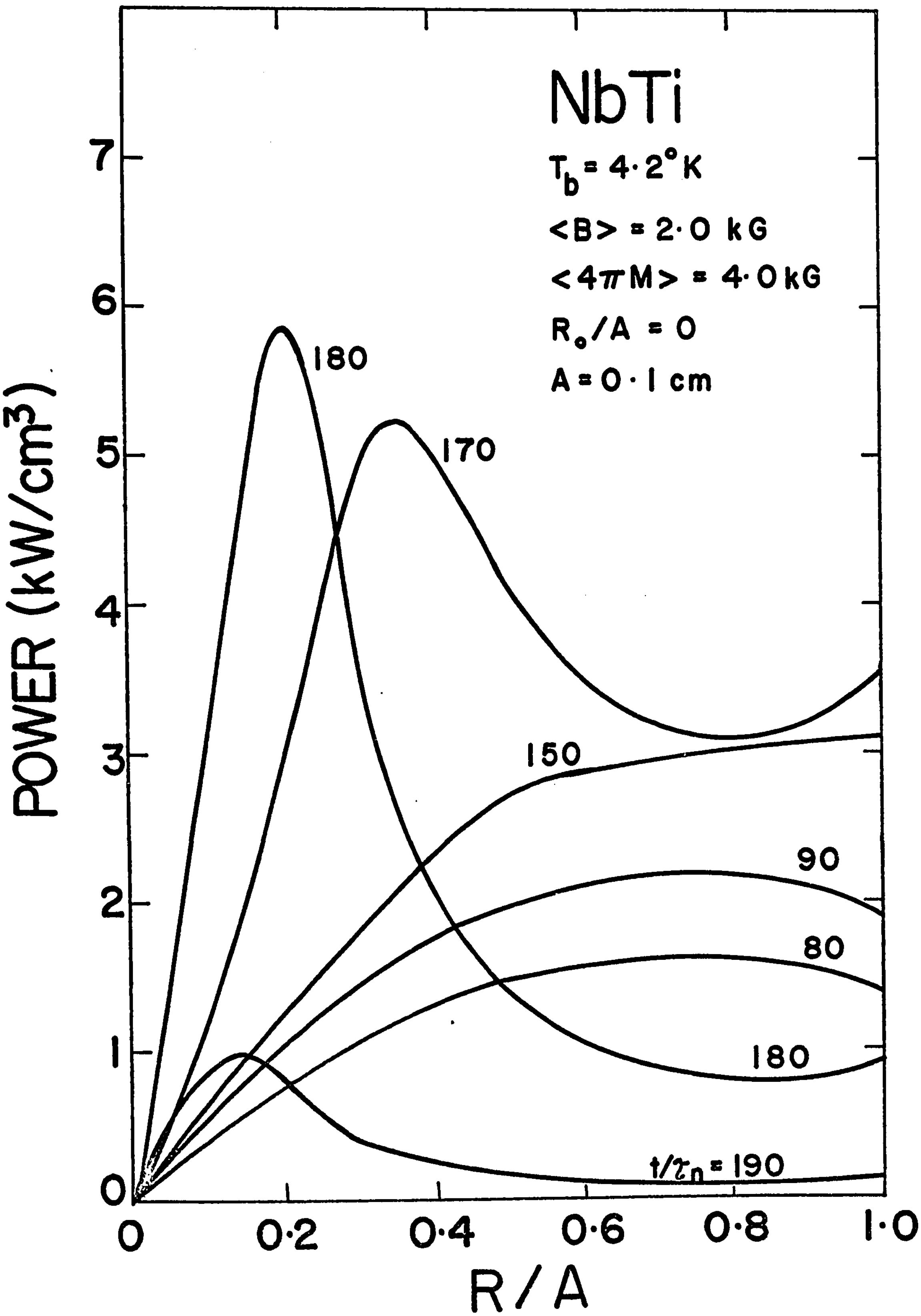

Fig. 4.23: Sequences of power dissipation density profiles in a NbTi cylinder of 0.1 cm radius during a flux jump when $<4\pi M> = 4.0$ kG, $R_o/A = 0$.

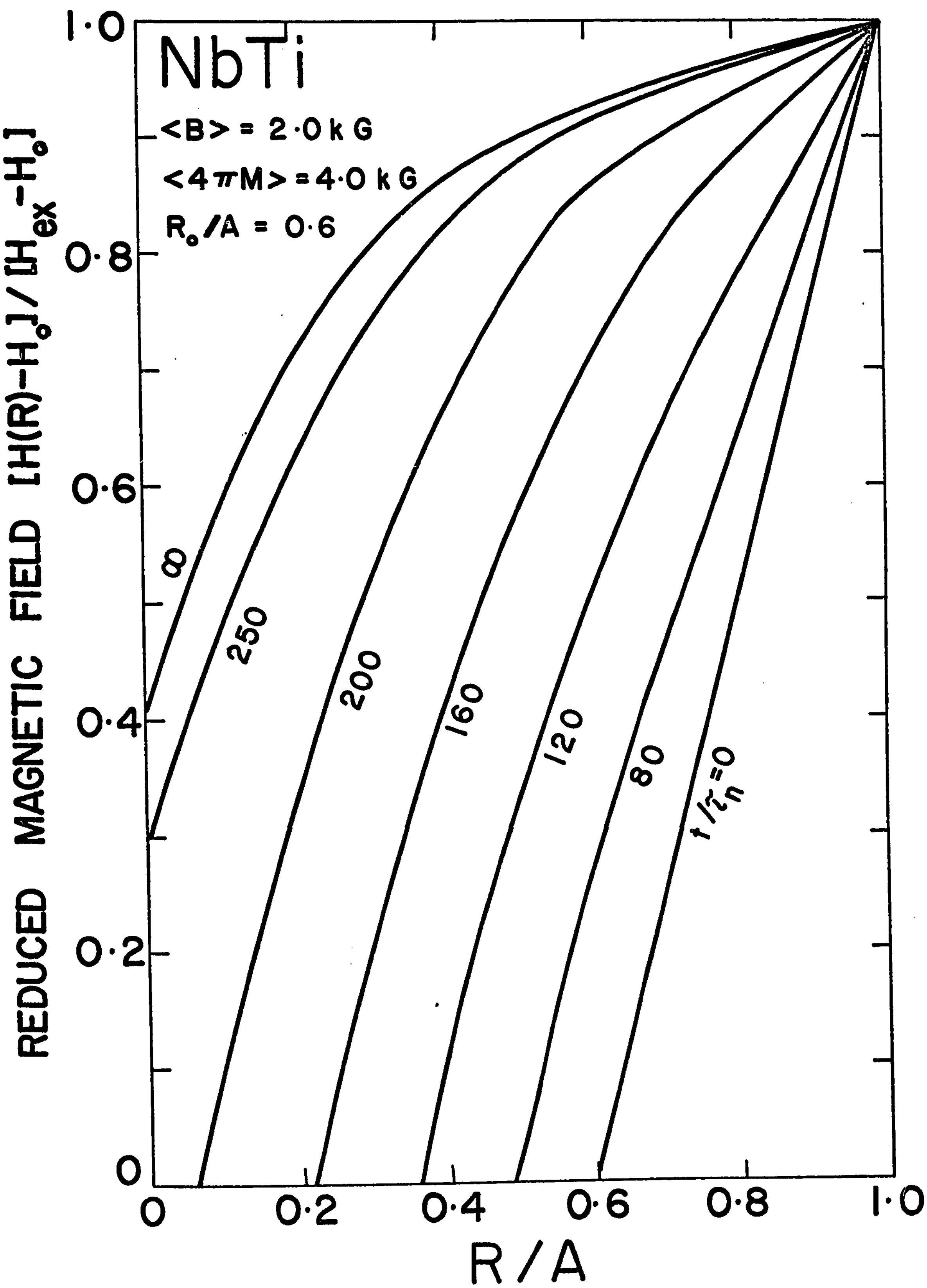

Fig. 4.24: Sequences of magnetic field profiles in a NbTi cylinder during a flux jump when $<4\pi M>$ = 4.0 kG, R_o/A = 0.6.

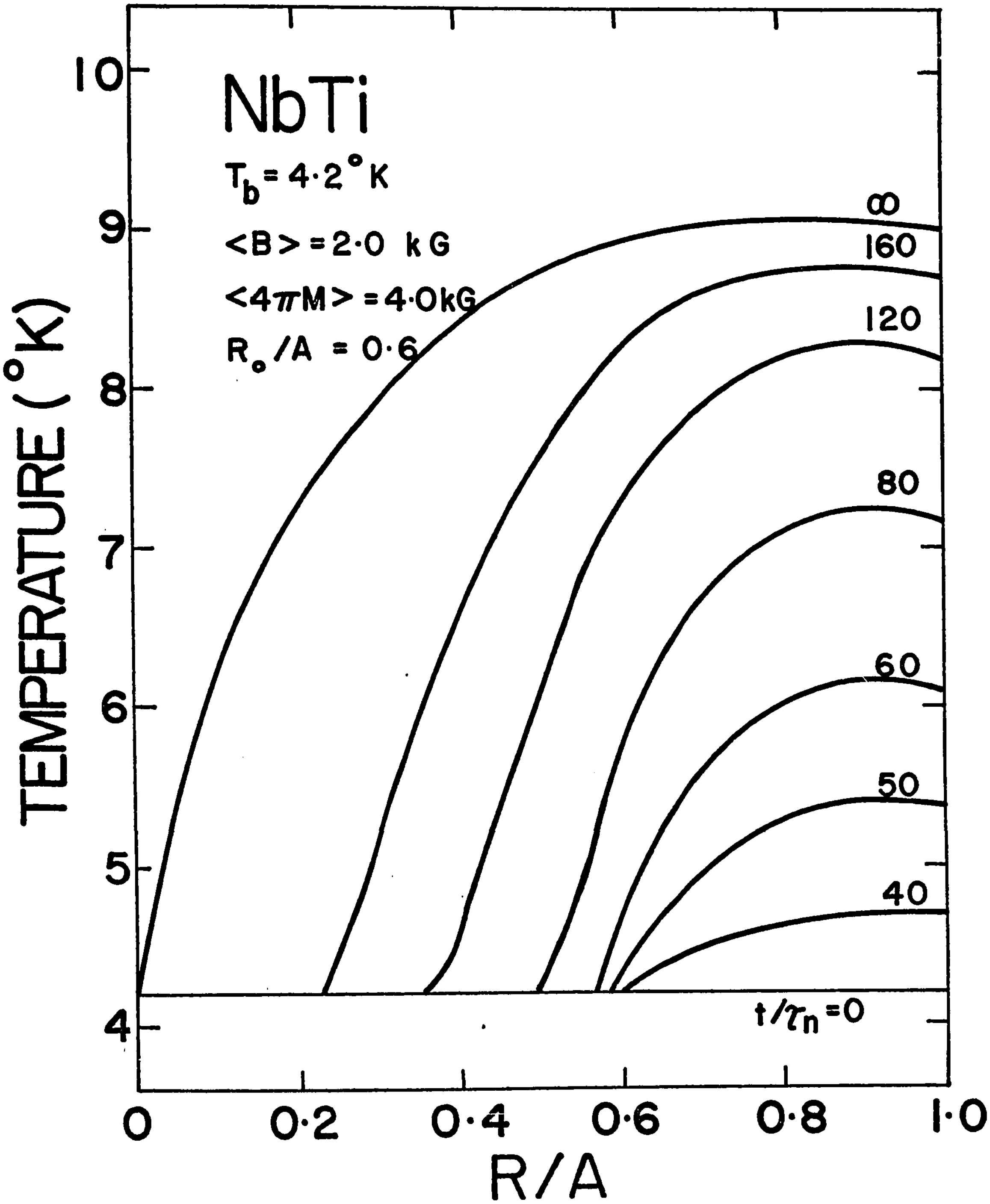

Fig. 4.25: Sequences of temperature distributions in a NbTi cylinder during a flux jump when $\langle 4\pi M \rangle$ = 4.0 kG, R_o/A = 0.6.

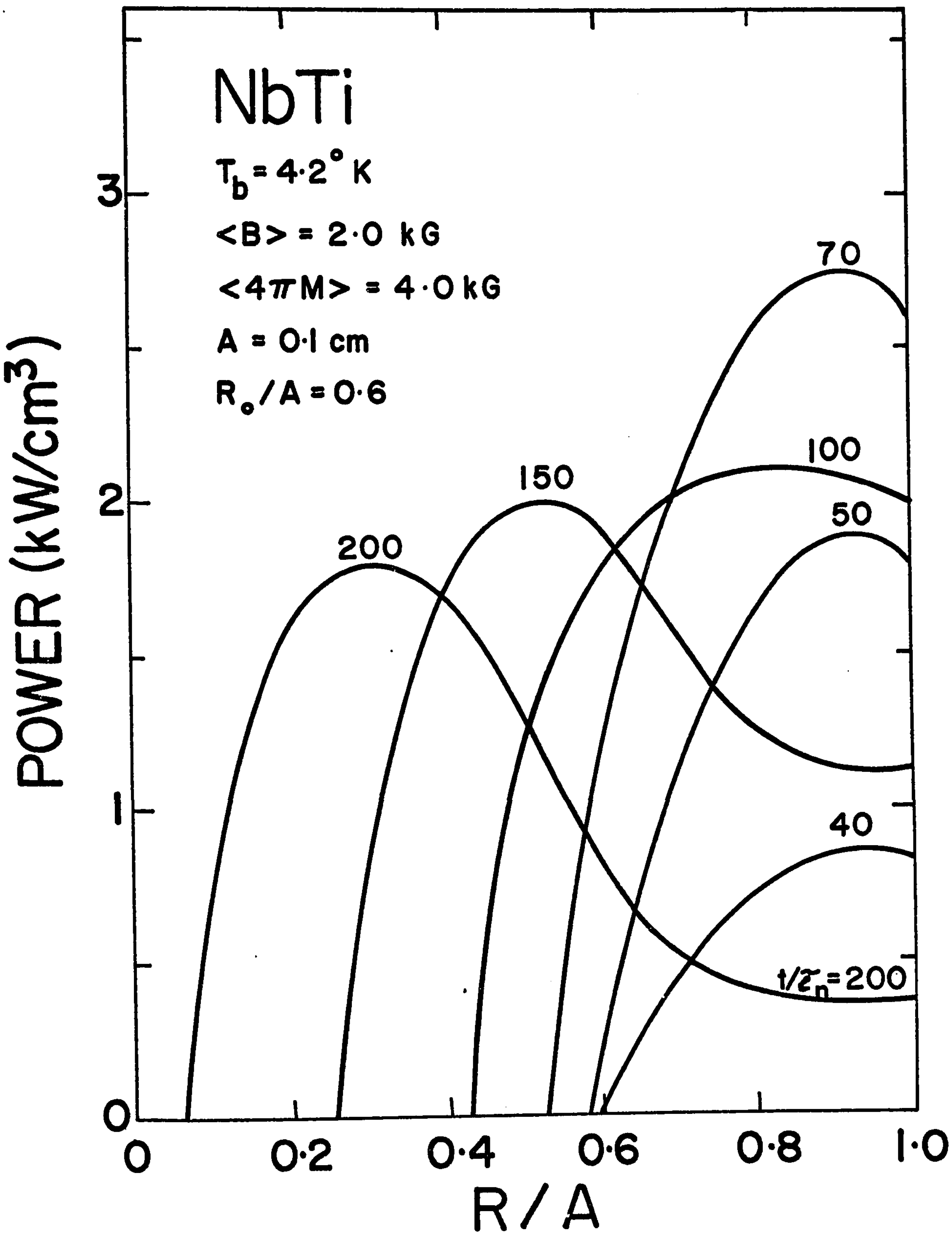

Fig. 4.26: Sequences of power dissipation density profiles in a NbTi cylinder of 0.1 cm radius during a flux jump when <4πM> = 4.0 kG, $R_o/A = 0.6$.

peak deeper and deeper into the sample.

iii) $R_o/A = 0.85$

The sequence of field profiles for $R_o/A = 0.85$ are shown in figure 4.27. In this case the flux jump penetrates only a small fraction of the volume of the cylinder. The increase in temperature (figure 4.28) therefore occurred close to the surface of the cylinder only. Again the maximum temperature reached during this flux jump is smaller than for the two previous flux jumps. The initial rise in temperature however occurred at a faster rate. The power dissipation during this flux jump is shown in figure 4.29. The maximum value of this power is larger than obtained for the two previous flux jumps. It peaks initially at points very close to the surface and then tends to flatten out with a small peak in the region $R_o/A \sim 0.8$ as time advances.

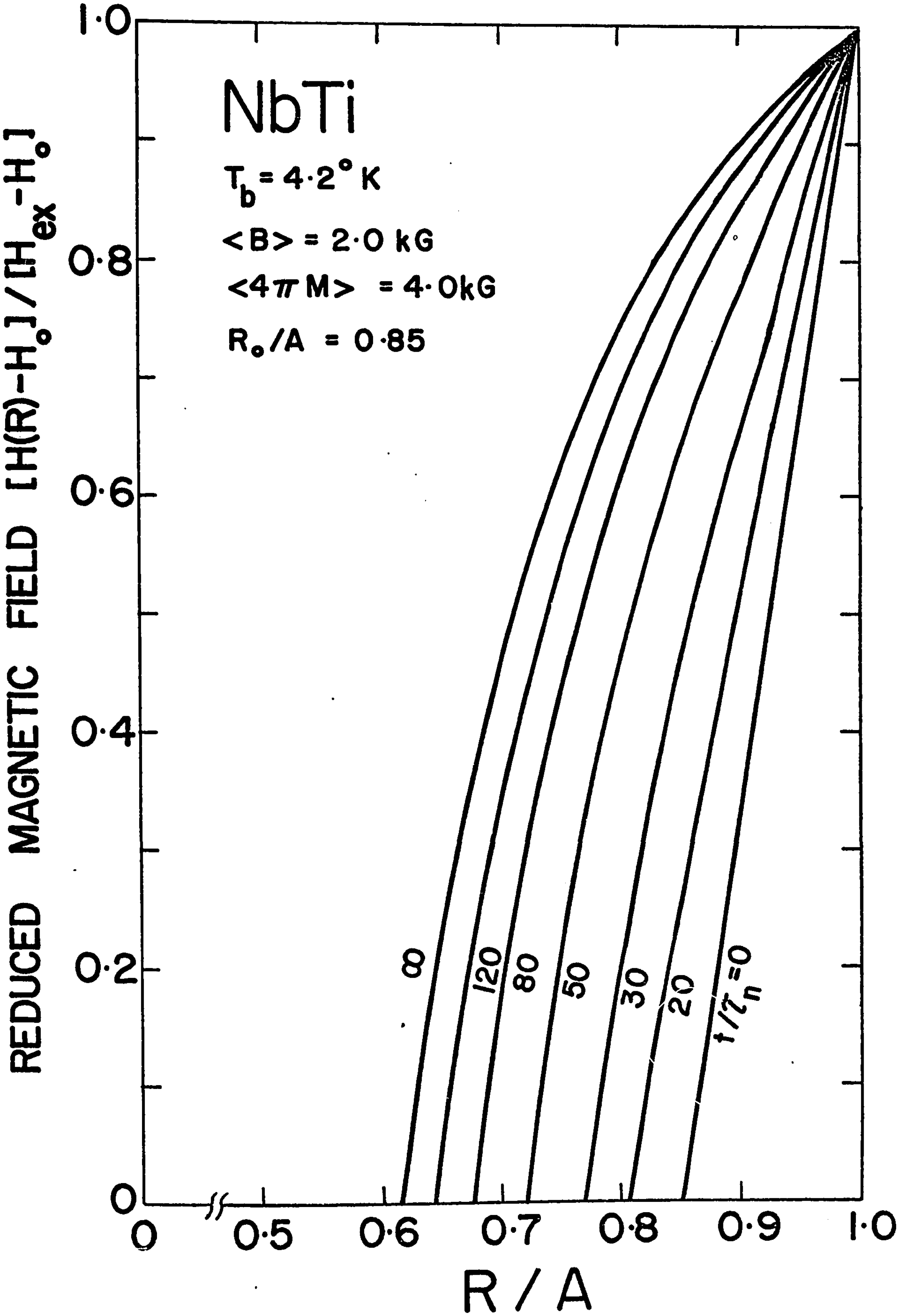

Fig. 4.27: Sequences of magnetic field profiles in a NbTi cylinder during a flux jump when $<4\pi M> = 4.0$ kG, $R_o/A = 0.85$.

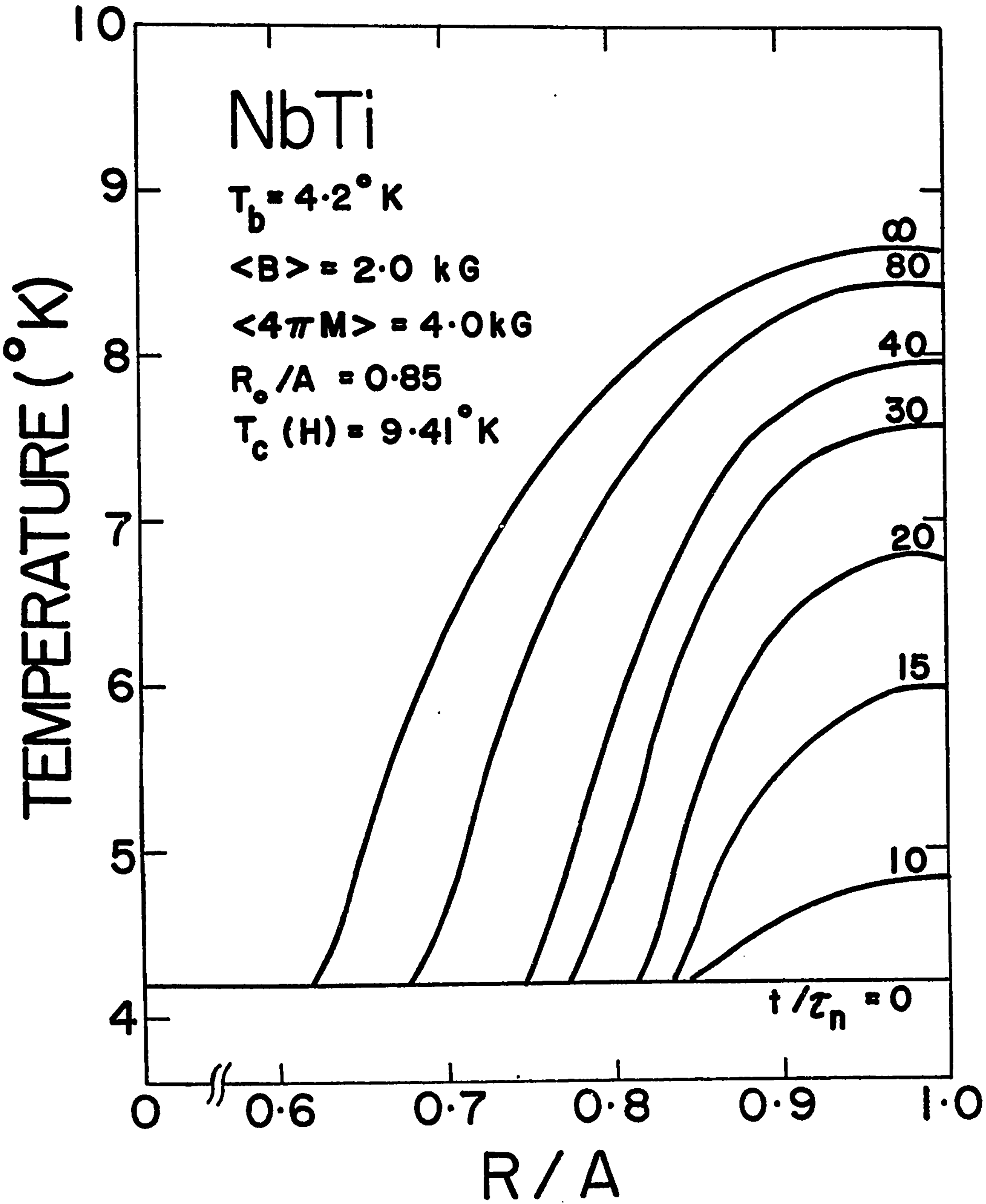

Fig. 4.28: Sequences of temperature distributions in a NbTi cylinder during a flux jump when $\langle 4\pi M \rangle = 4.0$ kG, $R_o/A = 0.85$.

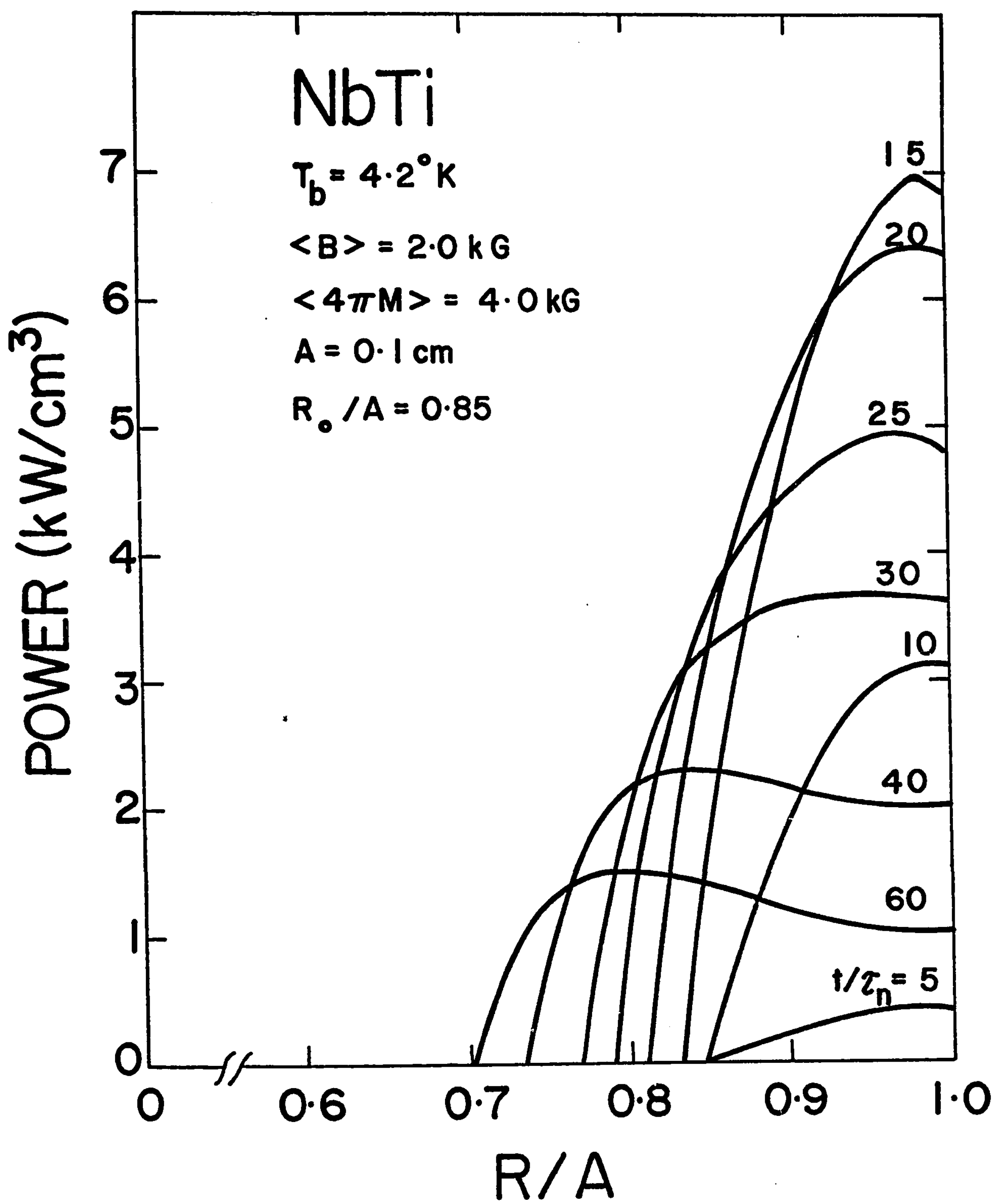

Fig. 4.29: Sequences of power dissipation density profiles in a NbTi cylinder of 0.1 cm radius during a flux jump when <4πM> = 4.0 kG, R_o/A = 0.85.

V. EFFECT OF THE AVERAGE MAGNETIC INDUCTION $\langle B \rangle$ ON RADIAL COLLAPSE OF FLUX

a) Introduction:

The average induction $\langle B \rangle$ existing in the sample during a flux jump is expected to affect the rate of collapse of flux in at least two ways:

i) An increase in field causes an increase in the flux flow resistivity (see figure 4.1). This increase is linear at low fields and temperatures and departs from linearity as fields and temperatures near the critical values are reached. Thus for small fields and temperatures in the superconductor, the time of radial flux collapse is expected to decrease as $1/\langle B \rangle$. Departures from this law will however occur as high average inductions $\langle B \rangle \sim H_{c2}$ or high temperatures $T \sim T_c(\langle B \rangle)$ are reached in the superconductor.

ii) An increase in $\langle B \rangle$ causes a decrease in the critical temperature and therefore a decrease in enthalpy. This decrease in enthalpy will permit an increase in the rate of flux collapse especially when the stored magnetic energy becomes comparable to the enthalpy.

b) Effect of <B> on τ_R and τ_t:

Figures 4.30 and 4.31 show respectively how the relaxation time τ_R and the total time of duration of flux jumps, τ_t vary with <B> in NbTi cylinders for magnetizations of 3 and 4 kG. We have only investigated the special case where the field has initially penetrated to the center of the cylinder. In these calculations, the field profile is maintained constant and only the average induction <B> is varied. In figure 4.30 the value of τ_t/τ_n is seen to decrease approximately as, but slightly faster than, 1/<B> for magnetizations of 3 kG and 4 kG. The relaxation time τ_R however behaves differently for the two magnetic moments shown in figure 4.31. For the magnetization of 3 kG, the value of τ_R decreases as 1/<B> for <B> smaller than $\sim$ 15 kG. As the field is increased, in the range of 20 to 45 kG, τ_R decreases more rapidly with <B>. Then, in the region <B> $\gtrsim$ 50 kG, the value of τ_R/τ_n tends more slowly towards one. For a magnetization of 4 kG and magnetic inductions <B> smaller than $\sim$ 10 kG the decrease in τ_R with <B> is faster than 1/<B> but for fields greater than $\sim$ 10 kG the value of τ_R/τ_n tends rather slowly towards one.

This difference in behaviour of τ_R with <B> for magnetizations of 3.0 kG and 4.0 kG can be accounted for as follows. For a magnetization of 3 kG the stored energy is insufficient to raise the temperature close to T_c(<B>) at low fields. As a consequence, in the low field region the linear variation of resistivity with <B> prevails

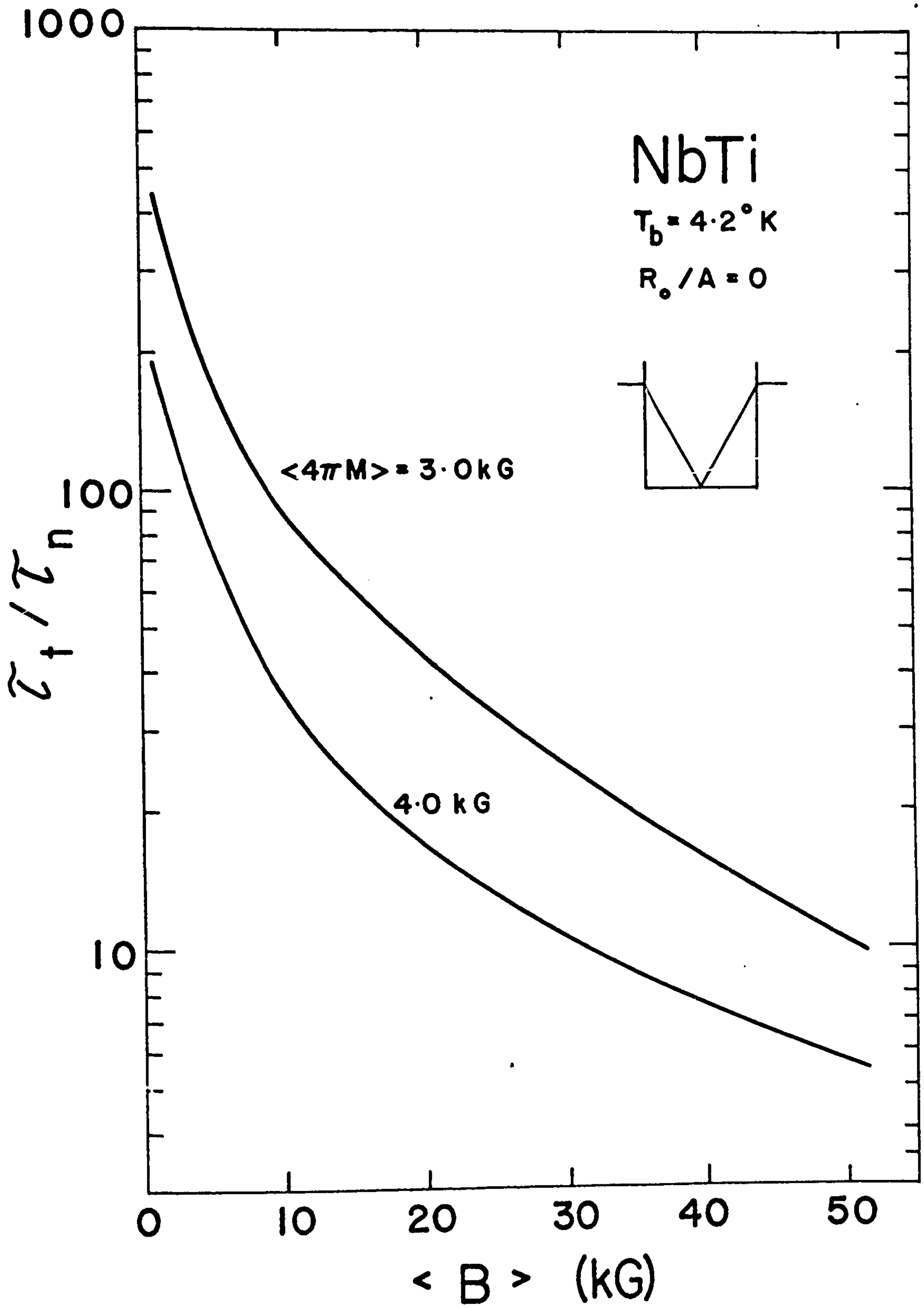

Fig. 4.30: Total time of duration of flux jumps τ_t as a function of <B> for NbTi cylinders when initially <4πM> = 3.0 kG and 4.0 kG.

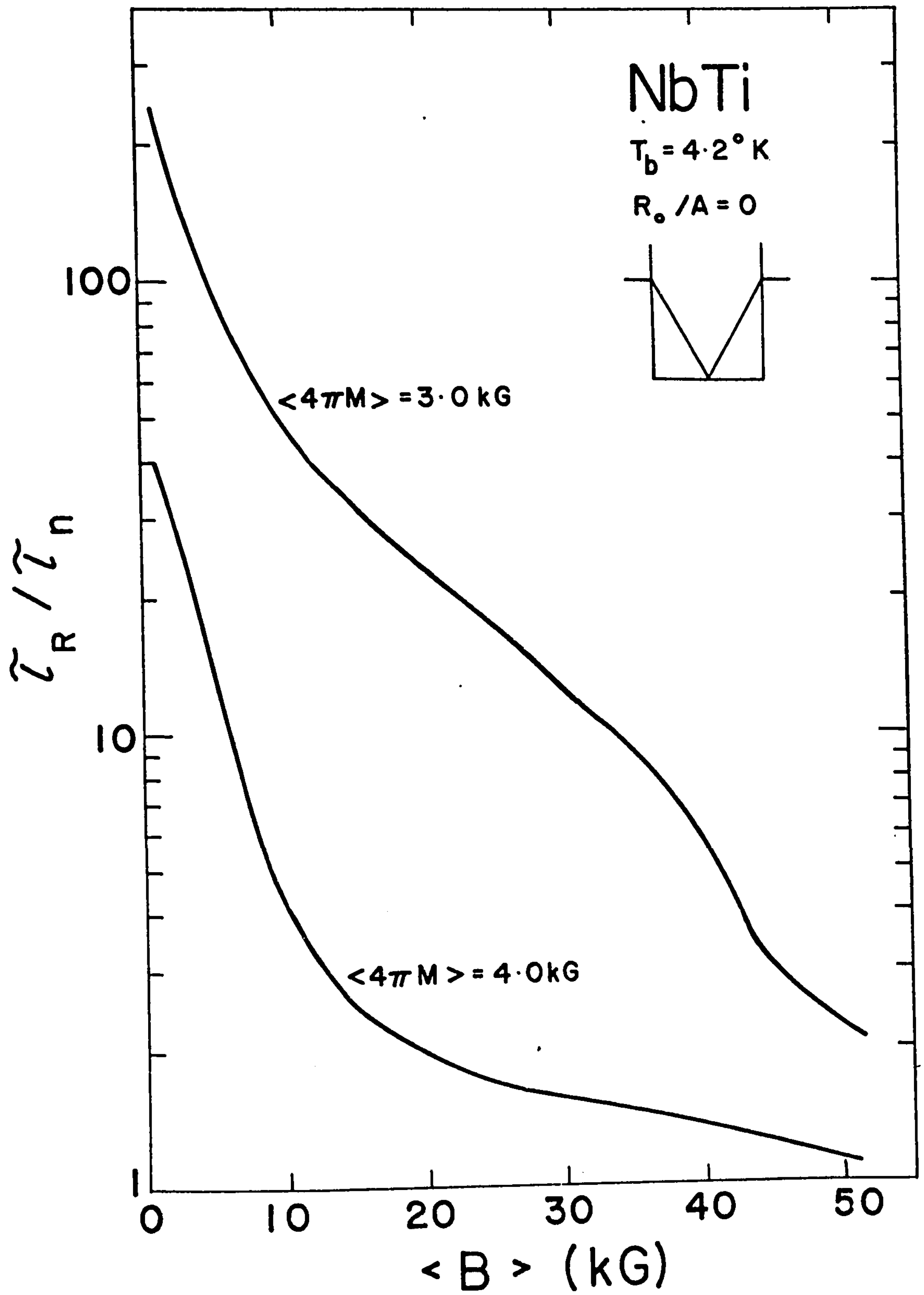

Fig. 4.31: Relaxation time τ_R as a function of <B> in NbTi cylinders when initially <4πM> = 3.0 kG and 4.0 kG.

during the entire flux jump. For higher fields (hence lower enthalpies) temperatures near $T_c(\langle B \rangle)$ are attained during the flux jump. These high temperatures are accompanied by a steep rise in resistivity which leads to a more rapid decrease in τ_R. With a magnetization of 4 kG, temperatures close to $T_c(\langle B \rangle)$ are reached during the flux jump even in low fields, hence τ_R decreases more quickly than $1/\langle B \rangle$ even for low values of $\langle B \rangle$. For large magnetic moments and/or fields, we expect τ_R/τ_n to tend towards unity because the decrease in enthalpy with field leads to significant ratios of stored magnetic energy to enthalpy. As a consequence, the entire specimen reverts to the normal state at the very beginning of the flux avalanche.

VI RADIUS OF FIELD PENETRATION AS A FUNCTION OF TIME

The penetration of flux during flux jumps has been observed experimentally for the case of discs in transverse fields (Wertheimer 67, Harrisson 72) using a fast camera and the Faraday rotation technique. In this case the experimental quantity measured is the radius of penetration R_o/A as a function of time. Recently, it has been shown (Harrisson 72) that this radius of penetration can be described with an expression of the type:

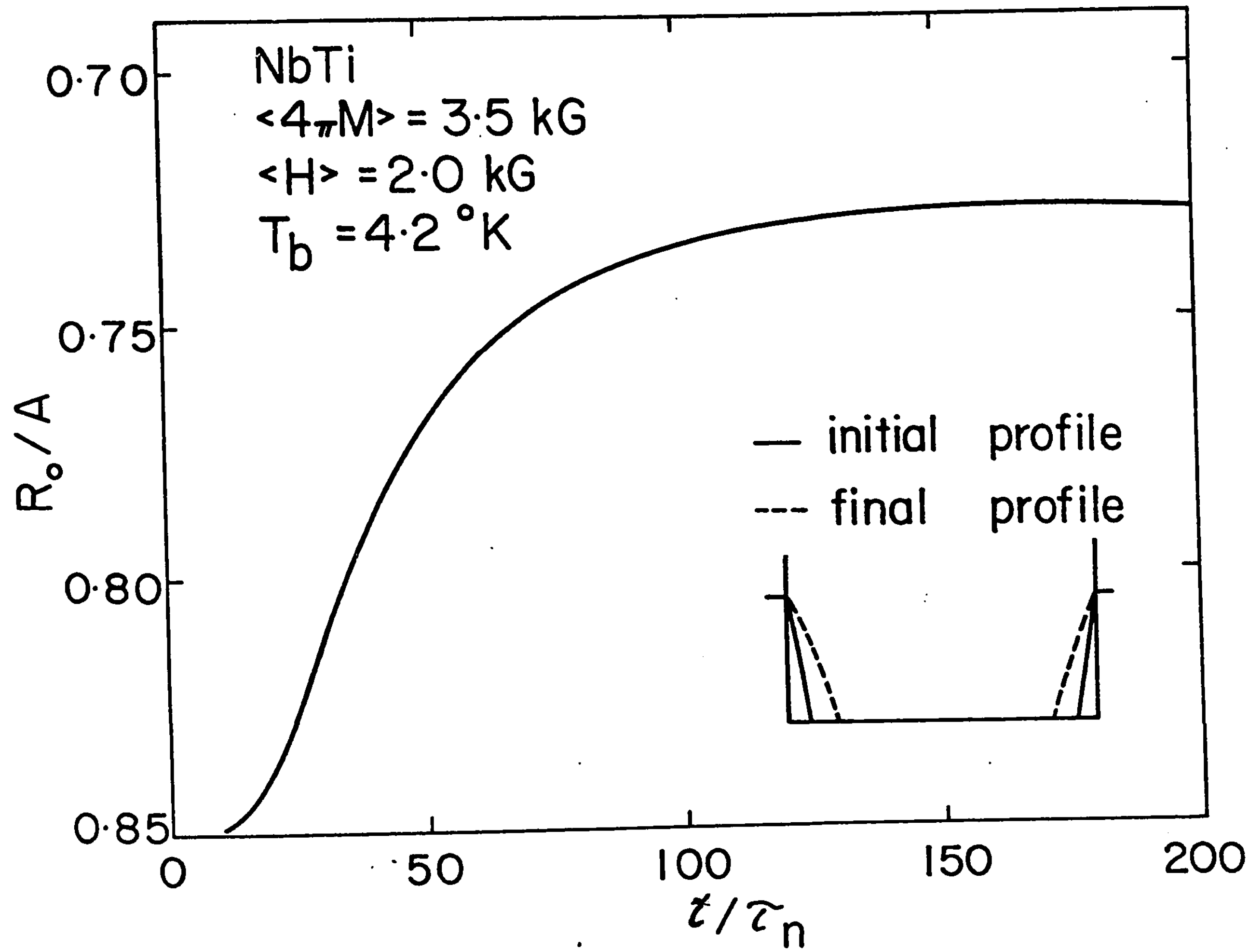

Fig. 4.32: Radius of field penetration R_o/A as a function of reduced time t/τ_n in a NbTi cylinder during a flux jump where initially $\langle 4\pi M \rangle = 3.5$ kG and $R_o/A = 0.85$

$$R_o(t) = [R_i - R_f]\, e^{-t/\tau} + R_f$$

where $R_o(t)$ is the radius of field penetration at time t, R_i and R_f are the initial and final radii of field penetration and τ is a time constant. In figure 4.32 we have plotted the value of R_o/A as a function of t/τ_n for a NbTi cylinder having an initial magnetization of 3.5 kG and an initial radius of penetration $R_i/A = 0.85$. The curve shown in figure 4.32 is in good qualitative agreement with the experimental results and the empirical relation of Harrisson et al (Harrisson 72, 73). Quantitative comparisons require a knowledge of the magnetization initially present in their discs and the value of the critical current density.

VII CONCLUSION

In this chapter we have investigated several features of the kinetics of radial flux collapse during flux jumps in type II superconducting cylinders (NbTi). Using the diffusion and heat equations given in chapter III we have explored the effect of the initial magnetization, field profile and average magnetic induction <B>. Although in a given sample these quantities are interdependent, we have in our calculations varied each of these parameters separately so as to give some insight on the role and importance of each of the parameters.

In section III of this chapter we have analysed the effect of changes in the initial magnetization $<4\pi M>$ for a given $<B>$ and field profile. We considered the case where the field had initially penetrated to the center of the cylinder. We found that, as the initial magnetization is increased, both the rate and extent of flux collapse increase. For the range of magnetization $1.4 \text{ kG} < <4\pi M> < 6 \text{ kG}$ the total time τ_t and the relaxation time τ_R were seen to change by two and three orders of magnitude respectively. The rate of diffusion of flux in a type II superconductor during a flux jump differs therefore dramatically from the diffusion of flux in normal conductors where it is independent of the initial configuration and intensity of the flux. Sequences of profiles of field, temperature and power density during flux jumps for three different magnetizations indicated that the general shape of both the field and power density profiles depends on the initial average magnetization.

In section IV we have analysed the effect of changes in the initial magnetic field profile for selected values of $<4\pi M>$ and $<B>$. The calculations indicate that the size of flux jumps $\Delta<4\pi M>$ decreases as the radius R_o to which the flux has initially penetrated increases. The size of flux jumps, hence the change in magnetization $\Delta<4\pi M>$, decreases slowly in the range $0 < R_o/A < 0.8$ then very rapidly in the range $0.8 < R_o/A < 1$ where very steep field profiles (ie high critical current densities) are encountered. The steepness of the initial field profiles was also shown to affect considerably the rate of collapse of flux. The time of radial collapse is governed by two competing contributions as the steepness of the profile is increased, i) a decrease in magnetic energy with R_o/A which tends to slow down the flux jumps, and ii) an increase in power dissipation density which tends to speed up the flux jump. The result of these two factors is an initial increase in τ_t and τ_R with R_o/A followed by a rapid decrease as values of $R_o/A \sim 0.85$ are exceeded. We have also shown that the main avalanche of flux (peak value of $\partial\phi/\partial t$) occurs at a later time when R_o/A is small (ie smaller values of J_c). To illustrate the characteristics of the flux jumping process for different initial field profiles we have presented sequences of field, temperature and power density profiles for $R_o/A = 0$, 0.6 and 0.85 and a magnetization of 4.0 kG.

In section V we have investigated the effect of the average magnetic induction $\langle B \rangle$ on the rate of radial flux collapse for two constant values of the magnetization. These calculations indicate that for small values of $\langle 4\pi M \rangle$ and/or $\langle B \rangle$ the total time of radial collapse τ_t decreases approximately as $1/\langle B \rangle$. If however the value of $\langle 4\pi M \rangle$ or $\langle B \rangle$ are such that the liberated magnetic energy becomes comparable to the enthalpy, the decrease in τ_R and τ_t with $\langle B \rangle$ becomes more rapid. This effect is attributed to the rapid increase in flux flow resistivity when temperatures close to the critical temperature are reached in the superconductor during the flux jump. When the magnetic energy is appreciably larger than the enthalpy both τ_t and τ_R

tend towards a limit which is determined by the normal state resistivity.

Finally, the depth of field penetration as a function of time was compared with experimental observations of other workers. The agreement between calculated and observed behaviour was seen to be satisfactory.

CHAPTER V

RADIAL COLLAPSE OF FLUX IN A NbTi CYLINDER: EXPERIMENTAL RESULTS AND COMPARISON WITH THEORY

I. INTRODUCTION

In chapter IV we have presented calculations of the effect of magnetization $\langle 4\pi M \rangle$, initial field profile, and average magnetic induction $\langle B \rangle$ on flux jumps in NbTi cylinders of arbitrary diameter. In these calculations, we have explored the role of each of these parameters separately. In practice, however, it is difficult to isolate and vary any single parameter independently. Experimentally one can readily trigger flux jumps at several convenient points along different magnetization curves obtained by first cooling the sample through T_c in a chosen external field H_o to a final temperature (usually the bath temperature) and then changing the field with the sample in the superconducting state. In this chapter we present theoretical and experimental results obtained with a rod of NbTi (denoted NbTi-3) where the magnetization curve was generated by first cooling the sample through T_c to 4.2^oK in a field H_o = 13.63 kG and subsequently increasing the field by various amounts ΔH.

Flux jumps were triggered in the final abient field by applying a field step of $\sim$ 250 G amplitude and $\sim$ 5 μs rise time over the entire length of the cylinder. In these calculations, however, we introduced a perturbation consisting of a temperature pulse equal to 1% of the bath temperature and extending uniformly to a depth equal to 1% of the radius from the surface of the cylinder.

In section II we compare the experimental and theoretical relaxation time τ_R for flux jumps triggered along the chosen magnetization curve starting at H_o = 13.63 kG. In section III we present the results of our calculations of profiles of field, temperature and power dissipation density for two different flux jumps triggered along this curve. In section IV we compare the observed and theoretical shape of the voltage pulses $\partial\phi/\partial t$ vs t detected by a pick-up coil intimately embracing the cylinder.

II. EXPERIMENTAL AND THEORETICAL VALUES OF τ_R

Figure 5.1 shows the magnetization curve of sample NbTi-3 along which flux jumps were triggered radially by applying a field step of $\sim$ 250 G and 5 μs rise time over the entire length of the cylinder. To obtain this magnetization curve the sample was first cooled through T_c to 4.2^{o}K in a field H_o = 13.63 kG and the field then raised by an amount

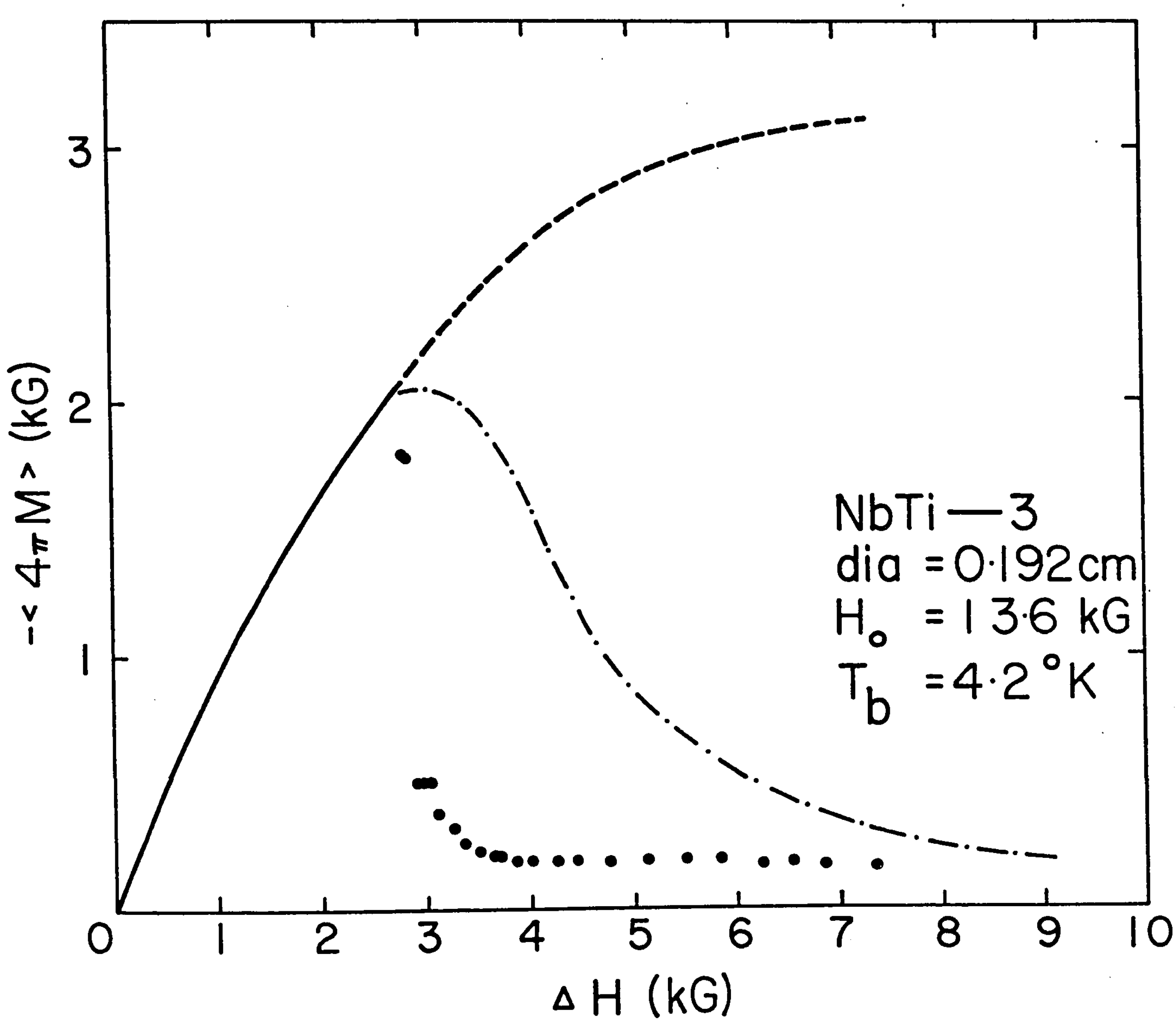

Fig. 5.1: Magnetization curve for NbTi-3 at 4.2°K for H_o = 13.63 kG. The solid and dashed lines indicate regions of stability and instability respectively. The dots show the experimental value of the residual <4πM> after a flux jump. The dash-dot line gives the theoretical value of the residual <4πM>.

ΔH. The region where flux jumps could be triggered is shown by the dashed line of figure 5.1. The solid line gives the region of full stability. The dots indicate the observed magnetization remaining in the sample after a flux jump. The dash-dot line indicates the calculated residual magnetizations after a flux jump. The theoretical magnetization curve used for this calculation was generated using the critical state model and assuming triangular field penetration (hence, J_c independent of field). The value of J_c was adjusted so as to produce a maximum magnetization (corresponding to full penetration of field) of 3.2 kG after a change in the external field $\Delta H = 9.6$ kG. The measured and calculated magnetization curves overlap closely over the range of field shown in figure 5.1. The values of the critical temperature, flux flow resistivity, and specific heat used in the calculations have been detailed in chapter IV. In these calculations, however, the average magnetic induction in the sample was taken to be the external field in the expressions for the flux flow resistivity and critical temperature. This approximation should not introduce any significant error since the variation of field within the sample is small compared to the external field.

We note that the size of the flux jumps observed experimentally increases very abruptly once the field $\Delta H \sim 3$ kG is exceeded, whereas the calculated (see figure 5.1) size of the flux jumps increases more slowly. The calculated and measured size of flux jumps are in good agreement when $\Delta H > 7$ kG. The reason for this discrepancy is not fully understood. It is probably associated with our choice for the dependence of H_{c2} and J_c on temperature together with our assumption that the initial J_c is uniform. Further calculations taking into account the dependence of J_c on the local magnetic field would be of interest and should lead to better agreement with observations.

In figure 5.2 we compare the experimental and theoretical relaxation time τ_R of flux jumps along the chosen magnetization curve (see figure 5.1). The qualitative agreement is encouraging. τ_R is large when $\Delta H \sim 3$ kG and its value decreases very rapidly as ΔH exceeds 3 kG. The appreciable discrepancy between the theoretical and experimental values in the range 3 kG $< \Delta H <$ 4 kG.is associated with the significant deviation between the observed and calculated sizes of flux jumps (figure 5.1). The quantitative agreement is satisfactory in the range 5 kG $< \Delta H \lessapprox$ 6 kG. For ΔH beyond 6 kG the experimental value of τ_R increases whereas the theoretical value decreases. This difference in behaviour may be associated with the fact that with our simplified model the theoretical magnetization continues to increase until $\Delta H = 9.6$ kG whereas the measured magnetization attains a maximum at $\Delta H \sim 7.5$ kG and then decreases as the external field continues to grow. This decrease in $\langle 4\pi M \rangle$ arises because J_c decreases with field. This feature is not taken into account in our calculations since J_c was taken independent of local field.

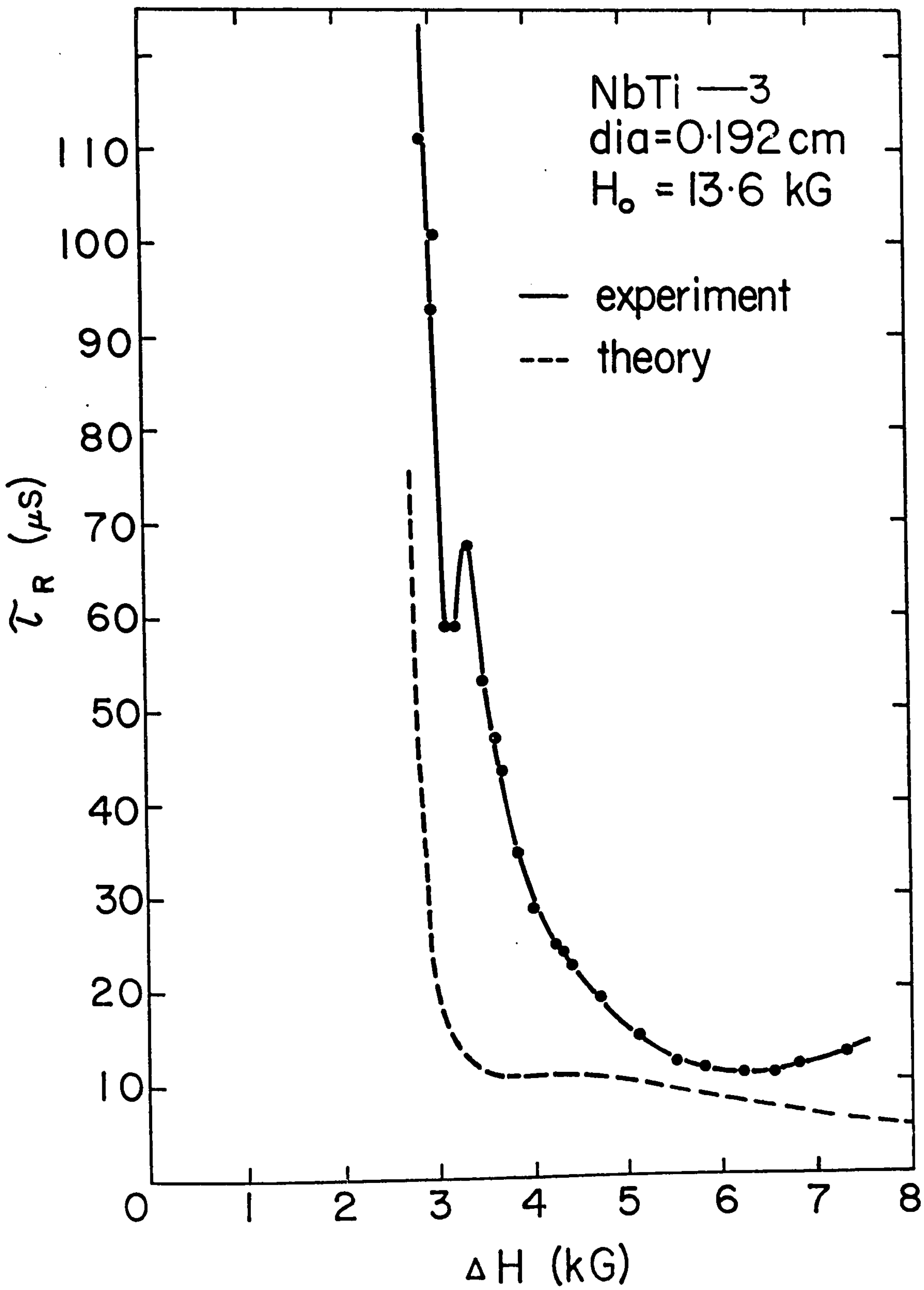

Fig. 5.2: Experimental and theoretical values of the relaxation time τ_R for flux jumps triggered along magnetization curve H_o = 13.63 kG of NbTi-3.

III SEQUENCES OF PROFILES OF FIELD, TEMPERATURE AND POWER DISSIPATION DURING FLUX JUMPS IN NbTi-3

In this section we present the result of calculations of sequences of profiles of field, temperature and power dissipation density encountered during two physically different flux jumps. We refer the reader to figure 5.1 for the pertinent magnetization curve.

The first flux jump is triggered when $\Delta H = 4.5$ kG and corresponds to a situation where initially the field has only superficially penetrated into the cylinder (see figure 5.3). The power dissipation during this flux jump therefore occurs mostly near the surface, reaching its maximum value after a time of approximately 7μs (figure 5.4). The temperatures attained (figure 5.5) also exhibit a maximum near the surface ($R/A \sim 0.8$) and remain equal to the bath temperature over the volume $R/A < 0.06$.

For the second flux jump $\Delta H = 9.0$ kG. This corresponds to a situation where the initial field profile has penetrated almost to the center of the cylinder (figure 5.6). In this case the flux jump is almost complete and the magnetization of the cylinder after the jump is very small (figure 5.6). The power densities (figure 5.7) encountered in this flux jump are considerable compared to the previous situation. The temperature distributions at different times during the flux jumps are shown in figure 5.8. In this case the final

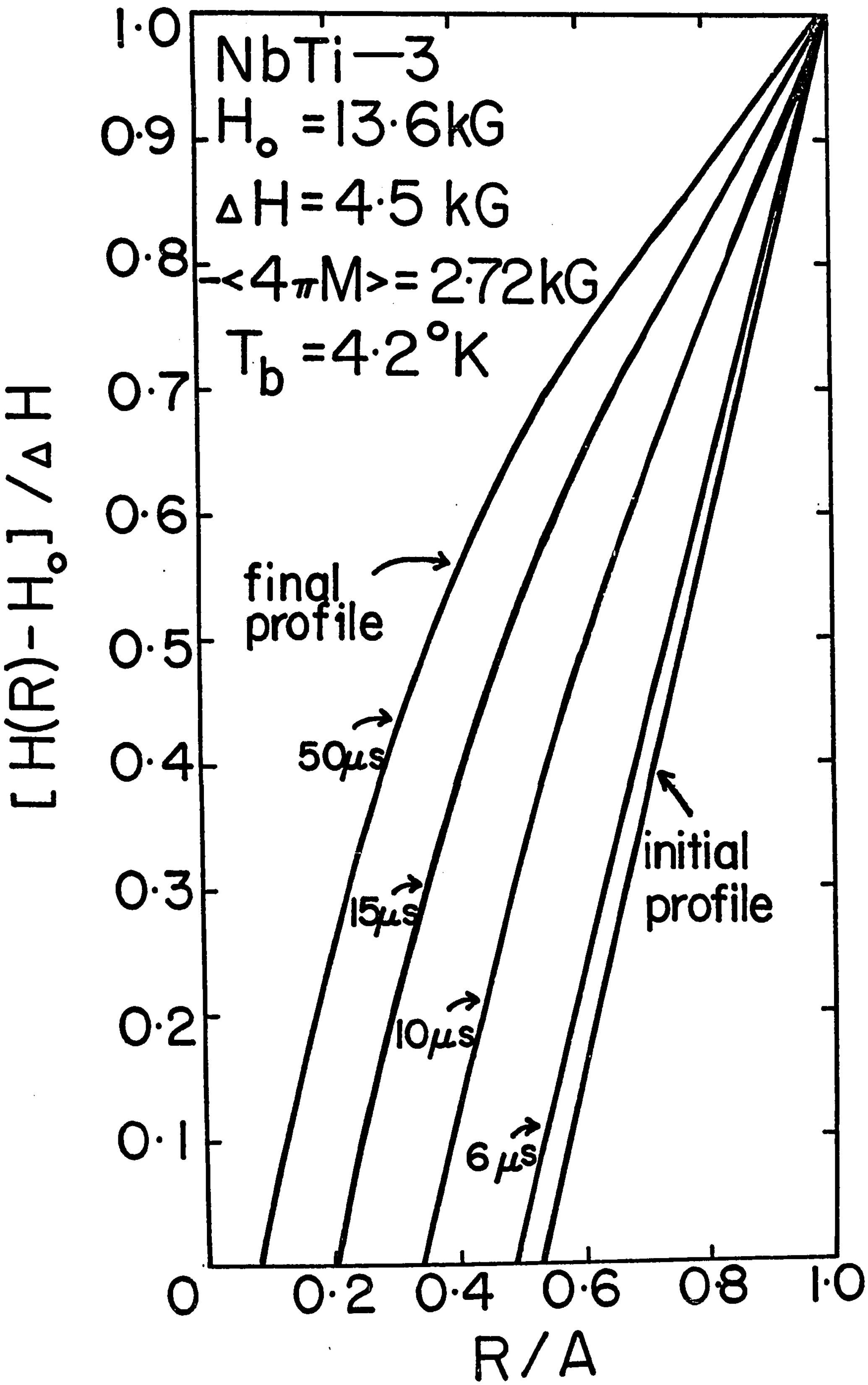

Fig. 5.3: Sequences of magnetic field profiles in NbTi-3 during a flux jump where ΔH = 4.5 kG.

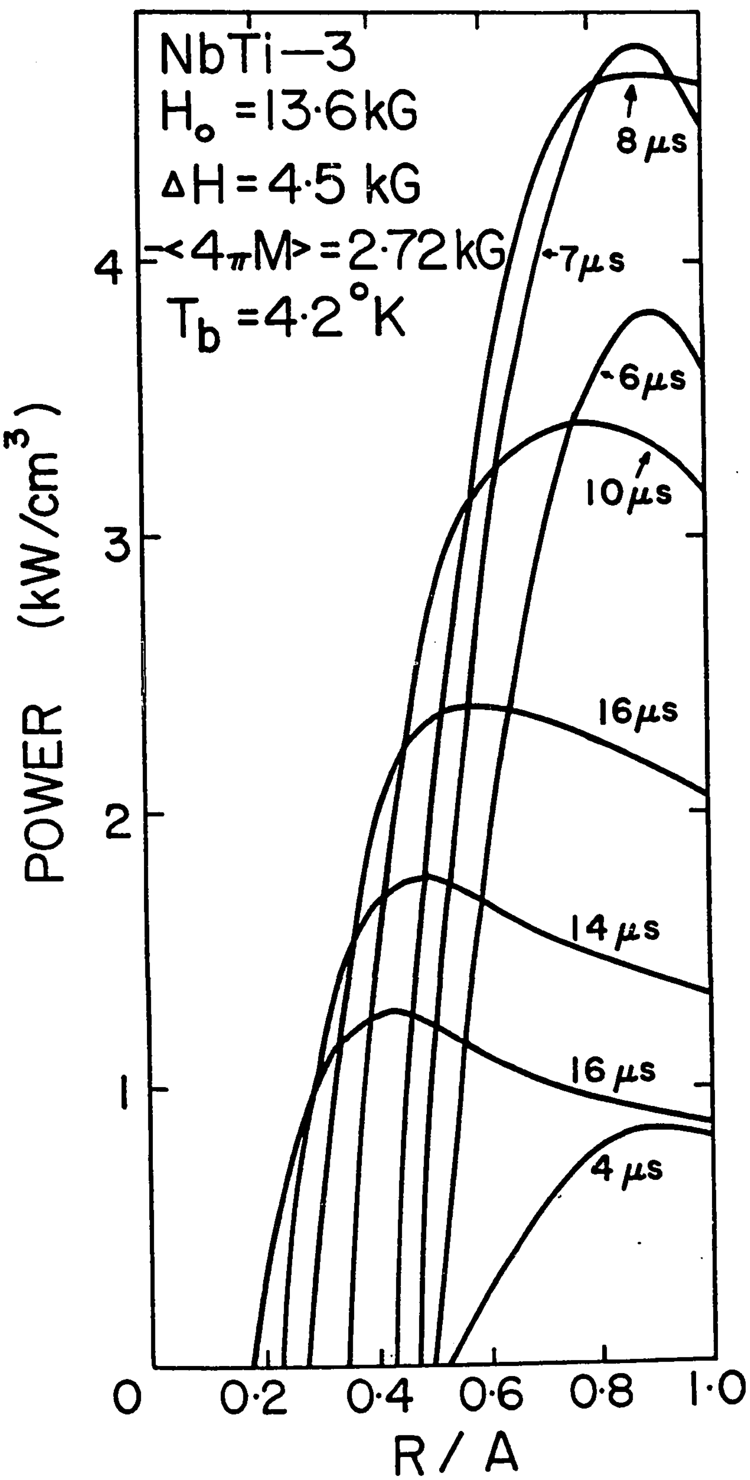

Fig. 5.4: Sequences of power dissipation density profiles in NbTi-3 during a flux jump where $\Delta H = 4.5$ kG.

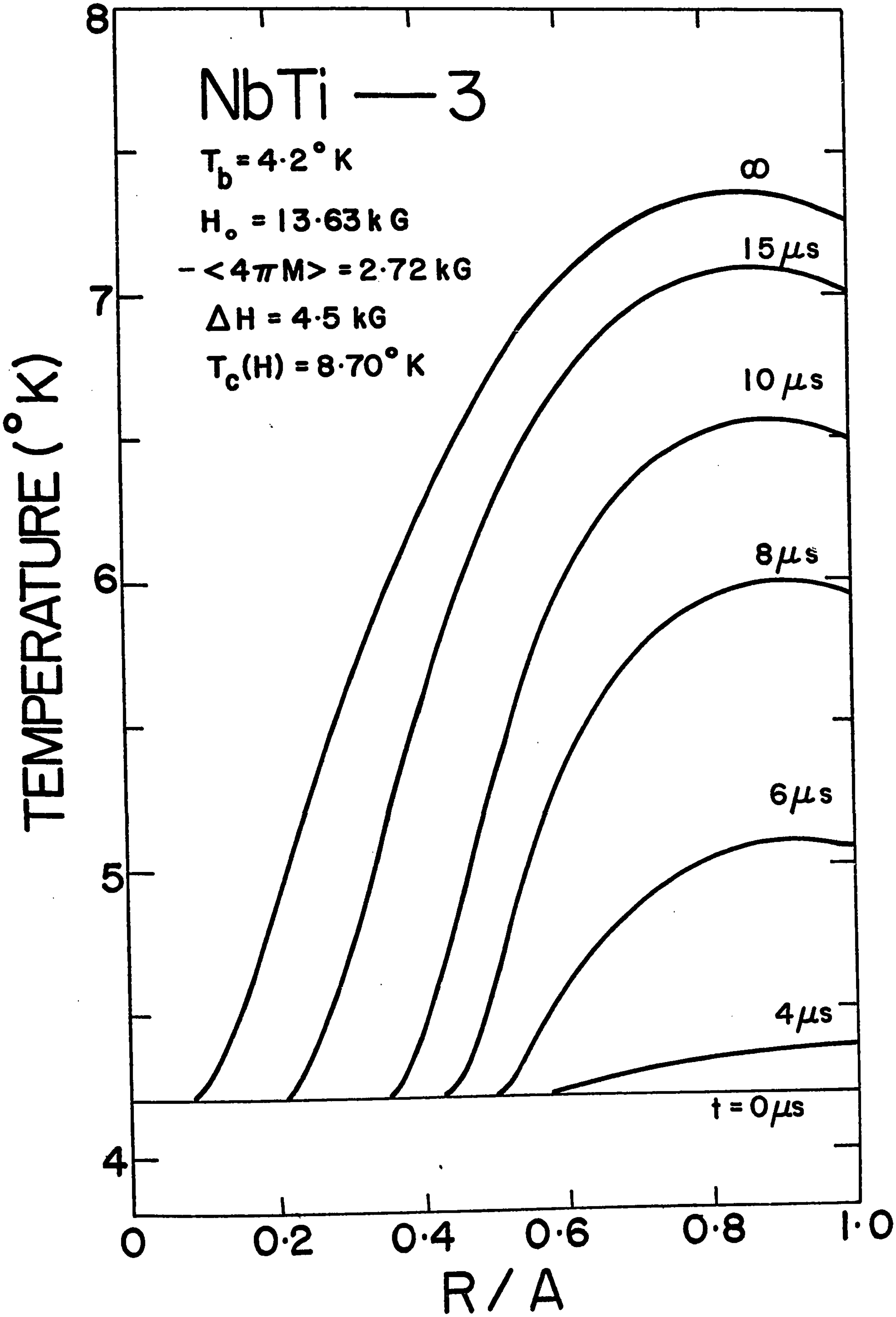

Fig. 5.5: Sequences of temperature distributions in NbTi-3 during a flux jump where ΔH = 4.5 kG.

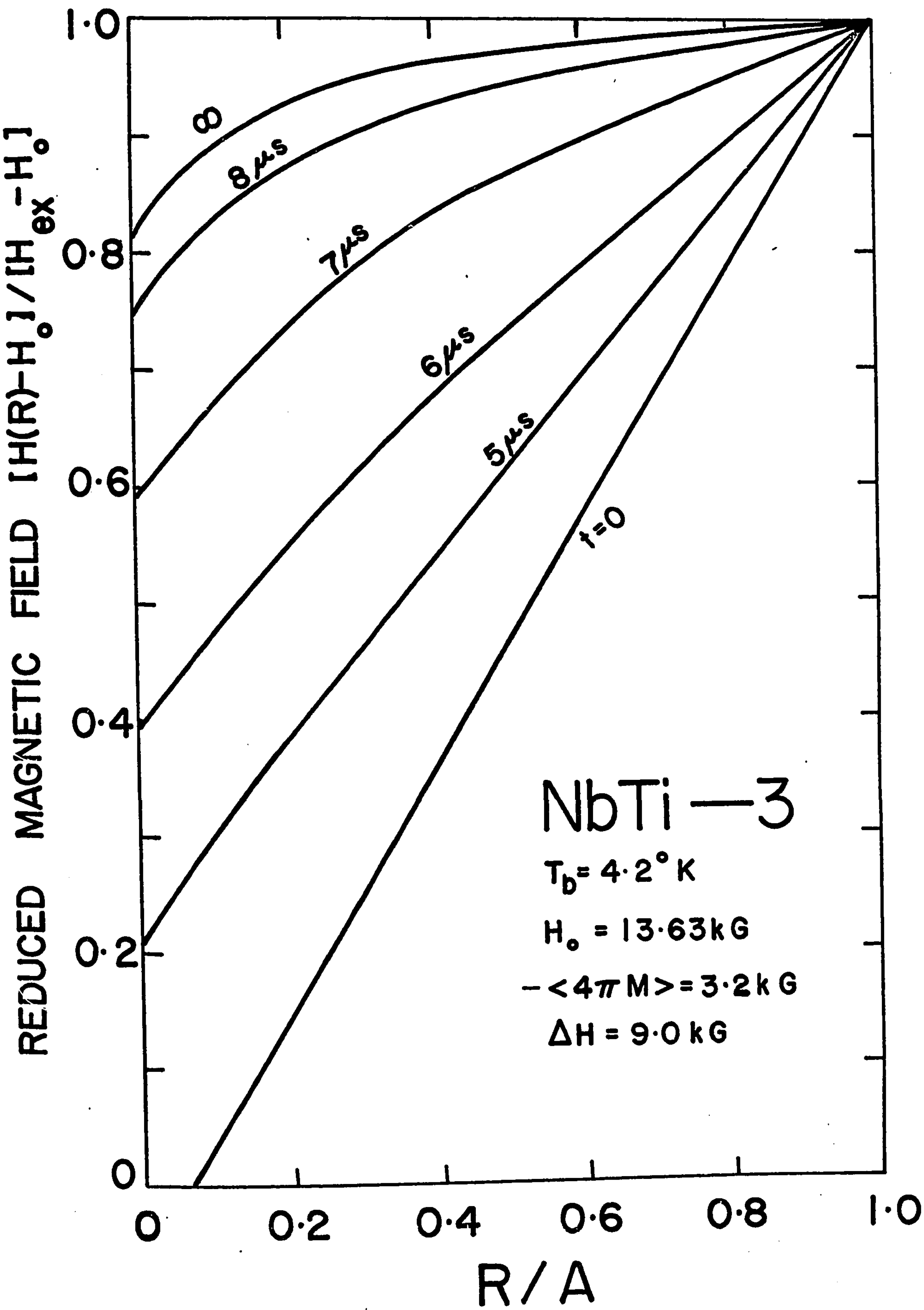

Fig. 5.6: Sequences of magnetic field profiles in NbTi-3 during a flux jump where ΔH = 9.0 kG.

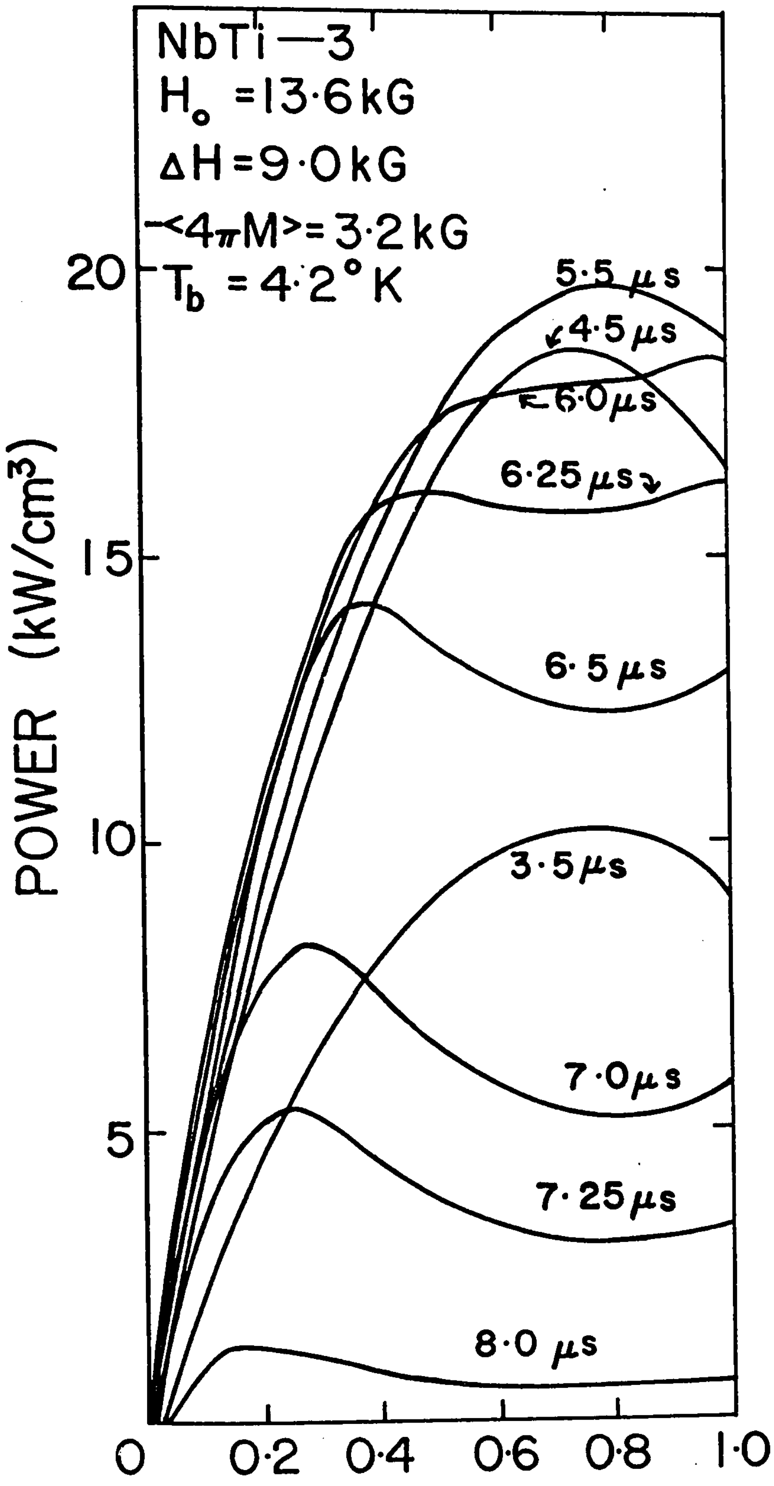

Fig. 5.7: Sequences of power dissipation density profiles in NbTi-3 during a flux jump where $\Delta H = 9.0$ kG.

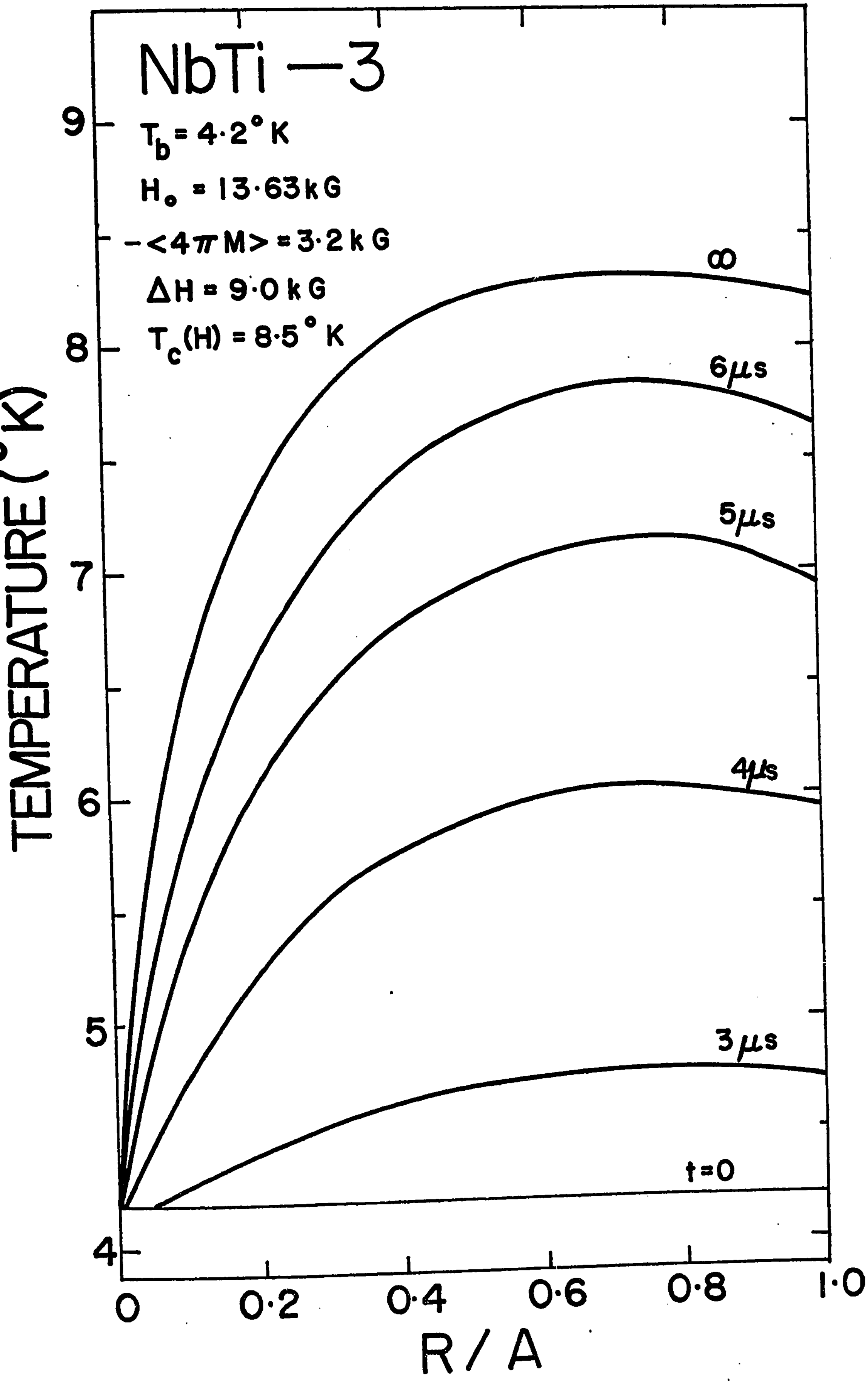

Fig. 5.8: Sequences of temperature distributions in NbTi-3 during a flux jump where ΔH = 9.0 kG

temperature is higher and attained in a shorter time than for the first flux jump.

IV EXPERIMENTAL AND THEORETICAL VOLTAGE PULSES: $\partial\phi/\partial t$ vs t

In this section we compare calculated and measured voltage pulses for flux jumps triggered at various points along the magnetization curve of the NbTi-3 sample (figure 5.1).

a) Theoretical Pulse Shapes:

Theoretical shapes of the voltage pulses seen by a pick-up coil of 1 turn surrounding the NbTi-3 cylinder are shown in figure 5.9 for flux jumps where the field increment ΔH varies. We note that the pulses reach a peak more rapidly for large ΔH and that the height of the peak also increases with ΔH. Calculated pulse shapes are presented using linear scales in figures 5.10 and 5.11 for comparison with observations. In figure 5.10 we note that the pulses where ΔH = 9.0 kG and ΔH = 6.0 kG are almost symmetrical whereas the pulse where ΔH = 4.5 kG is very asymmetrical, rising rapidly and decaying slowly. For ΔH = 3.0 kG (figure 5.11) the pulse becomes symmetrical again.

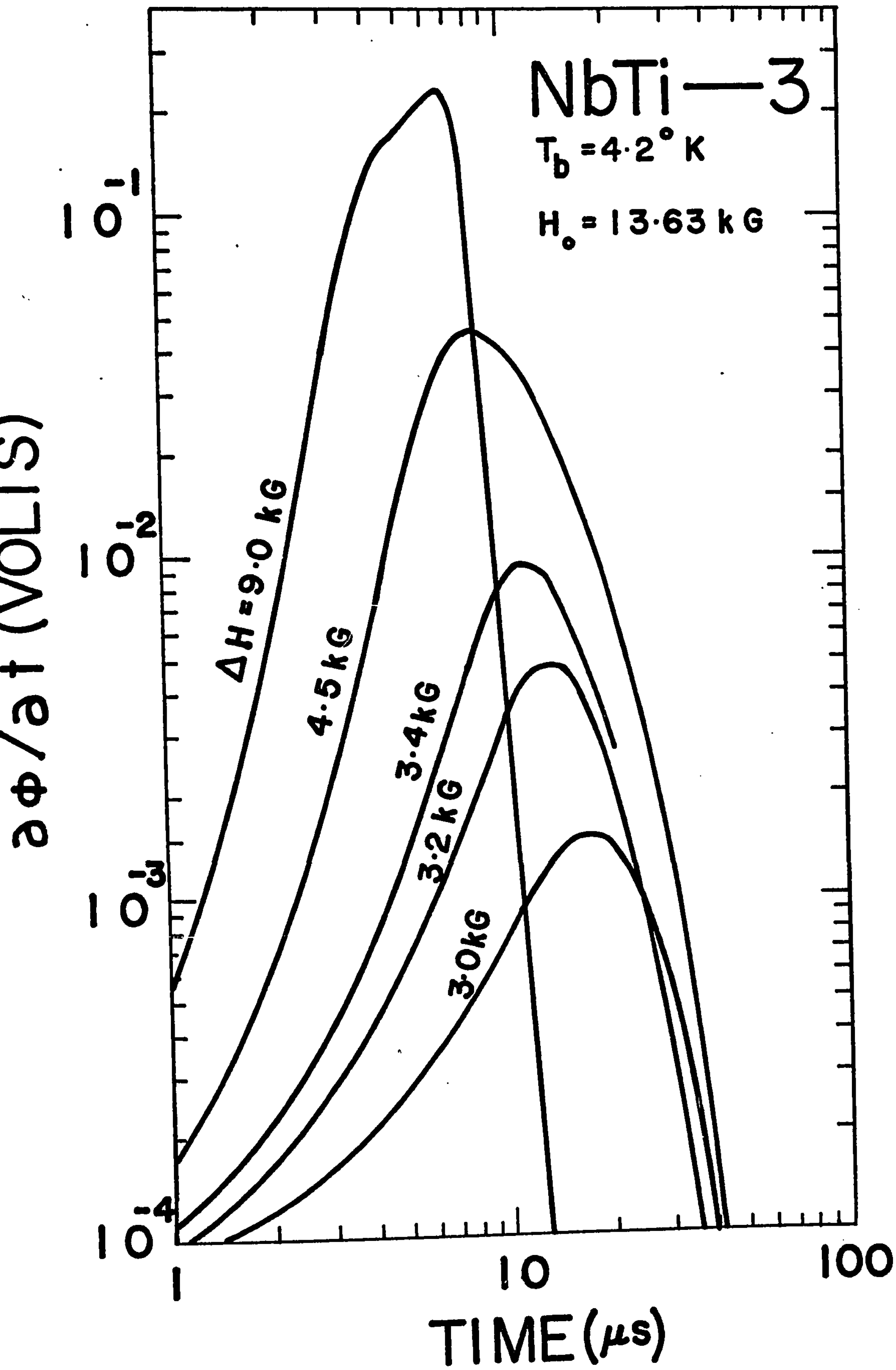

Fig. 5.9: Theoretical voltage pulses (log scale) seen by a pick-up coil of one turn surrounding NbTi-3 during flux jumps corresponding to several values of ΔH.

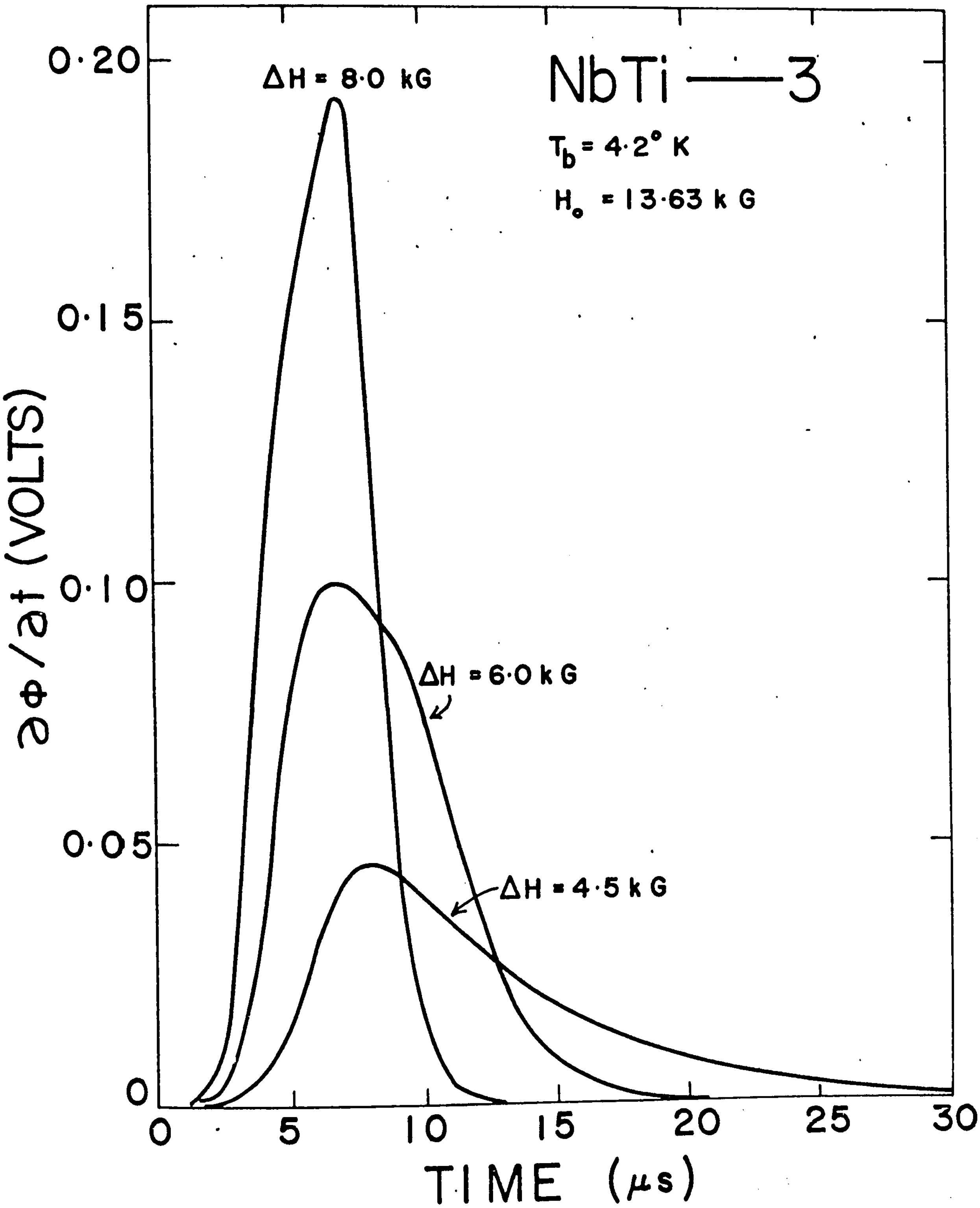

Fig. 5.10: Theoretical voltage pulses ($\partial\phi/\partial t$ vs time) (linear scale) seen by a pick-up coil of one turn surrounding NbTi-3 during flux jumps corresponding to several values of ΔH.

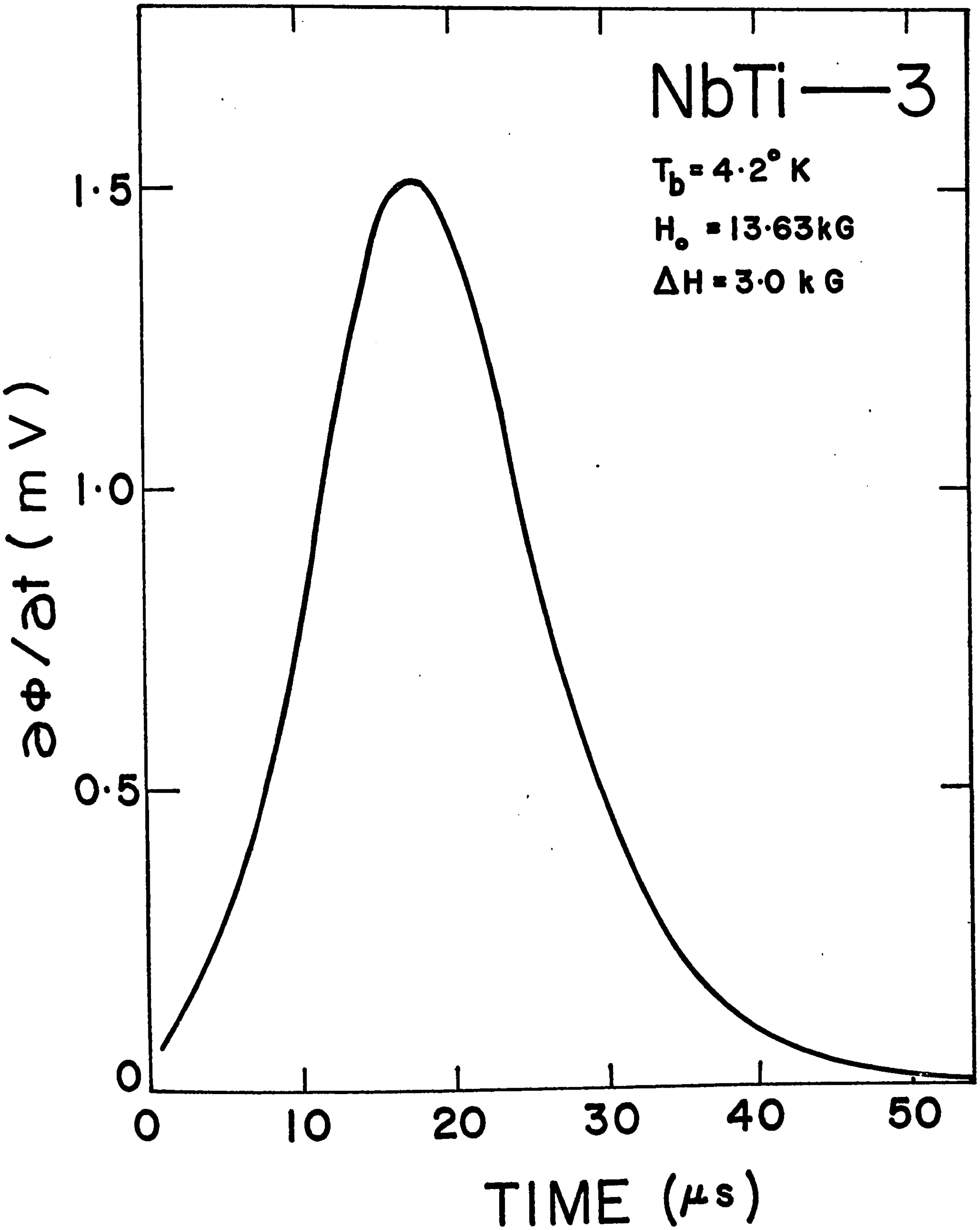

Fig. 5.11: Theoretical voltage pulse ($\partial\phi/\partial t$ vs time) seen by a coil of a single turn surrounding NbTi-3 during a flux jump corresponding to $\Delta H = 3.0$ kG.

b) Experimental Pulse Shapes:

Some experimental pulse shapes are shown in figure 5.12 for different values of the magnetic field increment ΔH. In each of these figures the upper trace corresponds to the voltage generated by two pick-up coils, one of 5 turns and the other 10 turns, wound in series and placed 4 cm apart on the cylinder. The lower trace gives the voltage produced by a single pick-up coil of 5 turns wound at the mid-point between the other two. The similarity of the sets of traces indicates that the radial collapse of flux occurred simultaneously everywhere along the cylinder. Thus a comparison between these curves provides a check on the characteristics of the flux jump and a guide to the validity of the data. We note (figure 5.12(a) to (d)) that the pulse shape depends on ΔH. The pulse shape changes from nearly symmetric to very asymmetric, then again to nearly symmetric over the range of ΔH shown. This sequence is qualitatively reproduced by the calculated pulses. Further the rise time tends to be shorter than the decay time in both the calculated and observed sets of pulse shapes.

The structures observed in the voltage pulses can be attributed to at least three different causes:

i) Although we endeavour to perturb the sample uniformly over its entire length, in practice the flux collapse may commence at one or several nucleation points along the sample. Thereafter the flux collapse will propagate both radially and longitudinally from each of these

(a)

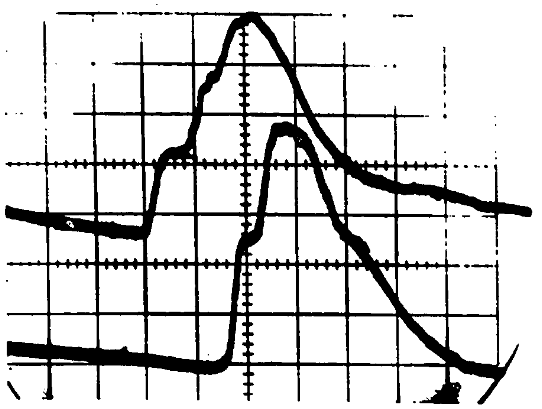

ΔH = 3.09 kG
upper = .02V/div, 20μs/div.
lower = .01V/div, 20μs/div.

(b)

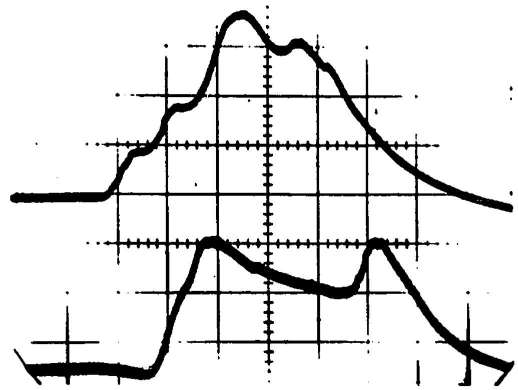

ΔH = 3.49 kG
upper = .05V/div, 10μs/div
lower = .02V/div, 10μs/div

(c)

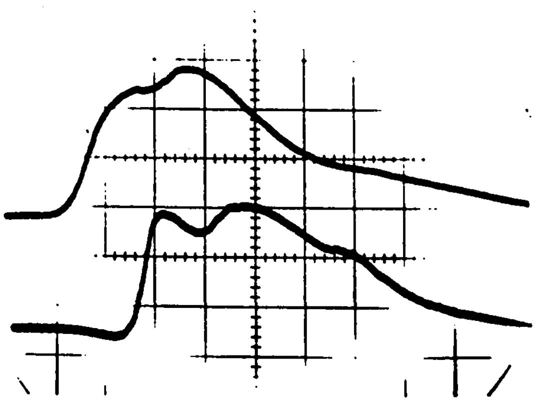

ΔH = 4.24 kG
upper = 0.1V/div, 5μs/div
lower = .05V/div, 5μs/div

(d)

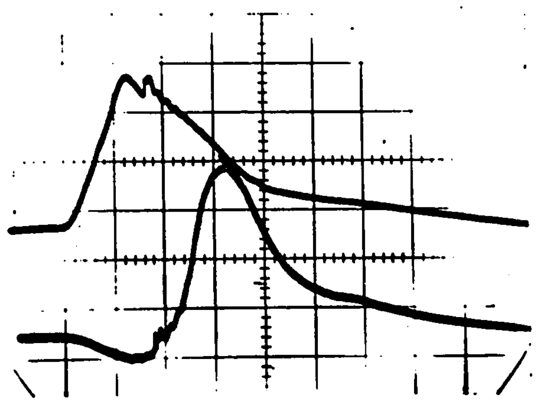

ΔH = 6.83 kG
upper = 0.2V/div, 5μs/div
lower = 0.1V/div, 5μs/div

Fig. 5.12: Experimental voltage traces observed during radial flux collapse in NbTi-3, H_o = 13.63 kG. Upper traces were produced by two coils (10 turns and 5 turns) wound in series, and lower traces by a single coil of 5 turns.

nucleation points. In these circumstances the radial collapse of flux will not occur simultaneously everywhere along the cylinder. Experimentally we can monitor the degree of simultaneity of radial flux collapse over the entire length by comparing the pulse from the two coils wound in series at different points along the cylinder with the pulse from the single coil wound at the midpoint. From inspection of the data (typical observations are shown in figure 5.13) we note that pure radial collapse, hence perfect correspondence of the timing and shape of the two sets of pulses is only partly achieved.

ii) Structure in the voltage pulses may also arise if the flux collapse nucleates at two or more regions around the periphery of the cylinder. Collapse of flux commencing at two or more spots around the circumference of the cylinder at different times and proceeding at different rates will give rise to "spikes" in the voltage pulses. "Spikes" have been observed in measurements of the longitudinal velocity of propagation and appear to be due to this type of sequential collapse of flux originating from different regions over the periphery of the cylinder. These phenomena are discussed in detail in chapter X. If however the collapse initiates more or less simultaneously from different spots over the circumference, the voltage pulses may be "regular" in shape and indistinguishable by our observation techniques from ideally symmetric events. We expect that the overall effect of either sequential or nearly simultaneous events nucleating around the circumference will be a lengthening of the pulses.

In our calculations we consider only flux collapse of a "one-dimensional" nature. Therefore our exploratory analysis only applies to events of a simple or ideal nature and cannot describe the variety of structures which can be encountered experimentally.

iii) Structure in voltage pulses may also occur when the flux penetration is cylindrically symmetrical. Our theoretical analysis shows that this can arise from the rapid increase in the flux flow resistivity when high temperatures are attained near the surface of the cylinder during the flux jump. Under certain conditions this may lead to voltage pulses exhibiting a peak and an adjoining plateau or hump. An example of this tendency to form two peaks which are not sharply resolved is shown in figure 4.6 (where $\langle 4\pi M \rangle = 3.5$ kG and $R_o/A = 0$). In some instances our calculations yield structure which is more pronounced than shown in this figure. The detailed structure we calculate depends on $\langle 4\pi M \rangle$, field profile, average magnetic induction $\langle B \rangle$, and the variation of flux flow resistivity with field and temperature. This type of structure should disappear altogether, if the increase in flux flow resistivity with temperature is gradual.

V CONCLUSION

In this chapter we have presented measurements of the relaxation time τ_R of radial flux collapse for flux jumps triggered along the magnetization curve of a NbTi rod. Calculations of τ_R for this experimental situation show satisfactory qualitative agreement with our observations. The calculated values of τ_R however always lie lower than the experimental values. This discrepancy may be ascribed to the simplifying assumptions and approximations introduced in the calculations. Among these assumptions are a linear dependence of J_c and H_{c2} on temperature and an initial current density which is independent of magnetic field (Bean model). In particular we have used a convenient analytic expression which only approximately describes the behaviour of the flux flow resistivity (see figure 4.1). We find from our calculations that the shape of the voltage pulses, hence τ_R depends on the detailed form of the flux flow resistivity. We have also assumed, for the derivation of the flux diffusion equation, a linear relation between electric field and current density, and have therefore neglected the non-linear region which is usually observed in flux flow resistivity measurements. Finally we note that in our analysis we have assumed that perfect adiabatic conditions prevail. In reality, diffusion of heat out of the sample and away from the hotter regions will take place. As a consequence we expect that our approach will overestimate the effective resistivity and hence the rate of flux collapse. Further, in some cases, the phenomenon observed experimentally may not correspond to the simple situation envisaged in the theory. In this context, we include the possibility of asymmetric and sequential flux penetration. Such modes of flux entry (or exit) cannot always be identified and extracted from the experimental data. Such events will tend to yield voltage pulses where the quantity

τ_R is lengthened.

The overall agreement between theory and experiment, however, is encouraging and leads us to believe that the agreement can be appreciably improved by introducing more refined and realistic approximations.

CHAPTER VI

RELATION BETWEEN PURELY RADIAL COLLAPSE OF FLUX IN A CYLINDER AND RADIAL COLLAPSE OBSERVED DURING LONGITUDINAL PROPAGATION.

I. INTRODUCTION

Walker and Hulm (Walker 66) have suggested that the width of the voltage pulses, detected during longitudinal propagation of a flux jump by a single pick-up coil wound locally on a wire, provides some information on the local rate of radial flux collapse. Although this situation differs from the case where flux is collapsing simultaneously over the entire length of a wire or cylinder these two phenomena should be related.

In this chapter we compare measurements of the relaxation time τ_R for flux jumps triggered over the entire length of a cylinder with that encountered during longitudinal propagation obtained for identical initial conditions. This comparison presented in section II, reveals that the relaxation time τ_R obtained under these two different sets of circumstances are indeed comparable and exhibit similar variations as ΔH, the increment in the external magnetic field, increases.

In section III we present several curves of τ_R extracted from voltage pulses observed during longitudinally propagating flux jumps for different materials and initial fields.

II VALUES OF τ_R MEASURED FOR PURELY RADIAL COLLAPSE OF FLUX AND FOR LONGITUDINAL PROPAGATION IN NbTi-3

In chapter V we presented values of τ_R for flux jumps triggered over the entire specimen at various points along a magnetization curve commencing at $H_o = 13.63$ kG for NbTi-3. We have also triggered flux jumps along the same magnetization curve using a small heater coil wound at one end of the sample. This mode of triggering gives rise to a flux jump propagating longitudinally along the cylinder as the flux collapses radially.

Regardless of the mode of triggering of the flux collapse, we define a characteristic time τ_R as the time interval between the increase and decrease to 1/e of the peak value of the voltage pulse detected by a pick-up coil locally embracing the cylindrical sample.

In figure 6.1 we compare the values of τ_R obtained using these two methods of triggering the flux jump. In one case the collapse of flux is purely radial and in the other the radial collapse in one region is preceded and followed by radial collapse in the adjacent volumes. The values of τ_R for these two types of events are seen to be comparable and to vary similarly with ΔH. The value of τ_R observed during longitudinal propagation, however, is somewhat greater that that observed

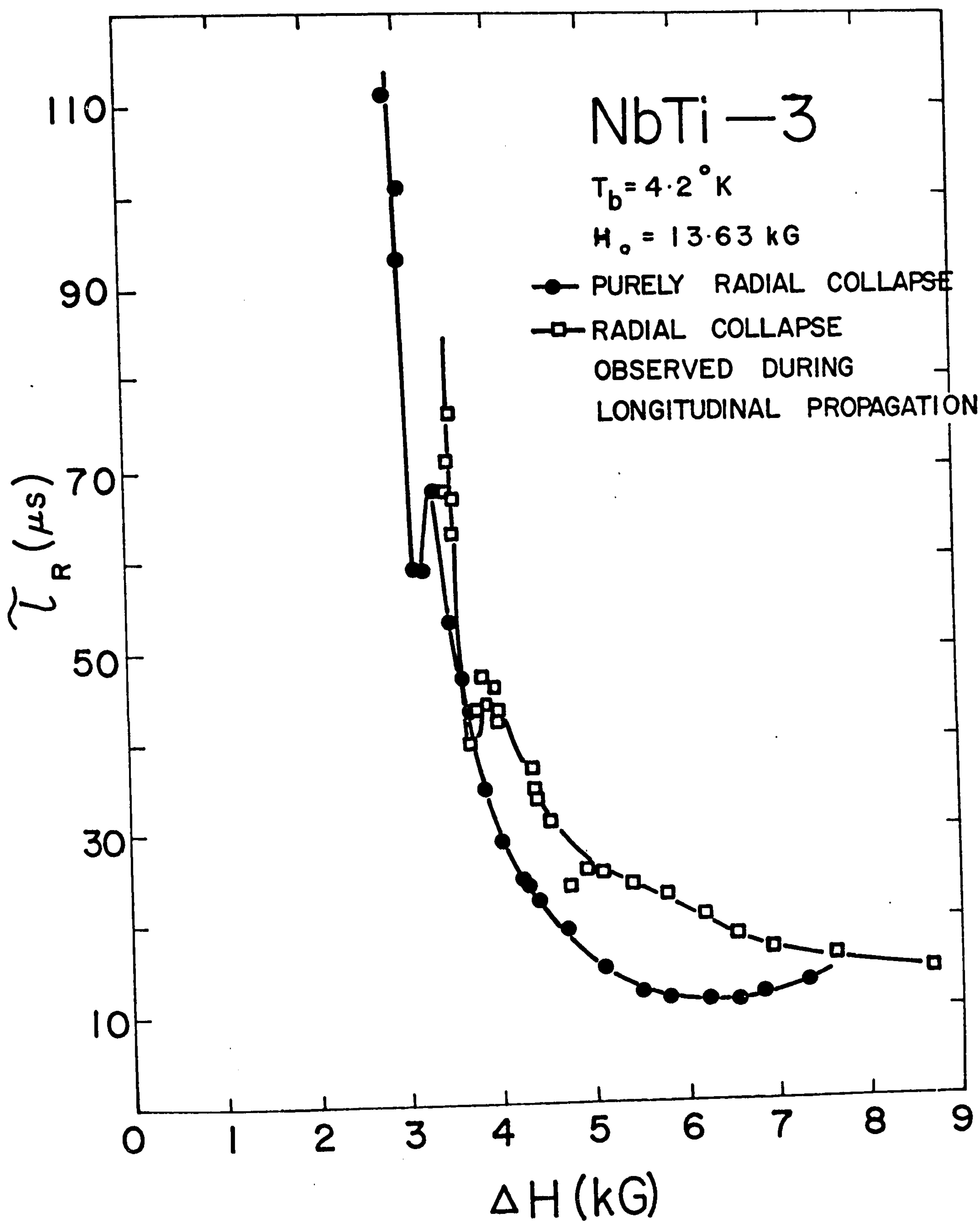

Fig. 6.1: Comparison of the relaxation times τ_R observed during purely radial flux collapse, and during longitudinal propagation in NbTi-3.

during purely radial collapse of flux. Part of this "dilation" of τ_R may be expected since for a longitudinally propagating flux jump, the pick-up coil will record the collapse of flux which occurs in the volumes adjacent to it before and after the local collapse of flux in the actual region embraced by the pick-up coil.

III VALUE OF τ_R MEASURED FOR LONGITUDINAL FLUX JUMPS IN NbTi-2, NbZr-1, V-2 AND NbTi-4.

Longitudinal flux jumps were also triggered along a number of magnetization curves in different materials. In this section we present curves of τ_R extracted from the voltage traces observed during these events.

In figures 6.2 to 6.6 we present values of τ_R as a function of external field H for flux jumps triggered along selected magnetization curves of samples NbTi-2, NbZr-1, V2 and NbTi-4. We refer the reader to figures 9.4, 9.3, 9.21, 9.34 and 9.19 respectively for the corresponding magnetization curves. In figures 6.2 to 6.5 we note that τ_R is larger near the limit of stability (values of H close to H_o), decreases rapidly for fields near H_o, and then varies rather slowly over a wide range of field. This large variation of τ_R near H_o followed by a relative plateau as H is further increased is similar to the experimental and theoretical behaviour of τ_R shown in figure

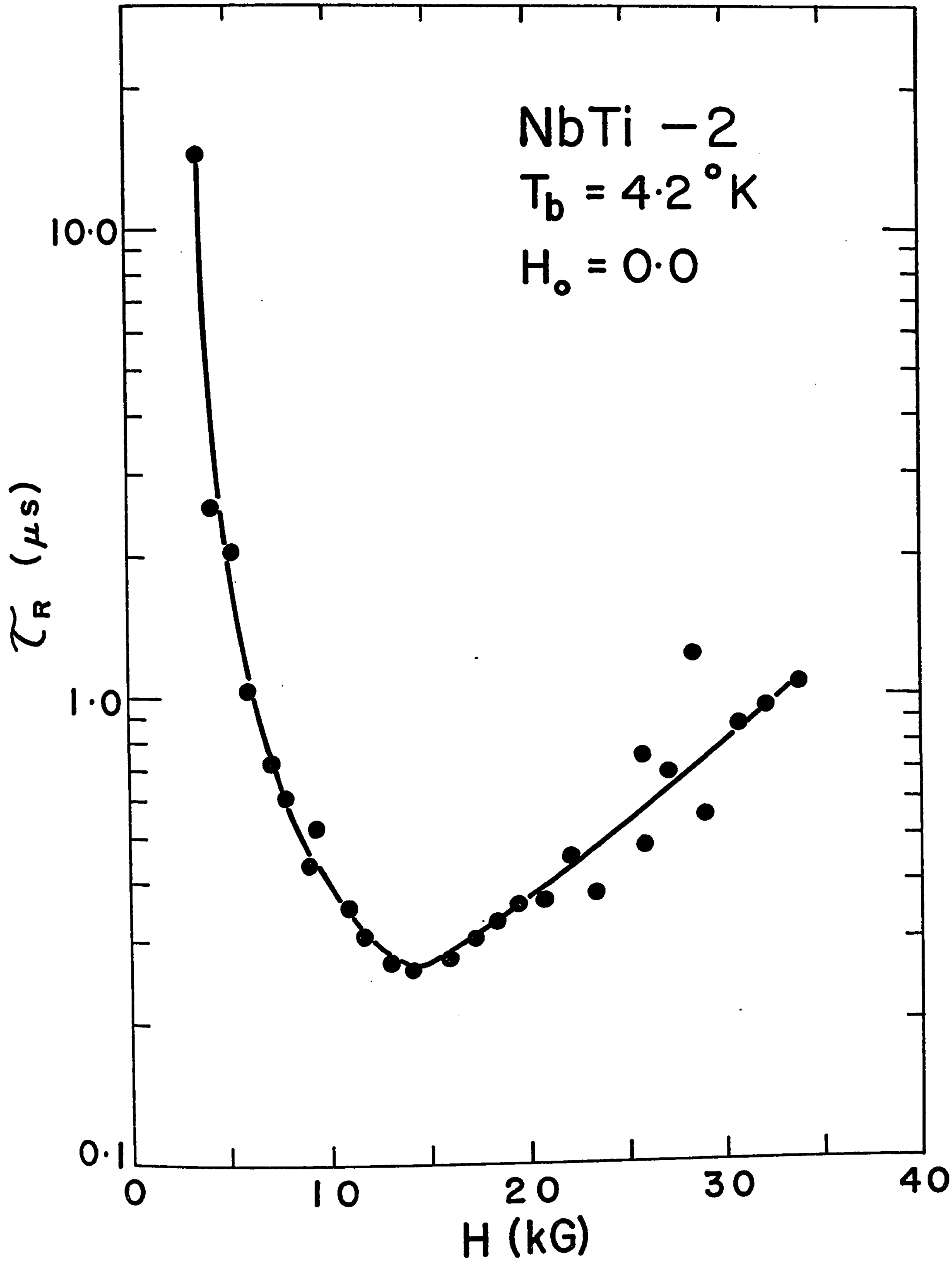

Fig. 6.2: Relaxation time τ_R observed during longitudinal propagation in NbTi-2 for magnetization curve where $H_o = 0$ (shown in fig. 9.4).

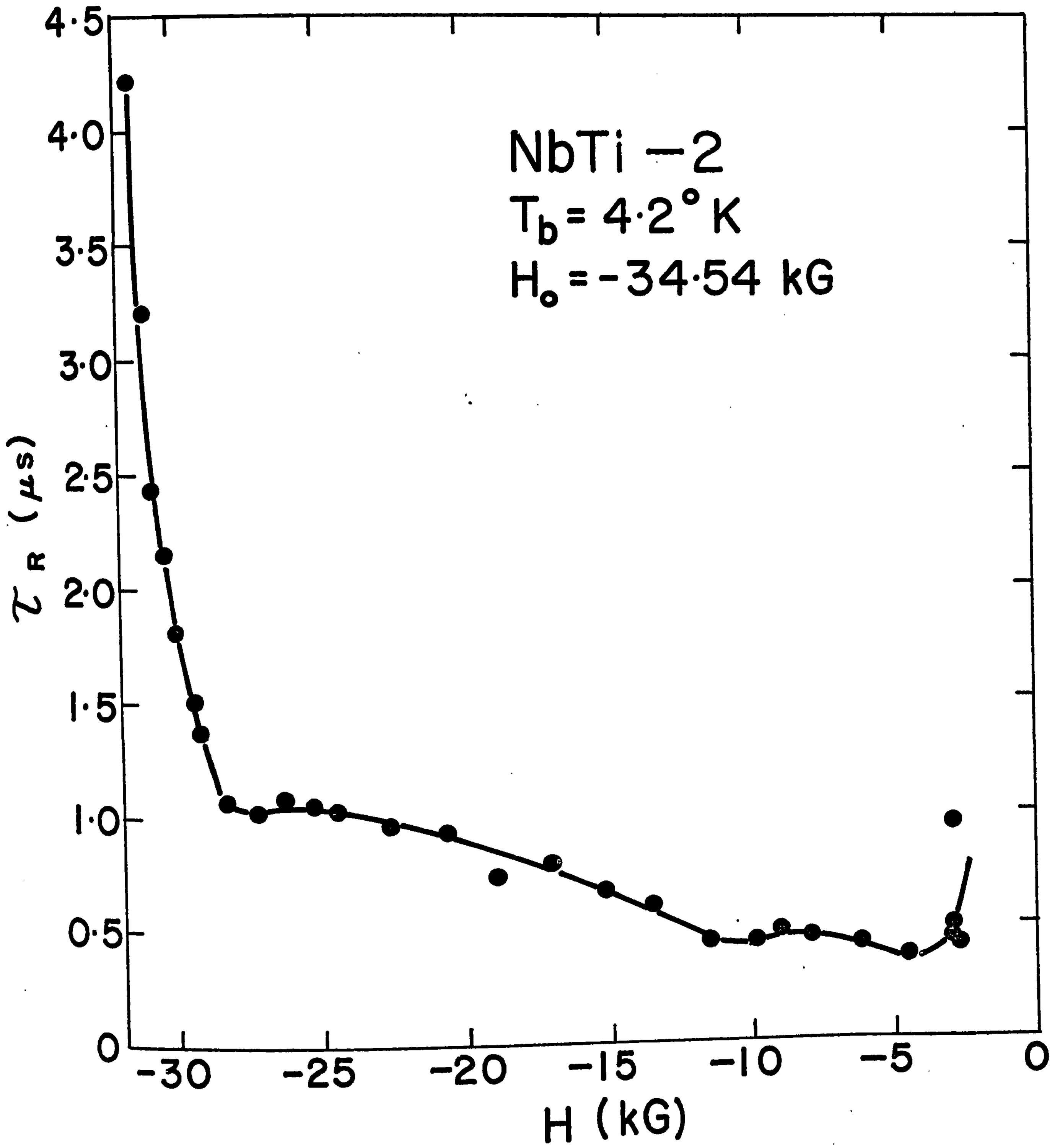

Fig. 6.3: Relaxation time τ_R observed during longitudinal propagation in NbTi-2 for magnetization curve H_o =-34.54 kG (shown in fig. 9.3).

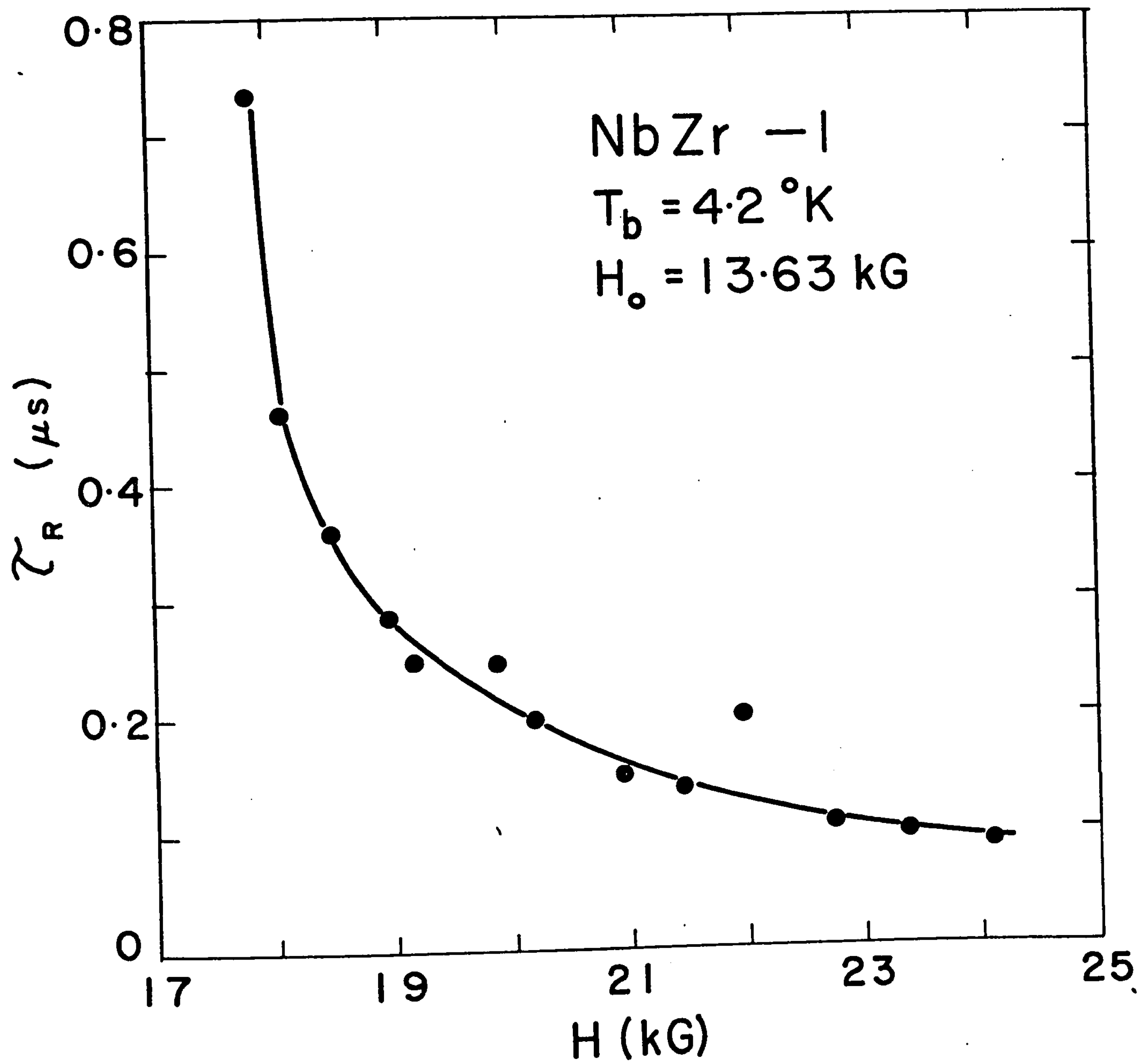

Fig. 6.4: Relaxation time τ_R observed during longitudinal propagation in NbZr-1 for magnetization curve H_o = 13.63 kG.

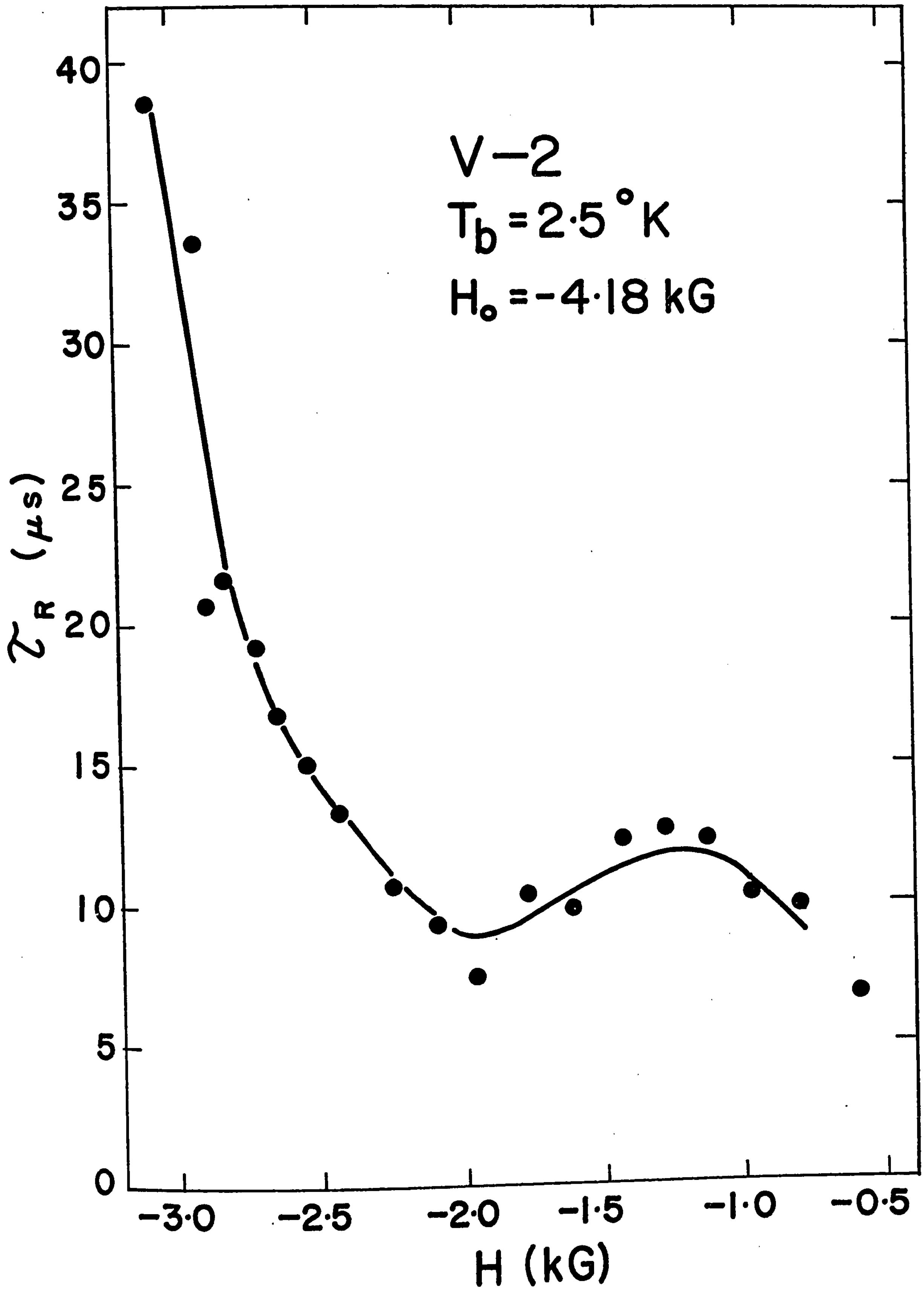

Fig. 6.5: Relaxation time τ_R observed during longitudinal propagation in V-2 for magnetization curve H_o =-4.18 kG.

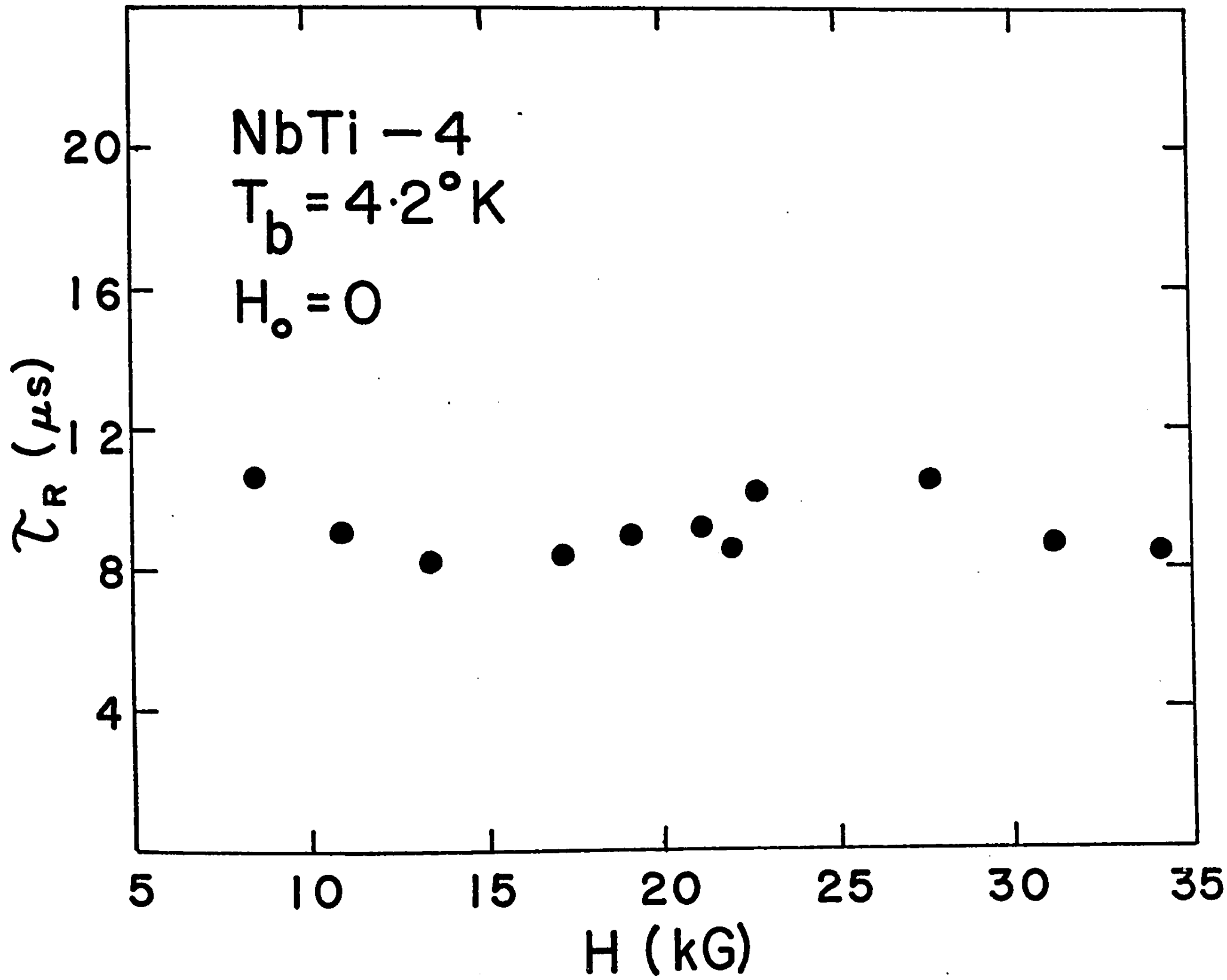

Fig. 6.6: Relaxation time τ_R observed during longitudinal propagation in NbTi-4 for magnetization curve $H_o = 0$.

5.2 for NbTi-3.

In the range of field distant from the limit of stability τ_R is seen to either increase gradually (figures 6.2 and 6.3), decrease slowly (figure 6.4), or remain nearly constant (figures 6.5 and 6.6) as the external field increases. These changes in τ_R with increasing field result from two main competing contributions:

i) a decrease in magnetization with H which leads to an increase in τ_R,

ii) an increase in flux flow resistivity with H which causes a decrease in τ_R. Depending on the characteristics of the sample the first contribution (due to a decrease in $\langle 4\pi M \rangle$) may overcome (figure 6.2, 6.3) be overcome by (figure 6.4), or approximately balance (figures 6.5, 6.6) the contribution due to the increase in flux flow resistivity.

IV CONCLUSION

In this chapter we have shown that the relaxation time τ_R measured by a single pick-up coil wound locally on a superconducting cylinder during the longitudinal propagation of a flux jump is similar in magnitude and in its dependence on magnetic field and magnetization to the "true" radial relaxation time. We then presented several curves of τ_R obtained during measurements of the longitudinal propagation of flux jumps in a NbTi wire, rod and hollow cylinder and in wires of NbZr and Vanadium.

PART II

THE LONGITUDINAL PROPAGATION OF FLUX JUMPS ALONG TYPE II SUPERCONDUCTING CYLINDERS IN AXIAL FIELDS

CHAPTER VII

INTRODUCTION TO PART II

It has been shown by Walker and Hulm (Walker 65, 66) that once the decay of persistent currents is initiated in a small region of a type II superconducting wire the resulting flux disturbance, feeding upon the stored magnetic energy, may propagate indefinitely along the wire. This phenomenon was investigated for situations where the external field is perpendicular (Walker 65, Iwasa 68) and parallel (Walker 66, 72, Bussière 72a) to the axis of the wire. The velocities encountered in NbZr wires in perpendicular fields (Walker 65, Iwasa 68) are of the order of 10^4 cm/s. In this case the flux collapse was observed to propagate in steps, leaving behind a spatially periodic variation in the residual magnetization of the wire. This variation was associated with large vortices of current uniformly distributed along the wire. The formation of a sequence of minima and maxima of magnetization was attributed to effects due to thermal conduction (Walker 65, Iwasa 68). Thermal conduction was also presumed to limit the propagation velocity and to play an important role in the mechanism of propagation.

In axial fields, velocities ranging between 10^4 and 10^6 cm/s have been reported for NbZr wires (Walker 66, 72). Velocities of the same order of magnitude have also been reported for wires of NbTi, NbZr and Nb (Bussière 72a). Although there is no theory available at present to predict the magnitude of these velocities we have shown (Bussière 72b) that the propagation arises through electromagnetic coupling between regions where flux is collapsing and unperturbed regions ahead. If this model is correct then we expect the longitudinal velocity to depend on the rate of radial collapse of flux and therefore to depend on parameters such as magnetization, magnetic field profile, external field, normal state resistivity, etc. In the following chapters we present measurements of the longitudinal velocity of propagation of flux jumps in wires of different materials and diameters. We show that the behaviour of the velocity observed for these samples can be related to the characteristics of radial collapse of flux described in part I of this thesis.

In chapter VIII we present measurements of the velocity of propagation of a normal front in axial fields when both a transport current and an axial magnetic moment are present in the wire. Some of these results have been reported earlier (Bussière 72b). From these measurements we conclude that below a certain critical magnetic moment the propagation is limited by thermal conduction, but as this critical moment is exceeded the propagation is controlled by electromagnetic coupling between the regions where flux is collapsing and the unperturbed regions ahead.

In chapter IX we show how the velocity of propagation of flux jumps in the absence of a transport current varies as a function of the initial magnetization $\langle 4\pi M \rangle$ present in the sample for a large number of magnetic histories and different samples.

In chapter X we present evidence that flux sometimes penetrates a given sample asymmetrically during propagation. The evidence for this type of phenomenon emerges from examination of the structure in the voltage peaks seen by the detector coils wound along the samples.

In chapter XI we explore an empirical relationship between the longitudinal velocity and the relaxation time τ_R. This relation depends on magnetic history and is explained partly in terms of the changes in the rise time of $\partial\phi/\partial t$ with magnetic theory.

Investigations of the role played by the external magnetic field, transport current, and bath temperature on the longitudinal velocity are reported in chapters XII, XIII and XIV respectively.

In chapter XV we report that the velocity of flux jumps tends to diminish as the diameter of the cylinder is increased with a given material when the magnetization is held constant. The effect of the diameter is explained qualitatively in terms of its role in radial flux collapse.

CHAPTER VIII

THERMAL VS ELECTROMAGNETIC PROPAGATION

I. INTRODUCTION

A heat pulse of suitable magnitude applied locally to a wire of type II superconductor carrying a steady transport current will initiate a small normal region. This region will propagate along the conductor if the generation of joule heat (ρJ^2) is greater than the heat flow to the outside and the neighbouring region. On the other hand a heat pulse applied locally to a wire of a type II superconductor carrying no transport current but supporting an axial magnetization will in some cases cause a collapse of flux to travel along the wire at velocities which can exceed the velocity of sound (Walker 62, 72, Bussière 72a). If the initial magnetic energy stored in the conductor is large enough, this results in the propagation of a normal front. In this chapter we present measurements of normal phase propagation in the absence of a magnetic moment and then explore how the presence of magnetic moments affects the velocity for constant transport current levels. In the light of these measurements we conclude that for small magnetic moments the mechanism of propagation is not altered by the presence of azimuthal persistent currents. When the magnetic moment exceeds a certain critical value, denoted $\langle 4\pi M_c \rangle$, the velocity increases abruptly and electromagnetic coupling rather than thermal diffusion appears to be the controlling factor. We therefore refer to these two types of propagation respectively as "thermal" and "magnetic".

The problem of the one-dimensional thermal propagation of a normal front has been studied by Cherry and Gittleman (Cherry 60), Broom and Rhoderick (Broom 60), Whetstone and Roos (Whetstone 65) and recently by Overton (Overton 71). The propagation is due to the flow of heat from the normal volume, where heat is being produced at a constant rate (ρJ^2), into the cooler superconducting region. The travelling superconducting-normal interface is taken to be at the critical temperature $T_c(H)$ characteristic of the applied field H for the material under study. Measurements on bare wires of Nb-Zr alloys as a function of current and magnetic field showed that the velocity of propagation was approximately linear in the current density J and independent of normal state resistivity ρ_n. The slope of velocity vs J was found to depend mainly on the thermal capacity and the transition temperature $T_c(H)$, (hence on magnetic field).

In section II we present measurements of this type of propagation in the absence of a magnetic moment for a wire of Vanadium (V-2). The variation of velocity with current density and magnetic field is in good agreement with the expression of Whetstone and Roos (Whetstone 65).

Then in section III we present measurements of the velocity of propagation of a normal front as a function of initial magnetic moment for constant levels of conduction current.

In section IV we discuss our conclusion that for magnetic moments where the magnetic configuration is stable, the mechanism of propagation is thermal although the velocity is influenced by the variations of the magnetic field in the sample and the additional joule heat due to the decay of the azimuthal persistent currents. The large velocities observed when the magnetization exceeds a critical value $\langle 4\pi M \rangle_c$ are attributed to the onset of unstable magnetic configurations and to a mechanism of propagation where electromagnetic coupling plays a dominant role.

II VELOCITY WITH NO MAGNETIC MOMENT

Our measurements of the velocity of propagation of the normal phase as a function of transport current density J are shown in figure 8.1 for different external fields H. The solid lines are theoretical curves obtained using the expression of Whetstone and Roos (Whetstone 65). The pertinent data for the normal and superconducting specific heats used in the calculation are given in table II. The transition temperature in zero field $T_t = 4.98^{\circ}K$ was estimated by extrapolation of the linear dependence of H_{c2} measured between $2^{\circ}K$ and

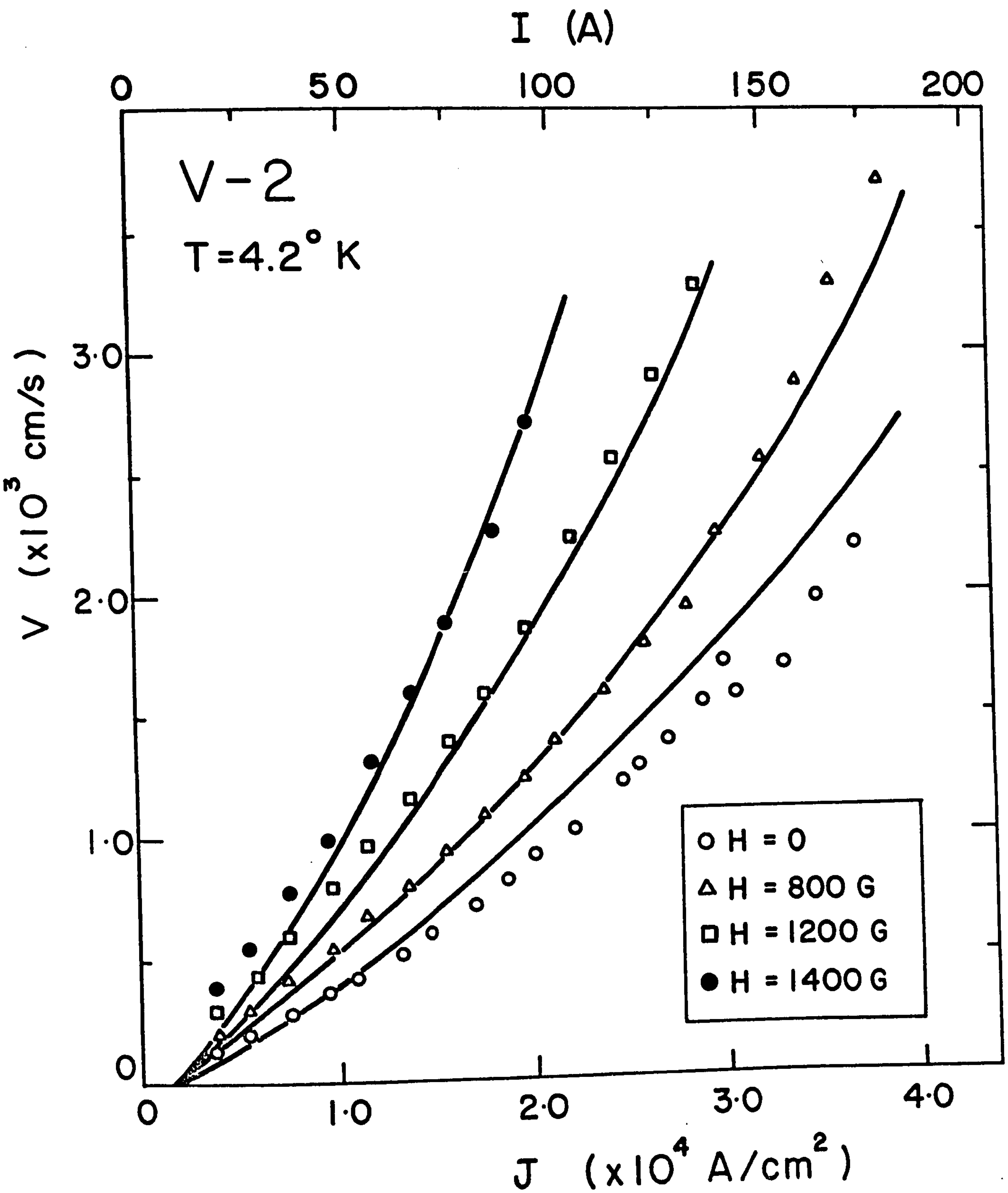

Fig. 8.1: Velocity of propagation of normal region with no magnetic moment. The points are experimental and the lines theoretical.

$4.2^{o}K$. H_{c2} was obtained from magnetization measurements. In the calculations we introduce an average magnetic field taken to be the vectorial sum of the external field and the average azimuthal field associated with the transport current. The self field of the conduction current is responsible for the non-linear increase of velocity with J exhibited by the calculated curves. In these calculations, the threshold current density J_o below which no propagation occurs is treated as an adjustable parameter and the value $J_o = 2 \times 10^3 A/cm^2$ was used.

III. VELOCITY WITH A MAGNETIC MOMENT PRESENT

The velocity as a function of $<4\pi M>$ was measured in a sample of Vanadium (denoted V-2) for bath temperatures of $4.2^{o}K$ and $2.6^{o}K$. For these measurements the sample was first cooled through T_c in the presence of different initial fields H_o. A constant current was then introduced and the applied field either reduced to zero (see for example inset of figure 8.2) or brought to a different value (see inset of figure 8.3), thereby inducing a magnetic moment in the sample dependent on the starting field H_o, the level of conduction current and the ambient temperature.

a) <u>Bath Temperature $T_b = 4.2^{o}K$</u>

The solid lines of figures 8.2 and 8.3 show the longitudinal velocity V of propagation of the normal front as a function of $<4\pi M>$ for several current levels with H = 0 and H = 1100 G respectively. For all current levels the velocity is seen to first vary slowly with $<4\pi M>$ and then to increase rapidly when a certain critical moment is exceeded. Below these critical moments $<4\pi M>_c$ the velocities encountered are comparable to those obtained with no magnetic moment, provided that in these circumstances the applied external field is comparable to the average induction $<B>$ existing in the sample before propagation. The dashed lines of figures 8.2 and 8.3 show the velocities obtained with no magnetic moment in fields equal to $<B>$, the average induction. These curves were obtained using data such as shown in figure 8.1, and substituting the measured $<B>$ for H. By comparing any set of dashed and solid lines in figures 8.2 and 8.3 we see that most of the variation in V is simply a magnetic field effect and arises from the change in the average field within the sample with magnetization. The decrease in $<B>$ then accounts for the initial decrease in V seen in figure 8.3 (see upper scale for values of $<B>$). The solid lines however always lie above the dashed ones, indicating the presence of another contribution which tends to increase the velocity regardless of the sign of $<4\pi M>$. We attribute this increase to the dissipation of the stored magnetic energy as the persistent currents decay near the normal-superconducting interface. We note

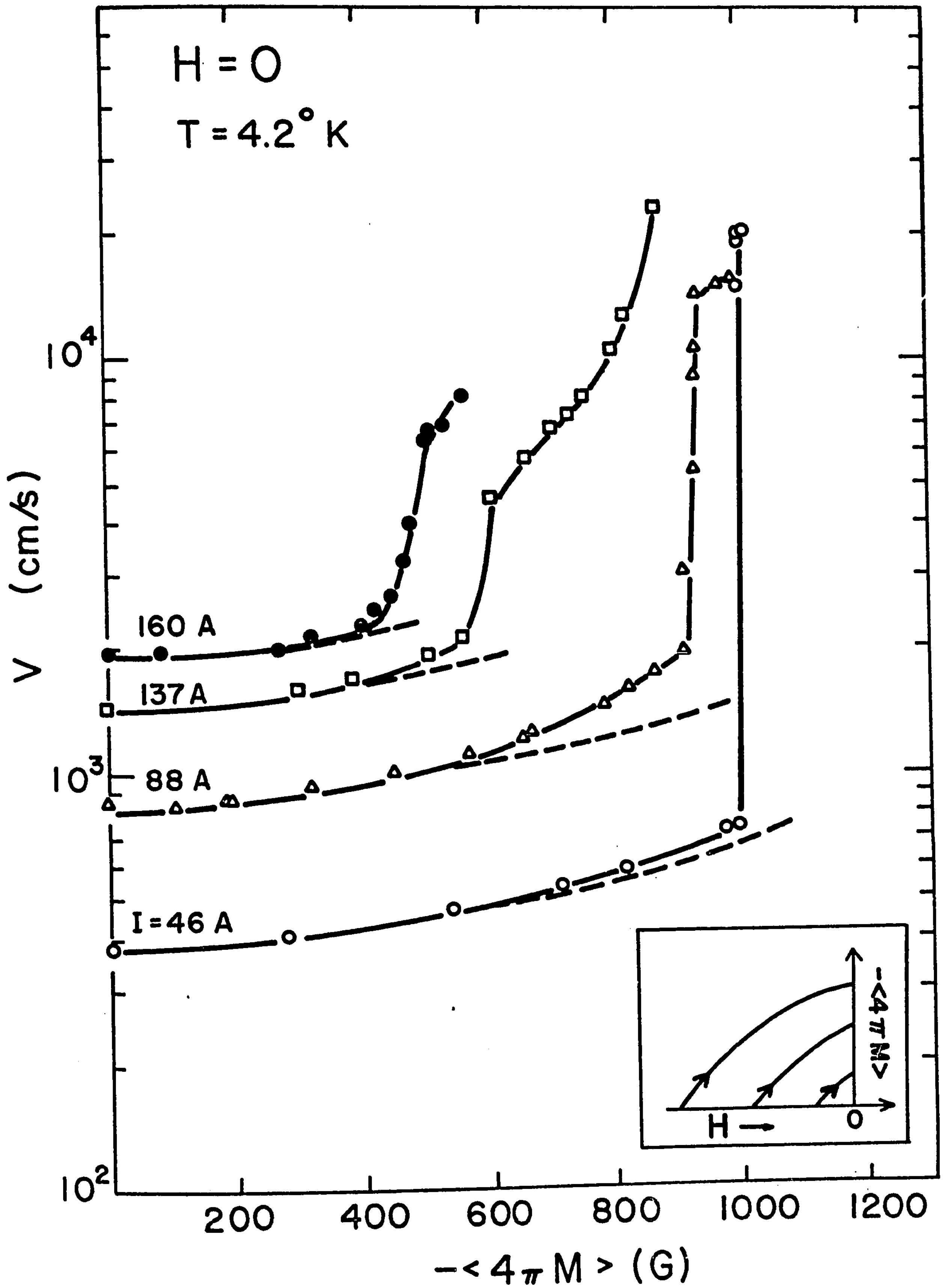

Fig. 8.2: Velocity vs remanent $\langle 4\pi M \rangle$ (H = 0) for several constant current levels at 4.2°K. Inset shows schematically magnetic history before measurement of V.

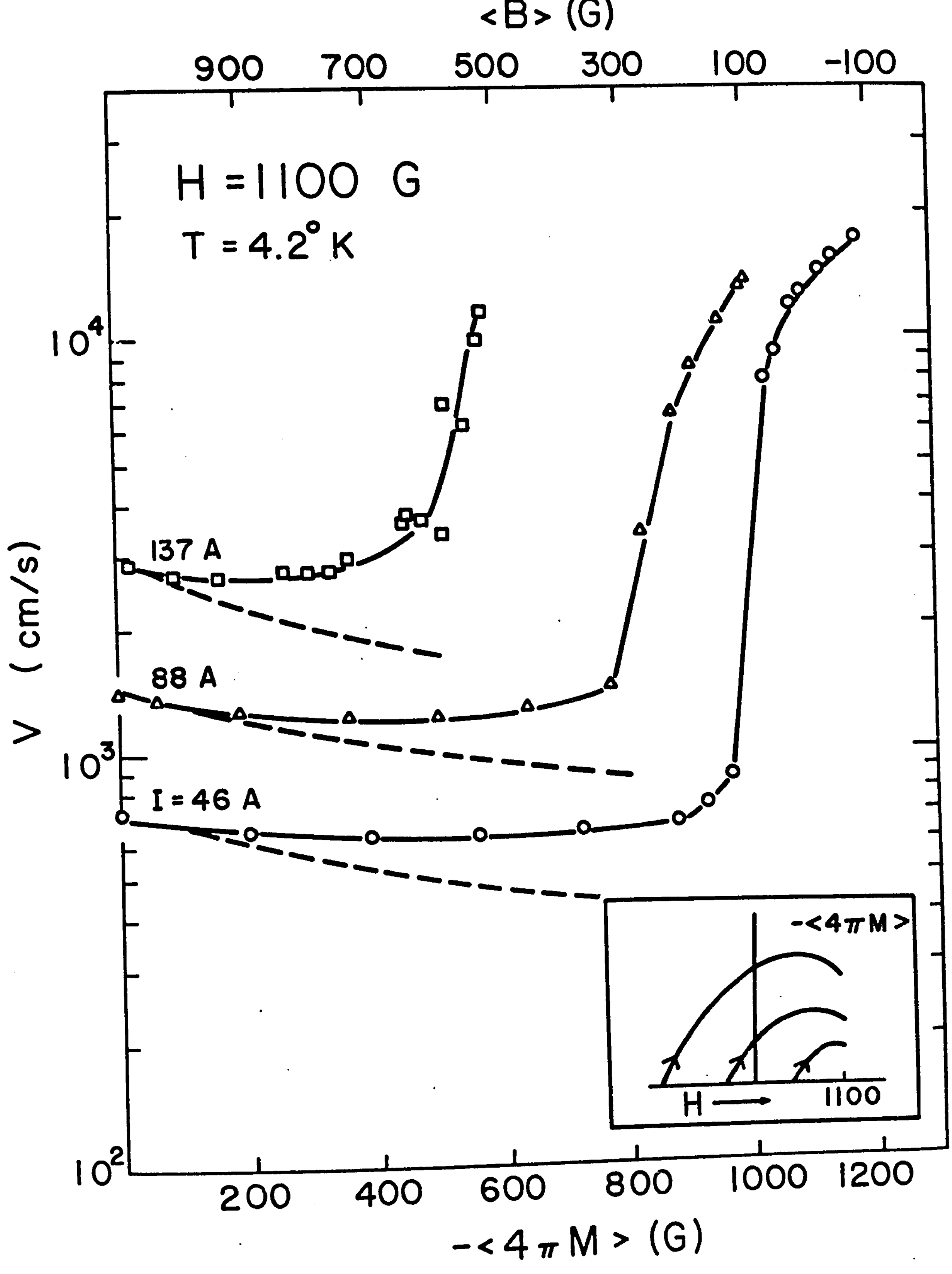

Fig. 8.3: Velocity vs <4πM> and <B> (upper scale) for several constant current levels when H = 1100 G at 4.2°K.

that the divergence between any two sets of curves is greater in figure 8.3. The reason for this is that in the situations under study the stored magnetic energy is greater in the presence of a field.

The velocity increases abruptly above $<4\pi M>_c$. This increase cannot be accounted for by the increased power dissipation due to the decay of the persistent currents and we must therefore postulate a change in the mechanism of propagation.

b) <u>Bath Temperature $T_b = 2.6^oK$</u>

The velocity of propagation was also measured for a bath temperature of 2.6^oK in zero field (figure 8.4) and in an external field of 2.2 kG (figure 8.5) for a current level of 190 Amps and zero current. Again the velocity is seen to first increase slowly with $<4\pi M>$ and then to increase abruptly by more than an order of magnitude as a threshold moment is exceeded. We note that the threshold moment is lowered by the presence of a current. The velocities encountered for a given moment, with and without transport current, are approximately equal.

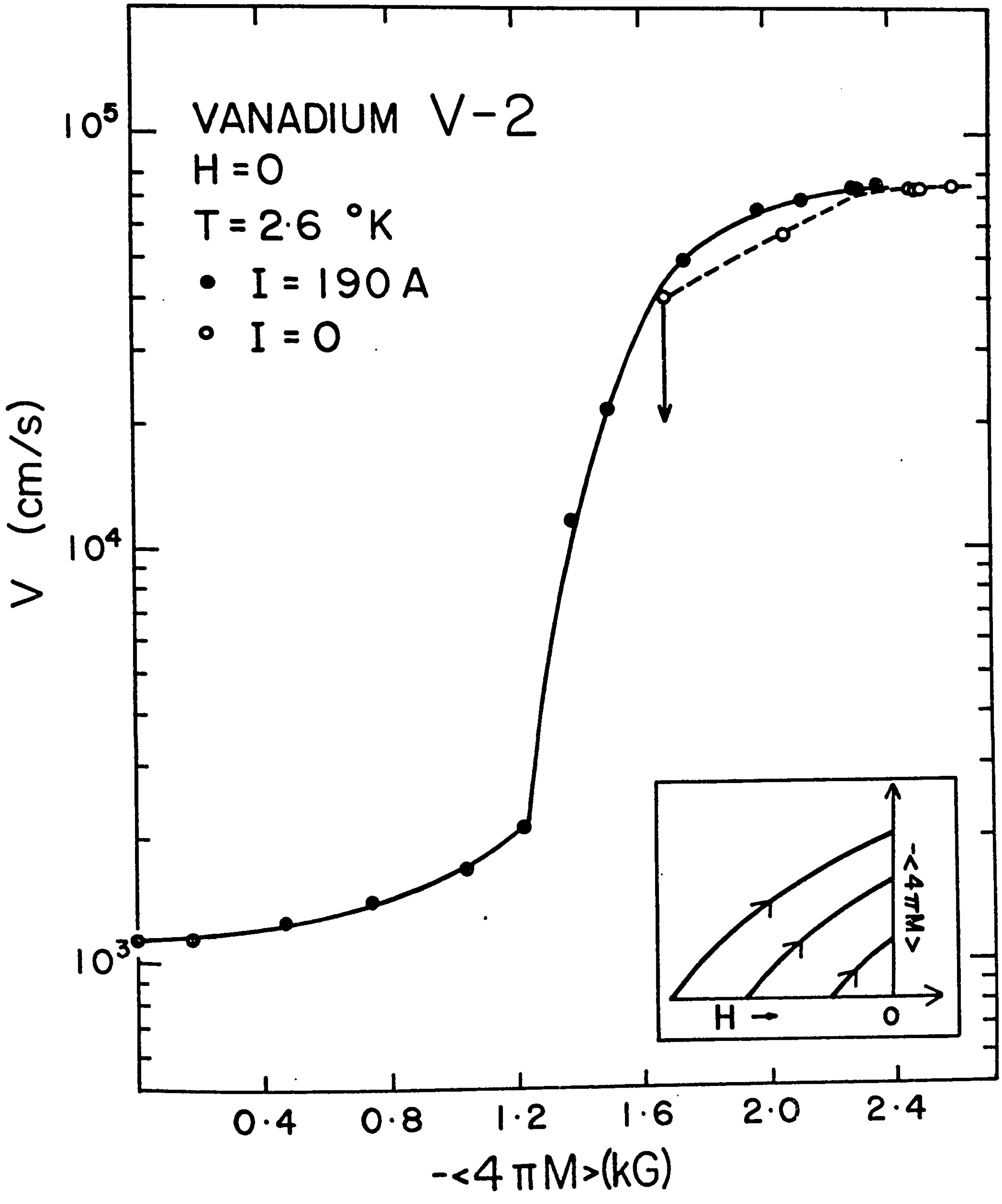

Fig. 8.4: Velocity vs remanent magnetic moment (H = 0) at 2.6°K. Inset shows schematically magnetic history before measurement of V.

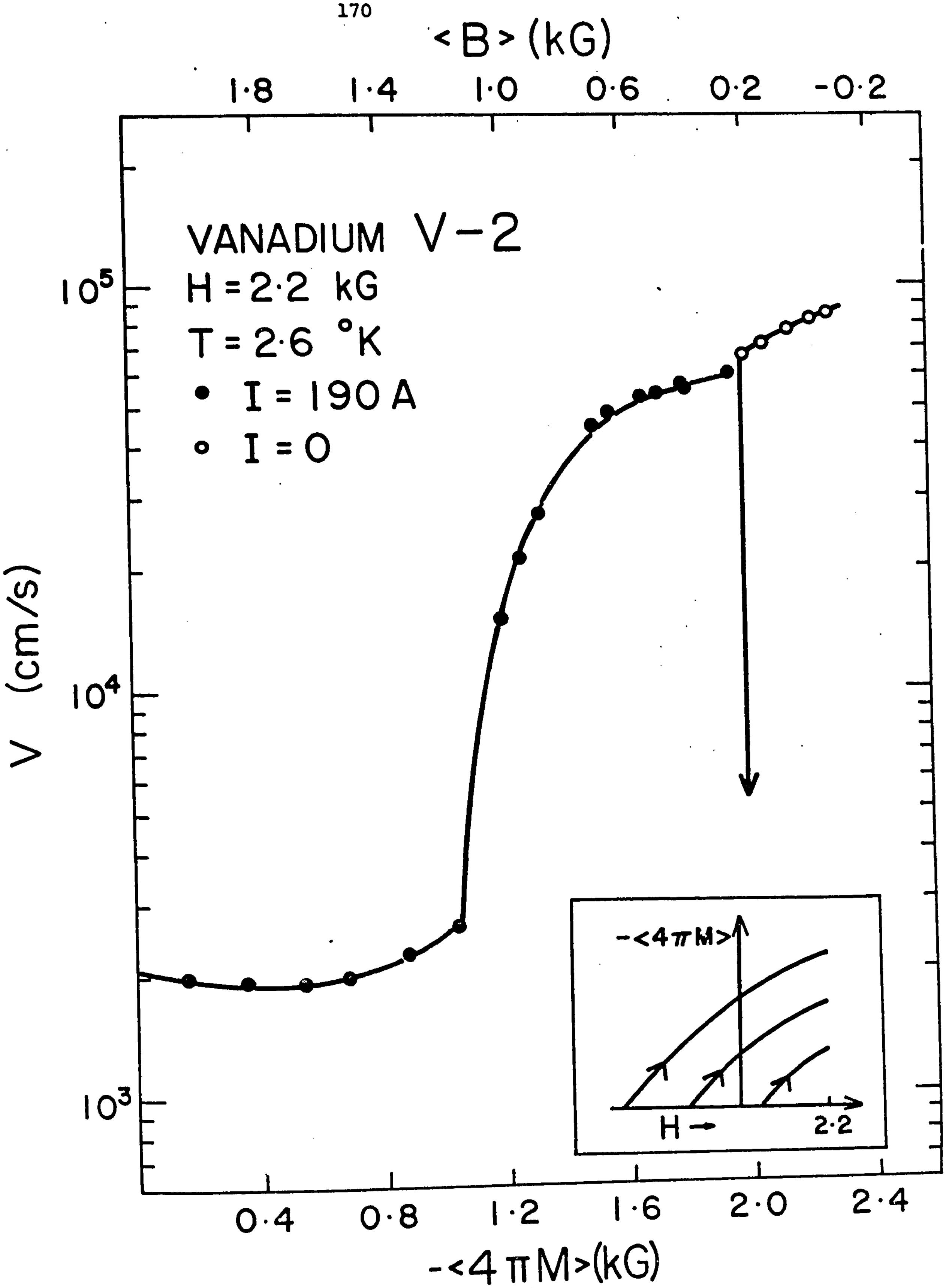

Fig. 8.5: Velocity vs <4πM> for H = 2.2 kG at 2.6°K. Inset shows schematically magnetic history before measurement of V.

IV CONCLUSION

The presence of a magnetic moment was shown in figures 8.2 to 8.5 to affect the velocity of propagation of a normal front in three different ways. Below a critical moment $\langle 4\pi M \rangle_c$, the model developed by Whetstone and Roos appears to be valid. The change in velocity with $\langle 4\pi M \rangle$ can be attributed to the change in average magnetic induction $\langle B \rangle$ in the sample and to the additional energy dissipated as the induced persistent currents decay near the normal superconducting phase boundary. In our measurements, the relative importance of these two contributions is comparable and can be estimated by comparing the solid and dashed lines of figures 8.2 and 8.3.

The main feature of our data is the almost vertical rise in velocity occurring when a threshold magnetic moment is exceeded. This threshold moment is seen to decrease with increasing current level. In the following discussion we attempt to account for this change in velocity.

According to the critical state picture, as the magnetic moment grows, persistent currents flowing azimuthally and steep gradients of magnetic induction penetrate deeper into the sample. It is also well known that under certain conditions the configurations of electric currents and magnetic field profiles become unstable and if perturbed, a fraction or all of the stored magnetic energy is released. In some cases this may drive the entire sample normal (Swartz 68). The propagation of such instabilities along wires can reach velocities of the order of 10^6 cm/s even in the absence of a transport current (Walker 72, Bussiere 72a). The velocity was found (Bussiere 72a) to depend specifically on the energy released by the instability and on the normal state resistivity. In part I of this thesis we have shown that the time of radial collapse of flux also depends on these two quantities.

We therefore attribute the abrupt rise in V above $\langle 4\pi M\rangle_c$ to the onset of unstable magnetic configurations. The decay of azimuthally circulating persistent currents in the region where the flux profile is collapsing causes a change in the flux threading the unperturbed region ahead. This change in flux induces an azimuthal emf $2\pi r\varepsilon$ in that region, thereby causing the local current density there to experience a transient increase. When the magnetic configuration is unstable (above $\langle 4\pi M\rangle_c$) this perturbation triggers an avalanche of flux. Subsequently both the collapse of persistent currents (stored magnetic energy) and the joule heating produced by the steady transport current drive the newly perturbed region irreversibly into the normal state. This heating process, however, now follows in the wake of the propagating magnetic disturbance. We stress that now the disturbance progresses through electromagnetic coupling because the region where it advances is in an unstable critical state. In the case where no transport current is present one should no longer speak of "normal phase" propagation since a magnetic disturbance can travel down the wire without driving the sample in the normal state. Since this new process is independent of thermal diffusion, the velocity can be very large. The velocity will now depend on the geometric and physical characteristics of the electromagnetic coupling between adjacent regions in the superconductor, the degree of stability, and on the characteristics of the radial flux collapse in the superconductor.

CHAPTER IX

LONGITUDINAL VELOCITY AS A FUNCTION OF MAGNETIZATION $<4\pi M>$

I INTRODUCTION

The initial magnetization $<4\pi M>$ was shown in chapter IV to be one of the dominant factors affecting the rate of radial flux collapse in a superconductor subjected to a small thermal perturbation. For a given $<4\pi M>$, the field profile and average magnetic induction $<B>$ were also shown to play an important role. In chapter VIII we have shown that the longitudinal propagation of flux jumps along type II superconductors is governed by electromagnetic coupling between regions where flux is collapsing and unperturbed regions ahead. We may therefore expect that the factors affecting the rate of radial flux collapse will also affect the velocity of longitudinal propagation of flux jumps.

In this chapter we present measurements of the longitudinal velocity of propagation of flux jumps in cylinders of different materials as a function of the initial magnetization $<4\pi M>$. A given magnetic moment in a particular sample may be achieved with a variety of different field profiles and external fields. As a consequence, the velocity is not a unique function of $<4\pi M>$. We will attempt in this chapter to relate these variations in velocity with magnetic moment to the various features of the radial flux collapse described in part I.

To organize and interpret our results it is helpful to introduce a distinction between magnetic moments which are produced before or after a peak occurs in magnetization curves. We refer to magnetic moments encountered on the increasing side of the magnetization curve as the α branch and those in the decreasing region as the β branch. The field gradient penetrates deeper and deeper into the sample as we proceed from the α to the β branch. In the β branch the penetration of the field gradient is either complete or nearly complete. A comparison of the stored magnetic energy E_m associated with magnetizations of equal magnitude along the α and β branch of a given magnetization curve reveals that E_m is always greater for the latter case. We will discuss this important point in more detail below.

The average magnetic field threading the sample will be lower for the α than for the β branch of a magnetization curve when the external field, whose change induces the magnetic moment, is increased. The situation is not so simple when the external field is decreased from some initial value through zero and then made to increase in the opposite direction. In such situations, the average of the magnitude of the magnetic induction in the α and β branches depend on several factors and several varieties of cases must be considered separately.

Finally, in many materials, an additional complicating phenomenon is encountered which remains unexplained to this day. This is the occurrence of a dip or valley in the magnetization curve as the external field is swept from some initial value through zero. The occurrence and extent of this dip or valley depends on previous magnetic history.

Independent of any detailed model, the appearance of such a valley means that the current carrying capacity of the specimen is diminishing as the magnetization declines. In some cases, the magnetization subsequently rises very steeply after the valley or dip has been traversed. This behaviour indicates a considerable increase in the critical current density which the region near the surface can support.

II VELOCITY VS $<4\pi M>$ IN NbTi

a) Samples NbTi-1 and NbTi-2

1) Experimental Results:

The pertinent properties of samples NbTi-1 and NbTi-2 have been summarized in Tables 1 and II of the experimental section.

Figure 9.1 shows two magnetization curves obtained for sample NbTi-1. The upper curve was obtained by first cooling the

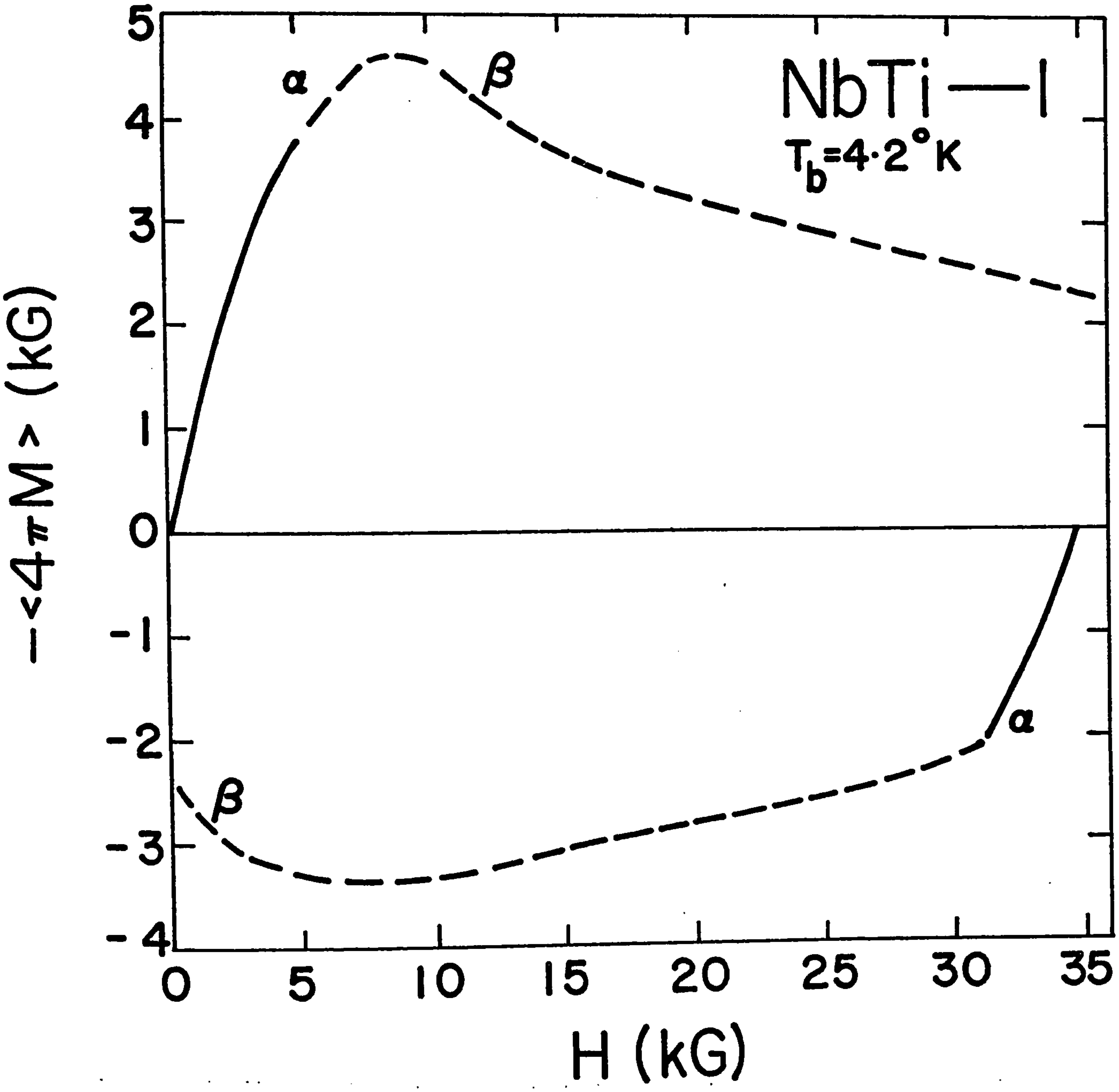

Fig. 9.1: Magnetization curves for sample NbTi-1 at 4.2°K. Solid lines indicate regions of full stability and dashed lines regions where flux jumps could be triggered.

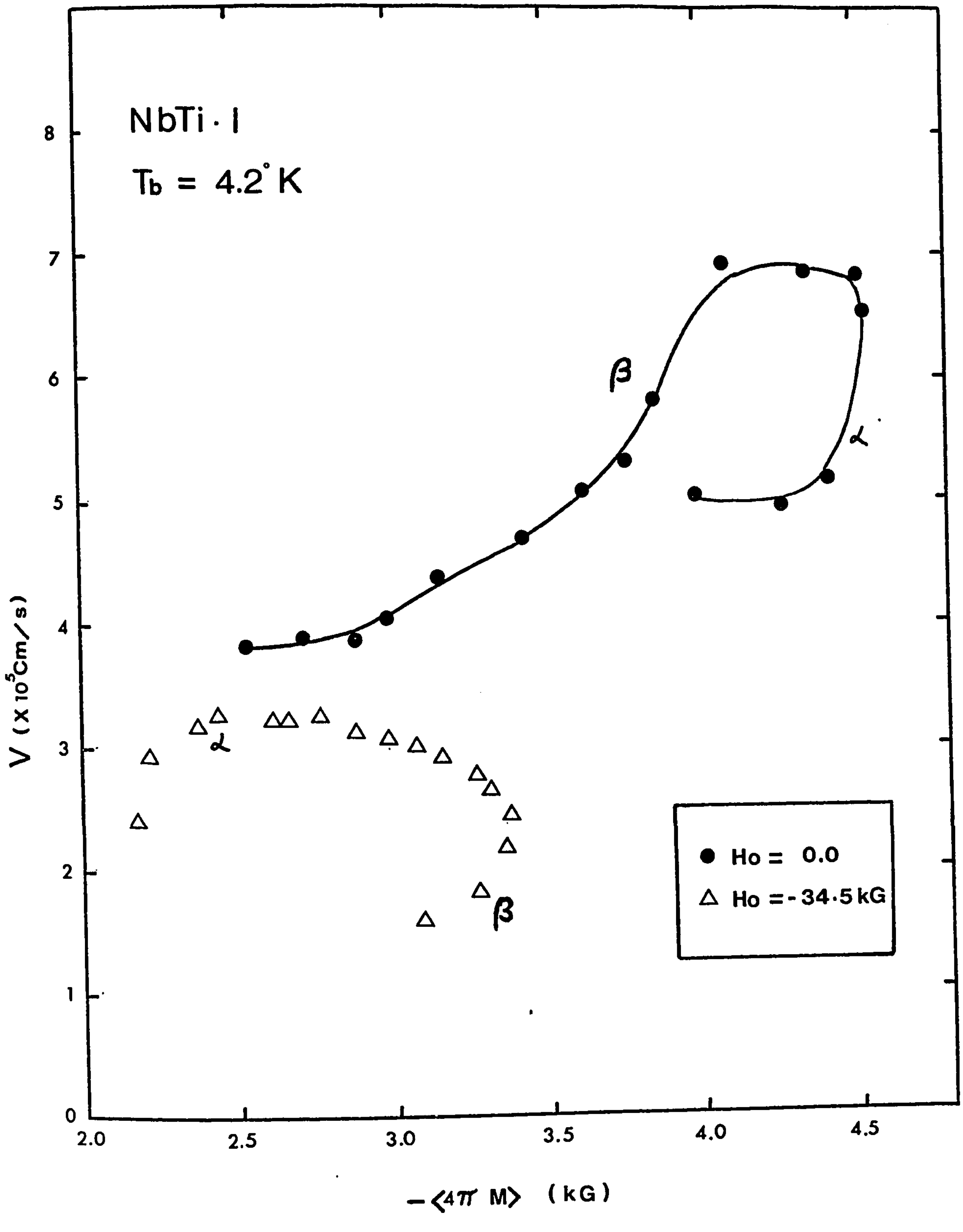

Fig. 9.2: Velocity vs <4πM> in NbTi-1 for $H_o = 0$ and $H_o = -34.5$ kG.

sample through T_c in zero field (H_o=0) and then increasing the field. The lower curve was obtained by cooling the sample in an initial field H_o = 34.5 kG and then reducing the magnetic field. In this and subsequent figures the solid lines indicate regions of stability and the dashed lines regions where flux jumps could be triggered by applying a small heat pulse to either of two small heater coils placed at each end of the sample (see figure 1, experimental section). Figure 9.2 shows the longitudinal velocity V as a function of initial magnetization $\langle 4\pi M \rangle$ for these two situations.

Figures 9.3 and 9.4 show a number of magnetization curves for sample NbTi-2. These curves were all produced by initially cooling the sample in a starting field H_o and then sweeping the field towards the "right". The curves in the left quadrant were therefore produced by cooling the sample in an initial field H_o (labelled negative) and then reducing the field. In some cases the field was subsequently increased in the opposite direction. We note that in this case the magnetization curves are anomalous (figure 9.3). As the field is reduced to a small value, the magnetization decreases and then increases very rapidly as the field is increased in the opposite direction. We also note that the two curves in the left quadrant of figure 9.3 cross each other, a phenomenon as yet unaccounted for within the critical state concept (LeBlanc 66).

Figures 9.5 and 9.6 again show the magnetization curves where H_o = 4.54 kG and H_o = -10.0 kG. In these figures the dots indicate the residual magnetization after a flux jump. We note that near the limit of stability the flux jumps are incomplete. For fields distant from this limit the flux jumps are nearly complete and only a very small amount of magnetization ($\sim$ 50 G) remains in the sample after the flux jumps.

Figures 9.7 through 9.13 show the velocity V of longitudinal propagation as a function of magnetization $\langle 4\pi M \rangle$ for flux jumps triggered along a large number of magnetization curves. From an examination of all of these figures as well as the upper curve of figure 9.2 we note that the velocity increases with $\langle 4\pi M \rangle$ regardless of the magnetization curve along which the flux jumps are triggered. We also note that in cases where flux jumps could be triggered along two different branches of equal magnetization (labelled α and β) the velocity differs along these two branches.

2) Discussion:

We distinguish two distinct types of behaviour:

i) For the flux jumps corresponding to magnetization curves in the right hand side quadrant (H_o positive) the velocities in the α branch (hence in lower fields) are lower than in the β branch (see figure 9.7 where H_o = 4.54 kG, figure 9.8 where H_o = 10.0 kG and 20.9 kG, and figure 9.9 where H_o = 0).

ii) For flux jumps triggered along magnetization curves where the initial field is in the left quadrant (H_o negative) and the field subsequently reduced to zero and increased in the opposite direction the velocities in the α branch are higher (see figure 9.9 where $H_o = -2.27$ kG, figure 9.10 where $H_o = -10.0$ kG, figure 9.11 where $H_o = -4.54$ kG, and figure 9.13 where $H_o = -20.0$ kG).

In this discussion we relate the general behaviour of velocity with $\langle 4\pi M \rangle$ and with magnetic history to the characteristics of radial flux collapse described in chapters IV and V. We proceed on the basis that the longitudinal velocity depends on the characteristics of radial flux collapse. Accordingly, when the radial flux collapse occurs at a fast rate we expect the longitudinal velocity to be large. In chapter IV we have shown that an increase in magnetization leads to a faster rate of radial flux collapse. Although the flux jumps triggered along different magnetization curves correspond to different field profiles and average magnetic inductions $\langle B \rangle$ (factors which also affect the radial collapse) the effect of magnetization is dominant for the two samples NbTi-1 and NbTi-2.

To understand the two distinct types of behaviour of the velocity when flux jumps of equal $\langle 4\pi M \rangle$ are triggered along branches α and β of a magnetization curve we need also consider the effects of field profile and magnetic field.

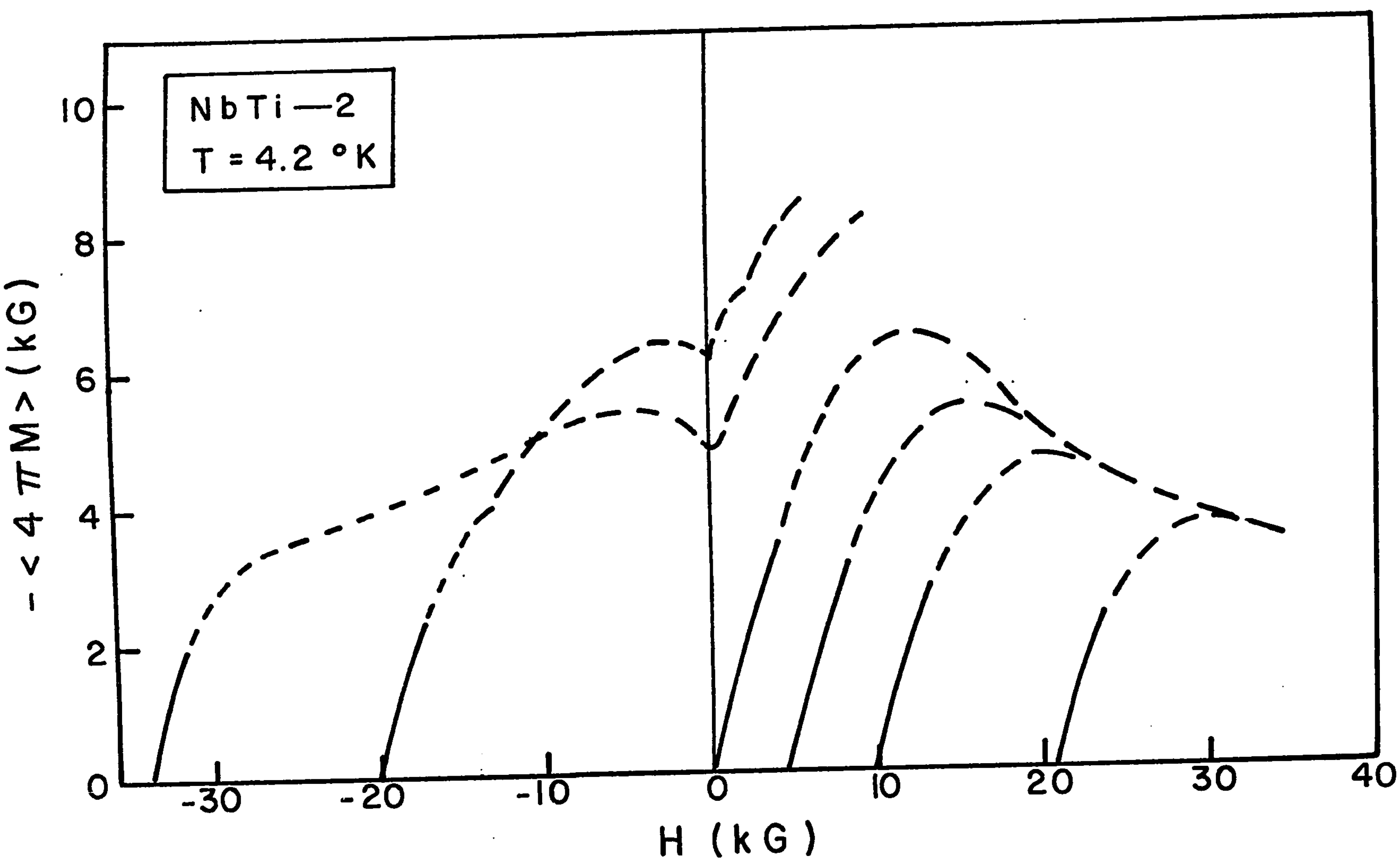

Fig. 9.3: Magnetization curves for NbTi-2 at 4.2^{o}K. Solid lines indicate regions of full stability and dashed lines regions where flux jumps could be triggered.

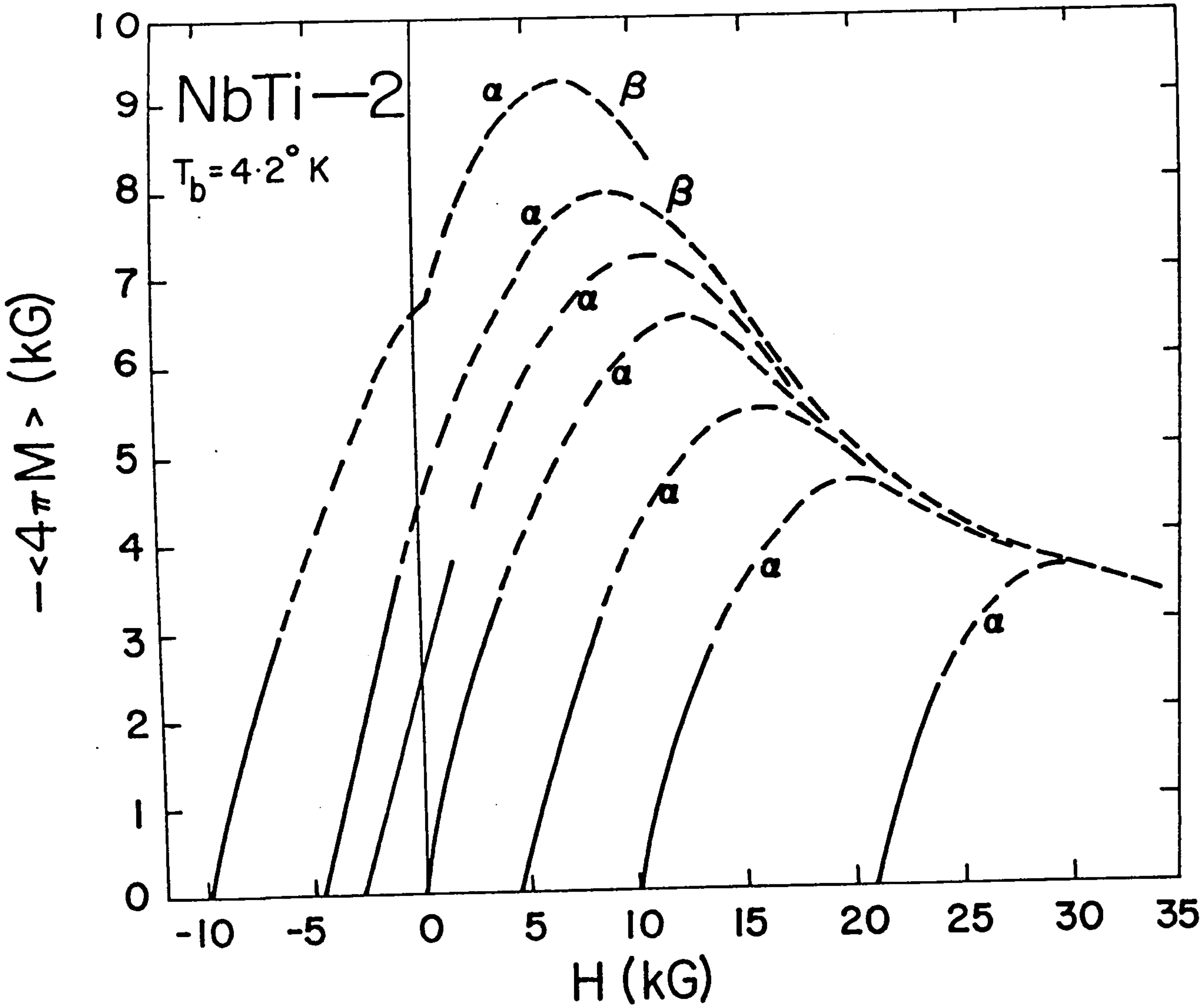

Fig. 9.4: Magnetization curves for NbTi-2 at 4.2°K. Solid lines indicate regions of full stability and dashed lines regions where flux jumps could be triggered.

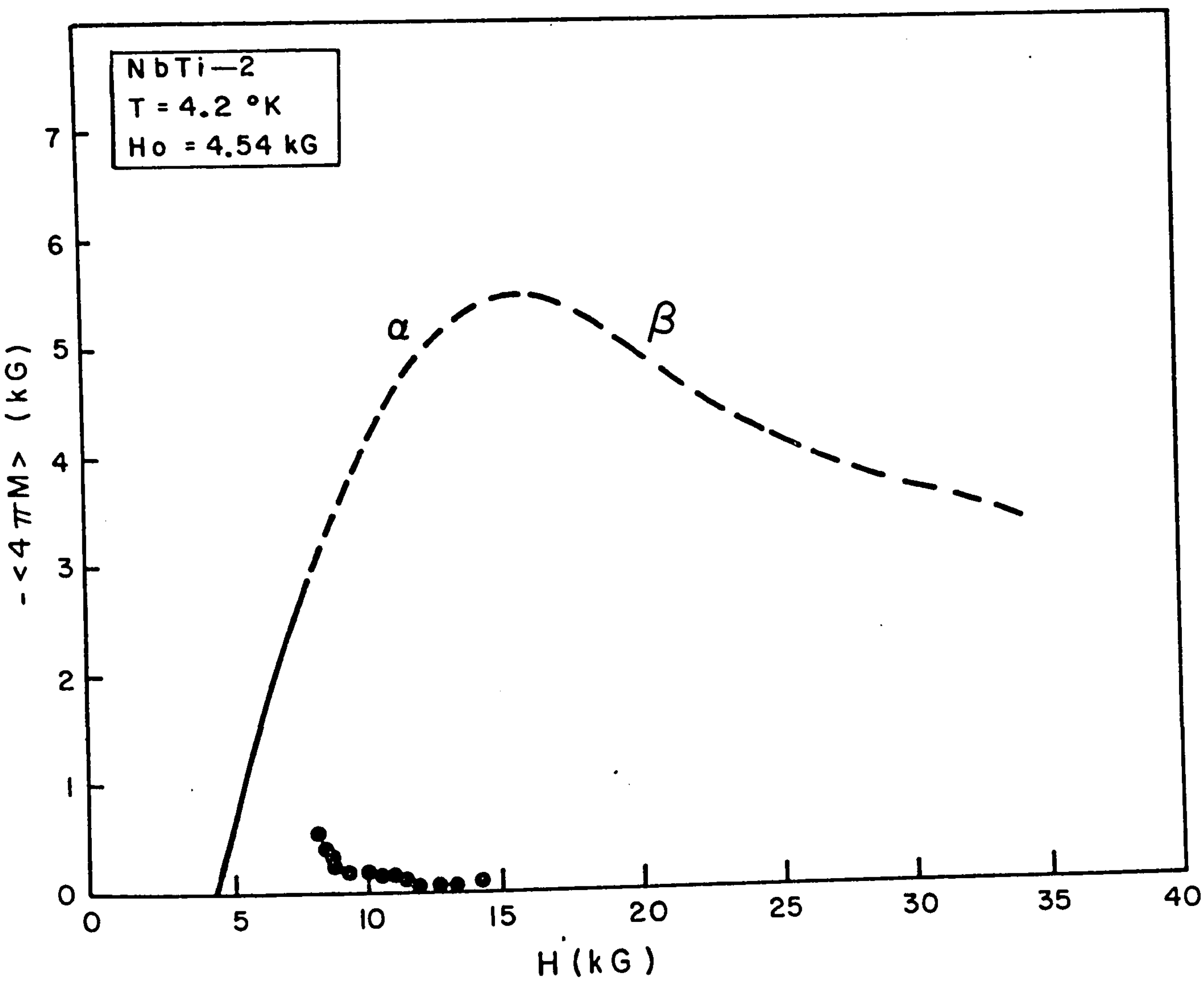

Fig. 9.5: Magnetization curve for NbTi-2 at $4.2^{o}K$, H_o = 4.54 kG. Dashed line indicates region of instability. Dots indicate the flux remaining after a jump.

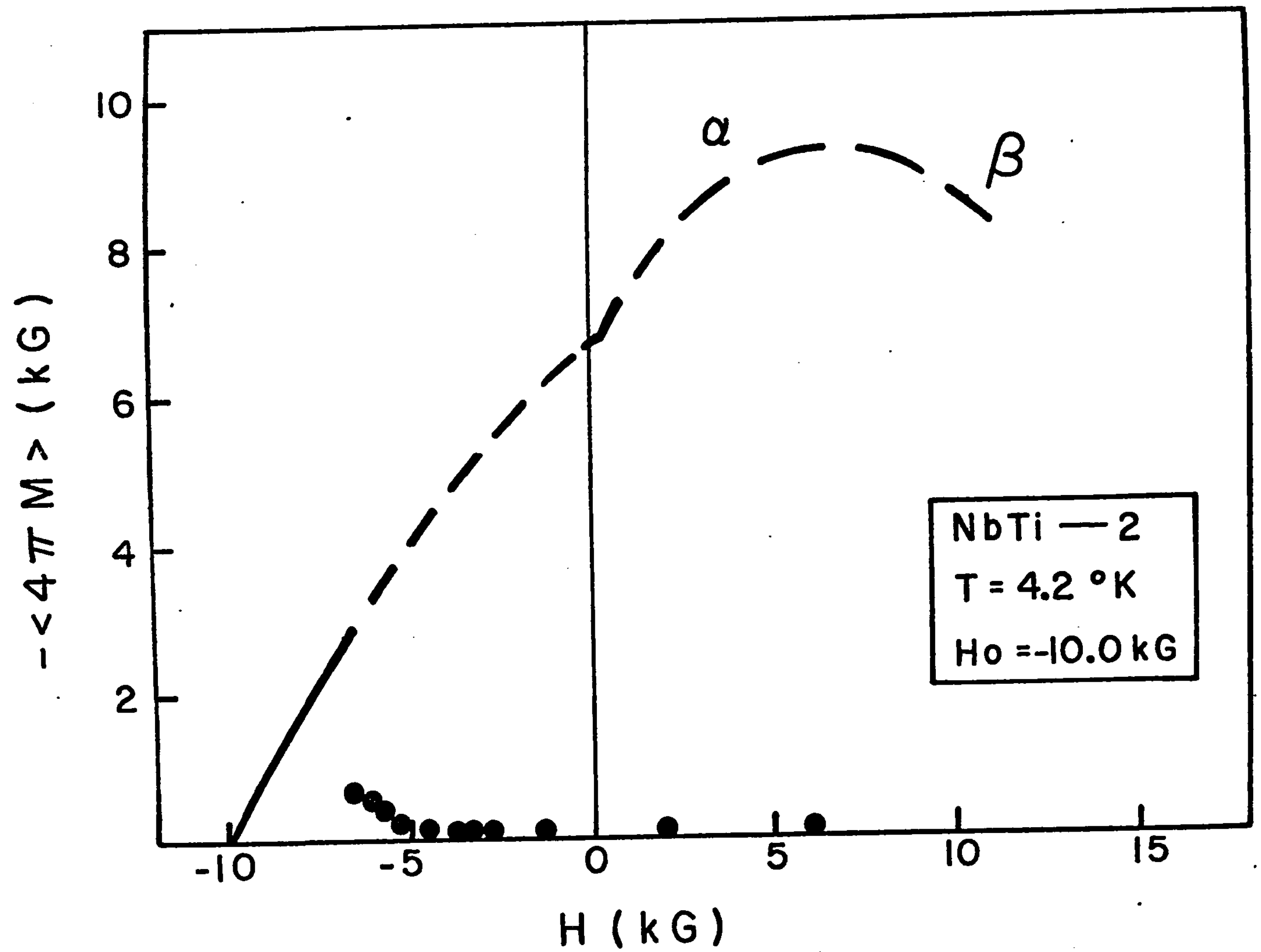

Fig. 9.6: Magnetization curve for NbTi-2, H_o = -10.0 kG. Dashed line indicates region of instability. Dots indicate flux remaining after a jump.

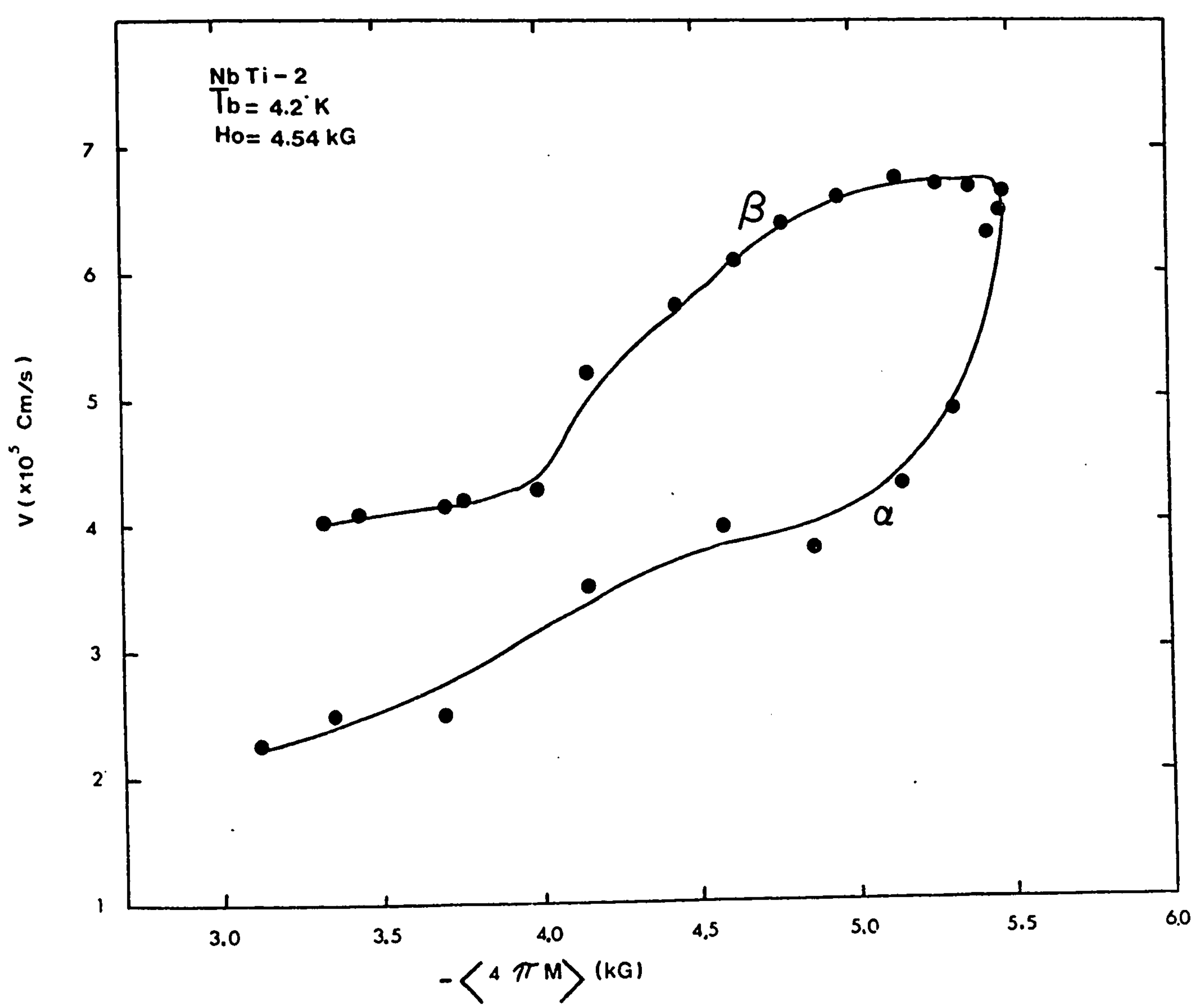

Fig. 9.7: Velocity vs <4πM> for NbTi-2, H_o = 4.54 kG. Branches α and β distinguish between flux jumps before and after the magnetization peak respectively.

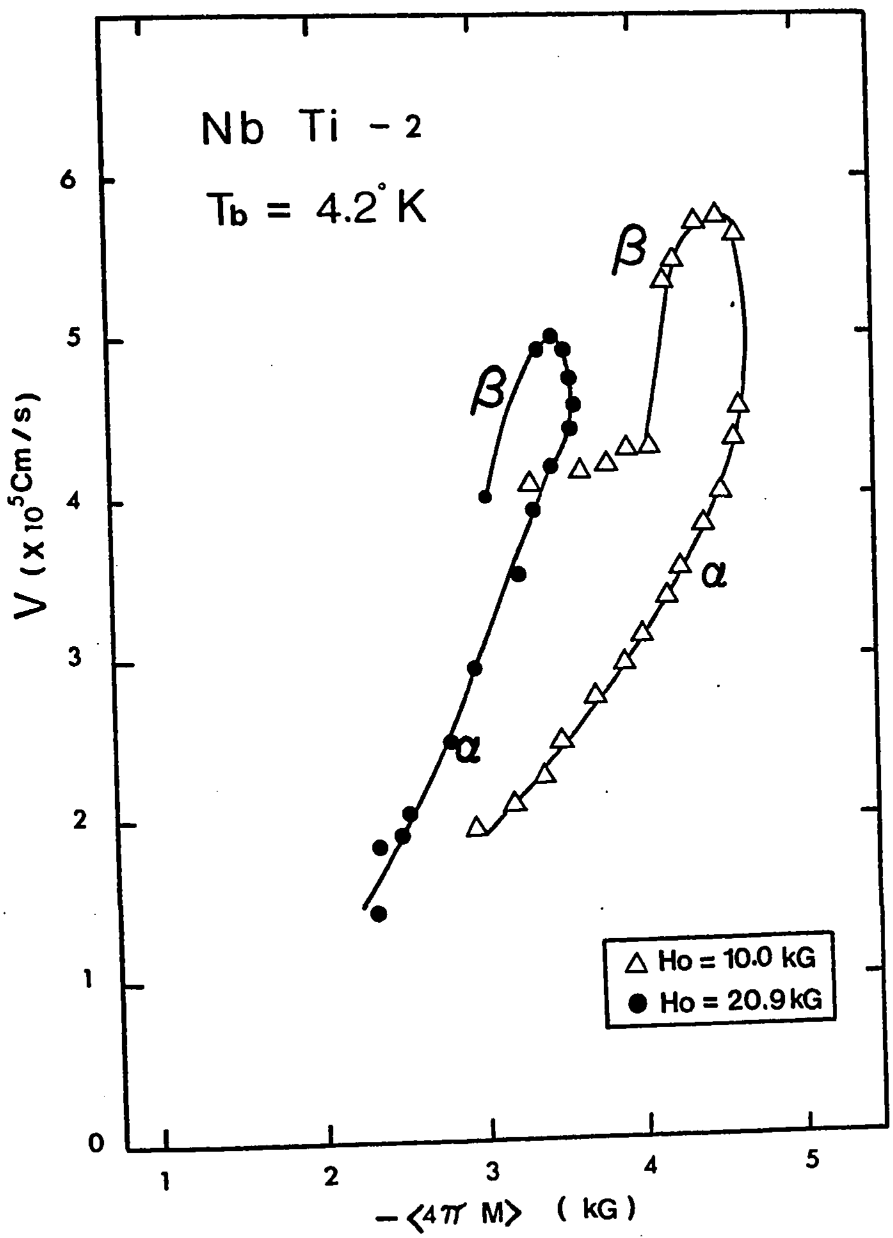

Fig. 9.8: Velocity vs <4πM> in NbTi-2 at 4.2°K for H_o = 10.0 kG and H_o = 20.0 kG.

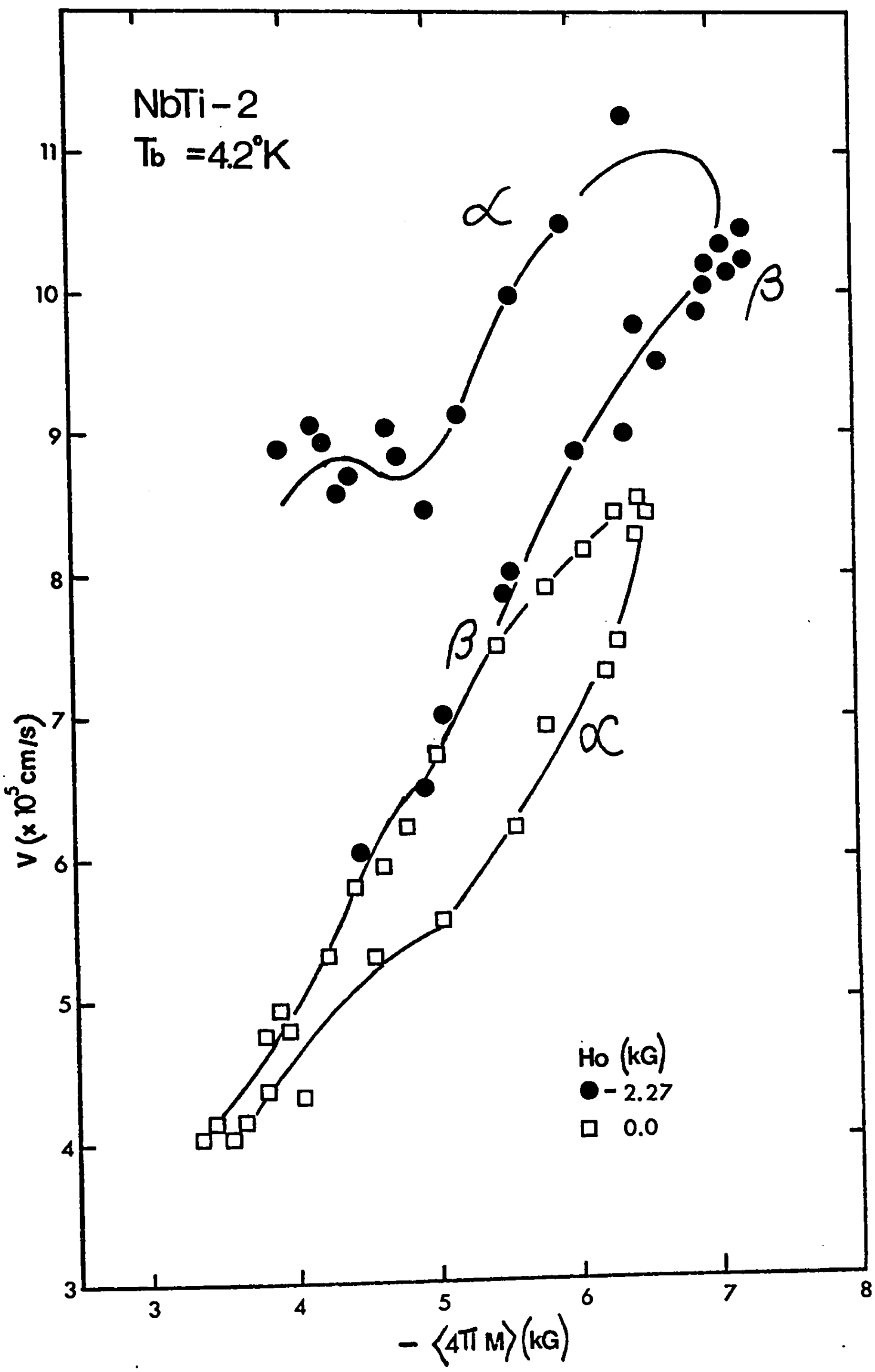

Fig. 9.9: Velocity vs $<4\pi M>$ in NbTi-2 at $4.2^{\circ}K$ for $H_o = -2.27$ kG and $H_o = 0$.

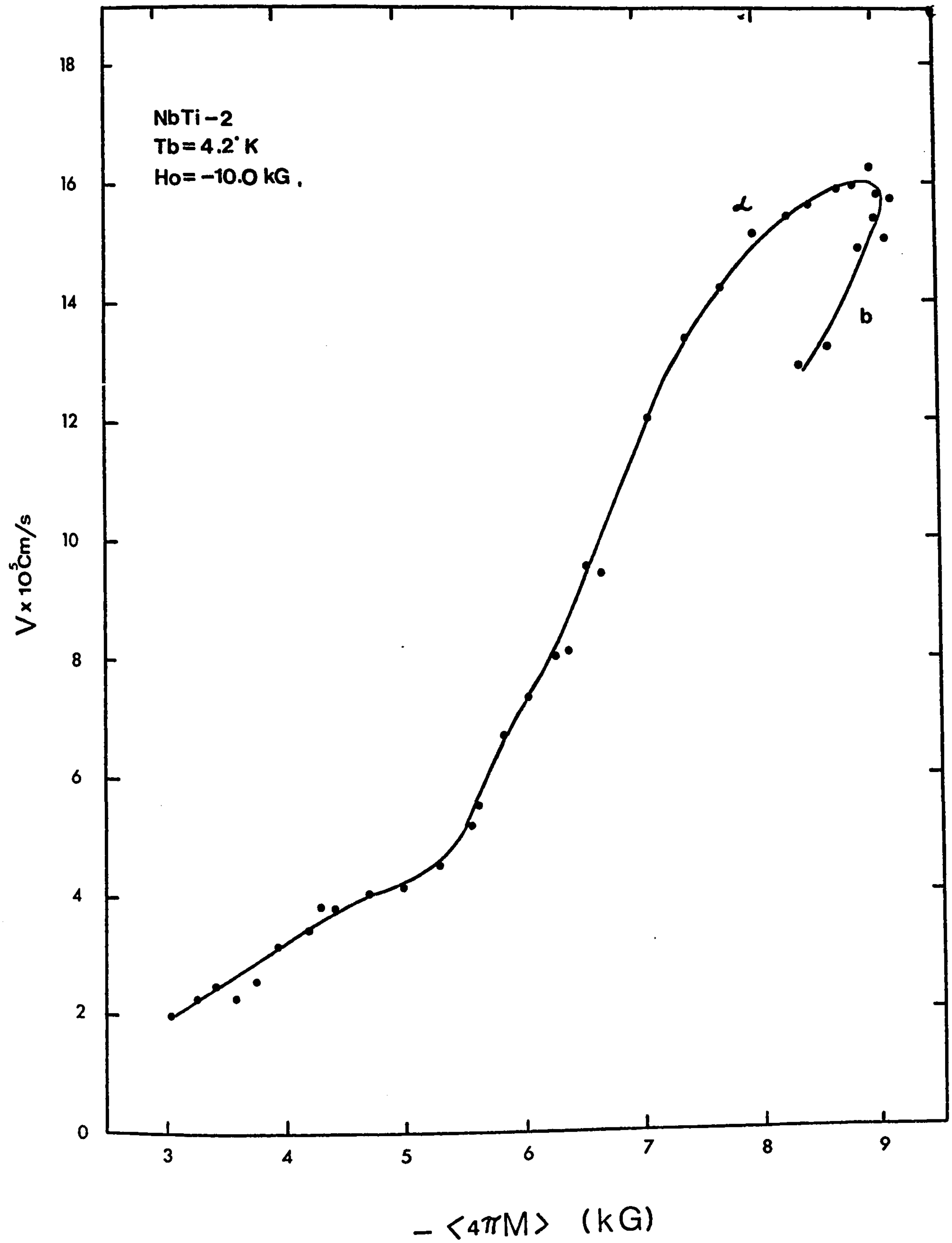

Fig. 9.10: Velocity vs <4πM> for NbTi-2, H_o = -10.0 kG. Branches α and β distinguish between flux jumps before and after the magnetization peak respectively.

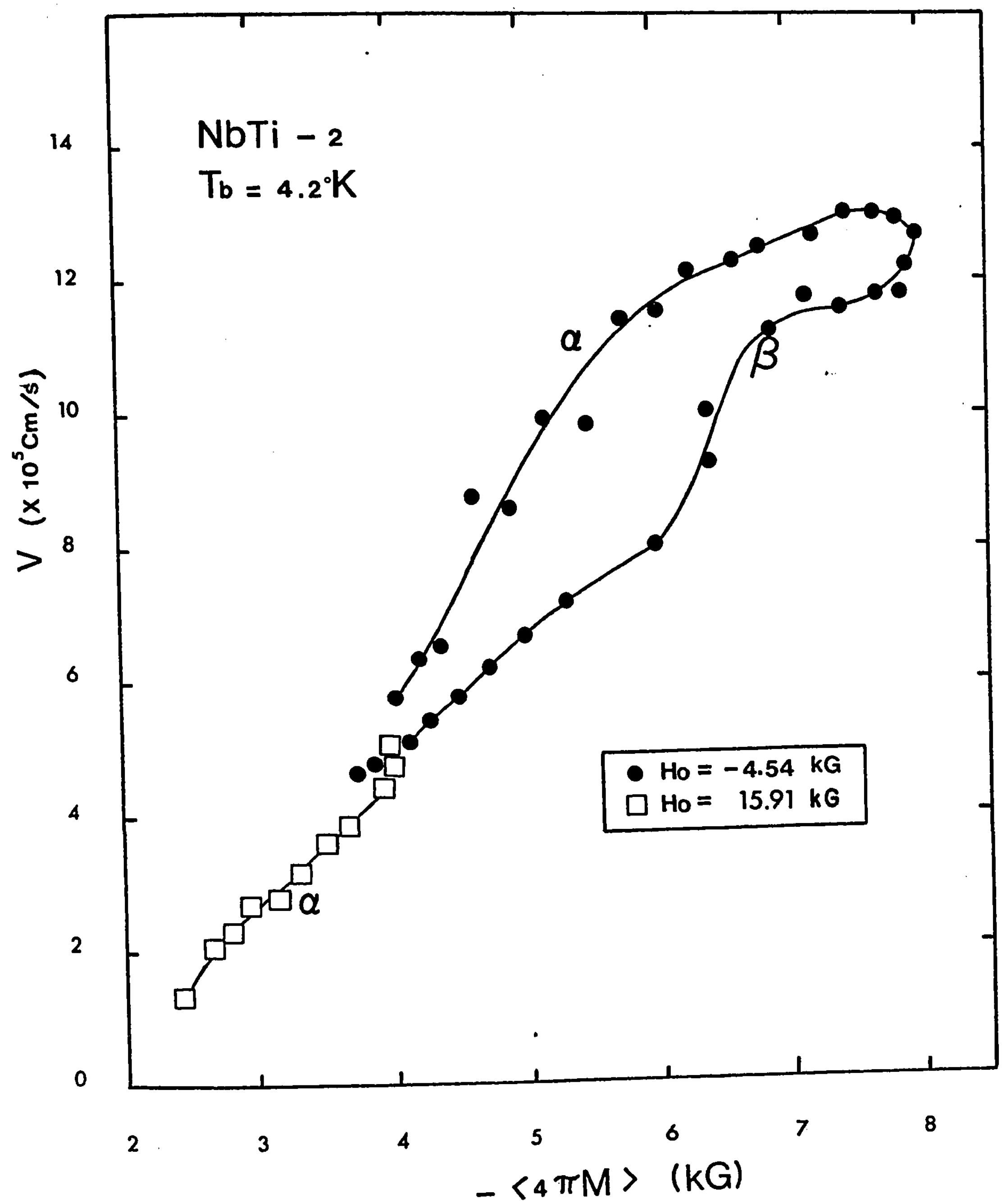

Fig. 9.11: Velocity vs <4πM> in NbTi-2 at 4.2°K for H_o = -4.54 kG, and H_o = 15.91 kG.

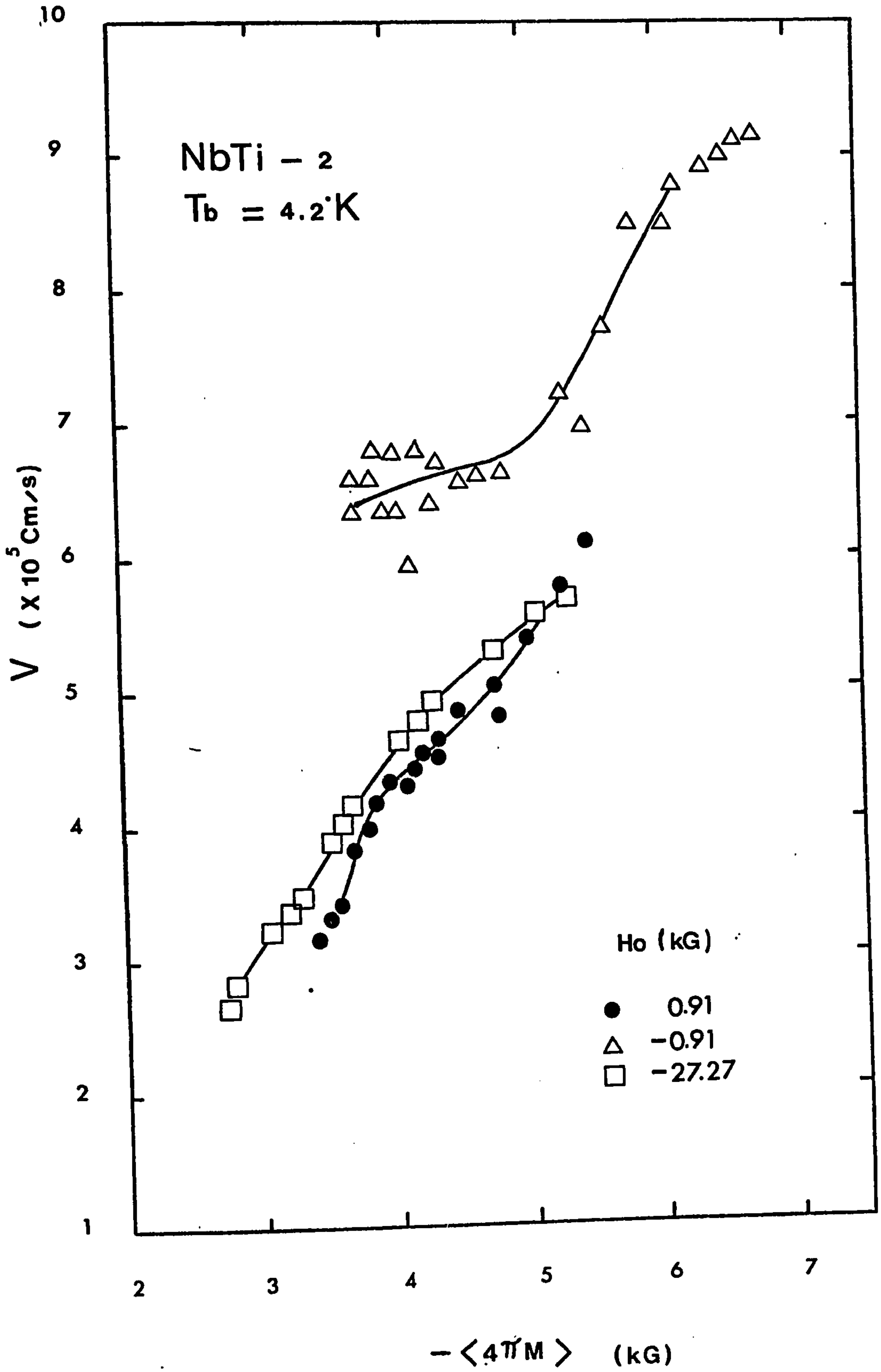

Fig. 9.12: Velocity vs <4πM> in NbTi-2 at 4.2^{O}K, H_o = 0.91 kG, -0.91 kG, and -27.27 kG.

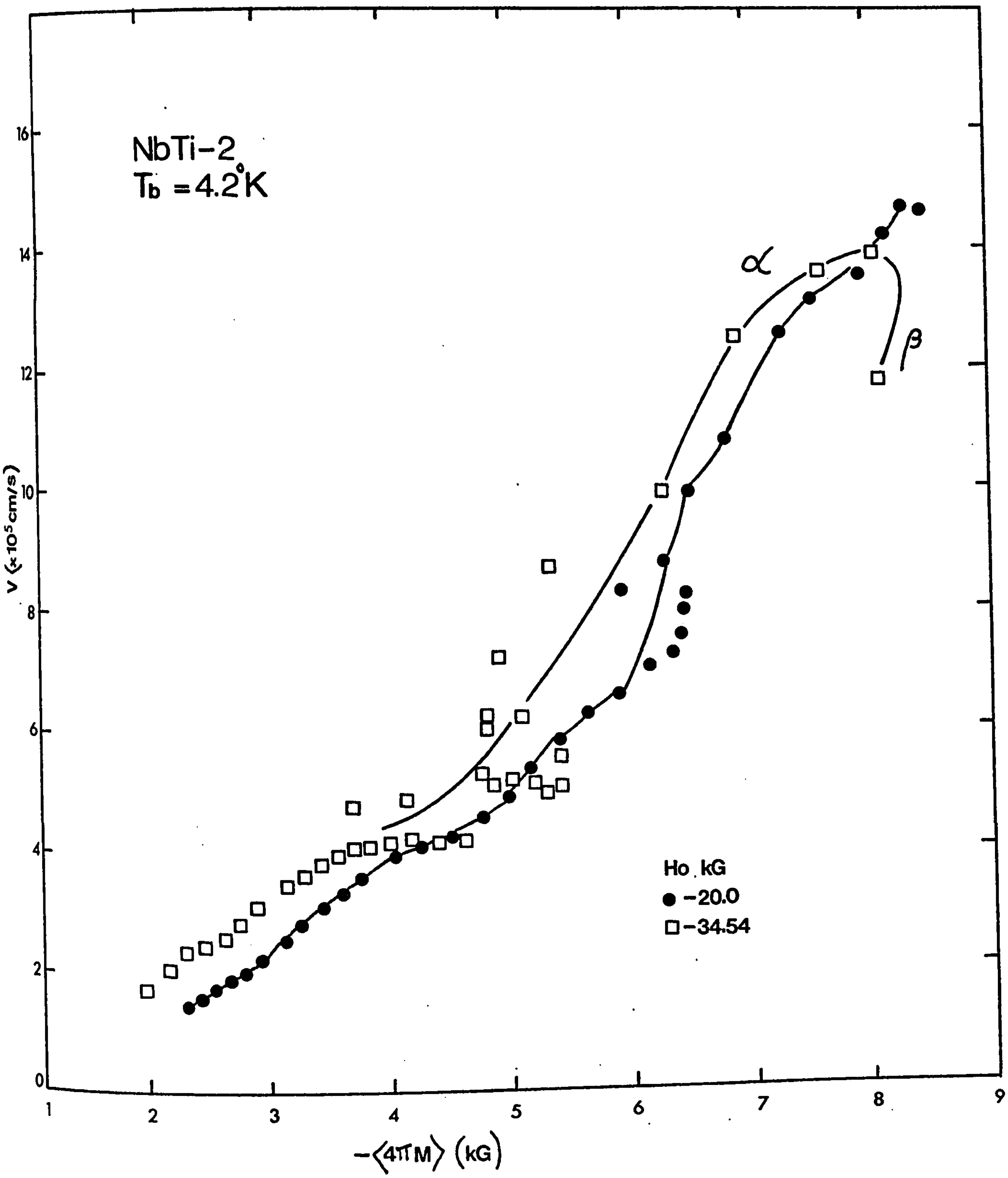

Fig. 9.13: Velocity vs <4πM> in NbTi-2 at 4.2°K, H_o = -20.0 kG and -34.54 kG.

i) Flux jumps where the magnetization curve originates in the right hand side quadrant:

We first analyse the situation in the right hand side quadrant (H_o positive). Figure 9.14(c) shows a typical magnetization curve obtained in this quadrant. The magnetic field profiles corresponding to equal magnetic moments in the α and β branch are shown schematically by the insets (a) and (b) respectively. In (a) the field gradient has not penetrated deeply into the cylinder whereas in (b), the field gradient, hence persistent currents have filled a large fraction of the volume. Therefore, in the α branch the average magnetic field is lower and the field gradient steeper than in branch β.

The analysis in chapter IV indicates that when the initial radius of penetration lies in the range $0 < R_o/A < 0.85$, the rate of radial flux collapse is slower for steeper profiles, hence shallower field penetration. An estimate of the depth of penetration of the profiles for sample NbTi-2 with magnetizations of the magnitude envisaged here indicates that in the right hand side quadrant $R_o/A < 0.85$. Accordingly, for the flux jumps triggered along magnetization curves originating in this same quadrant both the steeper profiles and the lower fields encountered in an α branch contribute to produce velocities lower than observed in the corresponding β branch.

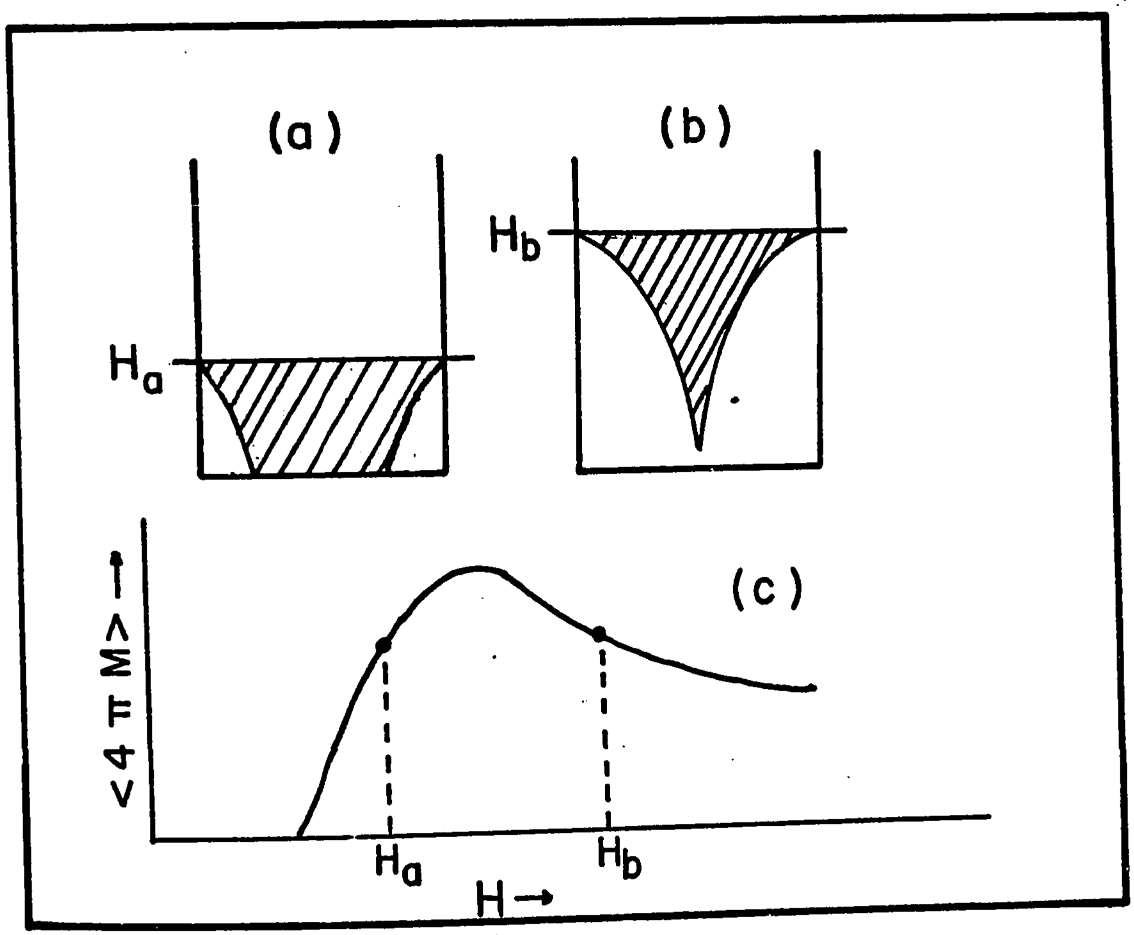

Fig. 9.14: Schematic of magnetic induction profiles before (a), and after (b) a peak in magnetization, for a magnetization curve originating in the right hand side quadrant (c).

Finally we note that simple considerations of stored magnetic energy, abstracting other important contributions, also lead us to expect higher velocities in the β branch for these simple situations (Bussiere 72a). To estimate the stored magnetic energy we have exploited the critical state concept and introduced a pinning function:

$$F_p = k\, B^{0.8}\, (1 - B/H_{c2})^{0.83}$$

where k is a constant and B is magnetic induction, which satisfactorily reproduces the observed magnetization curves. Using this pinning function and the corresponding distribution of induction B as a function of radial position r, we have calculated the magnetic energy per unit volume E_m where

$$E_m = \frac{1}{V} \int \frac{[B(r) - H]^2}{8\pi}\, dV$$

and V is the volume, for different external fields H. Figure 9.15 shows a plot of this energy as a function of $<4\pi M>$ for the magnetization curve of figure 9.5. This calculation shows that for a given $<4\pi M>$ the energy is greater on the right of the magnetization peak (branch β). This is a general result which together with the larger fields obtained in the β branch can account qualitatively for the larger velocities observed along these branches in the right hand side quadrant.

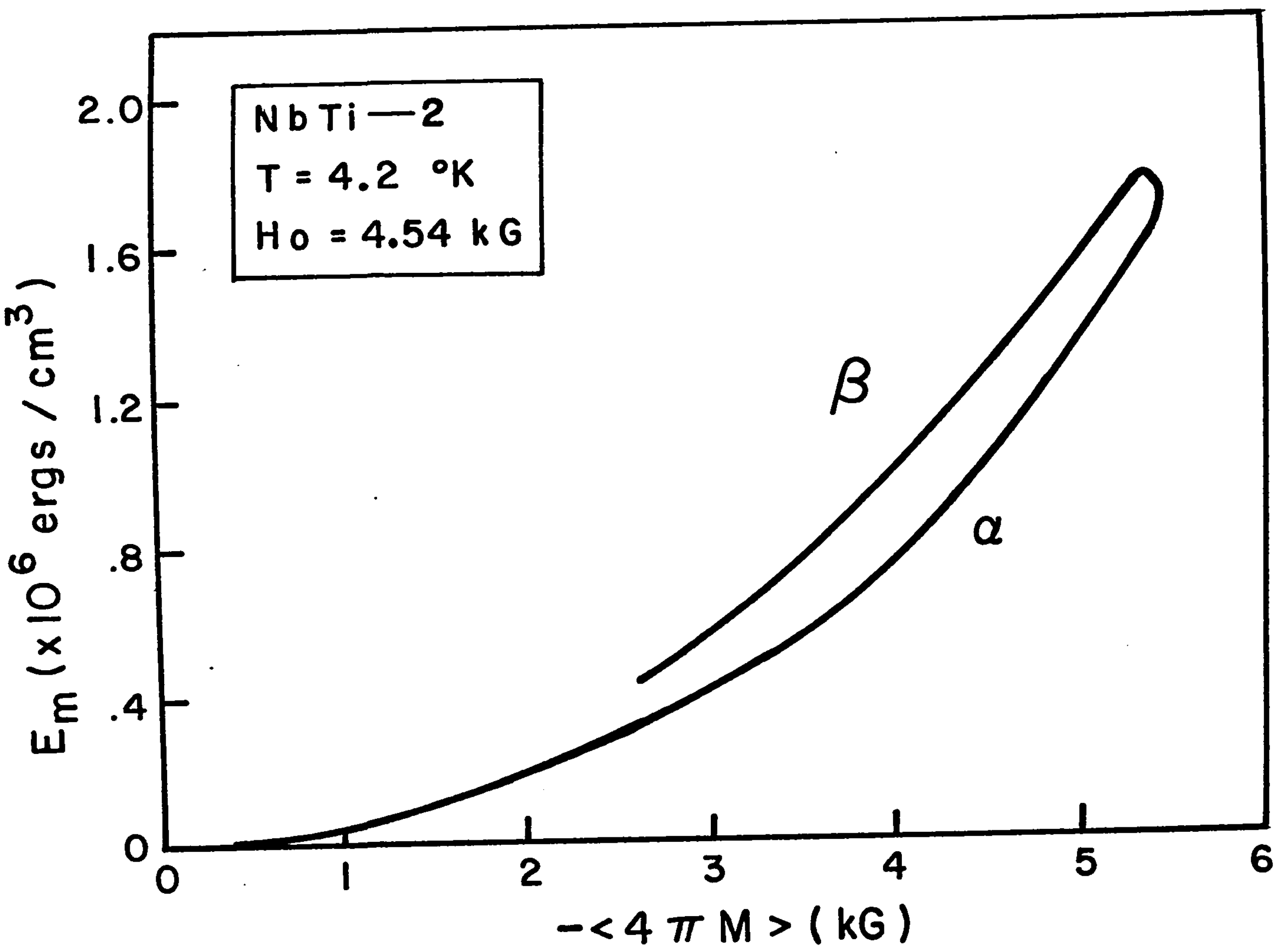

Fig. 9.15: Calculated magnetic energy vs $\langle 4\pi M \rangle$ for magnetization curve of figure 9.5. Branches α and β correspond to points before and after the magnetization peak respectively.

ii) Flux Jumps where the magnetization curve originates in the left quadrant (H_o negative).

The calculations discussed in chapter IV indicate that when the initial radius of field penetration R_o/A is greater than ~ 0.85, hence when the field gradient is very steep near the surface, the speed of radial flux collapse increases very rapidly with increasing field gradient. From considerations of the magnitude and the steep rate of growth of magnetization as the external field sweeps through zero, we may deduce, independently of any model, that the current density, hence the field gradient, is very steep when the magnetic induction is small in these two NbTi samples. Critical state model calculations indicate that very steep gradients penetrate to a depth $R_o/A > 0.85$ as the external field is swept through the region from ~ -2 kG to $\sim +2$ kG. A schematic magnetization curve corresponding to this situation is shown in figure 9.16(c). The inserts (a) and (b) depict the type of field profiles we infer must occur before and after the magnetization peak from consideration of the magnetization curves. For the β branch, eg. point (a), the field gradient is very steep near the surface of the cylinder since the magnetic induction is small over this volume. For the α branch, eg. point (b), large gradients also exist but these occur much deeper in the sample. The large field gradients occurring near the surface in branch α lead to a very rapid rate of radial flux collapse and therefore to very large longitudinal velocities although the average magnetic induction is smaller and the stored magnetic energy less than for the β branch.

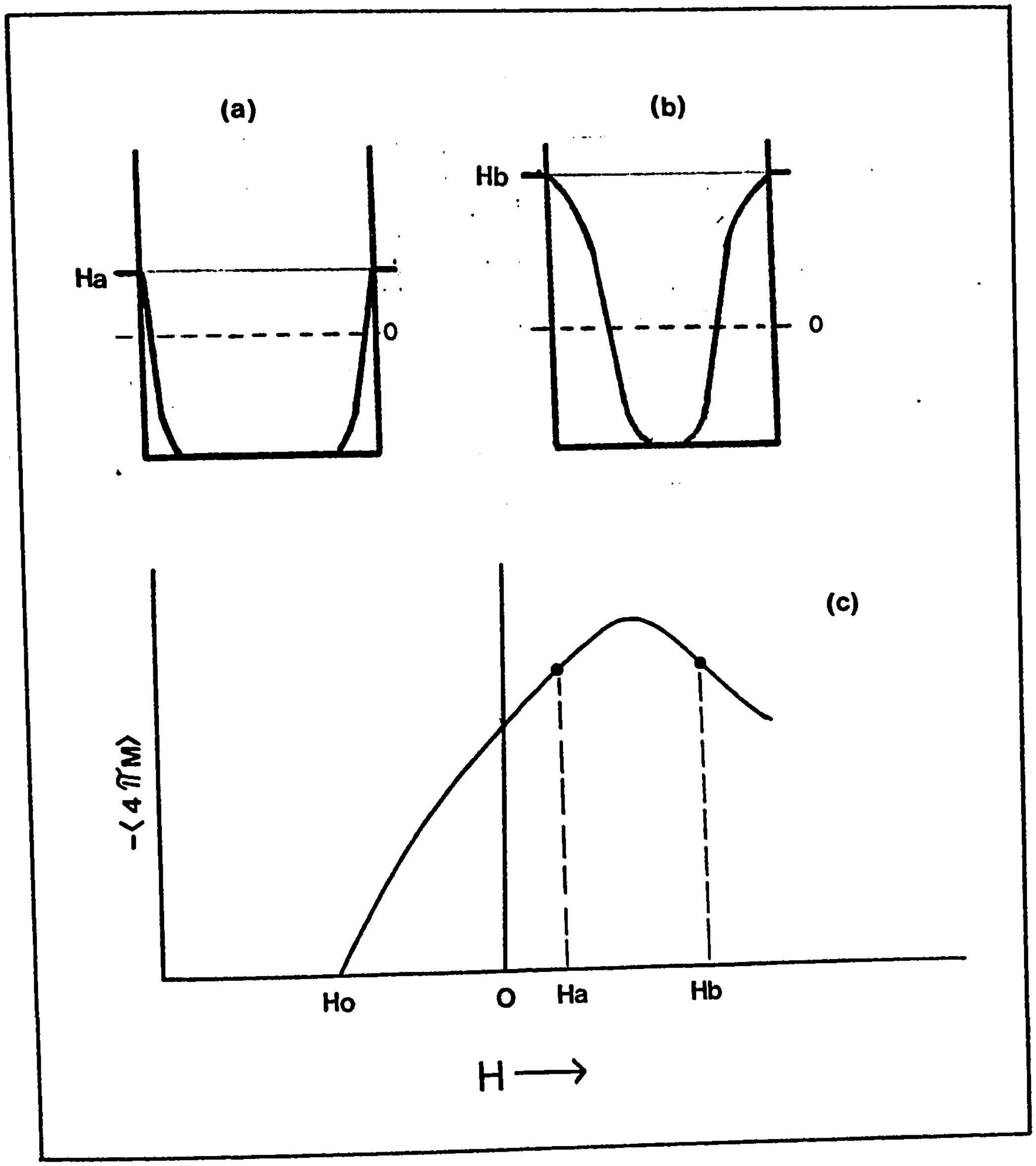

Fig. 9.16: Schematic profiles of magnetic induction before (a), and after (b) a magnetization peak for a magnetization curve originating in the left quadrant and where the field is swept across zero (c).

b) Sample NbTi-3:

This is a cylinder of much larger diameter and weaker bulk pinning than the two NbTi specimens just described. Typical magnetization curves for this sample are shown in figure 9.17. Flux jumps were triggered along the dashed parts of these curves and the velocities of these flux jumps are plotted as a function of $<4\pi M>$ in figure 9.13. Again we note an increase in velocity with $<4\pi M>$ and a dependence on magnetic field. For a given value of $<4\pi M>$, however, the velocities encountered in this sample are smaller than the ones obtained for NbTi-1 and NbTi-2. This appreciable difference in velocity is due to a "size effect" since for comparable magnetizations the field gradients are much shallower in the large cylinder. We discuss this feature in more detail later in this thesis (chapter XV).

c) NbTi-4:

This specimen is a hollow cylinder fabricated from the large cylinder just discussed. Magnetization curves for this hollow cylinder (NbTi-4) are shown in figure 9.19 where $H_o = 0$ and $H_o = -13.6$ kG. The velocities obtained for flux jumps triggered along these two curves are shown in figure 9.20. At first glance it may appear remarkable and anomalous that the velocities decrease with $<4\pi M>$. This decrease however is consistent with our earlier analysis since the average magnetic induction for the flux jumps where the magnetic

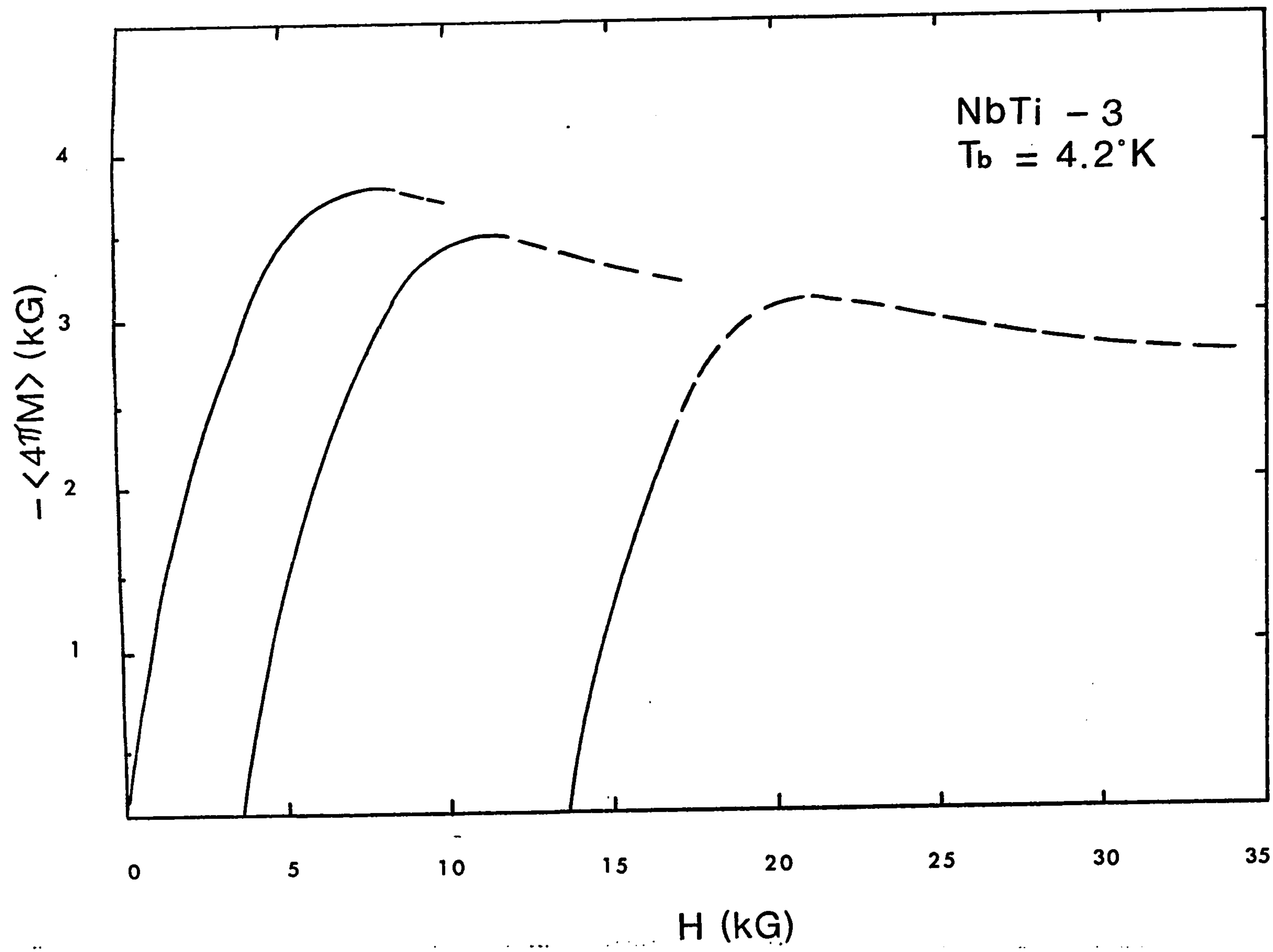

Fig. 9.17: Magnetization curves for NbTi-3 at 4.2°K, $H_o = 0$, 3.63 kG, and 13.63 kG. Dashed lines indicate regions where flux jumps were triggered.

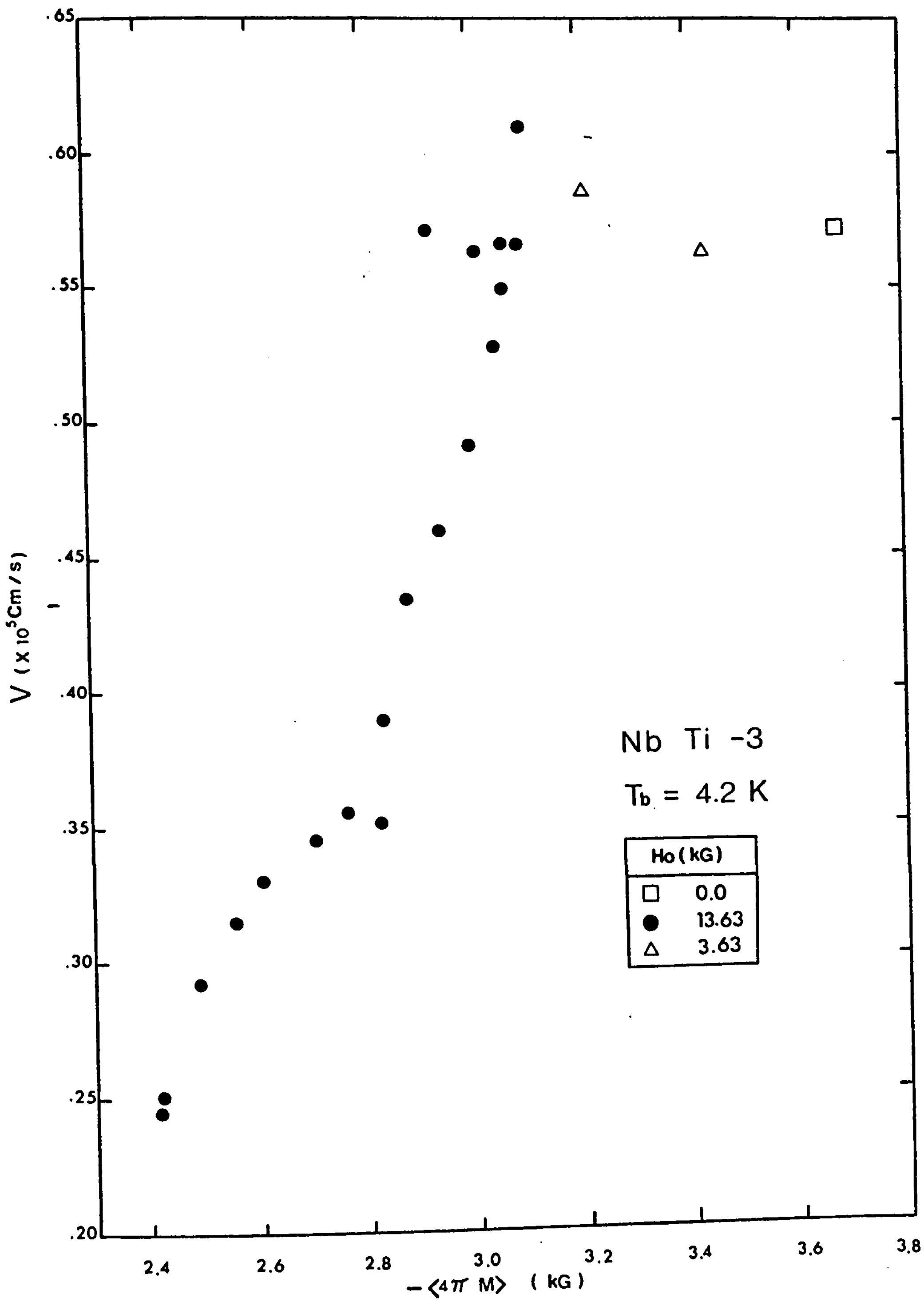

Fig. 9.18: Velocity vs <4πM> in NbTi-3 for H_o = 0, 3.63 kG and H_o = 13.63 kG.

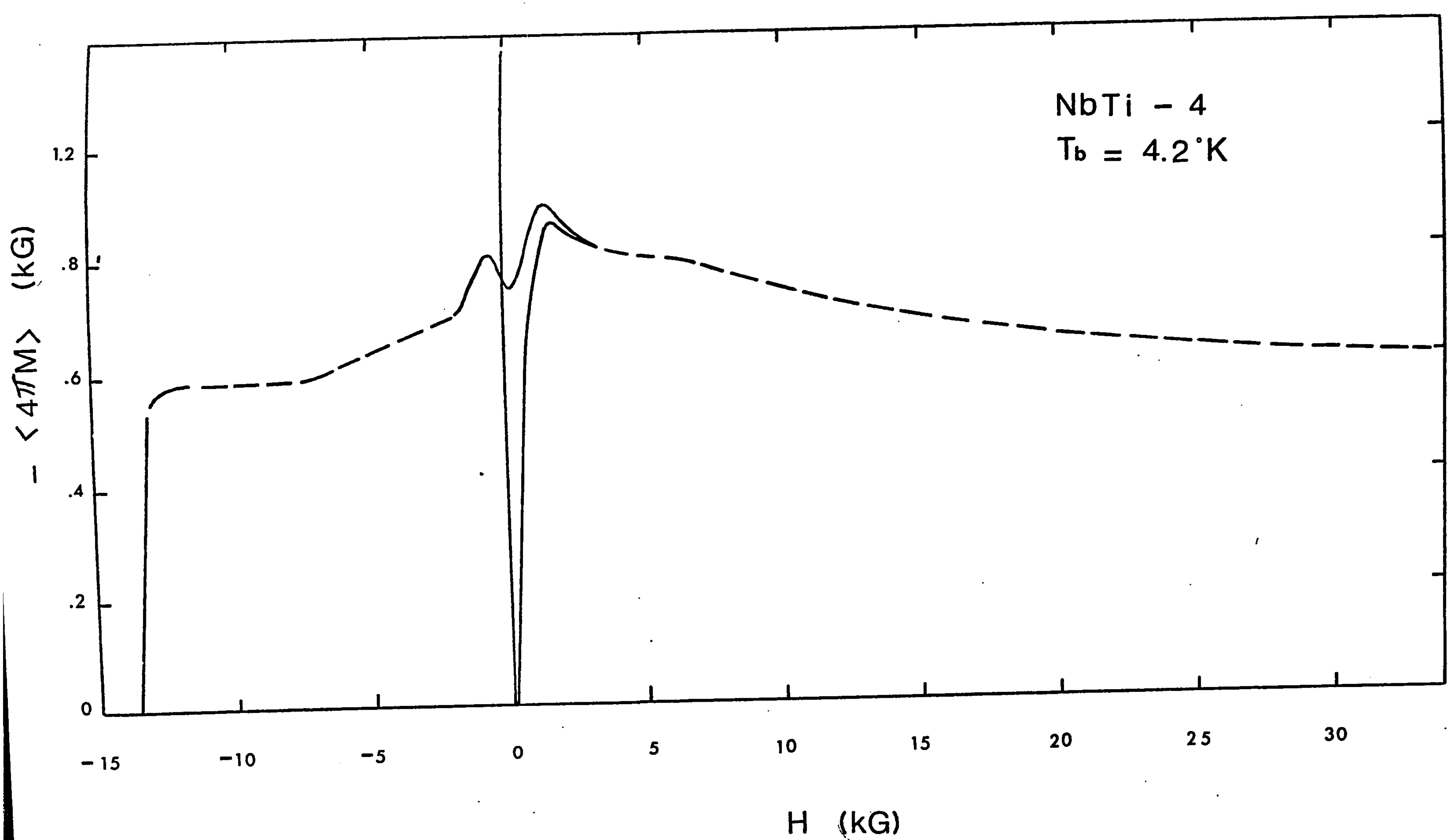

Fig. 9.19: Magnetization curves for NbTi-4 at $4.2^{o}K$, $H_o = -13.6$ kG, and $H_o = 0$. Solid lines indicate regions of stability and dashed lines regions where flux jumps could be triggered.

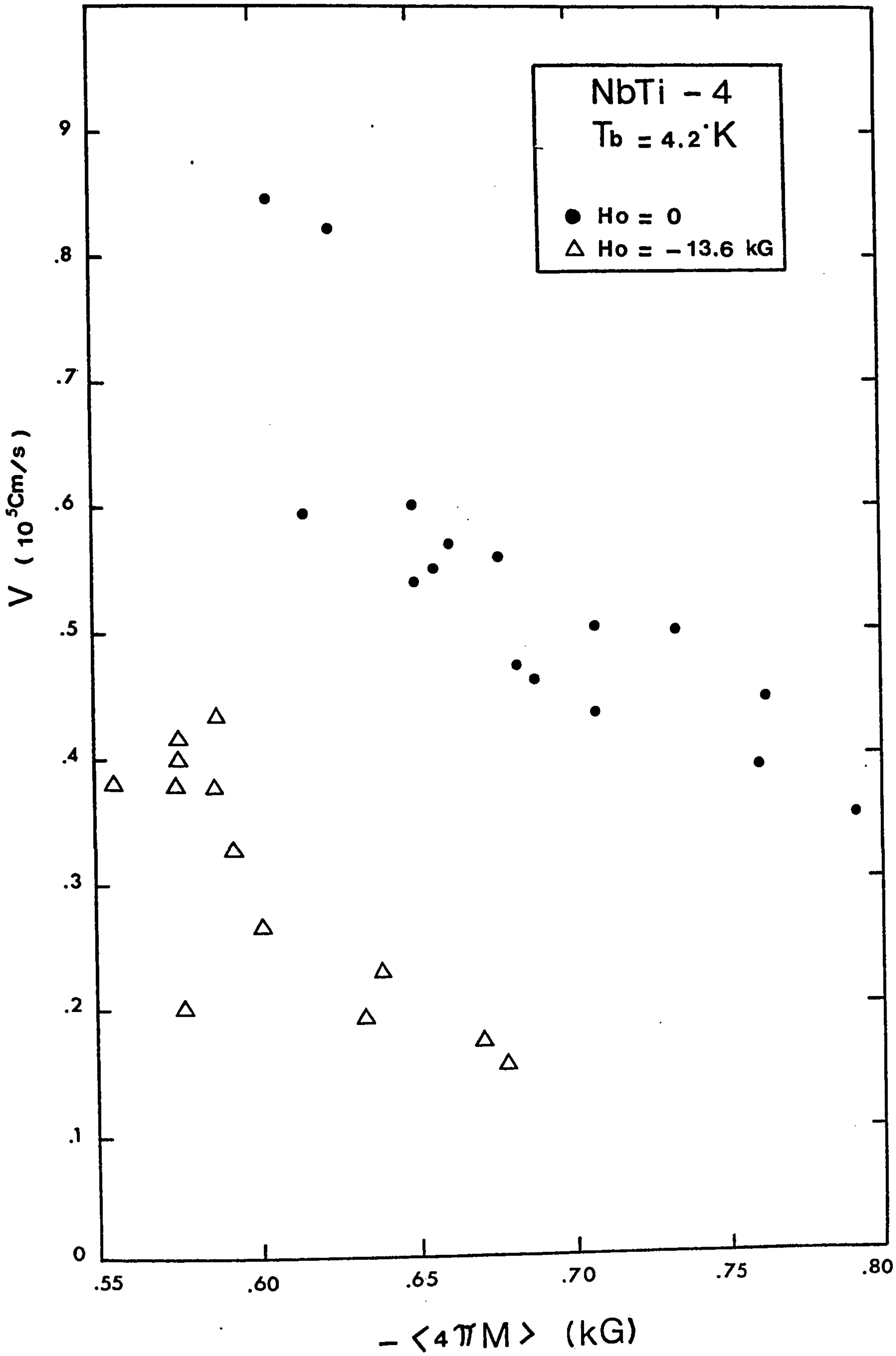

Fig. 9.20: Velocity vs <4πM> in NbTi-4, H_o = -13.6 kG and H_o = 0

moments are large is an order of magnitude smaller than that existing for the events where the moments are small. We also notice that the velocities are comparable to those obtained for the solid cylinder (NbTi-3) although the moments for the hollow cylinder are approximately 5 times smaller. The faster rate of decay of currents and the smaller entahlpy of the hollow cylinder account for these large velocities. Since the volume of the bore accounts for ∿ 4/5 of the total volume of this cylinder the ratio of magnetic energy to enthalpy in this case is approximately five times greater than for a solid cylinder of the same material and external diameter. This is simply a consequence of the fact that appreciable magnetic energy is stored in the bore or void of the hollow cylinder although there is no superconducting material in that space.

III VELOCITY VS $<4\pi M>$ IN NbZr

a) NbZr-1:

Magnetization curves for sample NbZr-1 are shown in figure 9.21. In figure 9.22 we have plotted the velocity as a function of $<4\pi M>$ for flux jumps corresponding to several values of the starting fields H_o. We note that for a given value of $<4\pi M>$ the velocity increases with the value of H_o (hence increases with external field).

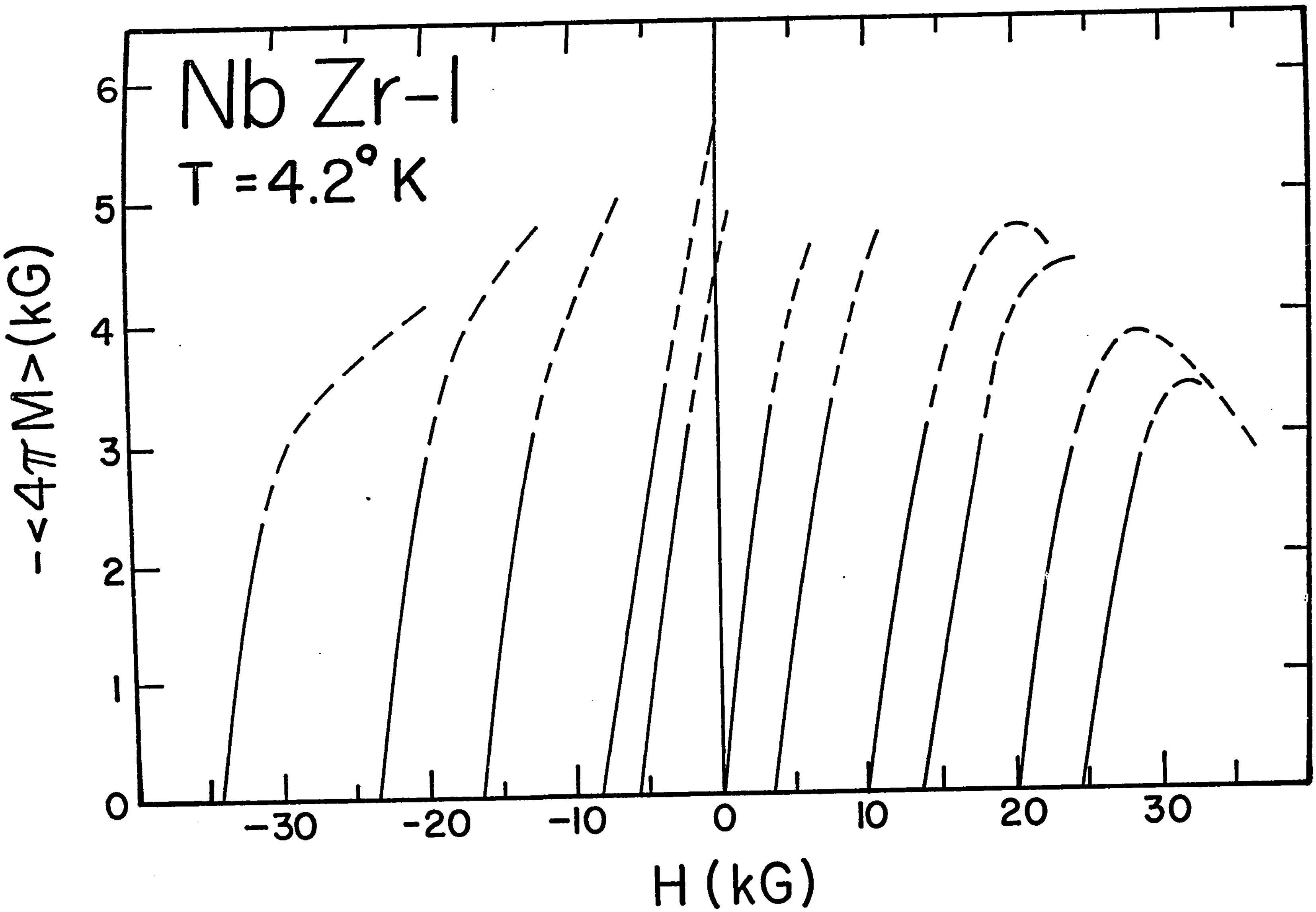

Fig. 9.21: Magnetization curves for NbZr-1 at 4.2°K. Solid lines indicate regions of stability and dashed lines regions where flux jumps could be triggered.

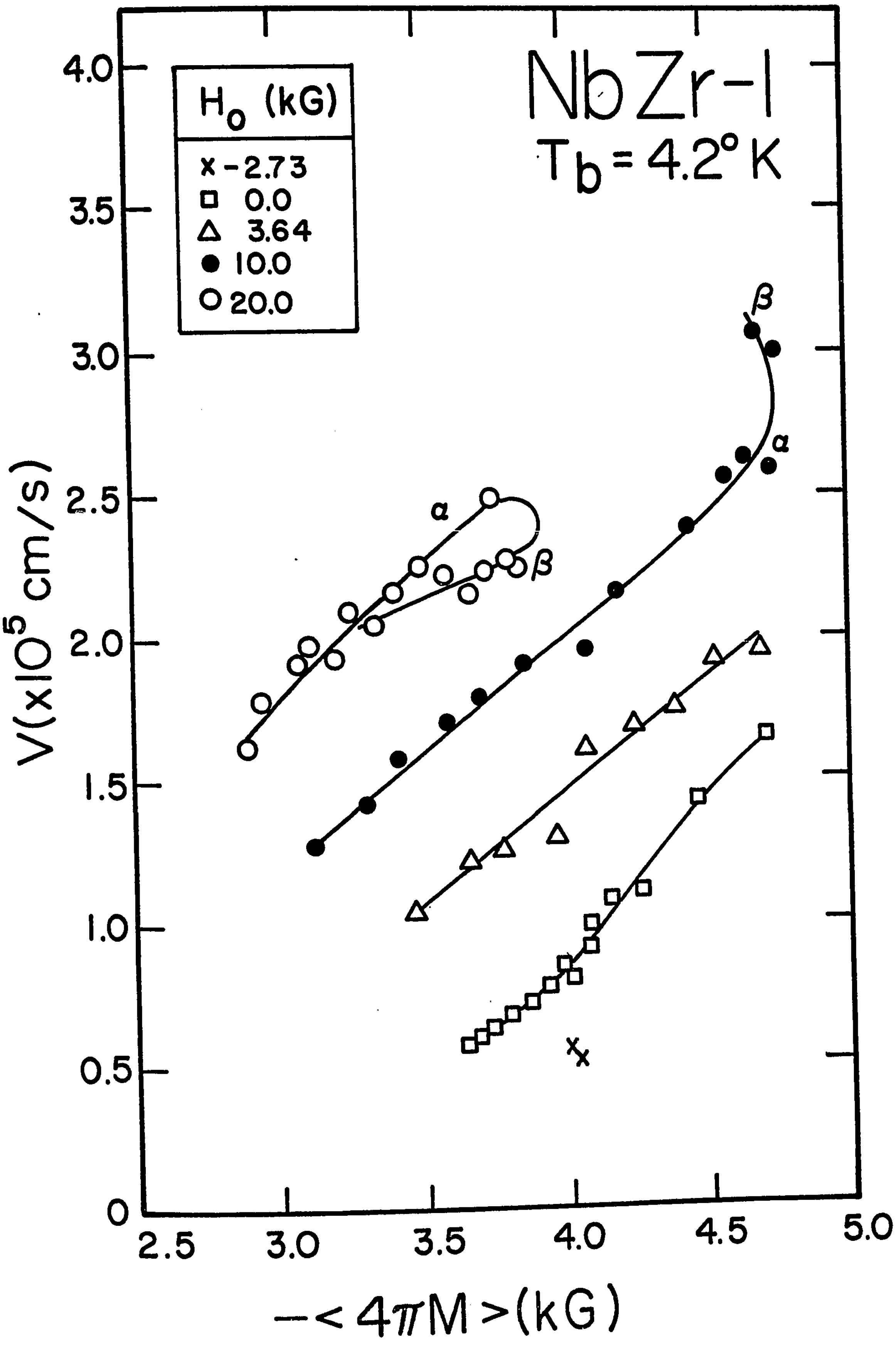

Fig. 9.22: Velocity V vs <4πM> in NbZr-1.

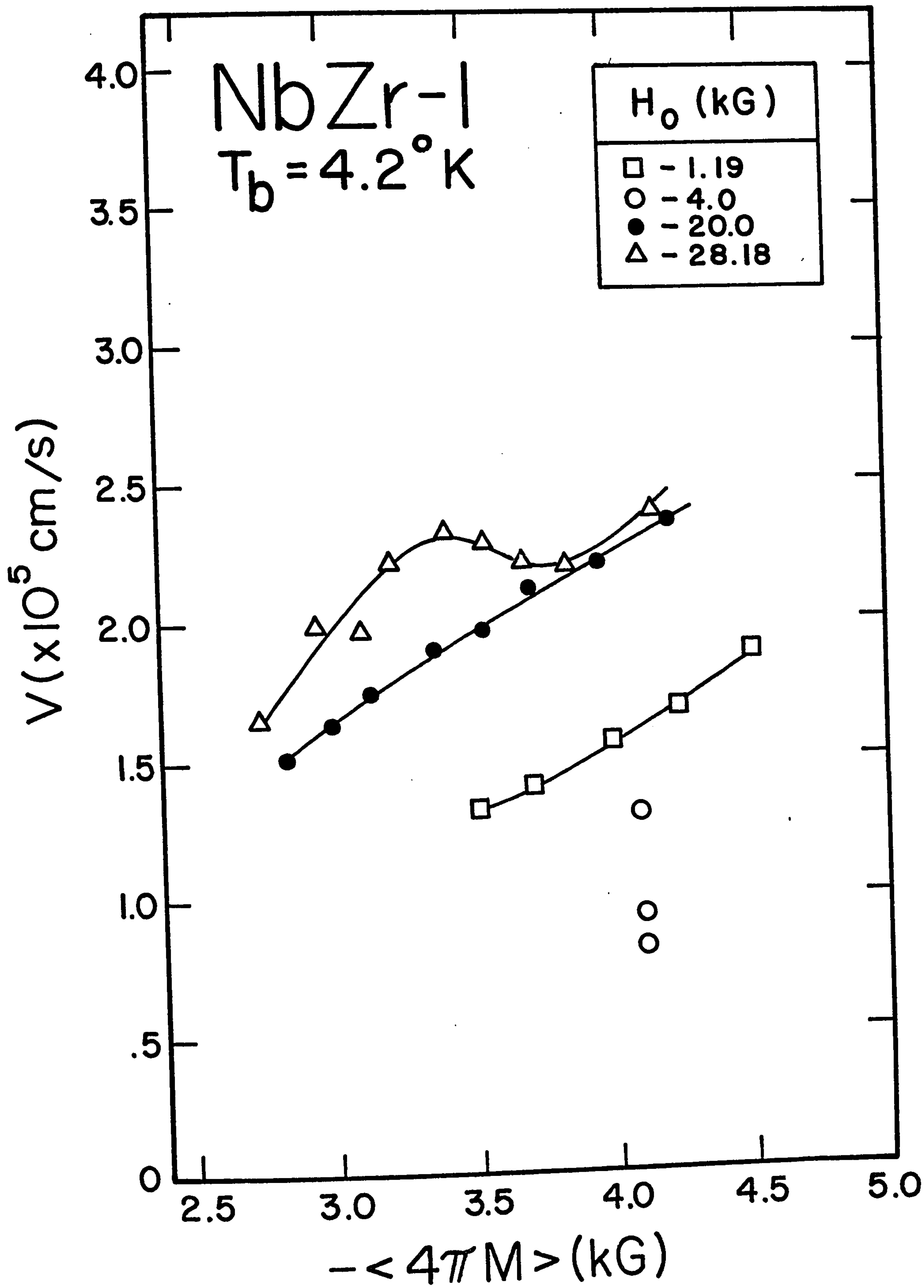

Fig. 9.23: Velocity vs <4πM> in NbZr-1

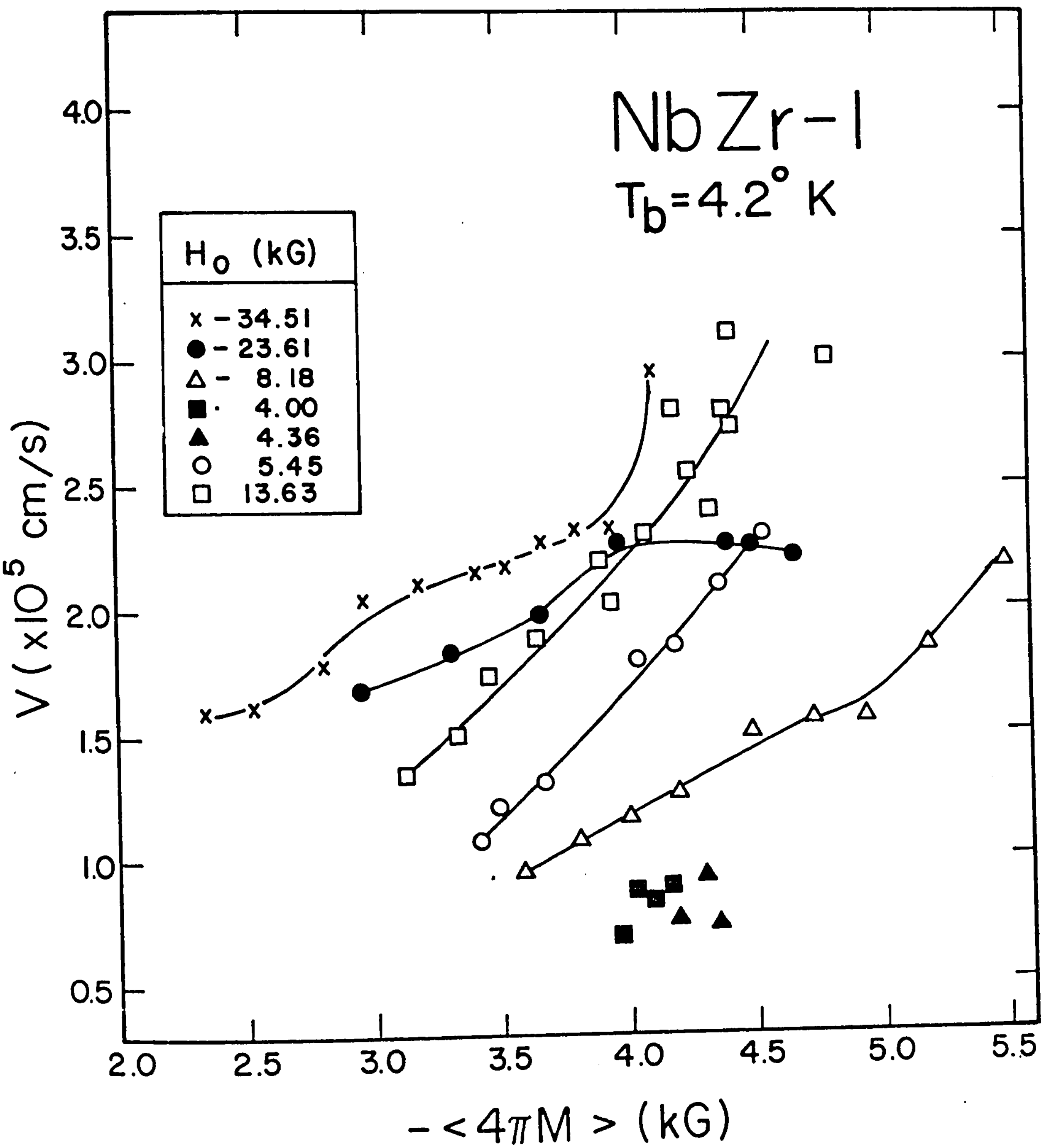

Fig. 9.24: Velocity vs <4πM> in NbZr-1.

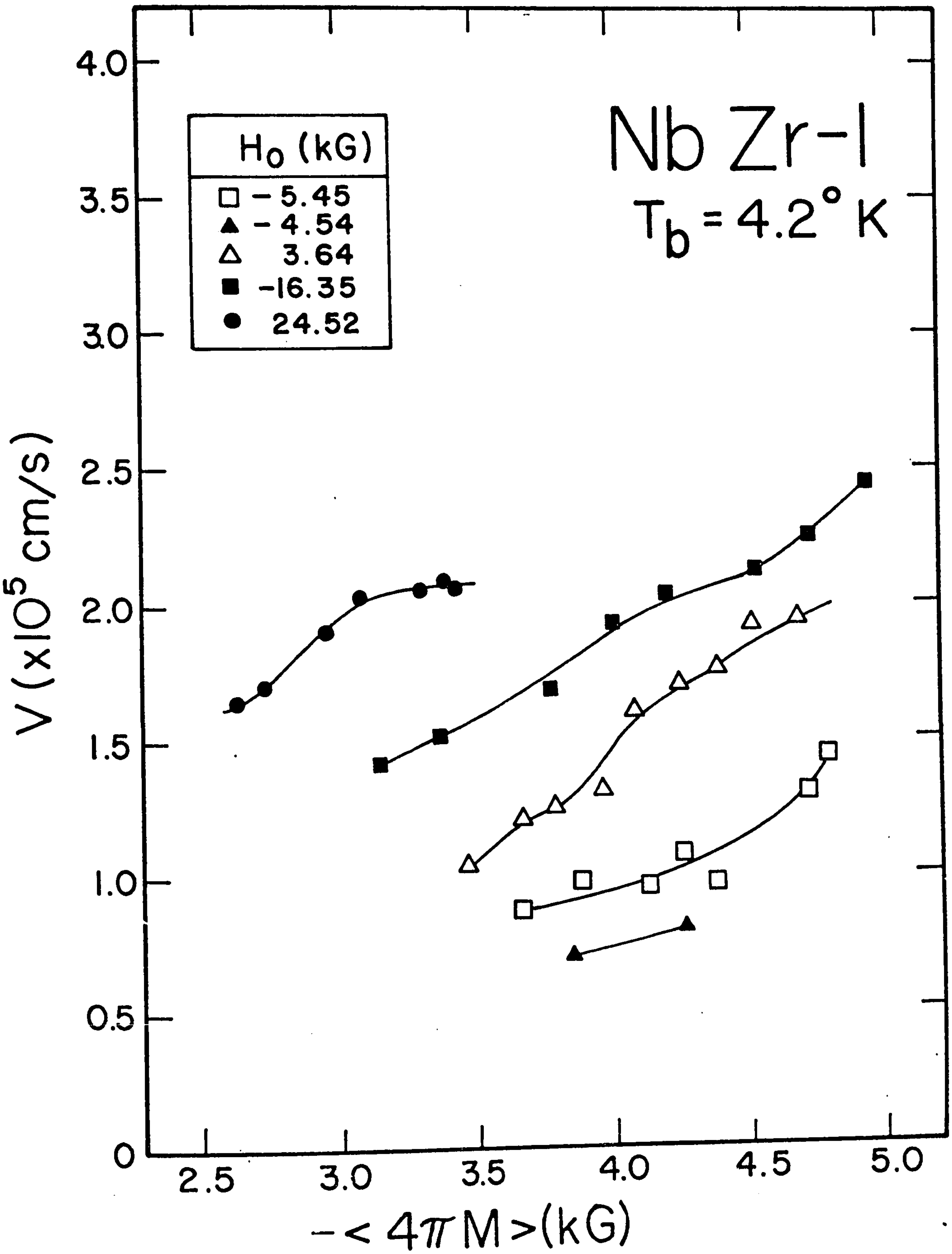

Fig. 9.25: Velocity vs <4πM> in NbZr-1.

We also note that for H_o = 10.0 kG the velocity in branch β (higher fields) are larger than in branch α. This behaviour has been explained earlier. For H_o = 20.0 kG however the velocities in branch β are slightly lower than in branch α. We cannot account for this special case.

Velocities vs <4πM> for a large number of magnetization curves are presented in figures 9.23 through 9.25. Again we note two basic trends: i) an increase of velocity with <4πM> and ii) an increase in velocity with H_o, hence with average magnetic induction, for a given value of <4πM>. The occurrence of spontaneous flux jumps made it impossible for us to extend the measurements beyond the regions indicated by the dashed curves. The field profiles over the range of magnetization curves available to us do not differ significantly hence the role played by this feature could not be explored.

b) NbZr-2:

This cylinder is of much larger diameter and weaker bulk pinning than the specimen just described. Magnetization curves for this sample are shown in figure 10.2. The velocity of longitudinal propagation was measured along the curve where H_o = 27.27 kG and the results are shown versus <4πM> in figure 9.26. Again we note an increase in velocity with <4πM>. For comparable magnetizations and magnetic fields H/H_{c2} the velocities are approximately three times

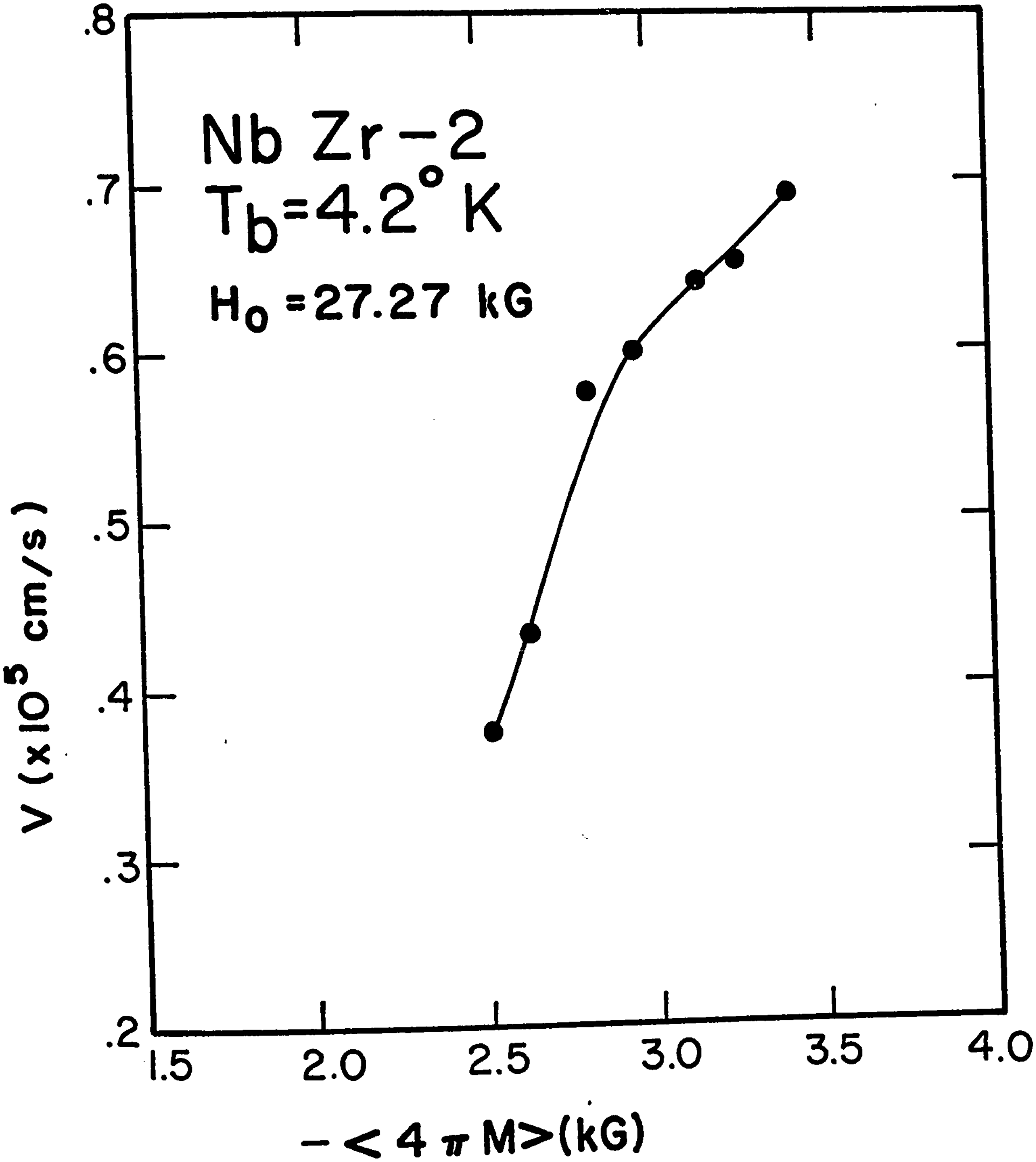

Fig. 9.26: Velocity vs <4πM> in NbZr-2, H_o = 27.27 kG.

smaller than that encountered in the specimen of smaller diameter and stronger pinning strength (NbZr-1). This difference is attributed to a "size" effect and is discussed in chapter XV.

IV VELOCITY VS <4πM> IN NIOBIUM

Magnetization curves for the Nb sample are shown in figure 9.27. The dashed and solid lines correspond respectively to regions of instability and stability. We point out that flux jumps of magnetization greater than ∿ 3 kG were all produced in external field between 0 and 2 kG, whereas flux jumps of small magnetization were all produced in relatively large fields. Unfortunately the constraints imposed by the range of stability and the onset of spontaneous flux jumps did not make it possible for us to explore velocities along α and β branches, hence a variety of field profiles, for any given magnetization curve in this material.

In figure 9.28 we have plotted the velocity of propagation of flux jumps triggered along a large variety of magnetization curves. Some of the scatter in the experimental points can be attributed to differences in field profiles. Figure 9.29 shows the velocity for the magnetization curves where $H_o = 0$, -3.52 kG and -4.11 kG. We note that flux jumps triggered along the magnetization curve where $H_o = -3.52$ kG lead to higher velocities than those of curve $H_o = -4.11$ kG.

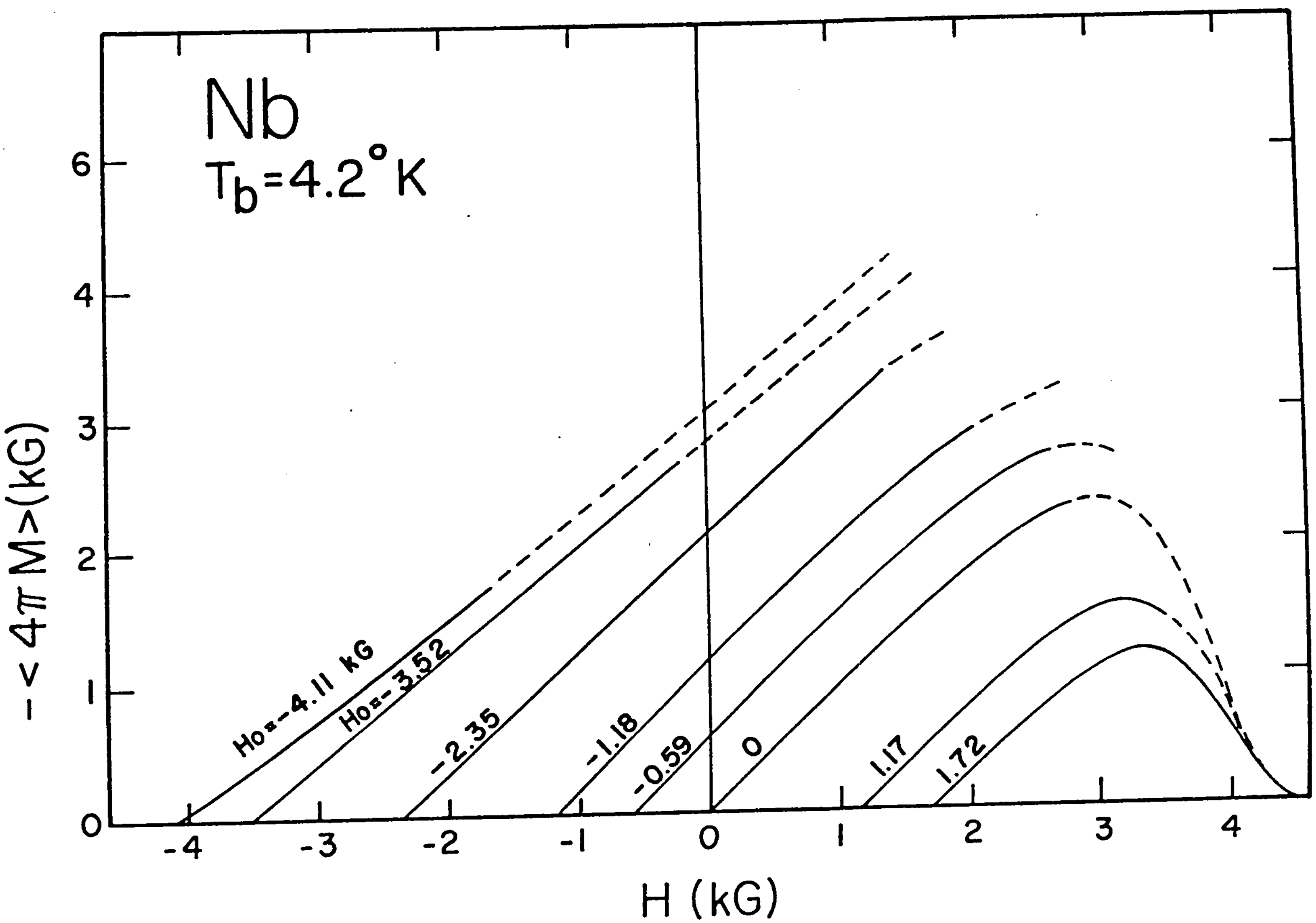

Fig. 9.27: Magnetization curves for Nb at 4.2°K. The solid and dashed lines correspond respectively to regions of stability and instability.

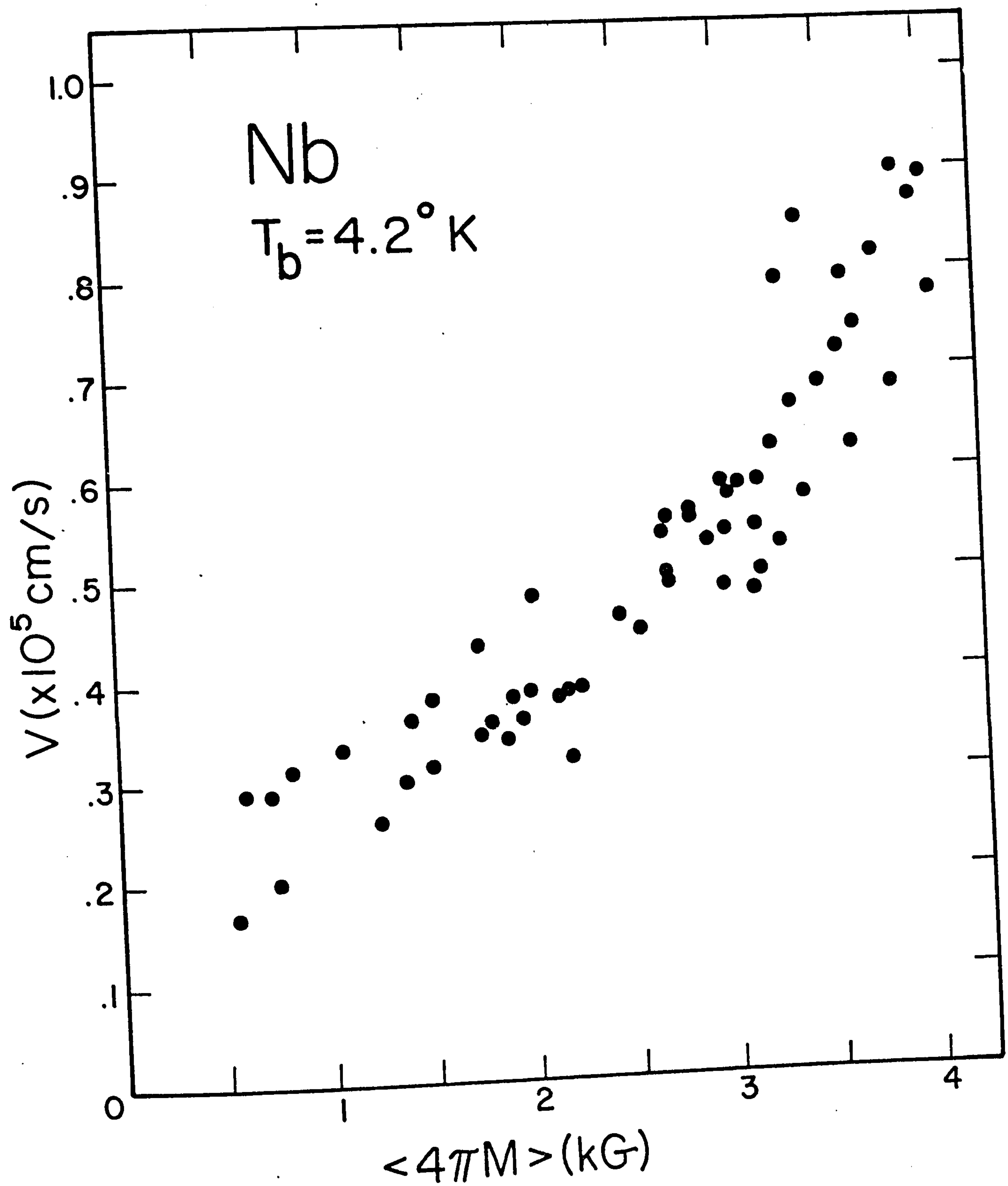

Fig. 9.28: Velocity vs $<4\pi M>$ in Nb for a wide variety of magnetic histories.

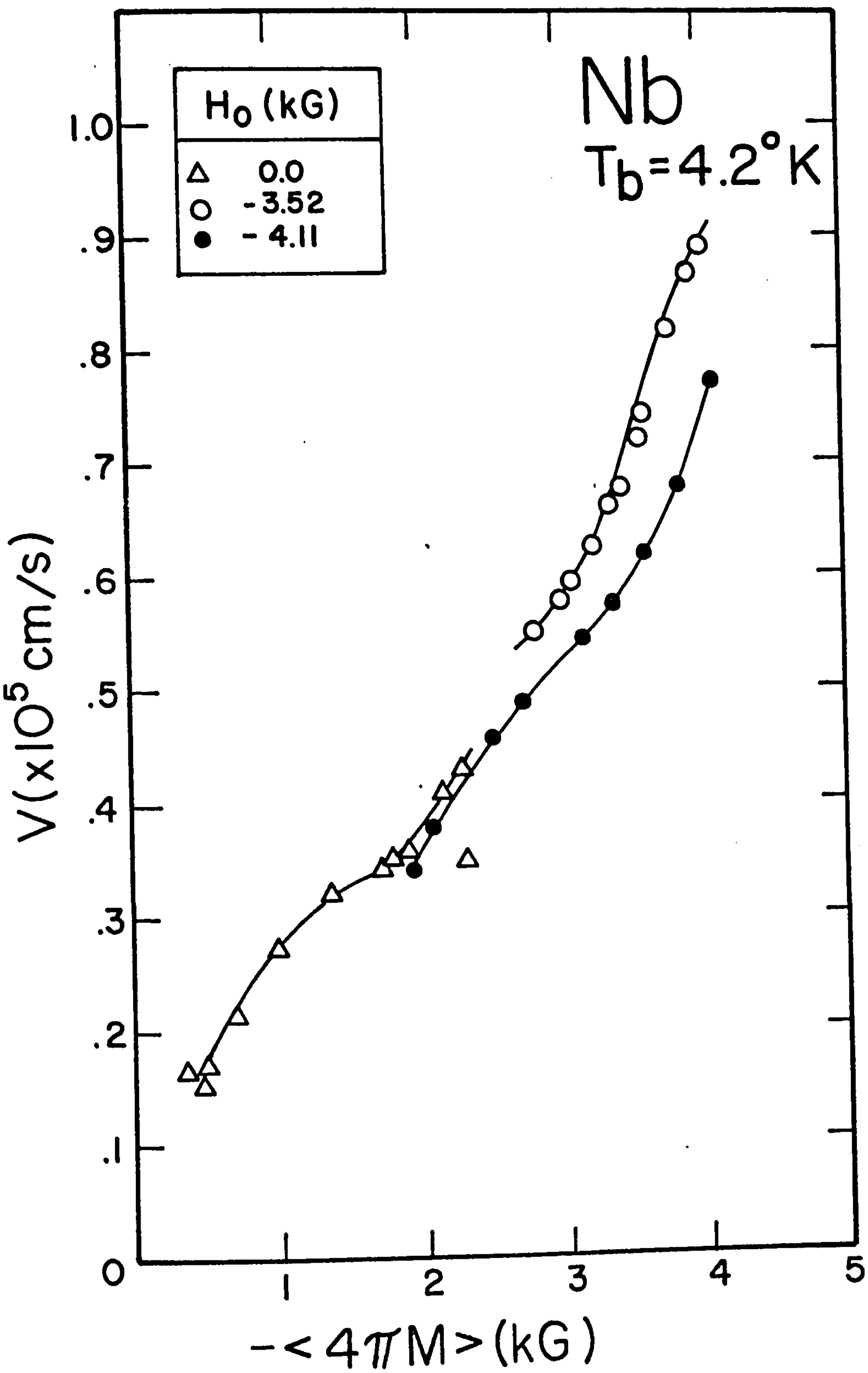

Fig. 9.29: Velocity vs <4πM> in Nb for H_o = 0, -3.52 kG and -4.11 kG.

This is consistent with our earlier discussion since the average magnetic induction is higher for the curve with the larger velocities.

The velocities observed for this material are much smaller than that encountered in wires of NbTi and NbZr of comparable diameter. The lower normal state resistivity of pure Nb partly accounts for this difference (see chapter XII).

V. VELOCITY VS <4πM> IN VANADIUM

a) V-1:

Figure 9.30 shows a series of magnetization curves for sample V-1 where the bath temperature is $T_b = 2.46^{o}K$. For this sample as with the Nb specimen, large flux jumps could be produced in low fields only and small flux jumps were produced in fields close to H_{c2}. Figure 9.31 shows the velocity as a function of $<4\pi M>$ for flux jumps triggered along a large variety of magnetization curves. Again the velocity increases with $<4\pi M>$ and differences in field profile probably account for the scatter in the data. The velocities encountered in this sample however are larger than those obtained for Niobium. This difference is due partly to the larger normal state resistivity of this sample and to its smaller enthalpy (see Table II).

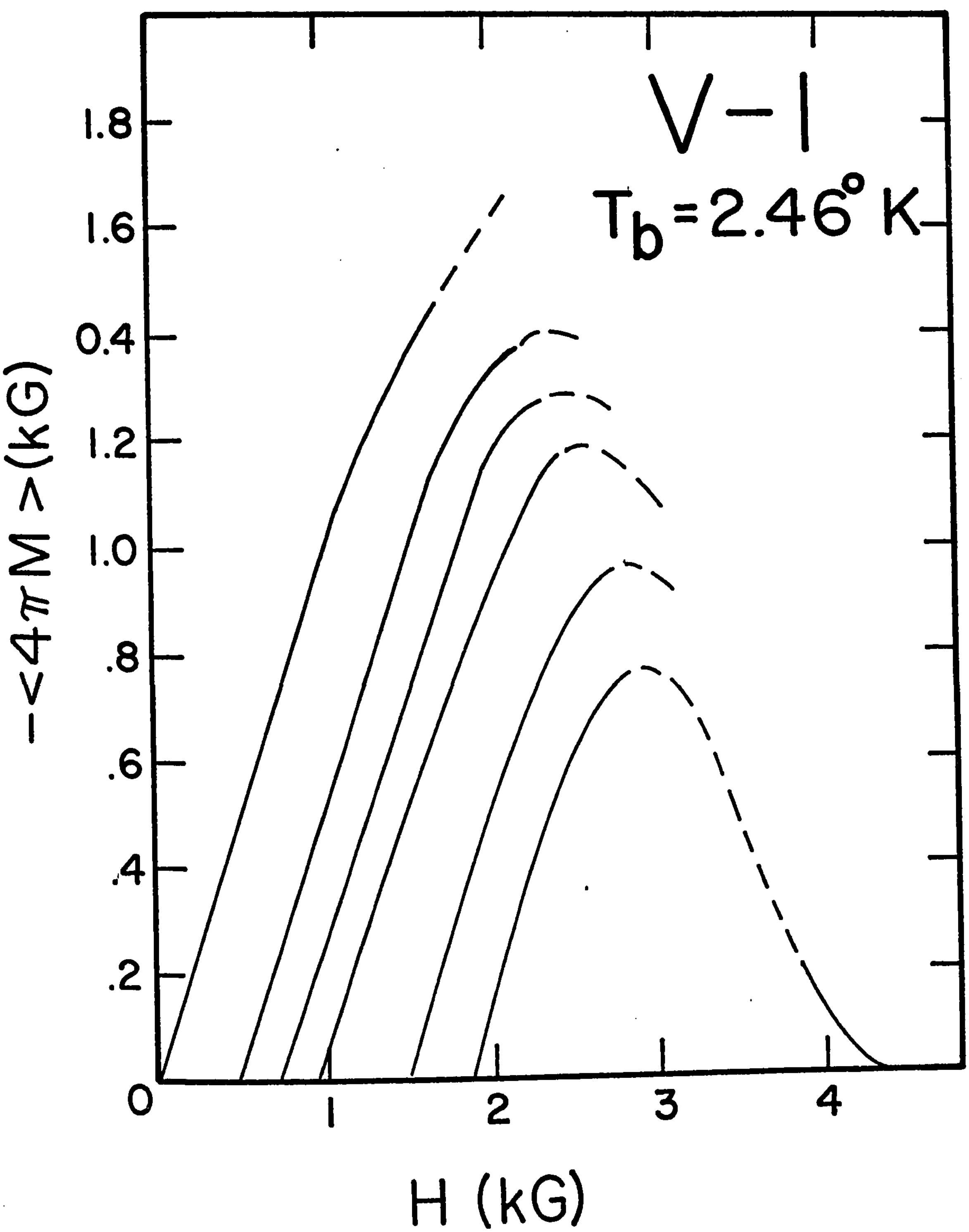

Fig. 9.30: Magnetization curves for Vanadium sample V-1 at 2.46°K.

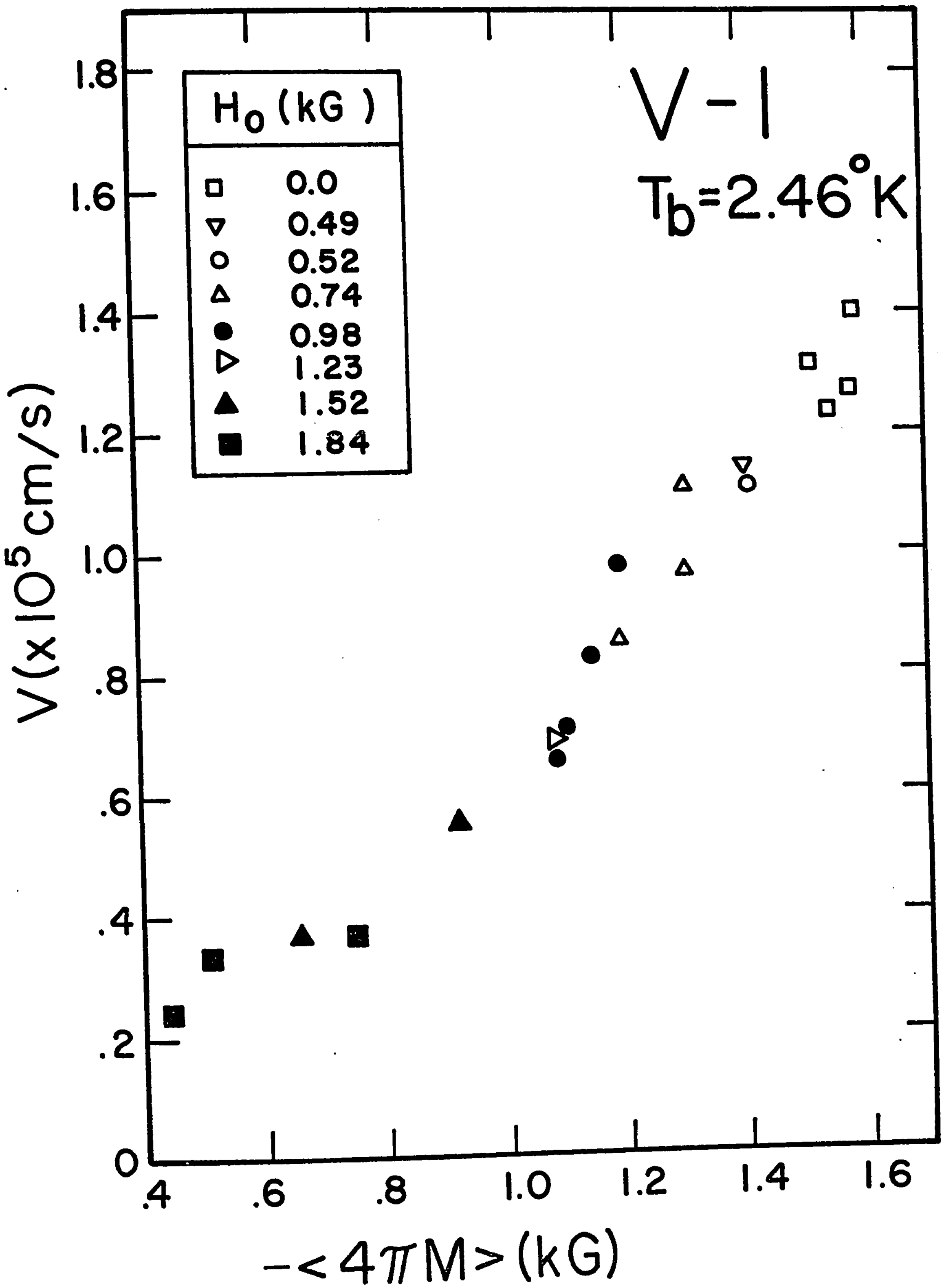

Fig. 9.31: Velocity vs <4πM> in sample V-1 at 2.46°K for a large variety of magnetic histories.

b) V-2:

This sample is a cylinder of slightly larger diameter than V-1 but with comparable pinning strength.

Figure 9.32 shows magnetization curves for sample V-2 where the bath temperature is $T_b = 4.2^oK$. This sample is stable over a large portion of its magnetization curves (solid lines) and is stable over the entire curve starting at $H_o = 0$. The velocities obtained along the dashed lines of figure 9.32 are shown in figure 9.33. Again the general trend is for the velocity to increase with $<4\pi M>$. It is difficult to identify trends due to average magnetic induction and the variety of field profiles. The largest velocities are obtained when the sample has cooled in a strong field which is subsequently varied through zero to small fields of opposite polarity. Similar behaviour has been encountered and discussed for specimens of NbTi.

Figure 9.34 shows a magnetization curve for this same sample where the bath temperature $T_b = 2.5^oK$. At this bath temperature, instabilities could be triggered over a large portion of the magnetization curves and larger magnetic moments could be obtained. The velocity of flux jumps along these curves is shown in figure 9.35. Again the velocity increases with $<4\pi M>$ and some dependence on average magnetic induction and type of field profile can be identified. We note that the velocities are smaller for similar magnetizations than observed at a comparable temperature in the Vanadium specimen of smaller diameter and similar pinning strength (V-1). This difference of a factor of 2 arises from a "size" affect and is discussed in chapter XV.

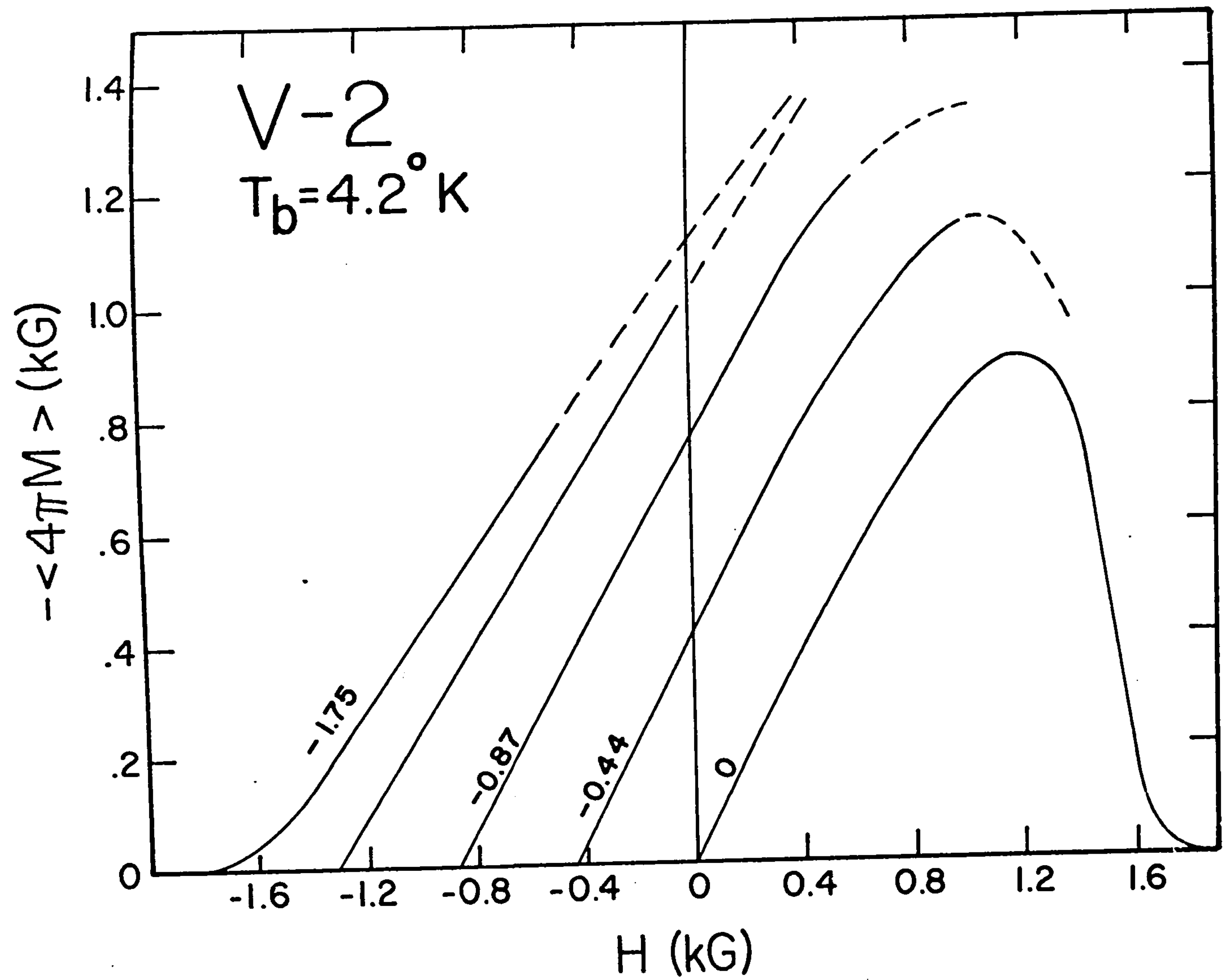

Fig. 9.32: Magnetization curves for sample V-2 at 4.2°K.

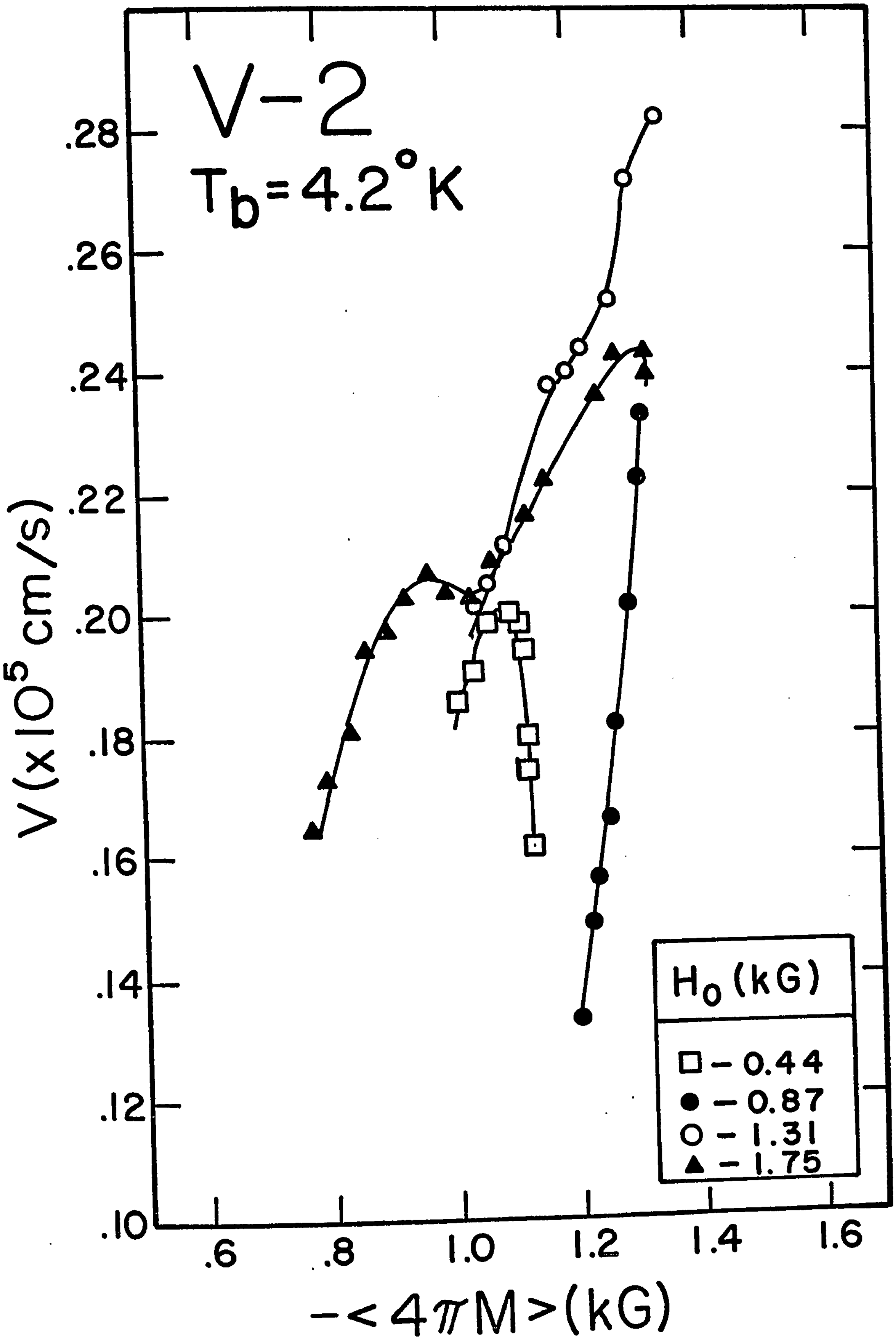

Fig. 9.33: Velocity vs <4πM> for sample V-2 at 4.2°K and several values of H_o.

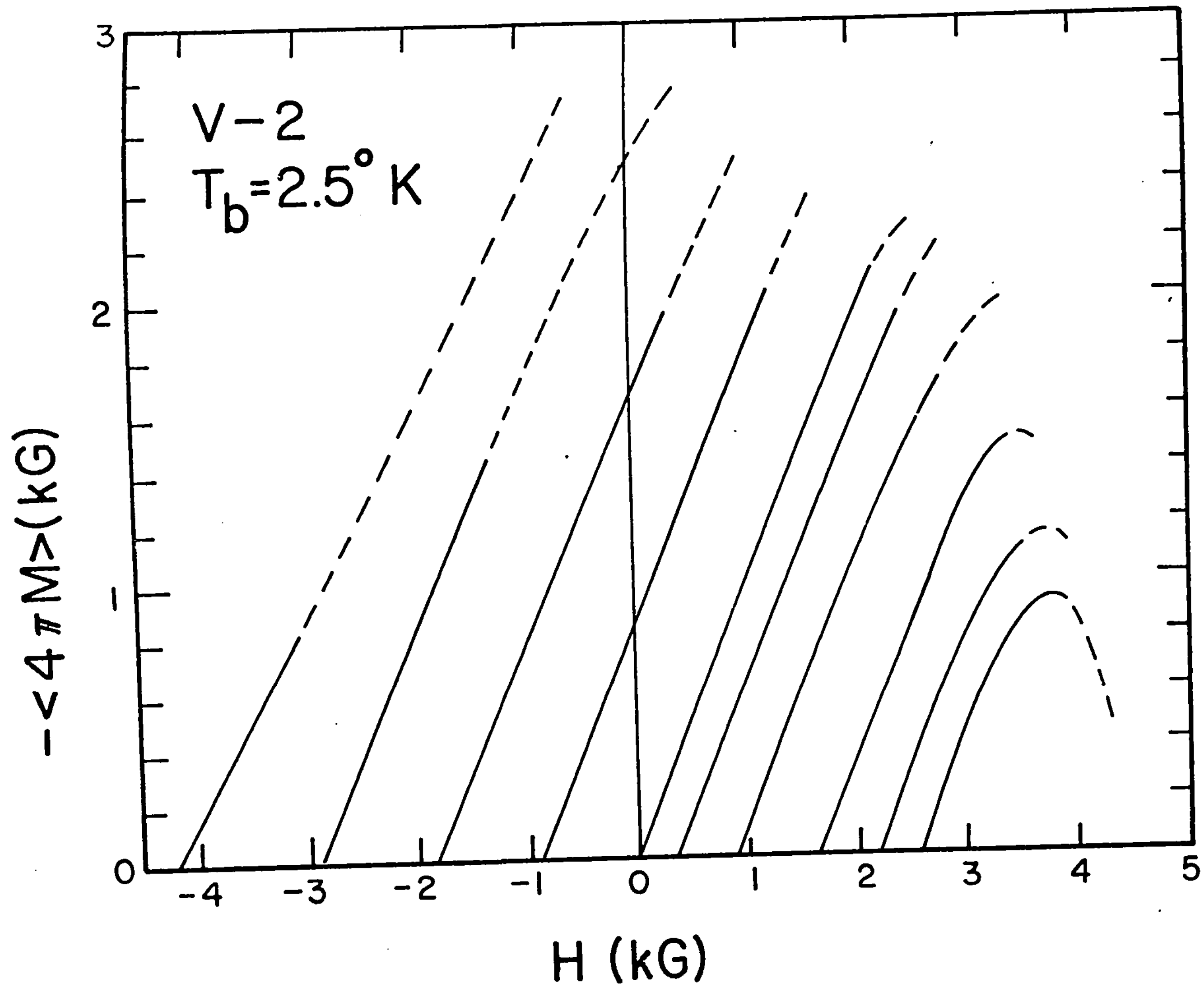

Fig. 9.34: Magnetization curves for sample V-2 at 2.5°K.

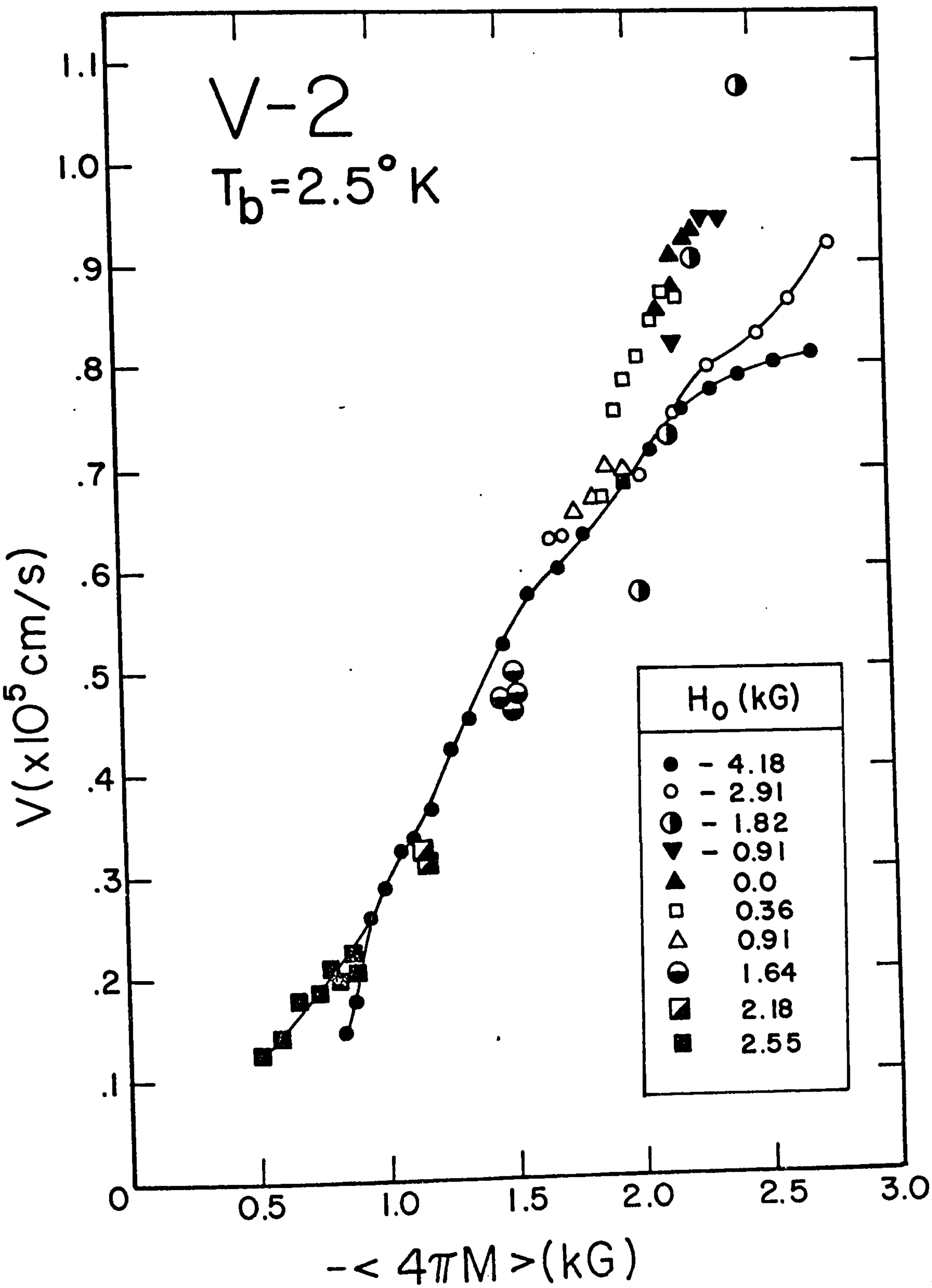

Fig. 9.35: Velocity vs <4πM> in sample V-2 at 2.5°K for a wide variety of magnetic histories.

V. CONCLUSION

In this chapter we have presented an assortment of measurements of longitudinal propagation velocity in several samples of various materials. We have demonstrated that the magnitude of the magnetization $\langle 4\pi M \rangle$ plays an important role in determining the longitudinal velocity of flux jumps. Almost invariably an increase in velocity is associated with an increase in magnetization. It is clear from the observations however that the magnitude of the magnetization does not provide a unique and unambiguous measure of the propagation velocity. The velocities encountered span broad ranges for a given material in comparable fields and at comparable temperatures (10^5 to 10^6 cm/sec for NbTi-1 and 2, and 10^4 to 10^5 cm/sec for NbTi-3 and 4) and for different materials (5×10^4 to 3×10^5 cm/sec for NbZr and $\sim 10^4$ to 2×10^5 cm/sec for Niobium and Vanadium).

For a given material various characteristics of the field profile and the average magnetic induction are also seen to have significant effects. The normal state resistivity is also seen to play an important role when velocities of different materials are compared. In subsequent chapters we examine these various other contributions separately and attempt to identify the role they play qualitatively and quantitatively.

CHAPTER X

STRUCTURE OF FLUX JUMPS AND ASYMMETRICAL FLUX PENETRATION DURING LONGITUDINAL PROPAGATION

I. INTRODUCTION

Although our analysis of flux jumps in Part I of this thesis assumes that flux collapse proceeds with cylindrical symmetry, flux does not, in general, penetrate along each point of the perimeter of a cylinder simultaneously even if the entire sample is perturbed uniformly, since the disturbance may start at one or several discrete nuclei. Asymmetrical and nonuniform flux penetration will give rise to structure in the voltage pulse observed by a pick-up coil surrounding a cylinder which is undergoing a flux jump . Faber (Faber 53) encountered differences between theoretical and observed voltage shapes in his investigations of the radial collapse of flux in type I cylinders subjected to a pulse of field higher than critical. In some cases he observed two weakly resolved peaks of voltage instead of one. He attributed this structure to two separate filaments of flux originating from different nuclei and arriving at the search coil one after another. Wertheimer and Gilchrist (Wertheimer 67) have photographed the penetration of flux in type II superconducting discs in transverse fields. Their photographs indicate that flux jumps in this geometry are usually incomplete and penetrate different parts of the disc in succession, as the external field is increased. The irregularity of flux penetration was greater in alloys than in pure metals. In their experimental work the flux jumps were not triggered externally but occurred spontaneously as the external field was increased. Under these circumstances, it is expected that flux penetration will nucleate at weak points on the edges of the disc. The large demagnetizing factor of the disc geometry may also enhance the occurrence of discrete penetration. We expect flux penetration to start from a larger number of nuclei and thereby achieve nearly symmetrical penetration when the perturbation is not too small.

In this chapter we present a variety of voltage pulses observed during longitudinal propagation. The pulses are detected by small coils wound locally around the sample. For a given specimen the pulse shape is seen to vary continuously with the position on the magnetization curve along which the flux jump is triggered. We account for our observations in terms of asymmetrical flux penetration and the propagation of independent flux threads along the sample.

II. SHAPE OF VOLTAGE PULSES OBSERVED DURING LONGITUDINAL PROPAGATION

A variety of voltage pulses are shown in figures 10.1, 10.3, and 10.4. In these figures the upper traces originate from two pick-up coils wound in series around the sample and placed approximately 4 cm apart. One of the coils has 10 turns and the other 5 turns. Except for figure 10.1(a) the first pulse in all the upper traces corresponds to the coil of 10 turns. The bottom traces originate from a single coil of 5 turns wound midway between the other two coils.

The voltage traces shown in figure 10.1(a) for sample NbTi-3 exhibit no structure, have a "classical" appearance and are similar in shape to that reported by Walker and Hulm (Walker 66, 72) for NbZr. Indeed, in certain samples, only this type of pulse was observed. In many instances, however, depending on the sample and the initial configuration of flux, the shape of the pulses is very irregular.

Figures 10.1(b) and (c), 10.3 and 10.4 show voltage traces observed during flux jumps in one of our specimens of NbZr (labelled NbZr-2). Although individual pulses originating from any of the three pick-up coils may exhibit very variegated structure, inspection of the traces reveals that, generally, the same complicated pattern is detected by each coil in succession. We conclude that in these instances we are observing a sequence of individual events which propagate independently but at the same velocity along the wire.

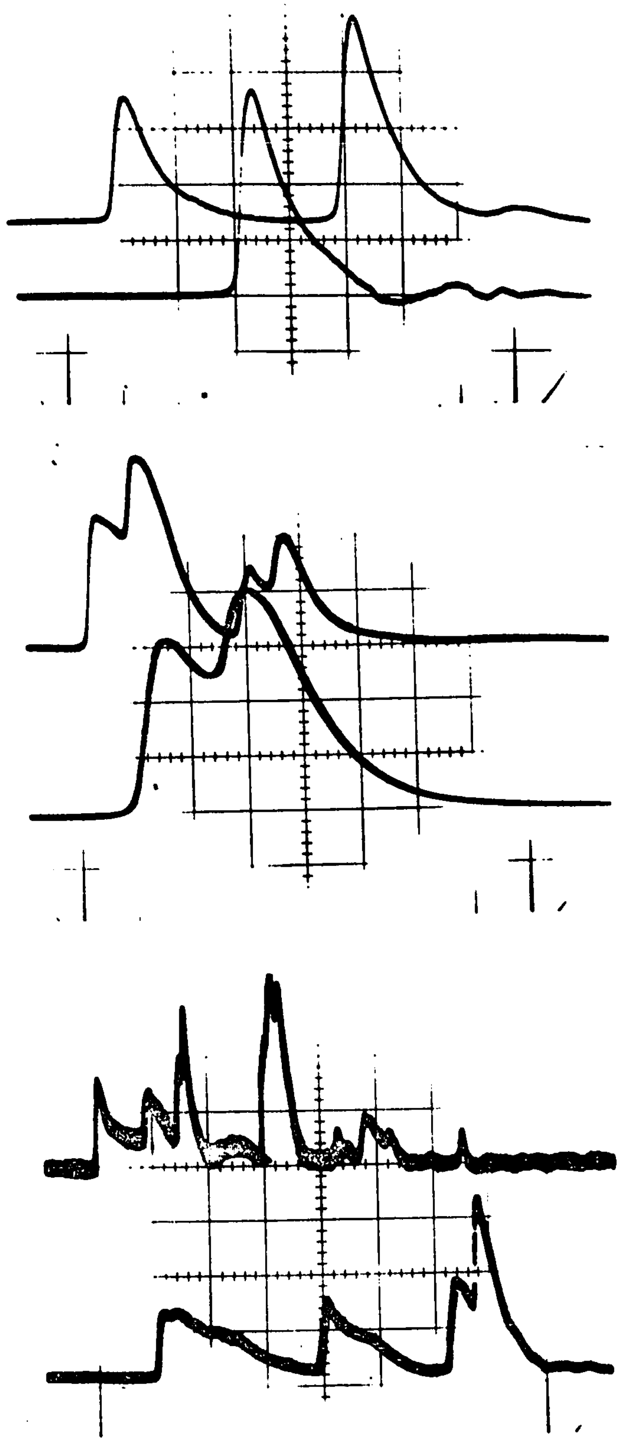

(a) NbTi-3
H_o = 13.63 kG, ΔH = 5.84 kG
upper = 0.1 V/div, 20 μs/div
lower = .05V/div, 20μs/div

(b) NbZr-2
H_o = 0, H = 7.14 kG
upper = 0.1V/div, 50μs/div
lower = .05V/div, 20μs/div

(c) NbZr-2
H_o = 9.01 kG, H = 12.91 kG
upper = .02V/div, 0.2ms/div
lower = .01V/div, 0.1ms/div

Fig. 10.1: Typical voltage peaks seen by two pick-up coils in series (upper traces, 10 and 5 turns) and a single pick-up coil of 5 turns (lower traces).

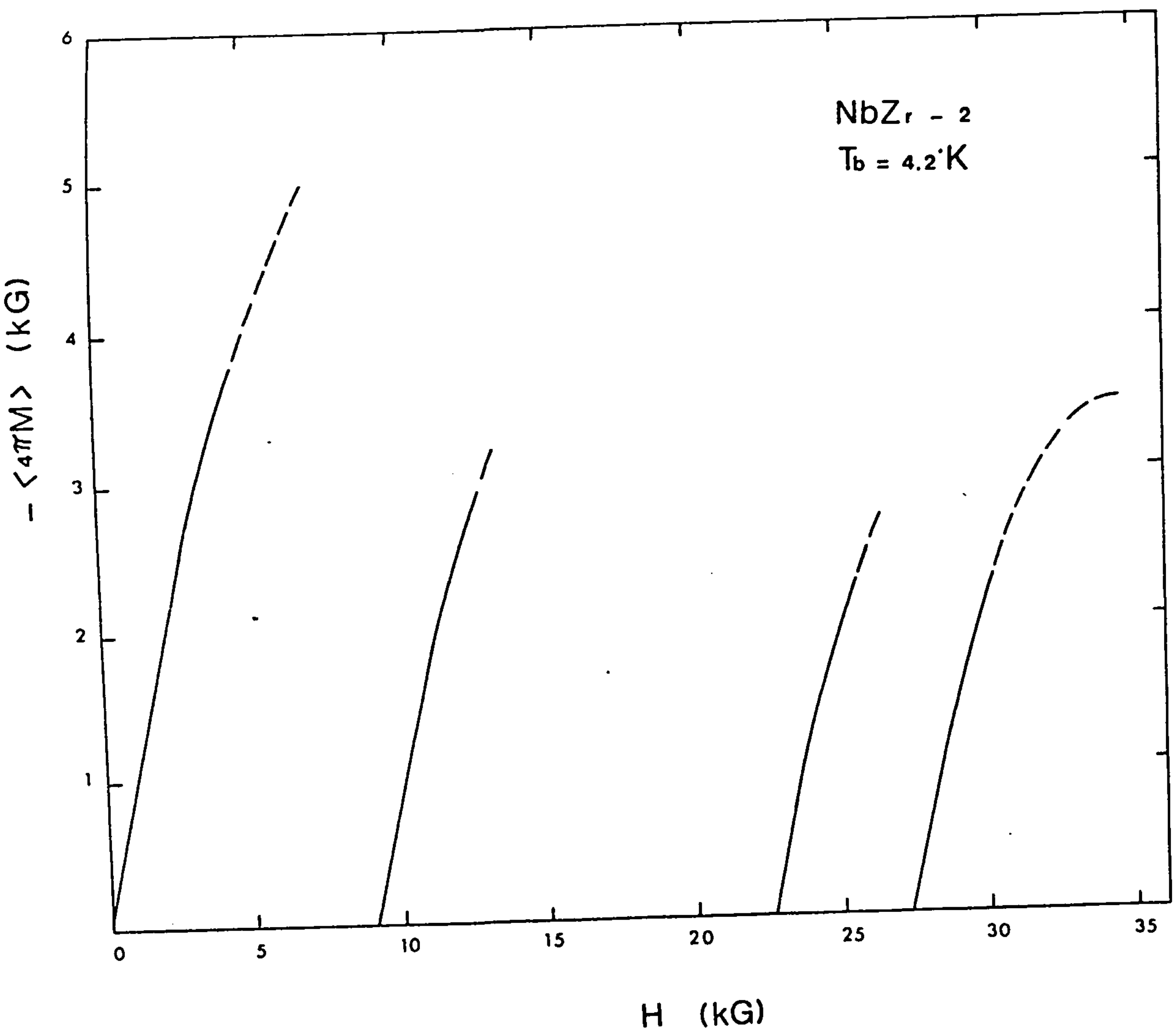

Fig. 10.2: Magnetization curves for NbZr-2 at 4.2^{o}K, H_o = 0, 9.09 kG, 22.7 kG, 27.27 kG. Dashed lines indicate regions of instability.

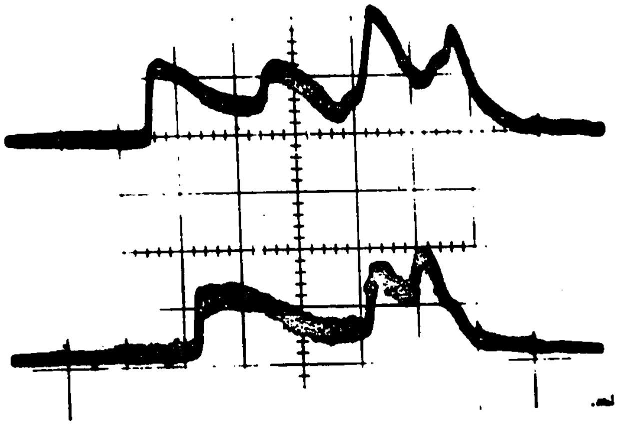

(a)

H = 4.82 kG, <4 πM> = 3.83 kG

upper = .02V/div, 0.2 ms/div

lower = .01V/div, 0.2ms/div

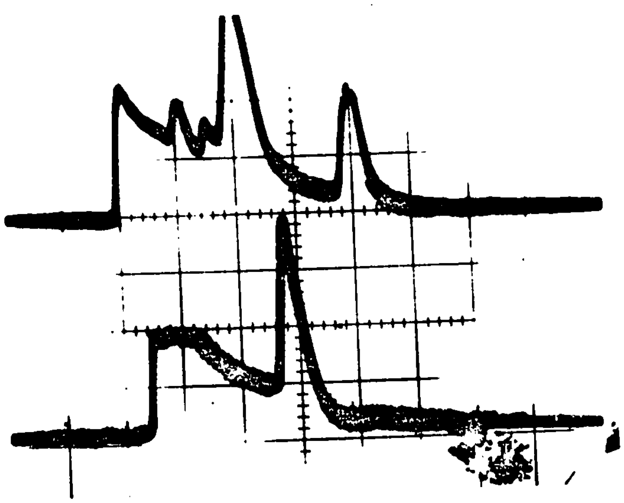

(b)

H = 5.09 kG, <4 πM> = 4.0 kG

upper = .02 V/div, 0.2 ms/div

lower = .01V/div, 0.2 ms/div

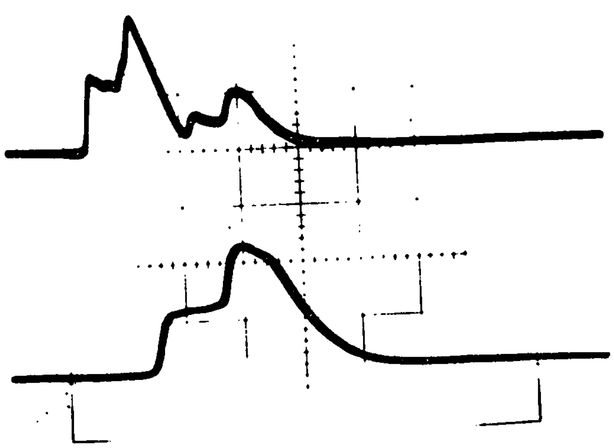

(c)

H = 6.09 kG, <4πM> = 4.55 kG

upper = 0.1V/div, 0.1ms/div

lower = .05V/div, 50μs/div

Fig. 10.3: Voltage traces in NbZr-2 for $H_o = 0$. Upper traces correspond to two pick-up coils in series (10 and 5 turns), lower traces to a single pick-up coil of 5 turns.

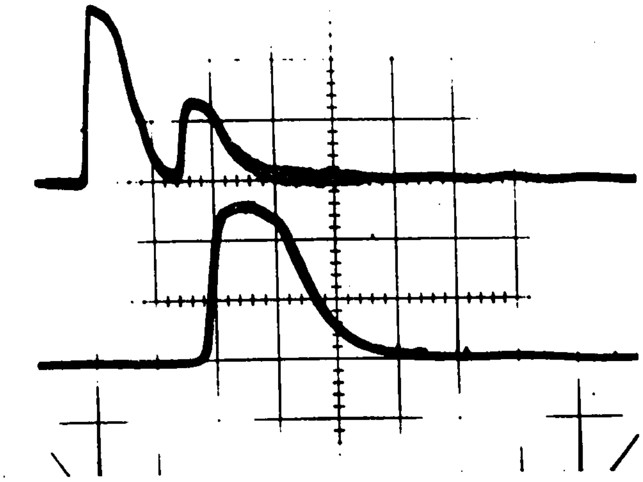

(d)

H = 6.32 kG $\langle 4\pi M \rangle$ = 4.67 kG

upper = 0.1V/div, 0.1ms/div

lower = .05V/div, 50μs/div

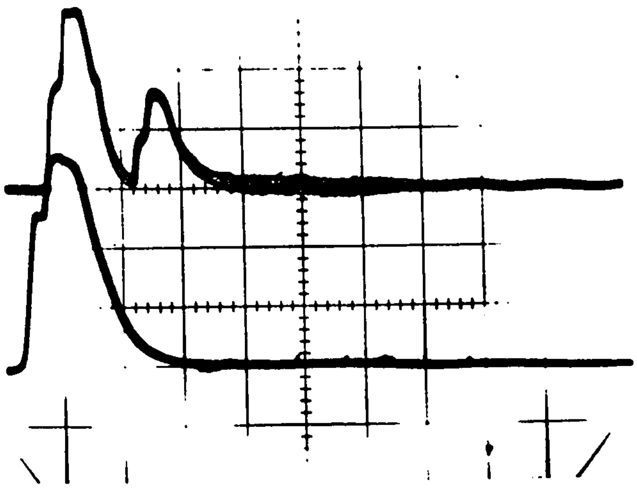

(e)

H = 6.73 kG $\langle 4\pi M \rangle$ = 4.81 kG

upper = 0.1V/div, 0.1ms/div

lower = .05V/div, 50μs/div

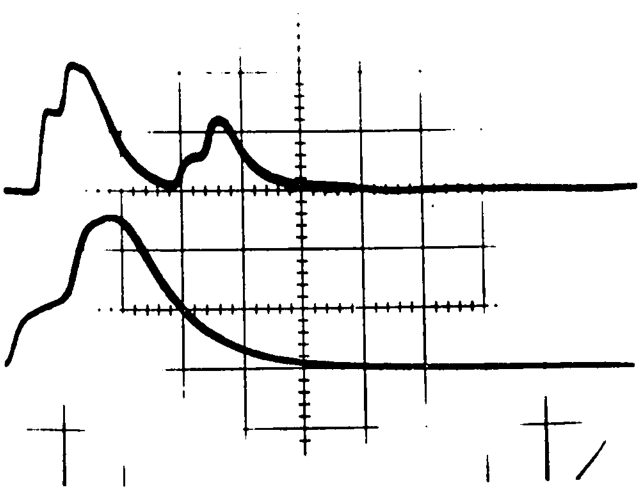

(f)

H = 7.68 kG $\langle 4\pi M \rangle$ = 5.10 kG

upper = 0.2V/div, 50μs/div

lower = 0.1V/div, 20μs/div

Fig. 10.3 (con't): Voltage traces in NbZr-2 for $H_o = 0$. Upper traces correspond to two coils in series (10 and 5 turns) and lower traces to a single coil of 5 turns.

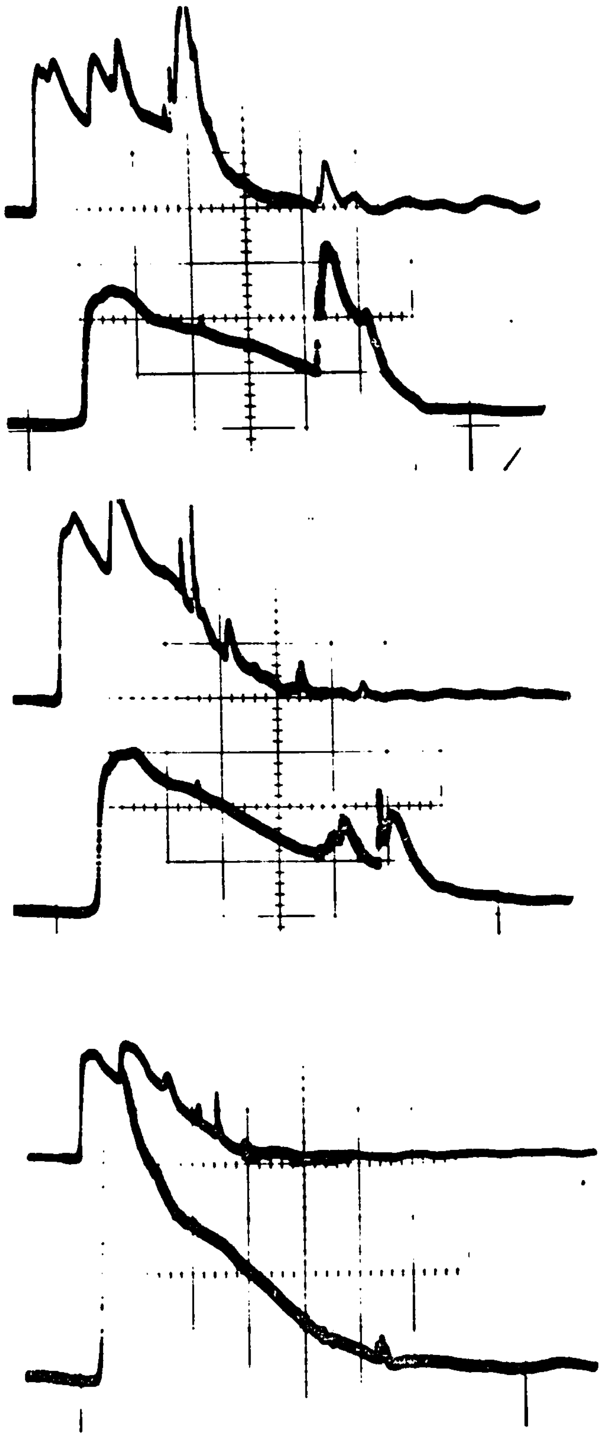

(a)

H = 30.63 kG $\langle 4\pi M \rangle$ = 2.54 kG

upper = .05V/div, 0.1ms/div

lower = .01V/div, 50μs/div

(b)

H = 30.90 kG $\langle 4\pi M \rangle$ = 2.63 kG

upper = .05V/div, 0.1ms/div

lower = .01V/div, 50μs/div

(c)

H = 31.31 kG $\langle 4\pi M \rangle$ = 2.82 kG

upper = .05V/div, 0.1ms/div

lower = .01V/div, 50μs/div

Fig. 10.4: Voltage traces in NbZr-2, for H_o = 27.27 kG. Upper traces correspond to two coils in series (10 and 5 turns), and lower traces to a single coil of 5 turns.

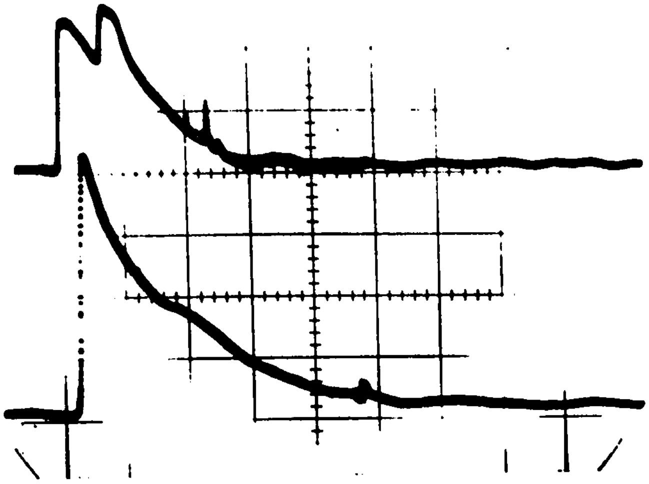

(d)

H = 31.67 kG <4πM> = 2.95 kG

upper = .05V/div, 0.1ms/div

lower = .02V/div, 50μs/div

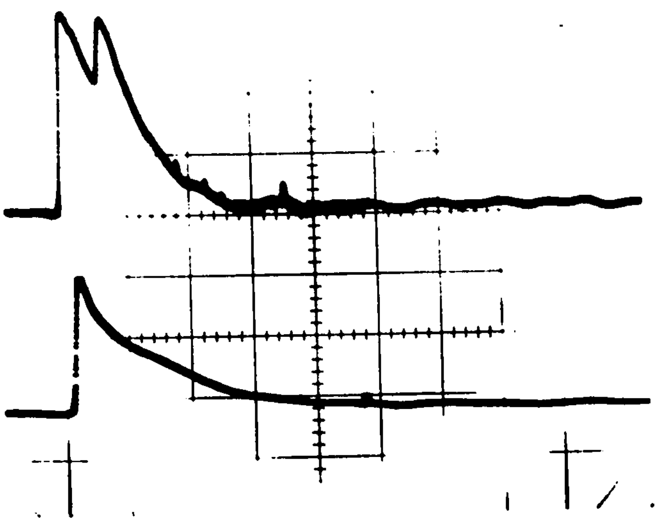

(e)

H = 32.17 kG <4πM> = 3.12 kG

upper = .05V/div, 0.1ms/div

lower = .05V/div, 50μs/div

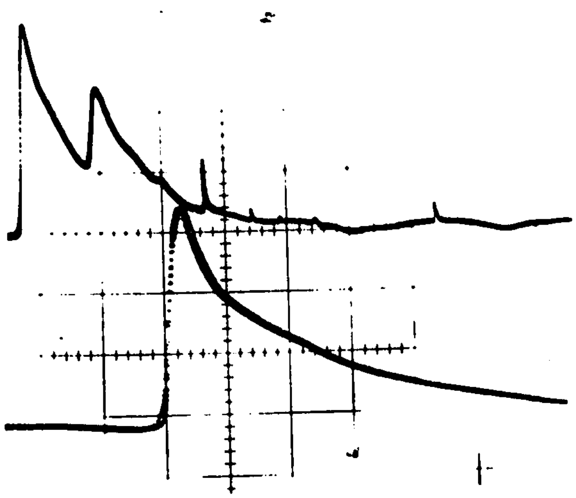

(f)

H = 34.49 kG <4πM> = 3.42 kG

upper = 0.1V/div, 50 s/div

lower = .05V/div, 20μs/div

Fig. 10.4 (con't): Voltage traces in NbZr-2 for H_o = 27.27 kG. Upper traces correspond to two coils in series)10 and 5 turns) and lower traces to a single coil of 5 turns.

A careful examination of our data reveals that for those samples where structure is encountered, the configuration of the individual pulses changes in a systematic way with position on the magnetization curve along which the flux jump is triggered. Figures 10.3 and 10.4 present the evolution of pulse shapes for the NbZr-2 sample for flux jumps triggered along two different magnetization curves. The magnetization curves are given in figure 10.2. From an examination of a particular series of pulses it appears that the spikes or peaks tend to coalesce, the irregular structure becomes less pronounced and the pulse shape assumes a smoother appearance as the flux jump is triggered further away from the region of stability. This behaviour was also observed in other samples although the structures in these samples were less pronounced.

III DISCUSSION AND CONCLUSION

Wertheimer and Gilchrist (Wertheimer 67) found in their work that for a disc in a transverse field, flux jumps do not generally penetrate the sample in a symmetrical way. They observed, instead, partial flux jumps occurring in different sections of the disc in succession. Asymmetrical flux penetration of this type can account for the irregular kind of structure (two or more peaks or spikes) we sometimes observe during longitudinal propagation. Figure 10.5(a) shows a cylinder along which two partial flux jumps have occurred.

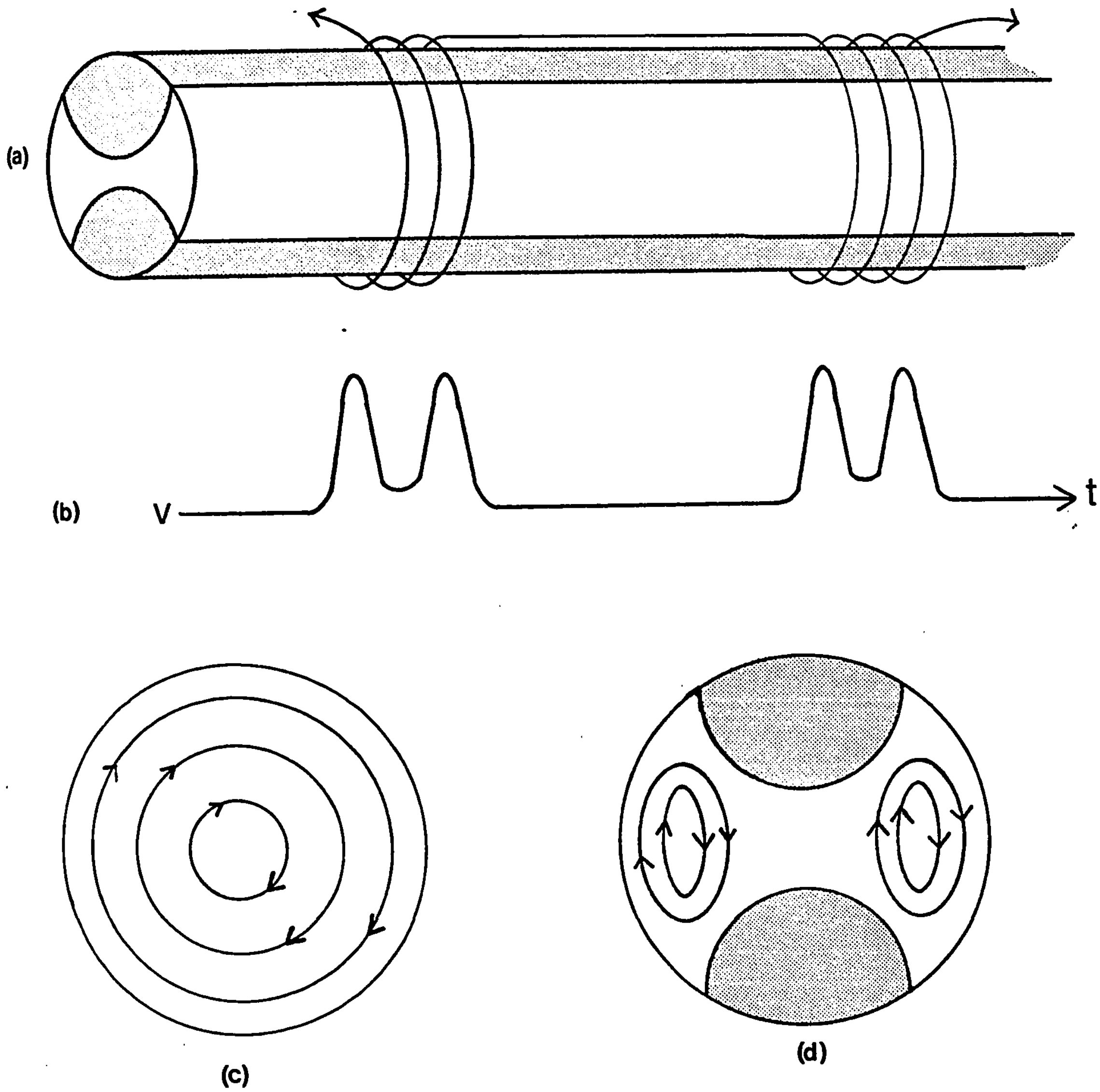

Fig. 10.5: Schematic representation of a flux jump consisting of two flux penetration regions (shaded areas) propagating along a cylinder (a). If these two regions propagate at different times they give rise to two voltage peaks from each pick-up coil (b). The initial and final current distributions are shown in (c) and (d) respectively.

The shaded areas indicate the regions where flux penetration has taken place. We visualize that initially currents were circulating azimuthally in the cylinder as shown schematically in figure 10.5(c). Suppose that when the flux jump is triggered at one end of the wire, flux penetration starts initially at a spot along the upper region of the perimeter of the cylinder. The penetration of flux in this region is accompanied by a change in the configuration of magnetic field in the neighbouring regions around the circumference of the cylinder. These changes can trigger a flux collapse in adjacent "weak" spots. In figure 10.5(d) such a weak spot is taken to lie diametrically opposite the initial region of penetration. The initial disturbance will propagate longitudinally with some characteristic velocity. The second flux jump (bottom) will also propagate longitudinally with the same characteristic velocity. Each disturbance or region of flux collapse travelling down the wire will give rise to a voltage peak as it passes through a pick-up coil. The time elapsed between the onset of these two disturbances will determine the spacing between the neighbouring peaks on the oscilloscope record of the event (figure 10.5(b)). The number of voltage peaks seen by a single coil should provide an indication of the number of disturbances occurring in succession.

The final current distribution after an incomplete flux jump where two regions of flux penetration propagated along the cylinder is shown schematically in figure 10.5(d). In the simple case we have envisaged the final profile of field and currents consists of two macrovortices of current. This situation we have postulated is very similar to the formation of a row of macrovortices along a cylinder in a transverse field, observed by Iwasa and Williams (Iwasa 68). The fact that a non-negligible magnetization still remains in our specimens after flux jumps where considerable structure is registered and which occurred near the limit of stability provides support for the picture we have proposed.

Voltage pulses generated by flux jumps triggered far from the limit of stability tend to be less irregular in appearance and exhibit a smooth and continuous shape. Here the entire periphery and an appreciable fraction of the volume of the cylinder is on the verge of flux collapse. As a consequence a perturbation (particularly a hefty perturbation), triggers local disturbances at many "weak" spots almost simultaneously. Hence the actual event is not very dissimilar from the ideal cylindrically symmetric collapse introduced in our calculations.

CHAPTER XI

RELATION BETWEEN THE RATE OF RADIAL FLUX COLLAPSE AND THE VELOCITY OF LONGITUDINAL PROPAGATION

I. INTRODUCTION

In chapter VIII we have developed the thesis that flux jumps propagate along type II superconducting wires through electromagnetic coupling. This model implies a close relationship between the rate of radial flux collapse and the velocity of longitudinal propagation. This view was seen to be consistent with the variation of velocity with $<4\pi M>$ observed for a variety of situations in a large number of samples (chapter IX).

In this chapter we explore quantitatively the relation between the velocity V and the relaxation time τ_R for a large number of flux jumps triggered in samples of different materials. The experimental values of τ_R are extracted from the voltage pulses photographed during measurements of the longitudinal propagation of flux jumps. We recall that we arbitrarily defined τ_R as the width of the voltage pulses at 1/e of maximum height. In chapter VI we have shown that τ_R measured during longitudinal propagation closely corresponds to and behaves like the "true" τ_R observed when the radial flux collapse occurs simultaneously along the entire specimen.

Walker and Hulm (Walker 66) have shown that V_ℓ/V_r, the ratio of the longitudinal velocity V_ℓ to the radial velocity V_r (where V_r was deduced from the width of the voltage peaks) was approximately constant for flux jumps triggered in NbZr wires of different diameters. We therefore assume, as a starting point, that the velocity V is inversely proportional to the relaxation time τ_R

$$V = k/\tau_R \tag{11.1}$$

and explore to what extent the value of k is a constant.

In section II we present values of $k = V.\tau_R$ for a large number of flux jumps triggered along a number of magnetization curves for various samples. We find that although the materials studied differ considerably in their characteristics (such as normal state resistivity, diameter, H_{c2}, T_c, etc) and the velocity V spans more than two orders of magnitudes, the product $V.\tau_R$ is constant within a factor of ~ 2 for most of the data for the different samples. Further, we note that for any given sample, the value of $V.\tau_R$ tends to increase significantly near the limit of stability. We relate this behaviour to the characteristics of the radial flux collapse and therefore to changes in the shape of the pulses $\partial\phi/\partial t$ vs. t.

In section III we present values of $V.\tau_R$ for flux jumps of constant $<4\pi M>$ triggered in different fields. Again we note that for the two samples where this aspect was studied (NbTi-2, NbZr-1) the values of $V.\tau_R$ correspond closely. Further the behaviour of this quantity vs field is very similar. In particular the value $V.\tau_R$ is seen to increase appreciably in low fields. We show that this behaviour is related to a decrease in the rise time of the voltage pulse $\partial\phi/\partial t$ when the field gradients become very steep.

III RELATION BETWEEN LONGITUDINAL VELOCITY V AND τ_R FOR FLUX JUMPS TRIGGERED ALONG A GIVEN MAGNETIZATION CURVE.

In this section we show how the product $V.\tau_R$ varies as a function of external field H for flux jumps triggered in different samples along a number of selected magnetization curves.

a) Experimental Results:

Figures 11.1 through 11.5 show curves of $V.\tau_R$ vs H for several magnetization curves for the NbTi-2, NbZr-1 and NbTi-3 samples. (The pertinent magnetization curves are given in chapter IX). From examination of these curves we note that $V.\tau_R$ varies rapidly with field near the limit of stability (fields near H_o). For the ranges of field distant from this limit, $V.\tau_R$ varies slowly and is approximately equal to 0.3 ± 0.1 cm for all the samples.

Figures 11.6 through 11.8 show curves of $V.\tau_R$ for flux jumps triggered along a wide variety of magnetization curves in the V-2 and NbTi-4 samples. Although there is considerable scatter in the data,

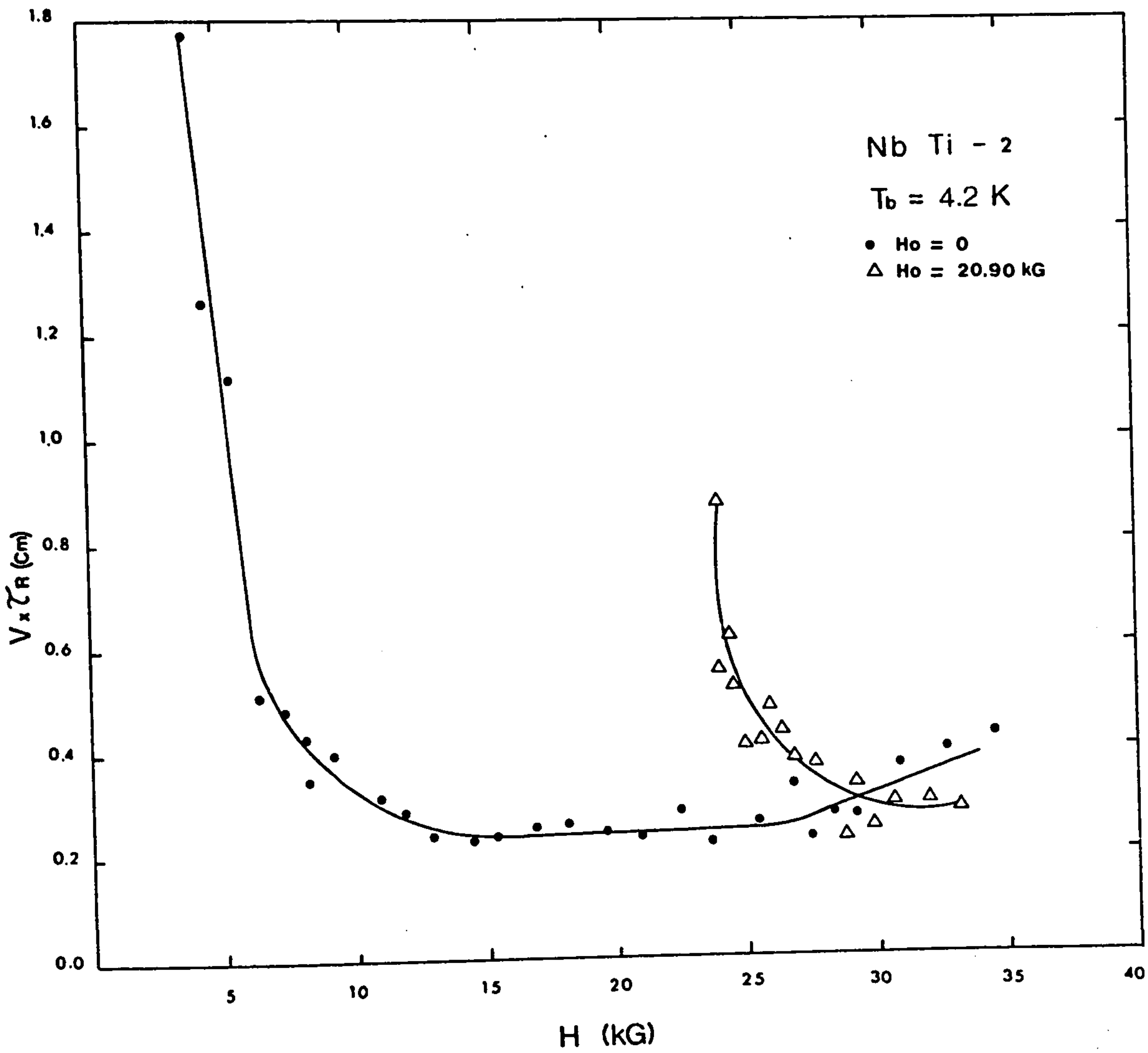

Fig. 11.1: Product V-τ_R vs H for magnetization curves where H_o = 0 and 20.9 kG in NbTi-2.

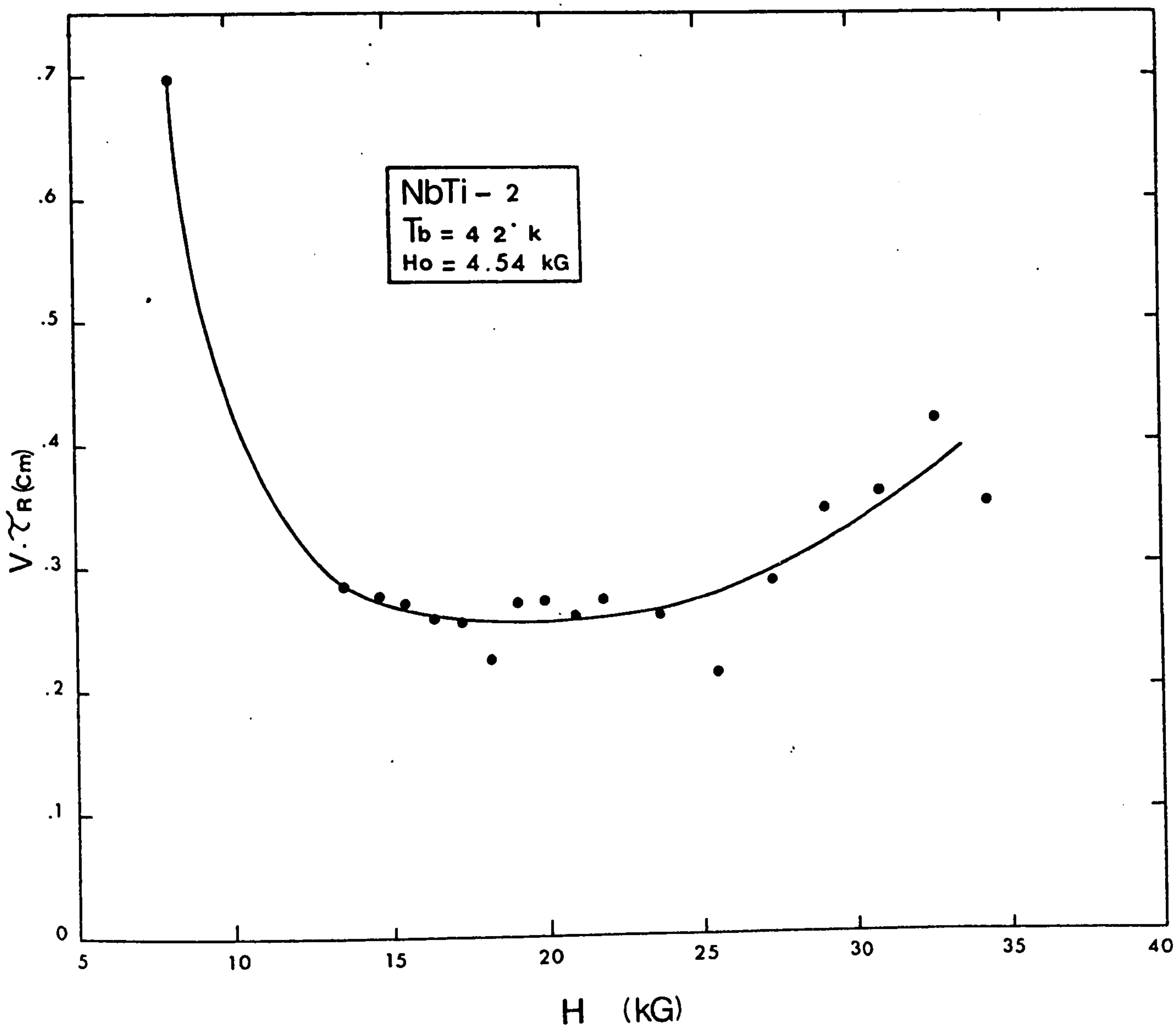

Fig. 11.2: Product $V\text{-}\tau_R$ vs H for NbTi-2 for magnetization curve H_o = 4.54 kG in NbTi-2.

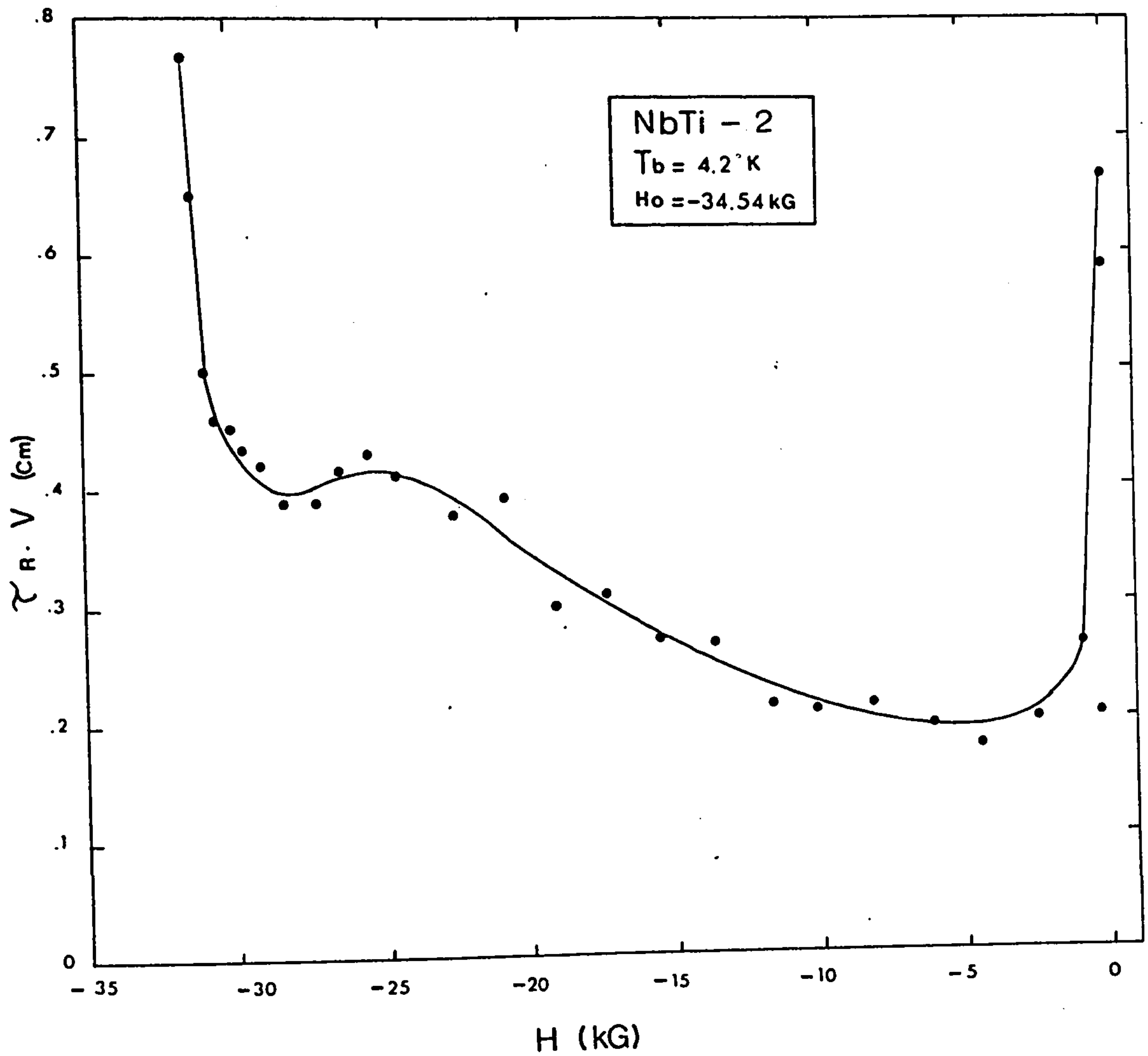

Fig. 11.3: Product $V.\tau_R$ vs H for magnetization curve H_o = -34.54 kG in NbTi-2.

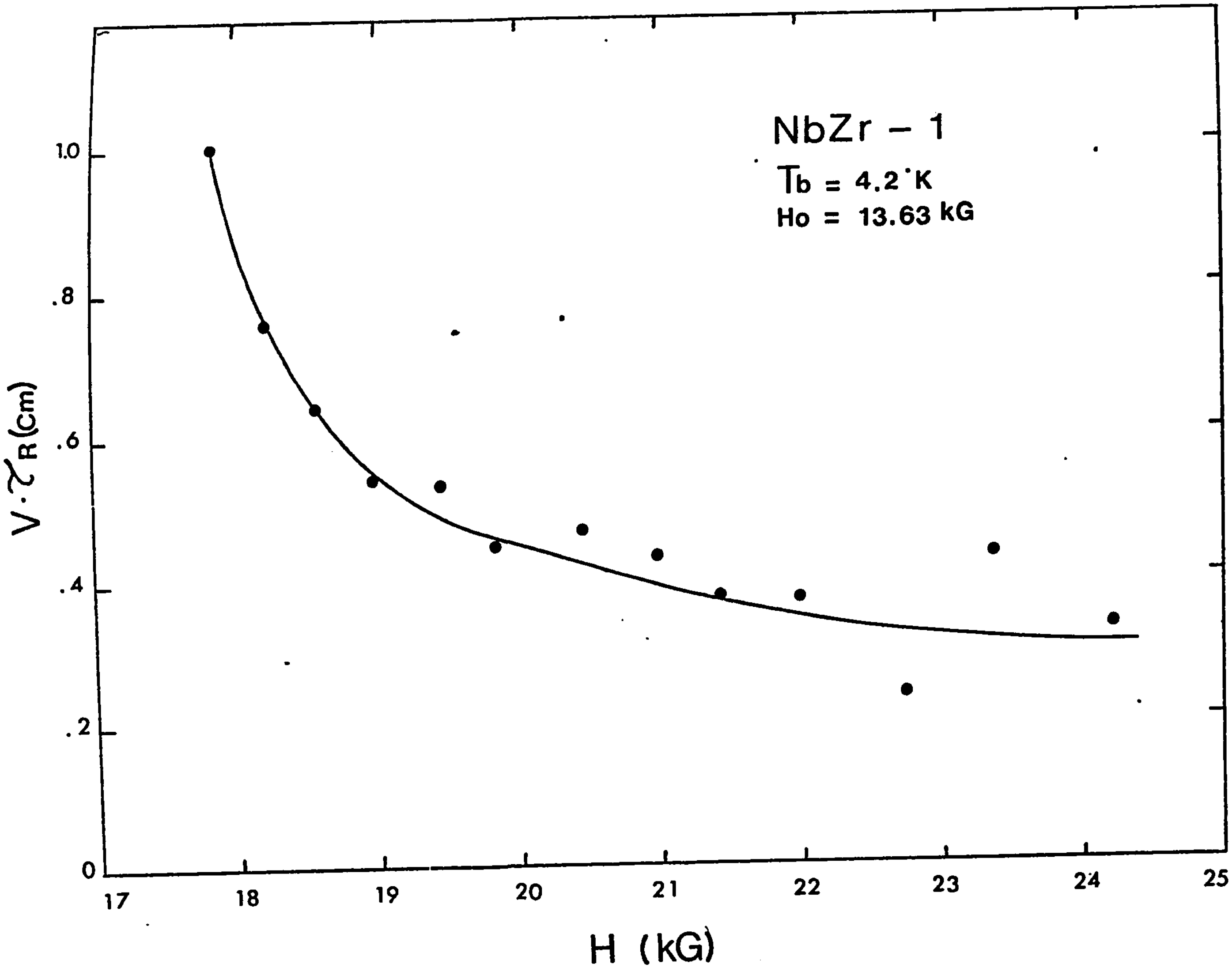

Fig. 11.4: Product $V.\tau_R$ vs H for flux jumps triggered along magnetication curve H_o = 13.63 kG of NbZr-1.

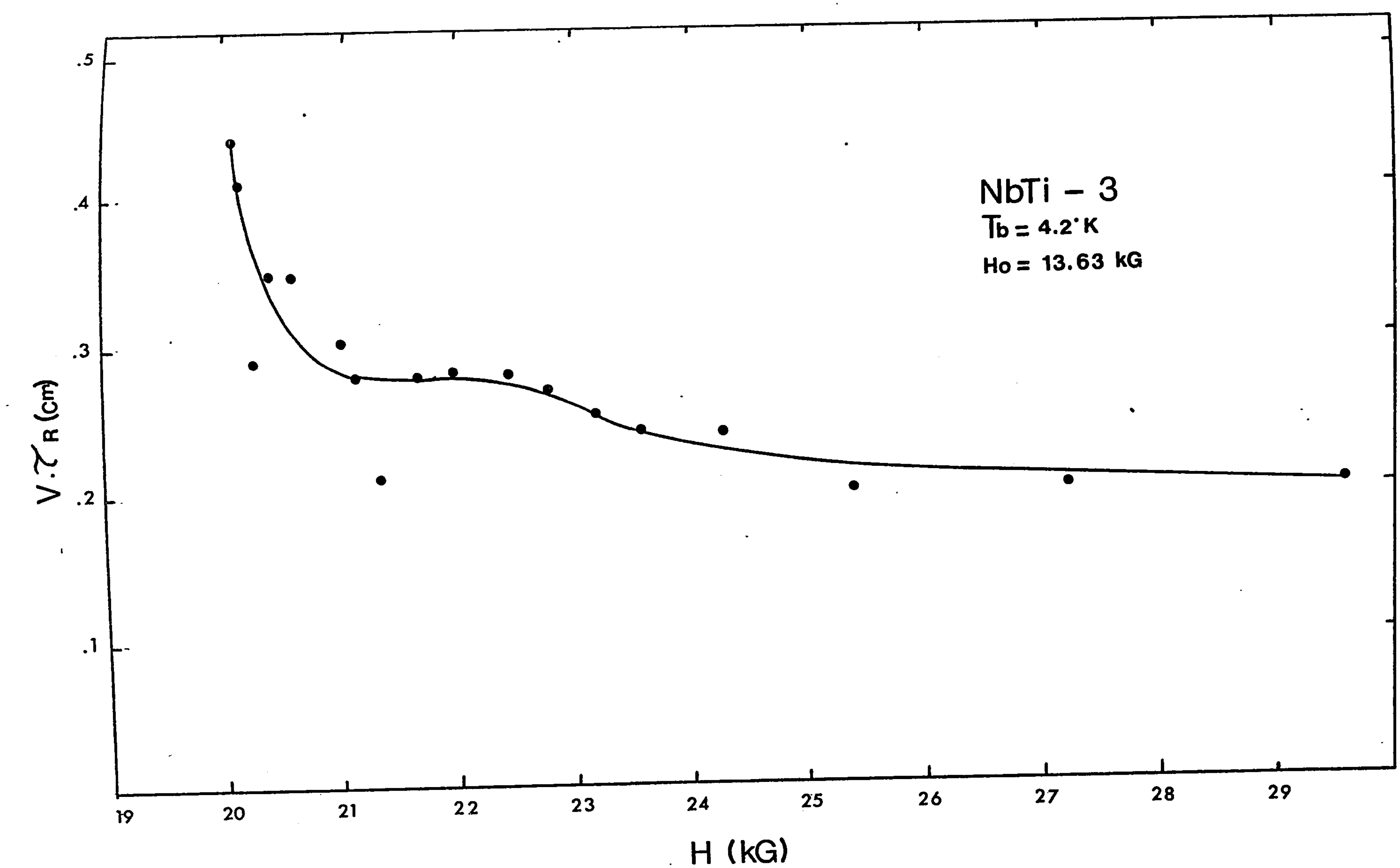

Fig. 11.5: Product $V.\tau_R$ for flux jumps triggered along magnetization curve H_o = 13.63 kG of NbTi-3.

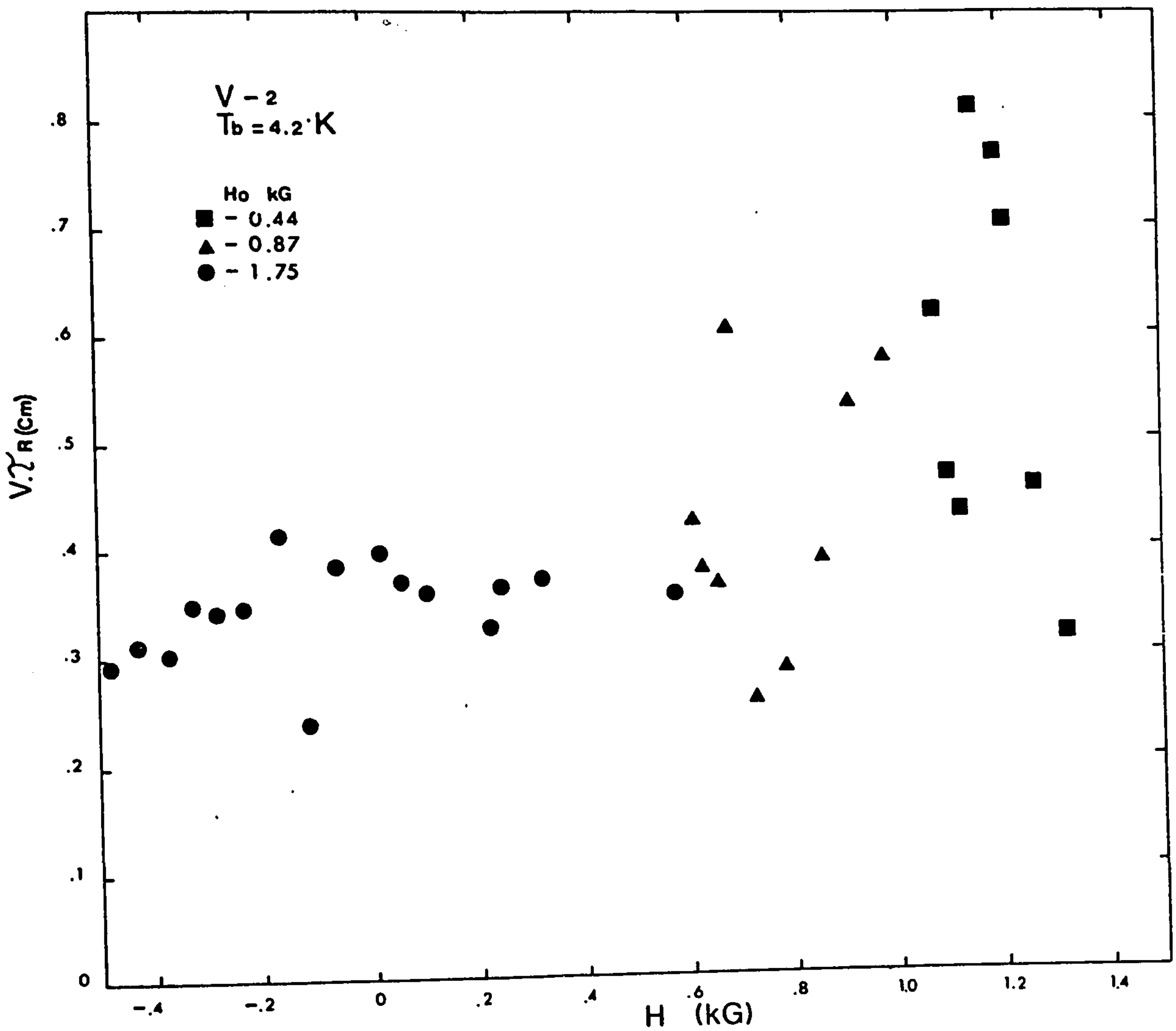

Fig. 11.6: Product $V.\tau_R$ vs H for flux jumps triggered along magnetization curves H_o = -0.44 kG, -0.87 kG and -1.75 kG in V-2 at 4.2°K.

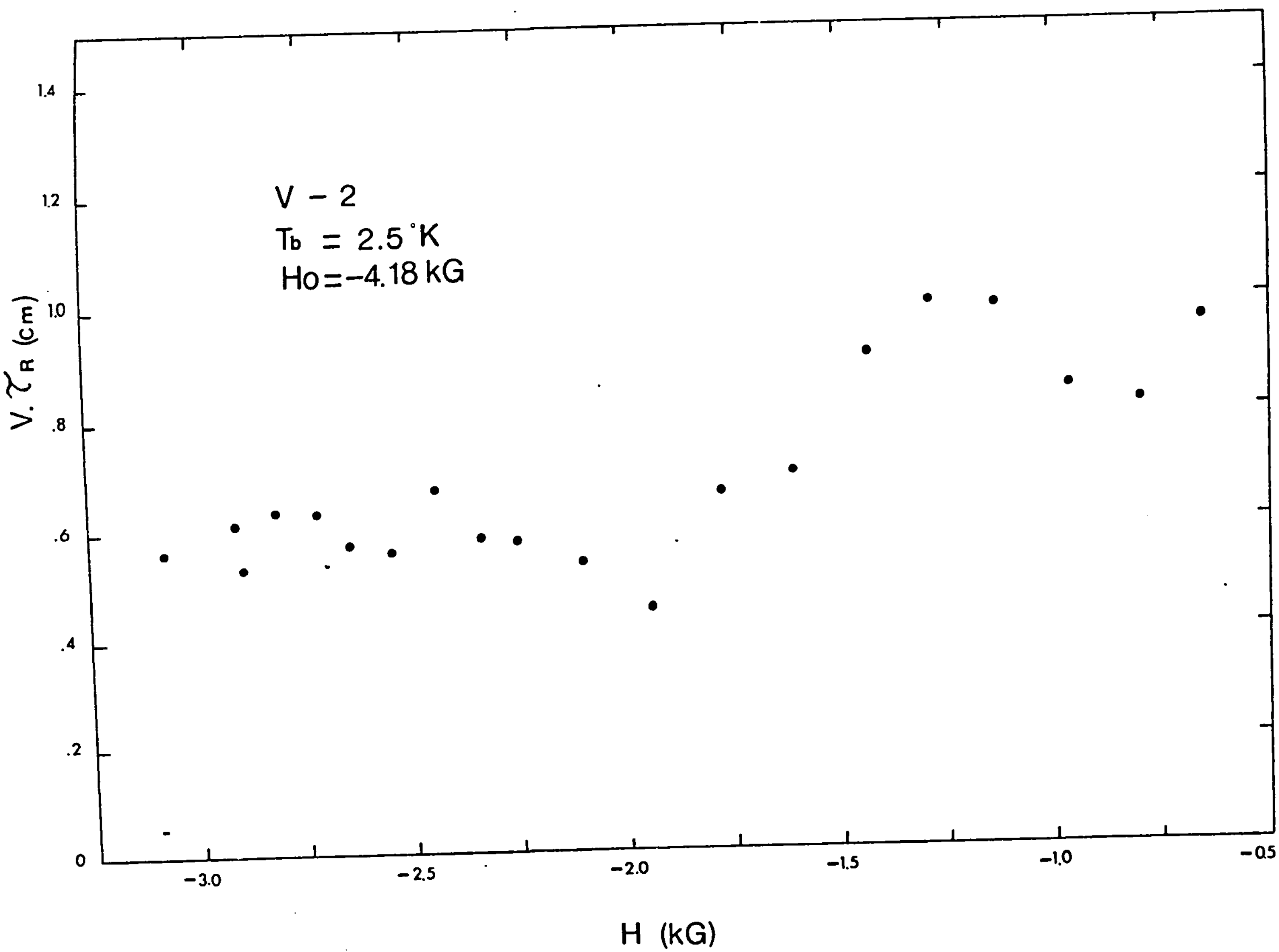

Fig. 11.7: Product $V.\tau_R$ vs H for flux jumps triggered along magnetization curve $H_o = -4.18$ kG of sample V-2 at 2.5^oK.

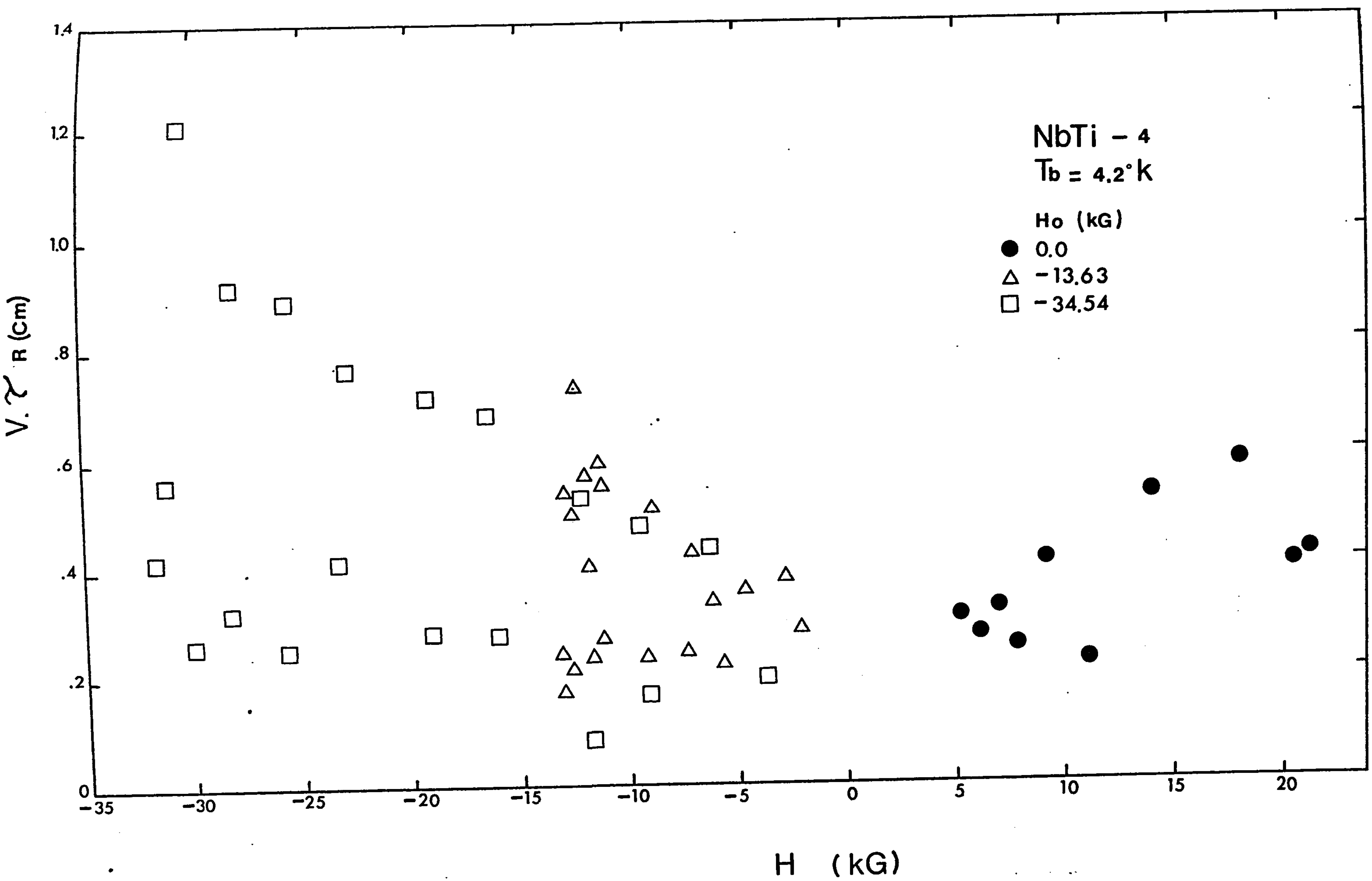

Fig. 11.8: Product $V.\tau_R$ vs H for flux jumps triggered along several magnetization curves of sample NbTi-4.

the product $V.\tau_R$ remains fairly constant over a wide range of field and is approximately the same for the two samples although their normal state resistivities differ by a factor of ~ 40.

b) Discussion:

From inspection of figures 11.1 through 11.8 we note that over broad ranges of field the value of k is nearly constant and is approximately the same for the different samples we have investigated. Further, the behaviour of k, in the ranges of field where it does vary is also very similar for the different specimens. These results indicate that the longitudinal velocity of propagation of flux jumps is intimately related to the characteristics of radial flux collapse.

As an initial attempt to relate the two phenomena we have chosen the pulse width τ_R to characterize the rate of radial flux collapse. In this respect we followed the lead of Walker and Hulm. Further, this choice, apart from its intrinsic merits, is convenient since information on τ_R is available in our photographic records of the voltage pulses measured during longitudinal propagation.

It is clear from inspection of figures 11.1 through 11.8 that the relationship

$$V = k/\tau_R$$

where k is a universal constant independent of the characteristics of the sample, is only approximate and fails to describe the behaviour of the longitudinal velocity for a number of situations. In particular we note that $V.\tau_R$ is approximately constant for fields distant from the limit of stability but increases rapidly near this limit. This feature which occurs in samples of widely varying characteristics, can be accounted for qualitatively in terms of the detailed characteristics of radial flux collapse with magnetic fields.

The pulse width τ_R provides information on the rate of radial flux collapse and is therefore intimately linked to the rate of longitudinal propagation. This quantity however does not provide a complete and unambiguous measure of the radial phenomenon. For instance, depending on the initial conditions, two pulses of equal τ_R may have significantaly different rise times. For detailed considerations we refer the reader to chapter IV (figure 4.20) where the results of calculations of voltage pulses for a variety of initial situations are presented.

We now summarize the pertinent features of this analysis. Consider two flux jumps where the initial magnetization $<4\pi M>$ and average induction $<B>$ are comparable but where the initial field profiles are very different. Figure 11.9 depicts these two situations schematically and also shows sketches of the corresponding voltage pulses $\partial\phi/\partial t$ when the flux jumps occur.

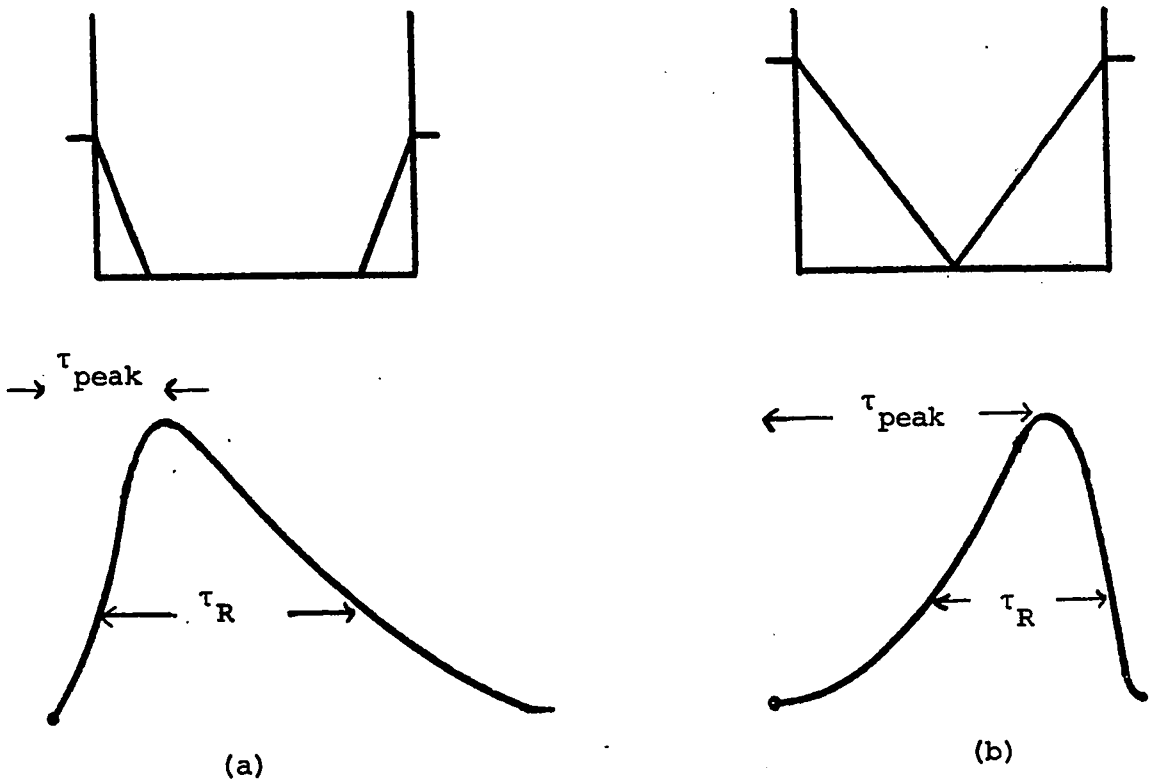

Fig. 11.9: Schematic representation of voltage pulses calculated for steep (a) and shallow (b) gradients of field. τ_{peak} is defined as the time required for $\partial\phi/\partial t$ to reach a maximum.

The pulse width τ_R is approximately the same for the two cases but the peak in the pulse occurs much earlier for the situation where the field profile is steeper (figure 11.9(a)). We note that the latter kind of profile is of the type encountered near the limit of stability as a magnetization curve is generated. We therefore attribute the increase in $V.\tau_R$ observed in the region near the limit of stability to the fact that, in this range, τ_R is not an appropriate measure of the rate of radial flux collapse. As a consequence, in these instances, this parameter does not relate to the rate of longitudinal propagation.

In order to distinguish the two kinds of situations just described we introduce a new time constant τ_{peak} where τ_{peak} is defined as the time required for the maximum (or peak) value of $\partial\phi/\partial t$ to be reached. Qualitatively it is reasonable to expect that in situations where τ_R is comparable, the longitudinal velocity will be larger when τ_{peak} is small since in this case the radial collapse of flux occurs initially at a faster rate.

Unfortunately, the quantity τ_{peak} cannot be monitored in the measurements of the longitudinal velocity. As a consequence in order to establish the relationship

$$V = k'/\tau_{peak}$$

(where k' is a universal constant independent of the characteristics of the material) we have to proceed in an indirect manner. We now outline one approach we have used to explore this point and establish the validity of the expression $V.\tau_{peak} = k'$.

We have selected a particular magnetization curve for the NbTi-3 sample (where H_o = 13.63 kG) and reproduced this curve in the context of the Bean critical state model. For the sequence of field profiles along this theoretical magnetization curve we have calculated the two quantities τ_R and τ_{peak}. The analytical details of such calculations are discussed in chapters IV and V. Figure 11.10 shows the ratio τ_R/τ_{peak} vs H calculated using this approach. A comparison of this figure with the corresponding experimental curve of $V.\tau_R$ (figure 11.5) shows that the two curves behave similarly. We may therefore conclude that τ_{peak} provides a better measure of longitudinal velocities than τ_R both away and in the region near the limit of stability. Accordingly, the increase in $V.\tau_R$ (hence k) near the limit of stability (see figures 11.1 through 11.5) appears to be due to the fact that in this region the pulse width τ_R does not reflect the effective rate of radial flux collapse adequately.

In the following section we will present further evidence that although τ_R is a useful guide for the prediction of longitudinal velocities, the quantity τ_{peak} is the appropriate and correct parameter which should be utilized.

III RELATION BETWEEN V AND τ_R FOR FLUX JUMPS OF CONSTANT MAGNETIZATION TRIGGERED IN DIFFERENT FIELDS

In this section we show how the product $V.\tau_R$ varies as a function of external field when the magnetization $<4\pi M>$ is constant in two different samples, NbTi-2, and NbZr-1. For a particular specimen and chosen $<4\pi M>$, since J_c decreases with field, the field profiles in

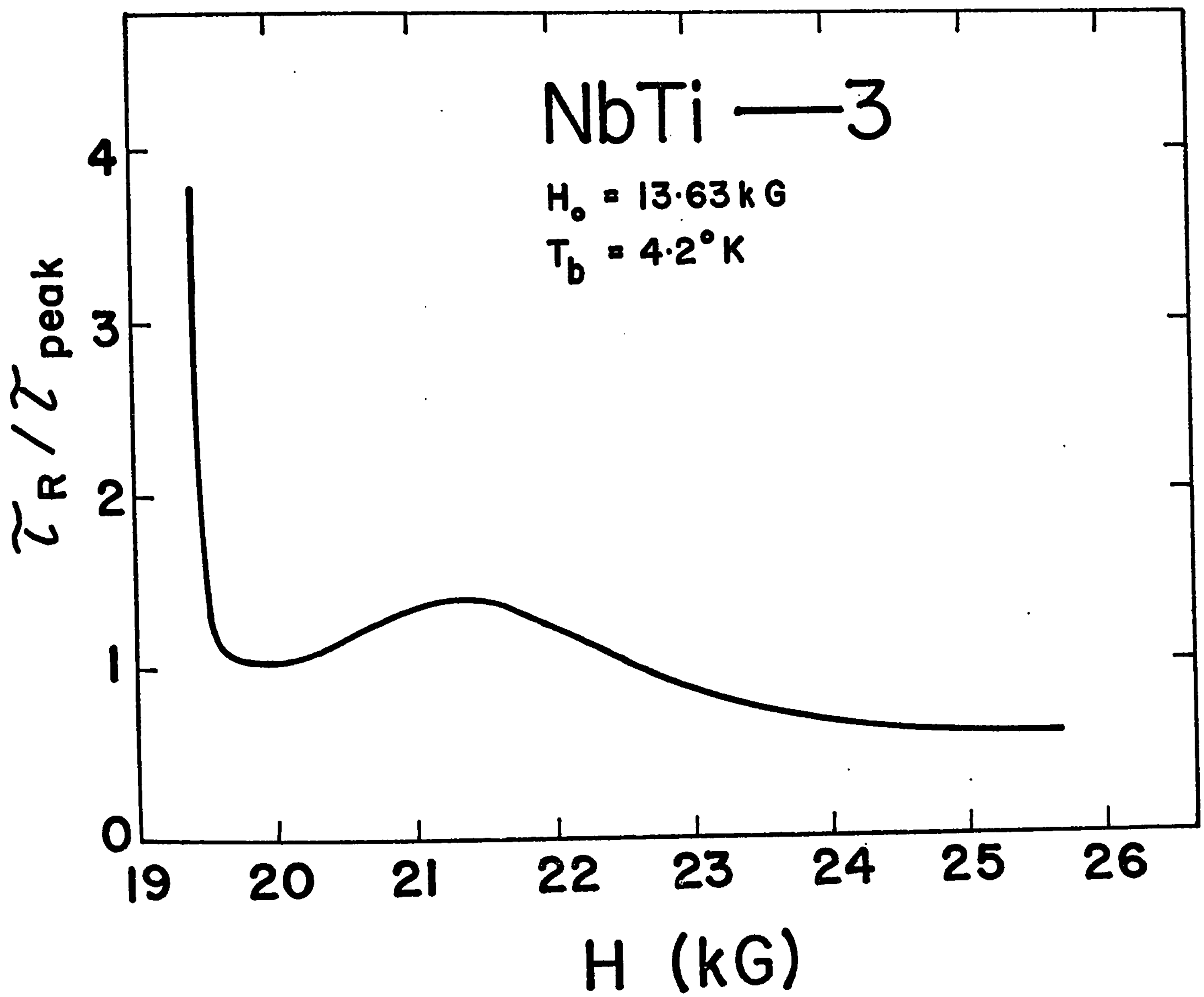

Fig. 11.10: Calculated values of τ_R/τ_{peak} for radial flux jumps triggered along magnetization curve H_o = 13.63 kG of sample NbTi-3.

low fields will be steeper than in higher fields. We examine the consequences of these changes in field profile in the relationship between the longitudinal velocity V and the parameters τ_R and τ_{peak}.

a) Experimental Results:

Figures 11.11 and 11.12 show curves of $V.\tau_R$ vs external field H for flux jumps of constant magnetization $-\langle 4\pi M\rangle$ = 4.0 kG and 4.4 kG respectively in NbTi-2. The pertinent magnetization curves are shown in figures 9.3 and 9.4. Figure 11.13 shows a curve of $V.\tau_R$ vs H for $-\langle 4\pi M\rangle$ = 4.0 kG in NbZr-1. In all three figures we note that $V.\tau_R$ is a maximum for H $\sim$ 2 kG and decreases monotonically for fields above and below this value. The magnitude of $V.\tau_R$ in a given field is similar for the two samples.

b) Discussion:

In section II we showed that although the product $V.\tau_R$ is approximately constant for flux jumps triggered in different samples some variation with the characteristics of the field profiles is encountered. This variation was attributed to changes in pulse shapes with field profile. The pulse shapes were characterized by the ratio τ_R/τ_{peak}. Since in the NbTi-2 and NbZr-1 samples the critical current density decreases rapidly with magnetic field the profiles obtained in different fields differ considerably. We emphasize that we present data where $\langle 4\pi M\rangle$ is the same.

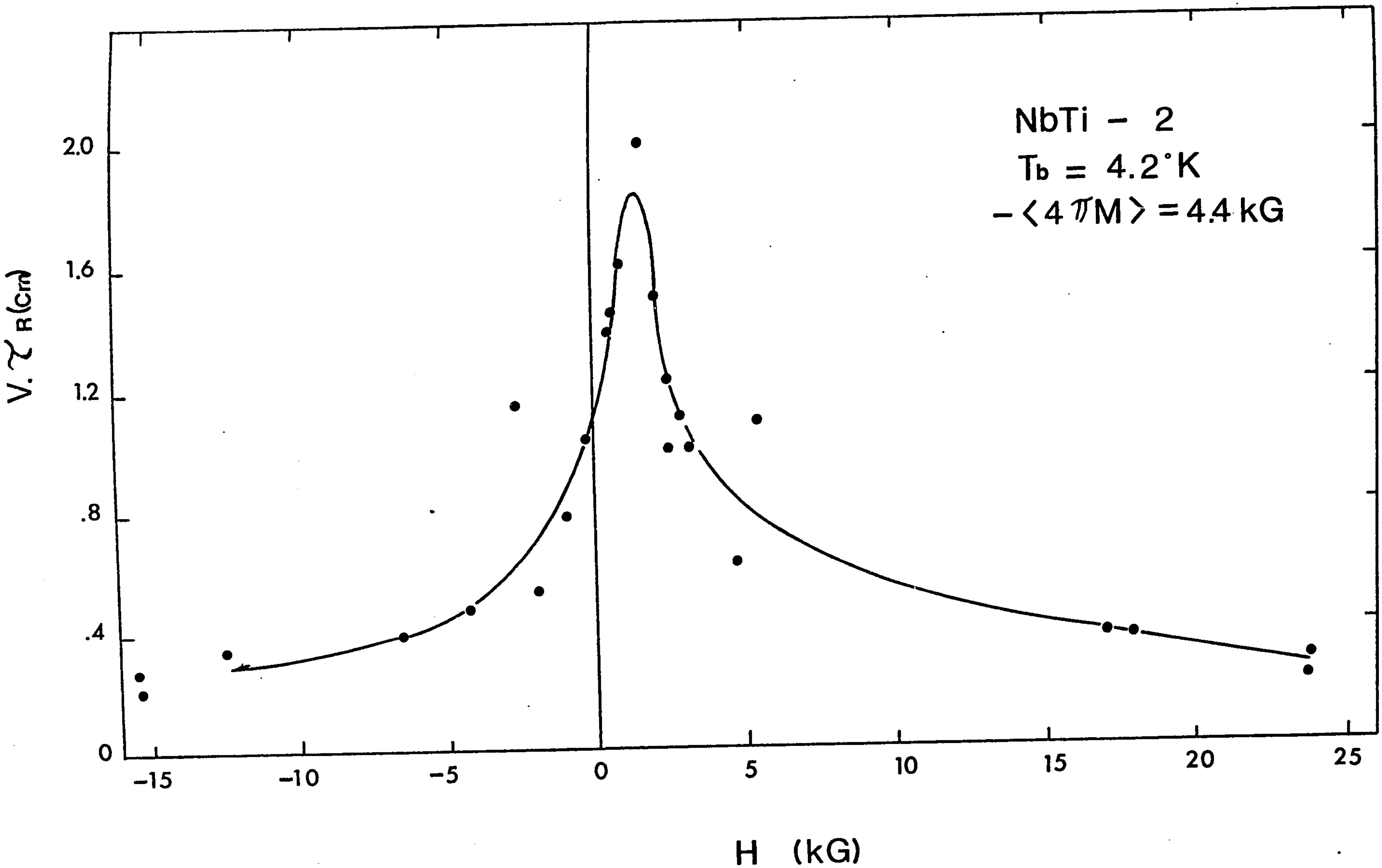

Fig. 11.11: Product $V.\tau_R$ vs external field H for flux jumps of constant magnetization $<4\pi M> = -4.4$ kG in NbTi-2.

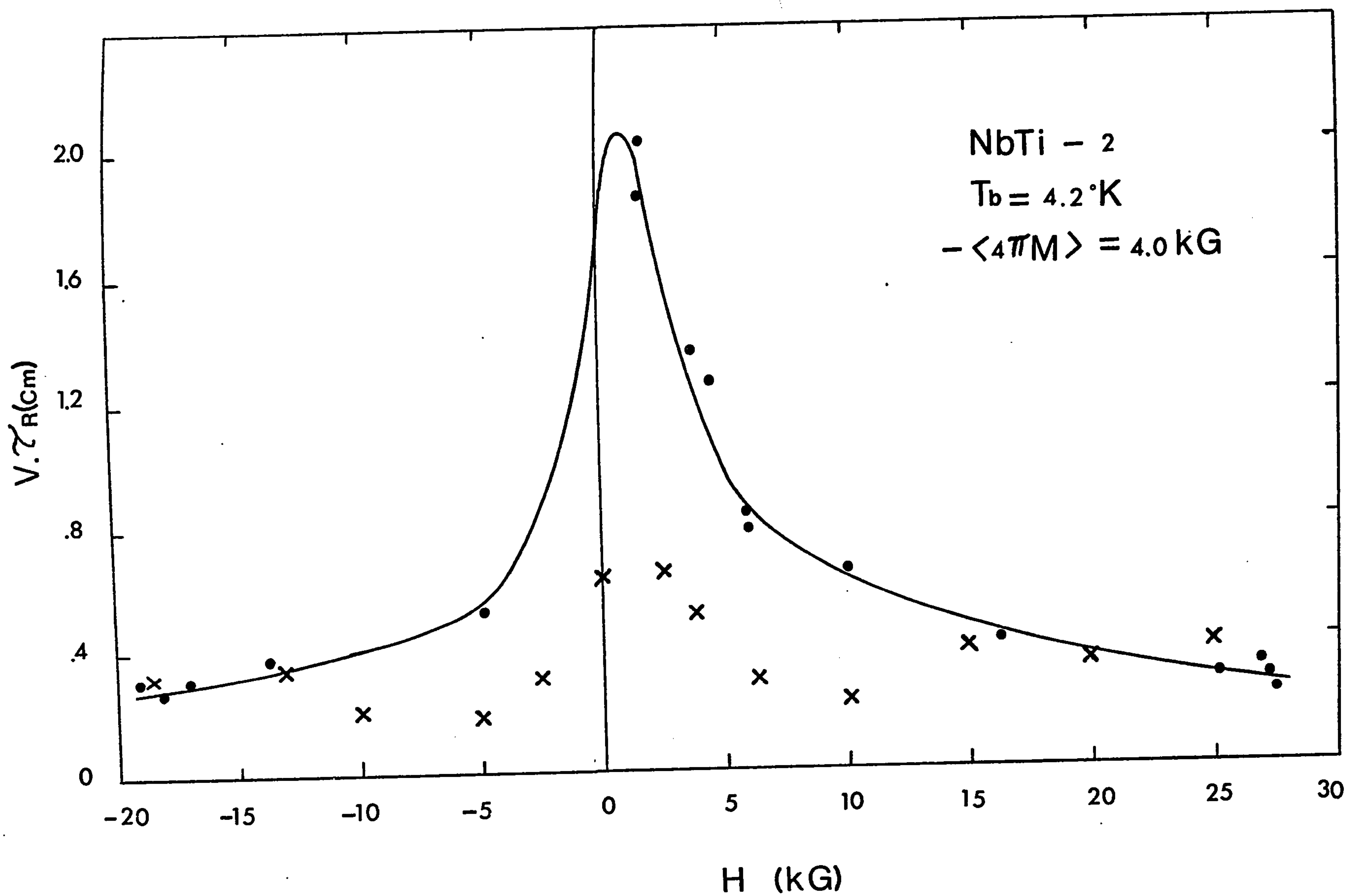

Fig. 11.12: Dots indicate experimental value of $V.\tau_R$ vs H in NbTi-2 for $-<4\pi M> = 4.0$ kG. Crosses show values of $V.\tau_{peak}$ estimated from the experimental velocity V and calculated values of τ_{peak}.

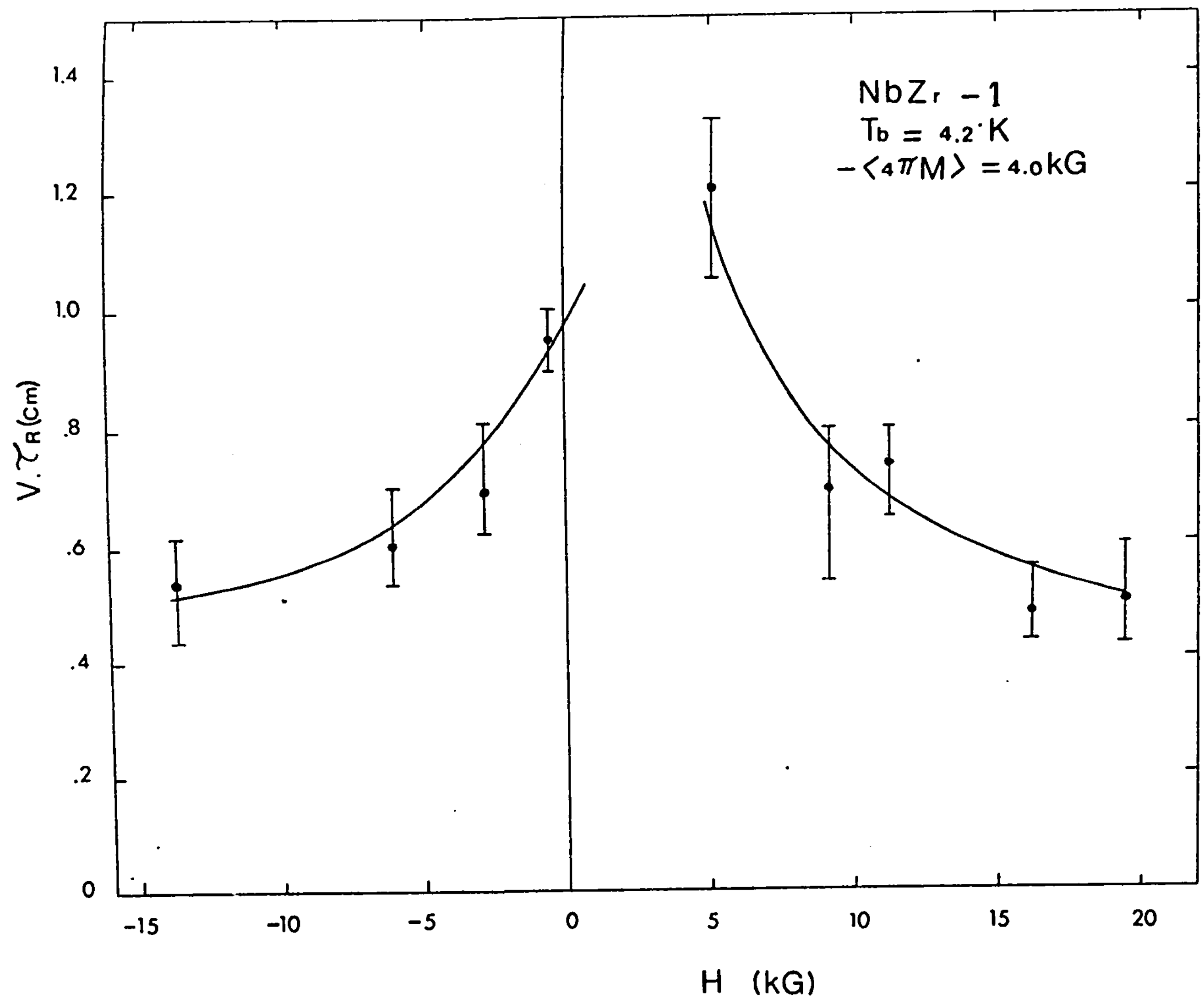

Fig. 11.13: Product $V.\tau_R$ vs H in NbZr-1 for a constant magnetization $-\langle 4\pi M\rangle = 4.0$ kG.

Figure 11.14 presents estimates of the radius of field penetration R_o/A as a function of H for the NbTi-2 sample when $-\langle 4\pi M\rangle = 4.0$ kG. To make these estimates we exploited the Bean critical state model (J_c uniform). The steepest profiles are seen to occur when H $\sim$ 2 kG, ie, in regions of field where $V.\tau_R$ is a maximum.

Since steep profiles lead to pulses with relatively rapid rise times (hence short τ_{peak}) the deviations of $V.\tau_R$ above a constant value are consistent with our discussion in the previous section of the relationship of τ_R and τ_{peak} with V.

The importance of introducing the appropriate quantity in order to predict longitudinal velocities emerges quantitatively from an examination of figure 11.15. Here we have plotted the ratio of theoretical values of τ_R and τ_{peak} for a specimen whose parameters correspond to our NbTi cylinders and where $\langle B\rangle = 2$ kG and $\langle 4\pi M\rangle = 4.0$ kG.

Using our estimates of R_o/A (figure 11.14) and our calculations of τ_R/τ_{peak} (figure 11.15) we have obtained values of $V.\tau_{peak}$ vs H applicable to the NbTi-2 sample (see x's in figure 11.12). It is encouraging to note that the results lie approximately along a horizontal line although this calculation neglects contributions due to changes in the average magnetic induction $\langle B\rangle$, since our calculations of τ_R/τ_{peak} are for constant $\langle B\rangle$. Introducing the dependence of τ_R/τ_{peak} on $\langle B\rangle$ should lead to smaller variations of $V.\tau_{peak}$ with field.

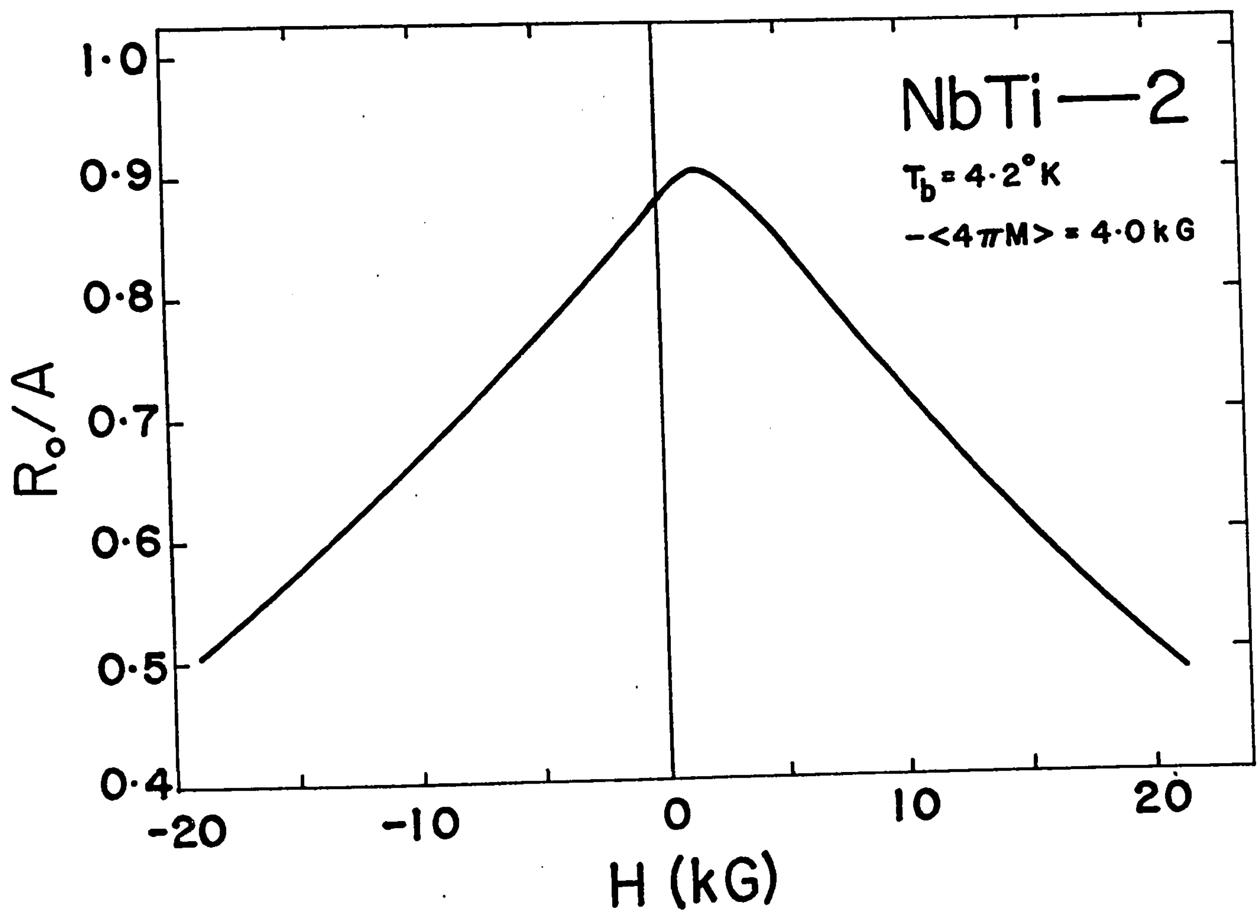

Fig. 11.14: Radius of field penetration R_o/A vs H in sample NbTi-2 when $-<4\pi M> = 4.0$ kG. These values were estimated with the Bean critical state model (J_c uniform).

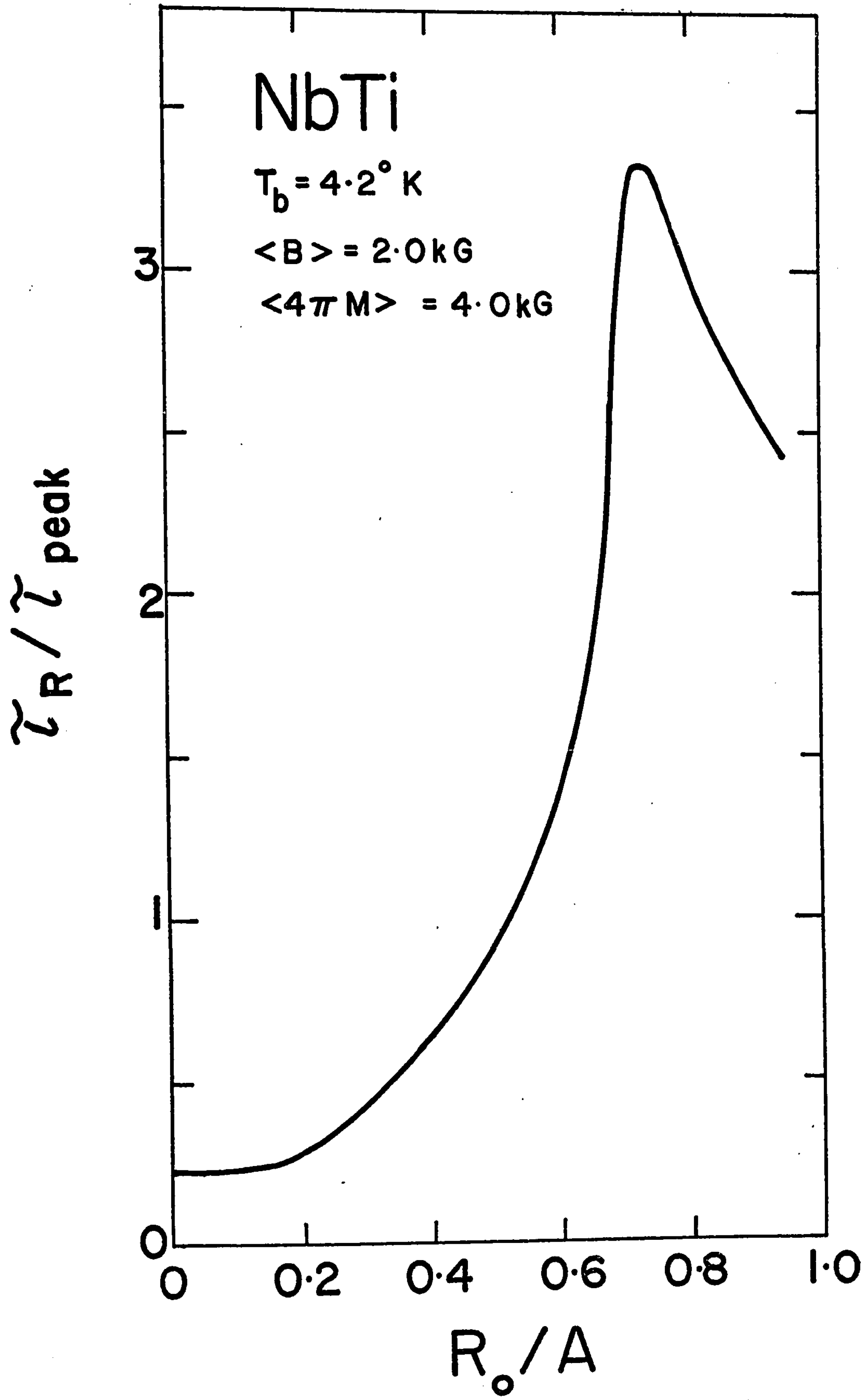

Fig. 11.15: Calculated value of τ_R/τ_{peak} as a function of profile steepness R_o/A for radial flux jumps in a NbTi cylinder when <B> = 2.0 kG and <4πM> = 4.0 kG.

Thus, from consideration of the nature of the profiles prevailing here (see figure 11.14) we can qualitatively and quantitatively relate the rises in $V.\tau_R$ at low fields (see figures 11.11, 11.12, and 11.13) to the steepness and depth of the profiles and hence to the result that τ_R/τ_{peak} is correspondingly large. We expect that graphs of $V.\tau_{peak}$ instead of $V.\tau_R$ in figures 11.11 and 11.13 would also yield nearly horizontal lines of the same height. Unfortunately, as mentioned earlier, we cannot determine τ_{peak} from our measurements of longitudinal velocities. We have not deemed it worthwhile to undertake similar calculations to that just outlined.

IV. CONCLUSION

In this chapter we have explored a simple relation between the longitudinal velocity of propagation of flux jumps V and the radial relaxation time τ_R. Our results indicate that for samples having widely different characteristics (normal state resistivities, and H_{c2} which differ by an order of magnitude) the relation $V = k/\tau_R$ where k is a universal constant is approximately valid. The values of k for the different samples and various sets of data agree closely. This relation however fails to describe the detailed variations of velocity with changes in magnetic profiles and field.

In section II we showed that the product $V.\tau_R$ (or k) is significantly larger for any given sample when flux jumps are triggered near the limit of stability. In section III we saw that k depends on magnetic field in cases where the magnetization $<4\pi M>$ is held constant. These features can however be related to changes in the characteristics of radial flux collapse with magnetic profile. Large values of $V.\tau_R$ were shown to correspond to large values of the ratio τ_R/τ_{peak}. This correspondence indicates that, for a given value of τ_R, voltage pulses with fast rise times (large values of τ_R/τ_{peak}) lead to larger velocities than pulses with lower rise times.

Since $V.\tau_R$ and τ_R/τ_{peak} vary similarly we conclude that

$$V.\tau_R \propto \tau_R/\tau_{peak}$$

hence

$$V = k'/\tau_{peak}$$

The value τ_{peak}, however, cannot be extracted from measurements of longitudinal propagation. As a consequence we could not verify experimentally that $V.\tau_{peak}$ equals a universal constant for all the situations investigated for the samples we studied. The results presented in this chapter indicate however that the longitudinal velocity of propagation of flux jumps is entirely determined by the characteristics of the radial collapse of flux. Further, we have shown that the parameter τ_{peak} encountered in the radial flux collapse provides an excellent guide to the prediction of longitudinal velocities of propagation of flux jumps.

CHAPTER XII

VARIATION OF THE LONGITUDINAL VELOCITY WITH EXTERNAL FIELD AND NORMAL STATE RESISTIVITY

I. INTRODUCTION

In part I of this thesis we have shown that the radial collapse of flux during a flux jump in type II superconductors can be described with a diffusion equation. We introduced the concept of flux flow resistivity in this diffusion equation and assumed a linear relation between electric field and current density above the critical current density J_c. The coefficient of proportionality in this relation is the flux flow resistivity ρ_f which is proportional to the normal state resistivity ρ_n and increases linearly with magnetic field H when H $<<$ H_{c2}. Keeping other variables constant, the rate of radial flux collapse is therefore proportional to ρ_n and at low fields (compared to H_{c2}) proportional to H. In chapter IV we have shown that the relaxation time τ_R is approximately inversely proportional to H at low fields. At higher fields, the decrease in enthalphy and the non linear behaviour of ρ_f with H introduces significant deviations from this law.

From these considerations we expect that the longitudinal velocity of propagation of flux jumps will increase approximately linearly with field and with normal state resistivity ρ_n. Experimentally, however, the external field cannot be varied independently in a given sample without affecting other properties such as critical current density, magnetization, field profile, etc. Similarly, it is difficult to change the normal state resistivity without causing changes in T_c, H_{c2} and J_c. In interpreting the effect of the field and normal state resistivity we will therefore have to take into consideration changes in the contributions of all the parameters affecting the characteristics of radial flux collapse.

In section II of this chapter we show how the velocity of propagation of flux jumps varies in different samples for flux jumps of constant magnetization triggered in different fields. Since J_c decreases with field these flux jumps will correspond to different magnetic profiles.

To estimate the effect of normal state resistivity ρ_n we present in section III a comparison of velocities obtained in samples of comparable enthalphy but of very different normal state resistivities.

II VELOCITY AS A FUNCTION OF EXTERNAL FIELD H

a) NbTi-4:

The hollow cylinder NbTi-4 is well suited to study the effect of external field H on the longitudinal velocity for two reasons:

i) The critical current density of this sample varies slowly with field. This can be seen from the relatively flat magnetization curve of this sample (figure 9.19). Contributions due to changes in magnetic profile with field should therefore be small in this sample.

ii) Since the sample is thin walled, the magnetization is small ($\sim$ 0.7 kG) and therefore variations of magnetic field inside this sample can be neglected even in relatively small external fields.

Figure 12.1 shows the velocity V as a function of external field H for this sample. These results were obtained by triggering flux jumps along the magnetization curves shown in figure 9.19. In all cases the sample was in the critical state ie, persistent currents were flowing throughout the entire volume of the cylinder. The magnetization is approximately constant with field and equal to $-\langle 4\pi M\rangle = 0.7 \pm 0.1$ kG. We note that the velocity increases by approximately an order of magnitude in the range of field studied.

b) NbZr-1 and NbTi-2:

In these two samples the critical current density is large (since we obtain large magnetizations) and is a rapidly decreasing function of field. We therefore expect contributions due to local

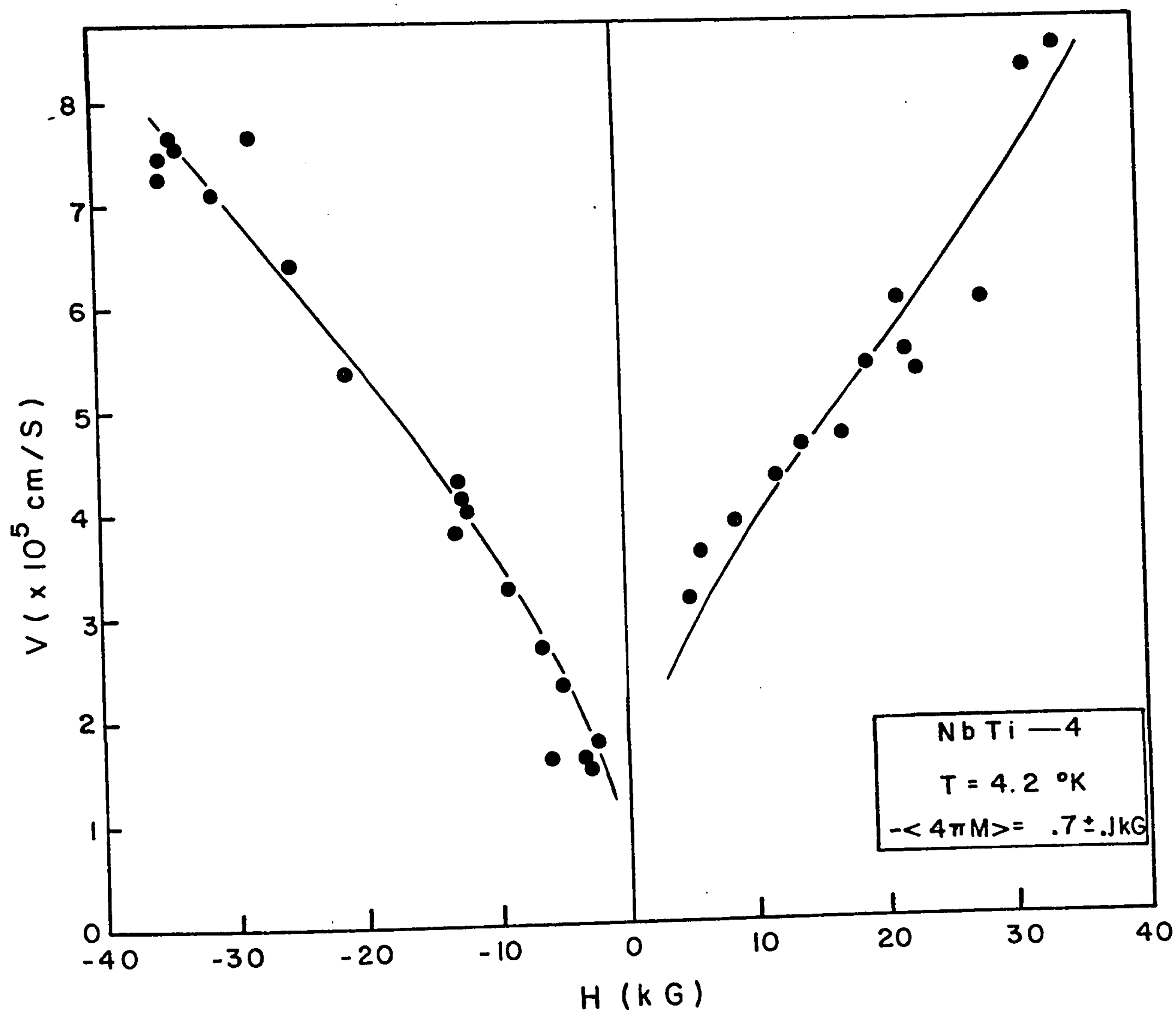

Fig. 12.1: Velocity vs H for a constant $\langle 4\pi M\rangle = 0.7 \pm 0.1$ kG in sample NbTi-4.

variations in magnetic field inside the samples and due to changing magnetic profiles with field.

Figures 12.2 and 12.3 show the velocity V vs H for sample NbZr-1 when $-\langle 4\pi M \rangle$ = 3.5 kG and 4.0 kG respectively. We note in these two figures that the velocity increases by a factor of $\sim$ 5 in the range of field studied.

Figures 12.4 and 12.5 show the velocity V vs H for sample NbTi-2 when $-\langle 4\pi M \rangle$ = 4.0 kG and 4.4 kG respectively. In these two curves we note that the velocity is a maximum in low fields H = 2 kG. In large fields H > 10 kG the velocity increases with the magnitude of the applied field.

c) <u>Discussion</u>:

The different behaviours of the velocity V vs H displayed in figures 12.1 through 12.5 for samples NbTi-4, NbZr-1 and NbTi-2 can be understood qualitatively by analysing the changes in the characteristics of radial flux collapse with external field. For a given sample, viewing the magnetization as constant in the presence of different external fields, we can identify two different contributions to the rate of radial flux collapse: 1) an increase in flux flow resistivity with H and; 2) a change in magnetic profile. The first contribution always causes an increase in the rate of radial collapse with field. The second contribution however depends on the type of field profiles encountered in different fields. If R_o/A is less than $\sim$ 0.85

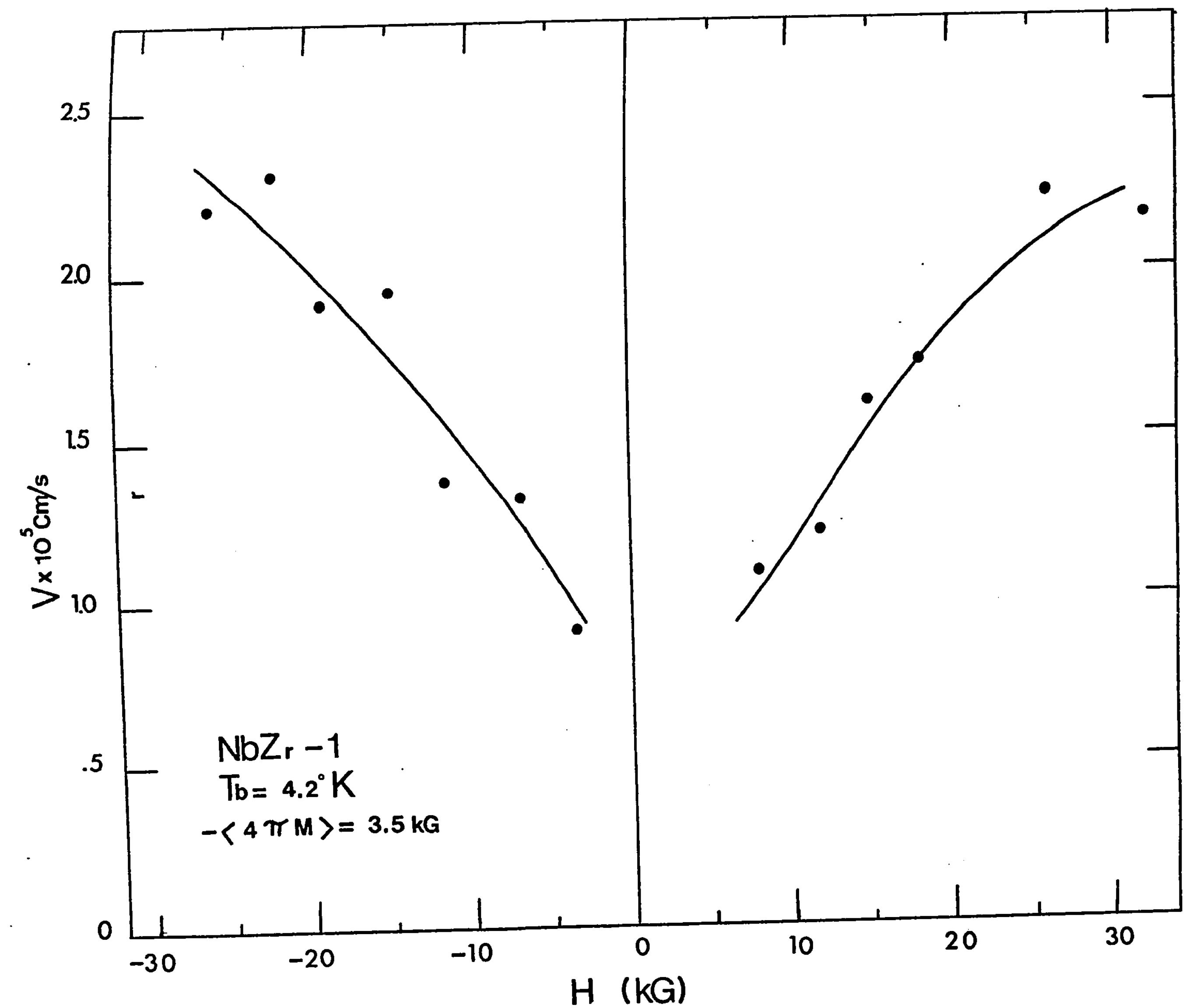

Fog. 12.2: Velocity vs H for a constant <4πM> = −3.5 kG in sample NbZr-1.

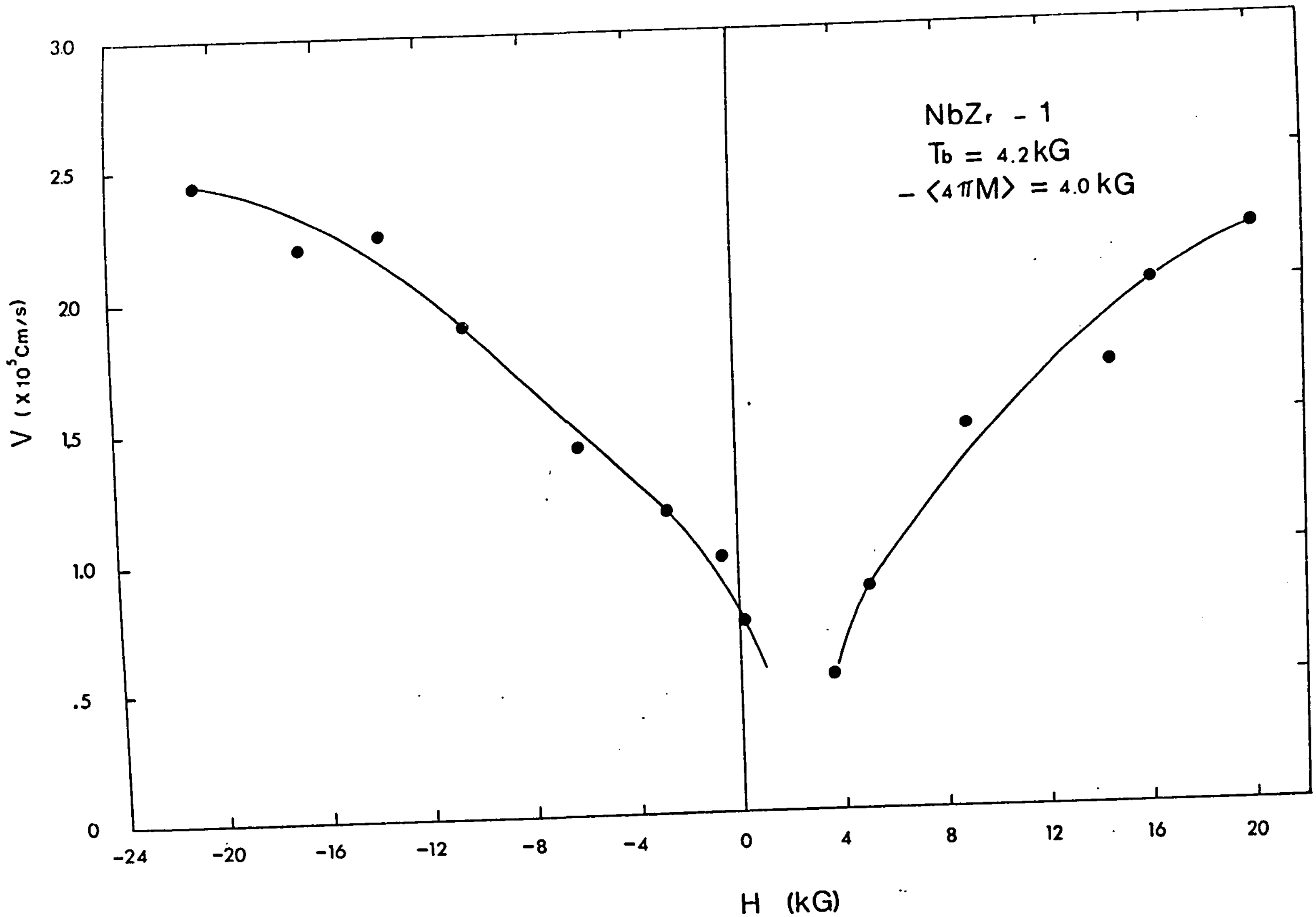

Fig. 12.3: Velocity vs H for a constant $<4\pi M>$ = -4.0 kG in sample NbZr-1.

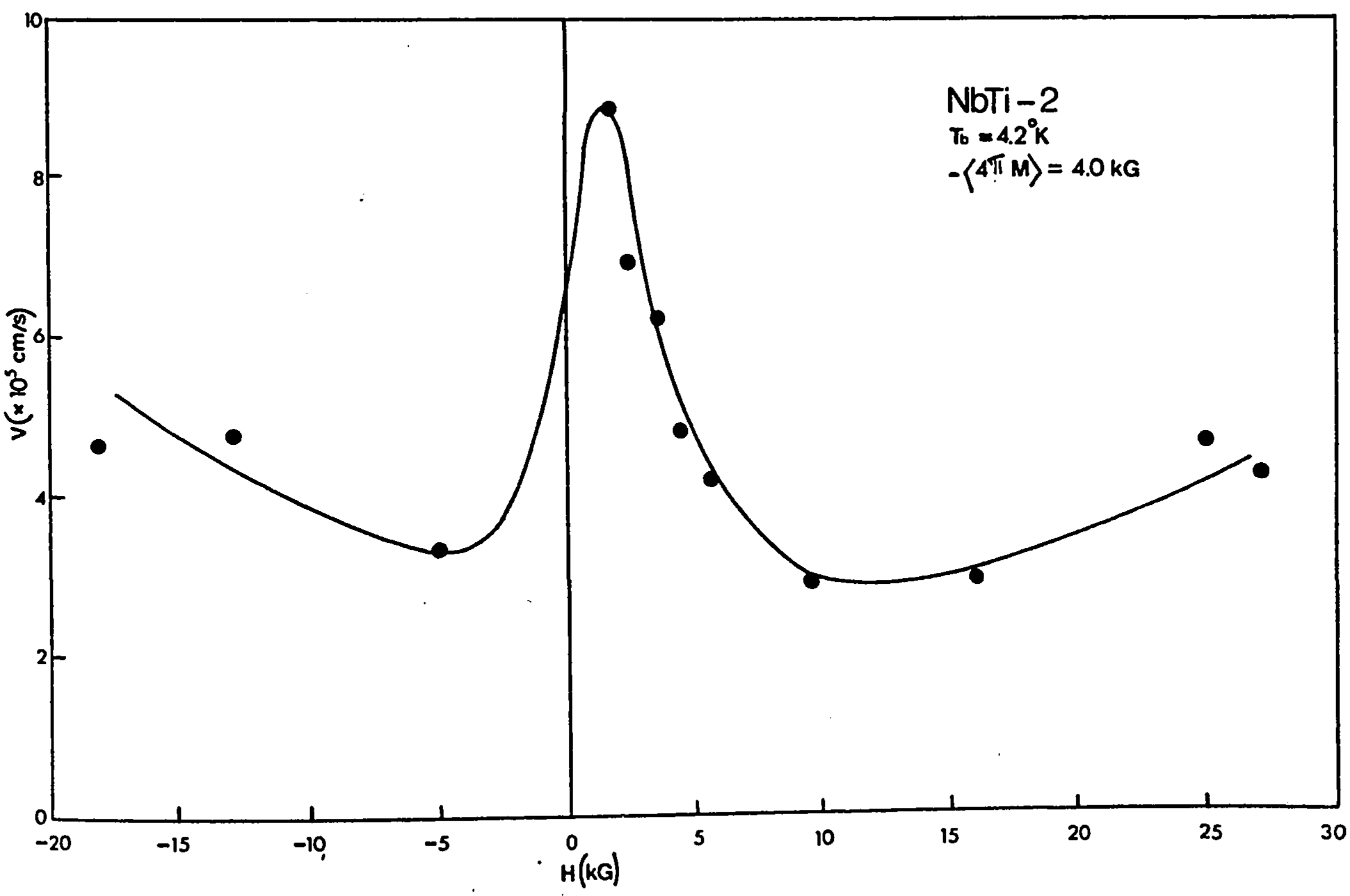

Fig. 12.4 Velocity vs external field H for flux jumps of constant magnetization $\langle 4\pi M \rangle = -4.0$ kG. The large velocities observed in low fields are attributed to steep profiles of magnetic field within the sample.

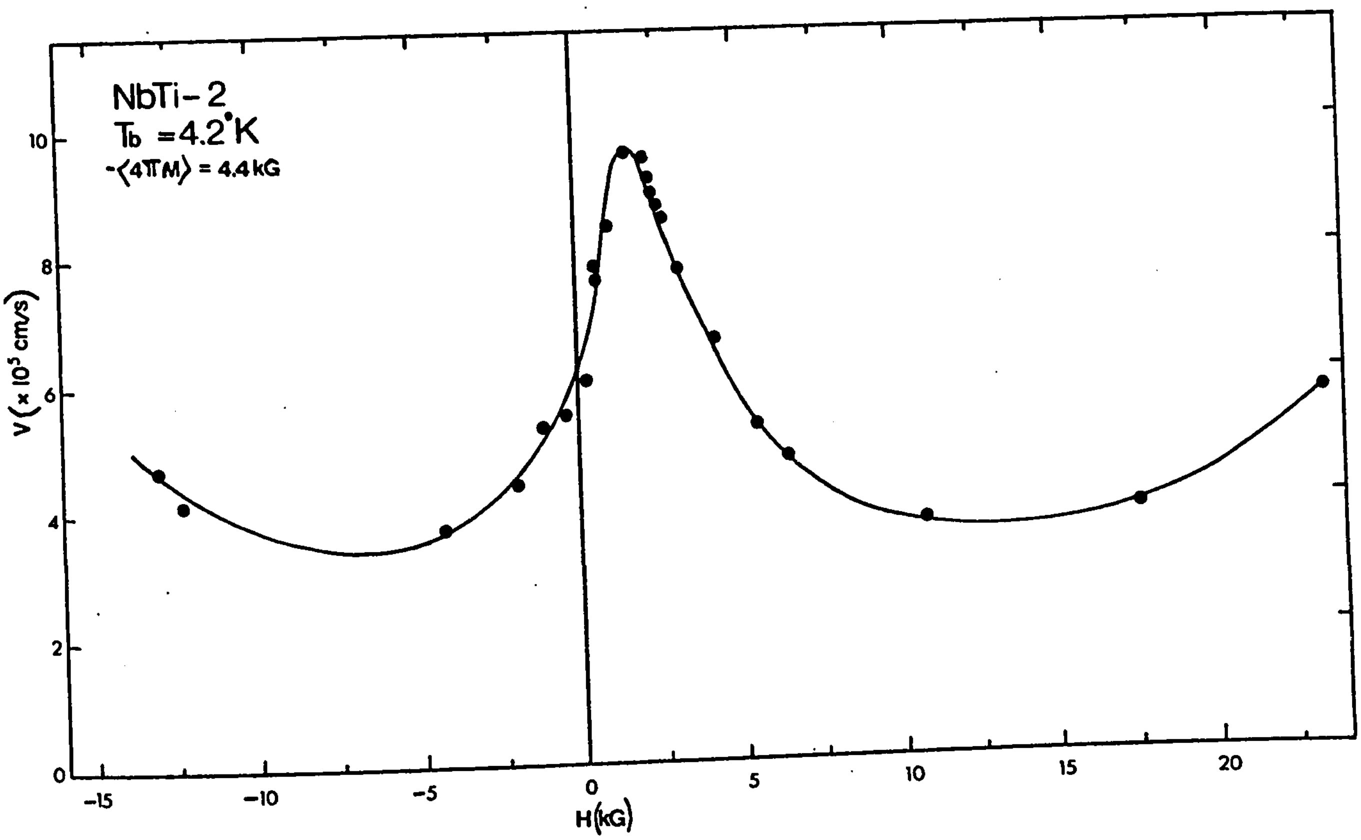

Fig. 12.5: Velocity vs external field H for flux jumps of constant magnetization $<4\pi M> = -4.4$ kG. The large velocities observed in low fields are attributed to steep profiles of magnetic field within the sample.

steeper profiles lead to slower rates of radial collapse whereas if R_o/A is greater than ~ 0.85 steep gradients of field can lead to very rapid rates of flux collapse. This behaviour was described in chapter IV where we have shown a graph of the relaxation time τ_R as a function of R_o/A for NbTi cylinders.

Figures 12.6(a) and (b) show schematically the behaviour of V vs H and of τ_R with R_o/A for the NbTi-4 sample. The thick line in (b) indicates the range of R_o/A spanned when the field is varied. Since the pinning strength of this sample is low only shallow gradients of flux are obtained even in low fields. In this case an increase in the field gradient leads to larger values of τ_R. The velocity is then a rapidly increasing function of field.

Figures 12.6(c) and (d) show similar curves for the NbZr-1 sample. In this sample the pinning is much higher than for NbTi-4 and therefore steep gradients (large values of R_o/A) are encountered in low fields. Here the velocity will increase rather slowly with field (see figure 12.6(c)).

For sample NbTi-2 the magnitude and the anomalous behaviour of the magnetization in low fields indicate that very steep gradients of field occur when the induction is small. Thus, the range of R_o/A is large for this sample and very fast relaxation times are obtained in low fields (figure 12.6(f)). As a consequence, for this sample, high velocities are encountered in low fields (figure 12.6(e)). In the

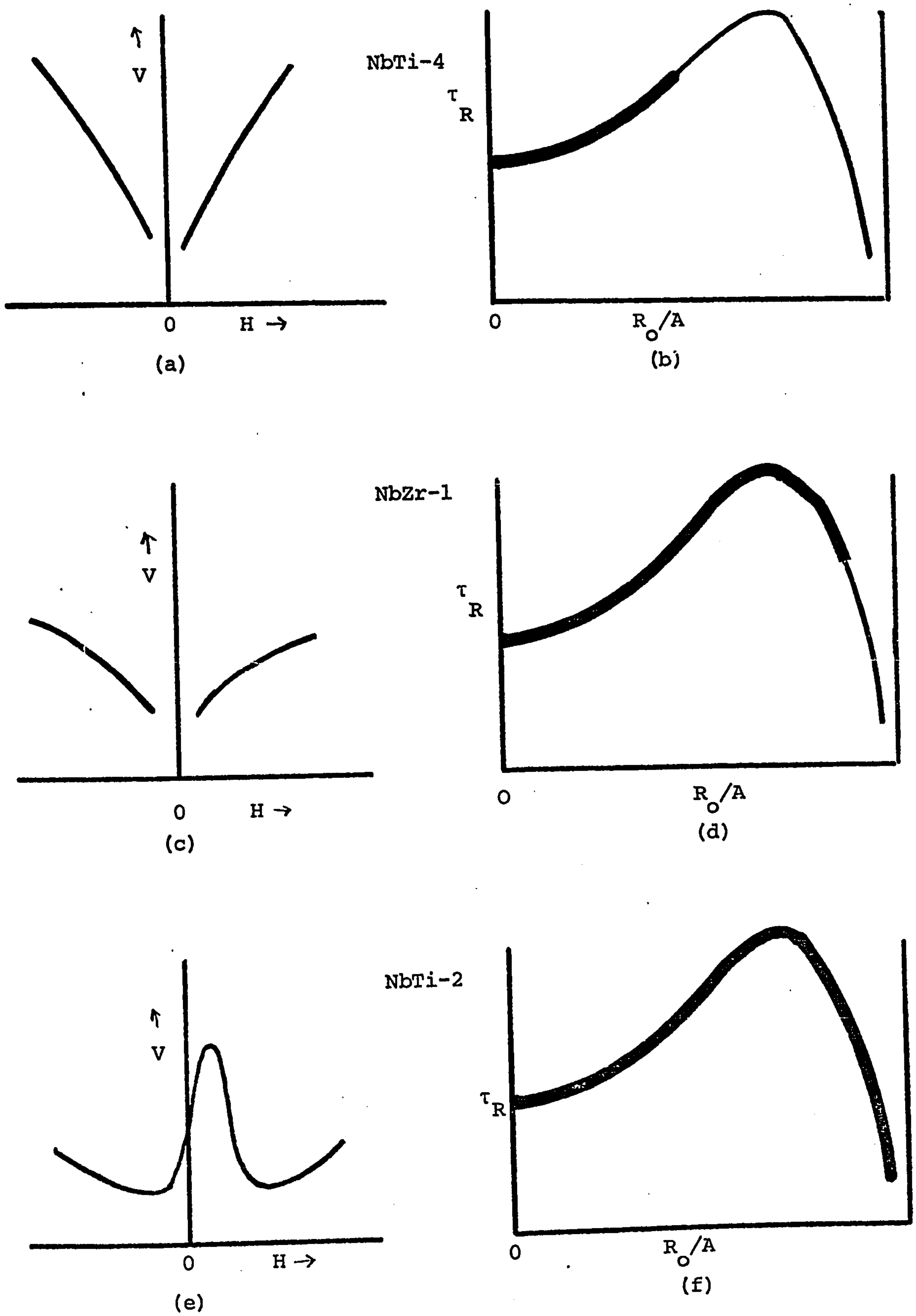

Fig. 12.6: Schematic representation of the behaviour of velocity V vs H and corresponding changes in τ_R vs R_o/A (thick lines) for the NbTi-4, NbZr-1, and NbTi-2 samples.

higher field regions the change of τ_R with field profile is gradual, hence an increase in field leads to an increase in velocity.

III EFFECT OF NORMAL STATE RESISTIVITY

For a given sample the velocity of propagation of flux jumps may be expected to increase linearly with normal state resistivity ρ_n since the speed of radial flux collapse varies linearly with ρ_n. Experimentally the effect of ρ_n is not easy to assess since it is very difficult to achieve changes in resistivity without also bringing in changes of other parameters such as pinning strength, critical field, critical temperature, etc. Faced with these constraints and difficulties we have elected to compare the velocities in three different materials (NbTi, NbZr and Nb) differing considerably in normal state resistivity but with comparable enthalpies (see Table II). The meaning of the results given here will therefore be of a qualitative nature only.

The velocity of propagation for the NbTi-2, NbZr-1 and Nb samples are compared in figure 12.7. The data for both NbTi and NbZr samples were taken for magnetization curve where H_o = 10.0 kG (see figures 9.4 and 9.21). The data for the Nb sample were taken for a wide range of magnetic histories. The points for the NbZr sample

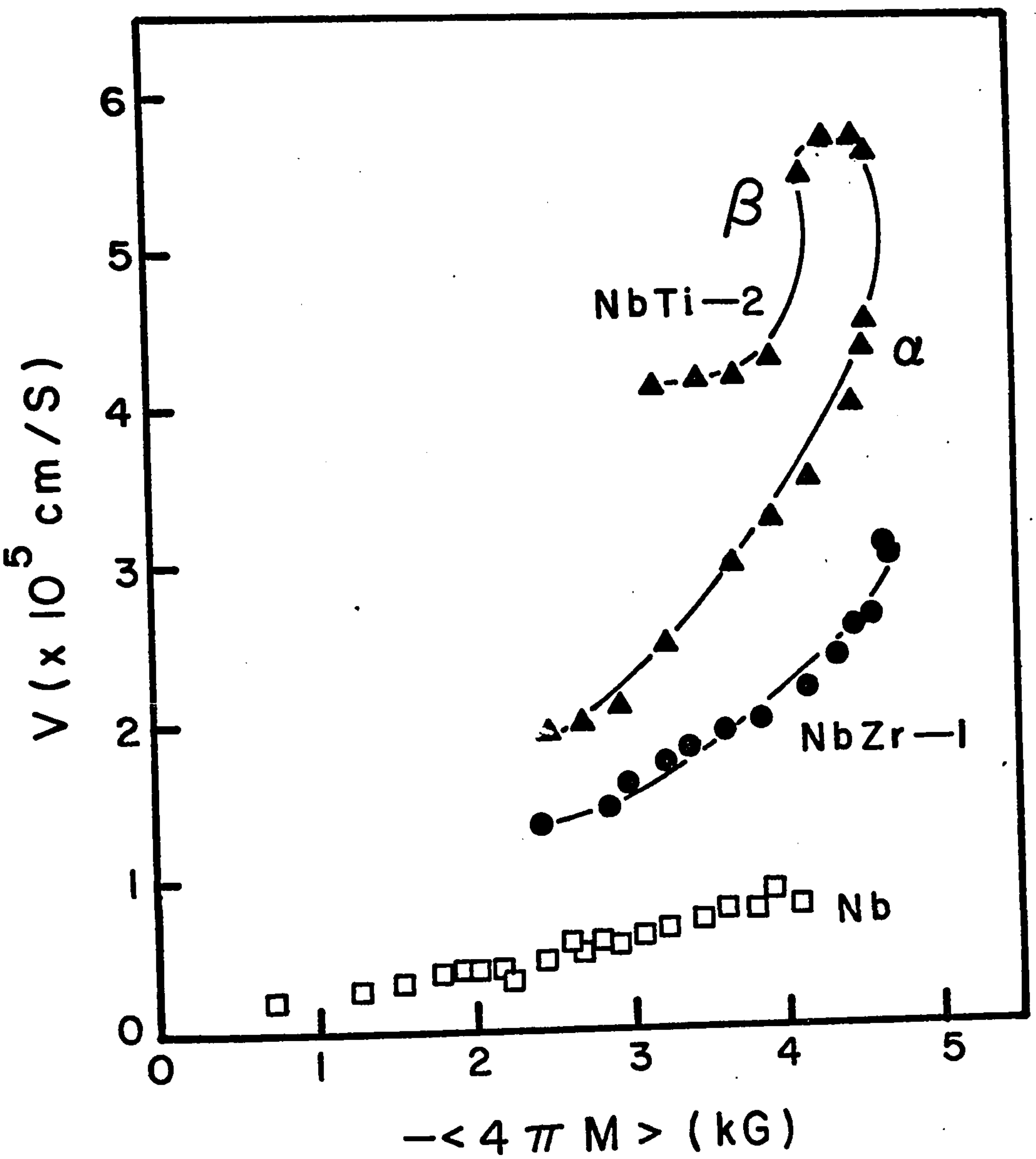

Fig. 12.7: Comparison of velocities obtained in samples NbTi-2, NbZr-1 and Nb. The difference in the velocities of these samples can be largely attributed to their normal state resistivity.

correspond to flux jumps triggered before the magnetization peak only. These should be compared to the α branch of the NbTi sample which also corresponds to flux jumps before the magnetization peak. Typically, the velocities for the NbTi-2 and NbZr-1 samples differ by a factor of approximately 1.5 whereas their resistivities differ by a factor of 2.2. If we compare the velocities of the NbZr and Nb samples, however, we notice a ratio of $\sim$ 2.7 for the velocities whereas the ratio of the resistivities is $\sim$ 30. These results indicate that an increase in normal state resistivity leads to an increase in velocity.

IV CONCLUSION

In this chapter we have investigated the effect of two parameters which affect the flux flow resistivity of type II superconductors.

We showed that for flux jumps of constant magnetization triggered in different fields the change in velocity can be attributed to the increase in flux flow resistivity and to changes in magnetic field profiles with increasing field. Depending on the steepness of the field profiles the velocity in low magnetic fields is either a minimum (NbTi-4, NbZr-1) or a maximum (NbTi-2). In high fields where effects due to changes in magnetic field profile are not dominant, the velocity was seen to increase with H in all three samples.

In section III we compared the velocities in three samples of the same diameter but with very different normal state resistivities. This comparison indicates that large velocities correspond to samples with large normal state resistivities. The dependence of velocity on ρ_n however is difficult to assess because of the different H_{c2}, T_c and J_c of the materials compared.

CHAPTER XIII

EFFECT OF A TRANSPORT CURRENT I ON THE LONGITUDINAL VELOCITY OF PROPAGATION

I. INTRODUCTION

In chapter VIII it was shown that for a constant transport current level the longitudinal velocity of propagation of a normal front increases abruptly as a threshold magnetic moment is exceeded. This threshold moment was seen to decrease with current level and to correspond to the limit of magnetic stability of the wire. In this chapter we explore the variation of the velocity of propagation for a constant magnetic moment as the transport current level is increased. We only examine situations where the sample is magnetically unstable even when no transport current is present. The measurements we present were taken on a Nb wire in zero external field and with a constant magnetization. The pertinent properties of the Nb sample are summarized in Tables I and II of the experimental section.

II. EXPERIMENTAL RESULTS AND DISCUSSION

Figure 13.1 shows the velocity of propagation of flux jumps as a function of transport current I in a Nb wire. These measurements were obtained by initially cooling the sample through T_c in a magnetic

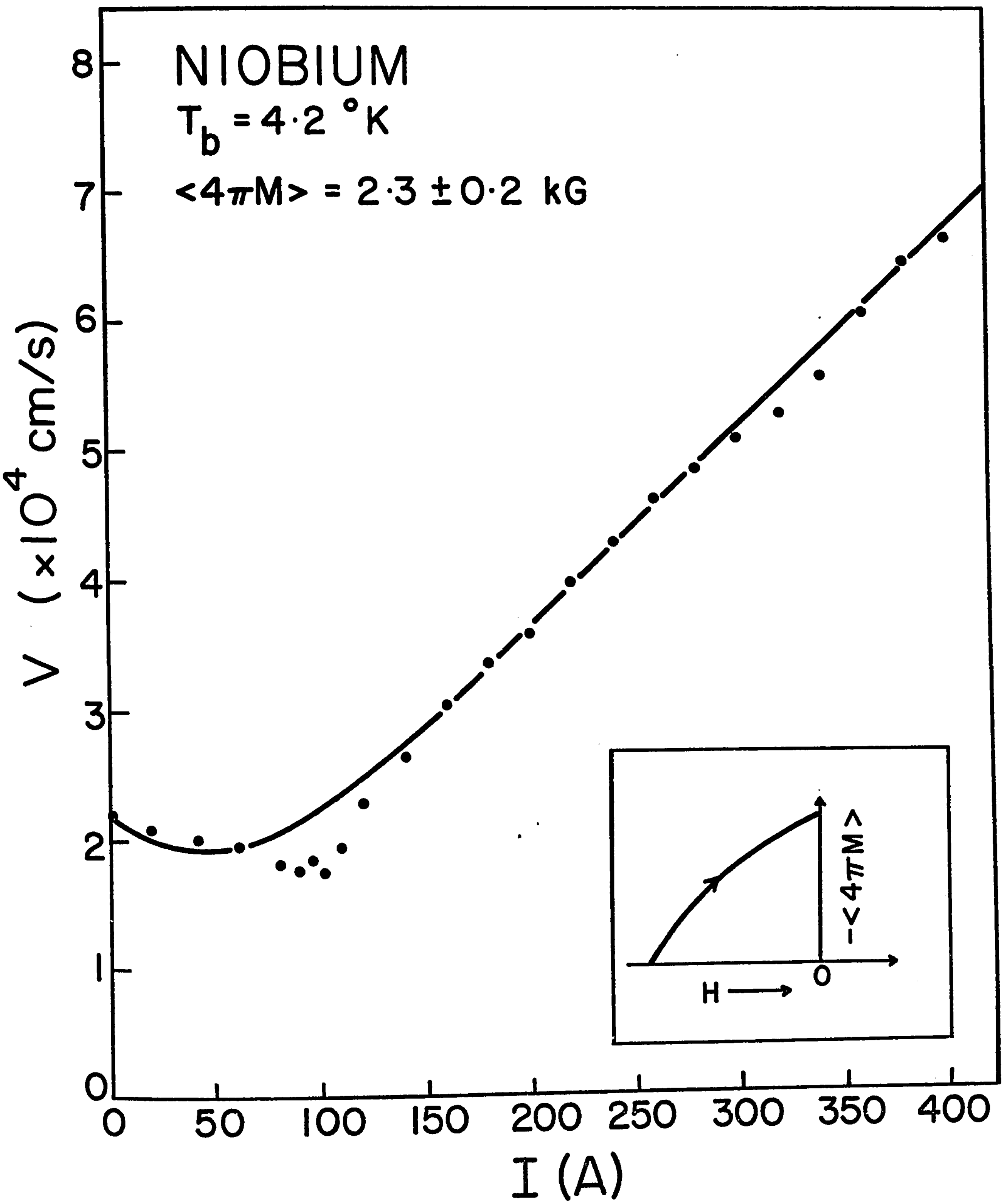

Fig. 13.1: Flux jump velocity vs conduction current I flowing in a Nb wire with a trapped axial field of ∿ 2.2 kG. Data points are experimental and solid curve theoretical.

field H_o selected to give a remanent magnetization $<4\pi M> = 2.3 \pm 0.2$ kG With the sample magnetized and in zero field, the transport current was then introduced. The application of the current caused the magnetization $<4\pi M>$ to decrease slightly.

We note in figure 13.1 that the velocity initially decreases slowly with current for small current levels $I < 100A$. For larger currents, $I > 100A$, the velocity increases approximately linearly with current. In this region, the slope of velocity vs I is an order of magnitude greater than encountered when there is no magnetization, hence when the propagation is purely thermal.

We also monitor the voltage drop along the superconducting wire during the measurements of the longitudinal propagation of the flux collapse. For currents smaller than $\sim$ 100A no voltages are observed within the sensitivity of detection (e.g. $\sim$ 1 millivolt), during and after the flux jump. For currents $I > 100A$, however, the flux jump is observed to be accompanied by the appearance of a non-transient voltage which increases nearly linearly as the flux jump advances along the specimen and which is nearly proportional to the current level I. We conclude from these observations that below a threshold transport current $I \sim 100A$, the sample remains in the flux flow regime , hence in the superconducting state during and immediately after completion of the flux jump.

Presumably, during the flux collapse, there is a transient axial voltage pulse which is generated as the azimuthal flux associated with the conduction current redistributes and both the azimuthal flux and conduction current penetrate deeper into the sample. This transient voltage pulse, however, is too small to be detected in our measurements. For currents below the threshold level, the energy dissipated during the flux collapse and in the flux flow regime which is established in the wake of the flux collapse are not sufficient to drive the sample normal while the disturbance is propagating along the entire length of the sample. For currents above the threshold level, the energy dissipation accompanying the flux jump presumably is adequate to heat the sample to the temperature region where the flux flow resistivity increases rapidly. Since the conduction current remains at a level $\gtrsim$ 75% of the initial value during the entire flux jump, the generation of heat in the flux flow state is now sufficient to raise the temperature above T_c. Indeed, the resistivity we infer from our traces of voltage and current vs time correspond to that for the normal state when I exceeds the threshold level.

We now present a model which adequately accounts for the behaviour of the velocity of propagation of the flux jump versus current level. This model is also corroborated by structure in the trace of the voltage detected by the pick-up coils in series.

When both a transport current and an axial magnetization, are present in a wire, the lines of flux in the superconducting specimen are helical. The pitch of the helix varies with radius, transport current and axial magnetization. We envisage the possibility that in such circumstances, a flux jump does not travel in a straight line along the superconductor but follows a helical path corresponding to the configuration of the flux lines. Let v_I denote the actual velocity of propagation of a disturbance along the path defined by a flux line. The resultant or effective velocity v_z along the sample axis can be geometrically related to v_I by the relation

$$v_z = v_I \, B_z/(B_\theta^2 + B_z^2)^{\frac{1}{2}} \qquad 1$$

where B_θ and B_z are the azimuthal and axial magnetic induction respectively.

When a conduction current of density j_z is superimposed on azimuthally circulating currents of density j_θ which sustain the axial magnetization, the instantaneous rate of energy dissipation can be written $(j_\theta^2 + j_z^2)\rho_f$ where ρ_f is the flux flow resistivity. This may be written as:

$$j_\theta^2 \rho_f \; (1 + j_z^2/j_\theta^2).$$

We have seen in chapter XI that with $j_z = 0$, the velocity of propagation of a disturbance along the flux lines was linearly proportional to the rate of radial flux collapse. This latter is directly related to the rate of energy dissipation $j_\theta^2\rho_f$. Consequently it is reasonable to write as an approximate guess

$$v_I = v_o \; (1 + kI^2) \qquad 2$$

where v_o is the velocity of propagation of a disturbance along the flux lines when only azimuthally circulating currents are flowing (zero transport current). k is a coefficient related to the average relative density of azimuthal and axial currents.

At the surface of the specimen the azimuthal field B_θ is related to the conduction current by $B_\theta = I/5R$ where R is the radius of the wire. Introducing this and equation XIII.2 in equation XII.1 yields

$$v_z = \frac{v_o(1 + kI^2)}{(1 + KI^2)^{\frac{1}{2}}} \qquad \text{XIII.3}$$

where $K = (1/5RB_z)^2$.

The solid line in figure 13.1 shows v_z versus I calculated using $k = 2.25 \times 10^{-4}$ and $K = 9.0 \times 10^{-4}$. Although k and K are chosen to obtain a good fit to the data, the values selected are quantitatively consistent with the model on which equation XIII.3 is based. When $I \sim 67A$, we note that $kI^2 \sim 1$ hence $j_\theta \sim j_z$. This is realistic for initially, with a magnetization $\sim$ 2 kG and $I \sim 70A$ although $j_\theta > j_z$, the average densities are comparable during the flux jump since j_θ vanishes while j_z remains constant during the event. Since R = 0.025 cm, choosing $K = 9.0 \times 10^{-4}$ leads to $B_z \sim 300$ Gauss. This value for the axial magnetic induction in the vicinity of the surface is quantitatively consistent with auxillary measurements of the azimuthal current carrying capacity of the surface of these Nb wires in zero external field.

We now present additional evidence that flux jumps travel along helical paths which are determined by the lines of flux in the vicinity of the surface of the sample when it is carrying a conduction current.

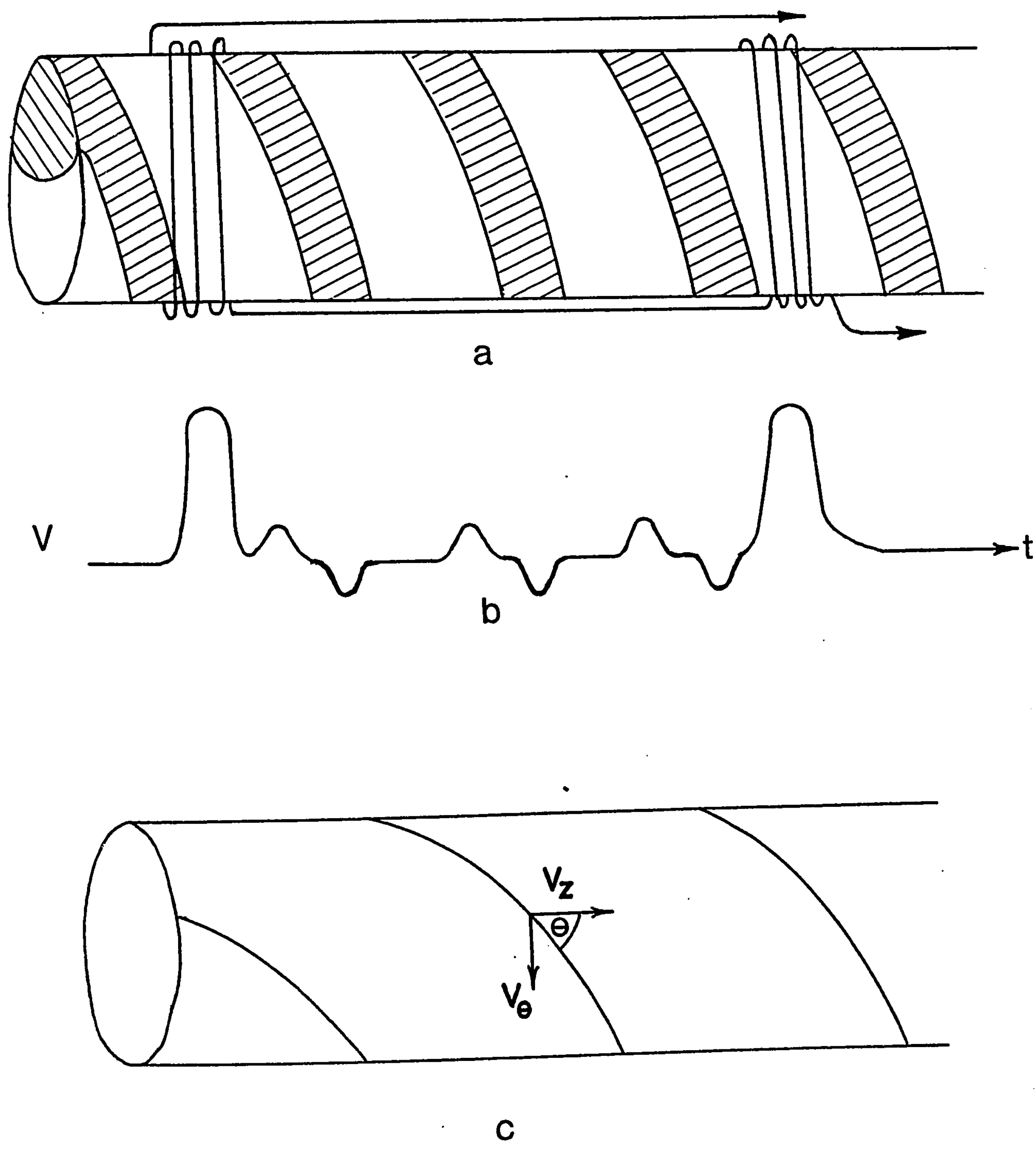

$$\tan \theta = V_\theta / V_z$$

Fig. 13.2: (a) Schematic of arrangement of leads on opposite sides of simple and pick-up coils in series; (b) Signal expected if a local perturbation advances along a helical path as shown in (a); (c) velocity components.

The experimental arrangement is shown schematically in figure 13.2(a) which depicts two pick-up coils connected in series. The leads joining the coils and the coils to the oscilloscope are purposely positioned along opposite sides of the cylinder. These then form a coil of one turn embracing a plane parallel to the axis of the wire.

With this arrangement of leads and pick-up coils, a disturbance propagating helically, as shown in figure 13.2(a), and which spreads out over the volume of the cylinder as it advances, will give rise to many regular small pulses intermediate between the two main pulses detected in succession by the two separate pick-up coils. The resulting signal expected is shown schematically in figure 13.2(b) and corresponds to that observed when transport current is flowing in the wire. The number of intermediate pulses then provides a measure of the helicity of the path followed by the disturbance as it travels along and around the wire, since each set of small positive-negative pulses are thought to correspond to a revolution of the propagating flux jump.

We estimate the frequency f of intermediate pulses as follows. Firstly, by definition

$$f = \frac{v_\theta}{2\pi R} \qquad \text{XIII.4}$$

where v_θ is the azimuthal component of the velocity of propagation of the disturbance and R is the radius of the wire. Now, if the path followed by the propagating flux jump coincides with the configuration of the flux lines in the vicinity of the surface, then

$$\frac{v_\theta}{v_z} = \frac{B_\theta}{B_z} \qquad \text{XIII.5}$$

where v_z is the axial component of the velocity of propagation.
Since $B_\theta = I/5R$ and $K = (1/5RB_z)^2$ at the surface, introducing this and equation XIII.5 into equation XIII.4 we obtain

$$f = \frac{v_z I\sqrt{K}}{2\pi R} \qquad \text{XIII.6}$$

Taking $I \sim 100A$ and the corresponding $v \sim 1.7 \times 10^4$ from our data (figure 13.1) and using $K = 9 \times 10^{-4}$ from above, we then expect $f \sim 2.7 \times 10^5$ whereas we observe $f \sim 1.2 \times 10^5$ at this current level. The quantitative agreement is adequate to augment our confidence in the validity of the model we have proposed.

Finally, we note that the frequency f appears to increase nearly linearly with I. This observation is, at present, only semi-quantitative but the fact that f increases with I tends to corroborate the picture we have developed.

III. CONCLUSION

With a chosen amount of flux initially trapped into a Nb wire we have measured the velocity of propagation of flux jumps versus the level of transport current I. We have also monitored the voltage along the wire during and immediately after the flux jump.

For currents $I < 100A$ the dissipation of energy during the flux jump and in the flux flow state immediately after this event, appears insufficient to raise the temperature of the wire into the steeply rising part of the flux flow resistivity and into the normal state. The wire becomes normal during and/or immediately after the collapse of the trapped flux when $I > 100A$. This behaviour is consistent with our detailed analysis of the radial collapse of flux.

The curve of the velocity of propagation of flux collapse v along the wire versus I and the observation of intermediate pulses by a single turn coil embracing part of the length of the sample are quantitatively accounted for on the basis that the disturbance advances along helical paths which coincide with the configuration of the flux lines in the vicinity of the surface.

CHAPTER XIV

EFFECT OF BATH TEMPERATURE ON THE LONGITUDINAL VELOCITY OF PROPAGATION OF FLUX JUMPS

I INTRODUCTION

In this chapter we present measurements of the longitudinal velocity of propagation of flux jumps for different bath temperatures in samples of NbTi, NbZr and Vanadium. Temperatures above 4.2^{o}K were achieved by passing a constant current in a single layer bifilar manganin wire heater which was wound uniformly around each of the samples. The temperatures above 4.2^{o}K were estimated from the peak in the initial magnetization using the Bean critical state model and assuming a linear decrease in J_c with temperature. Temperatures below 4.2^{o}K were obtained by pumping on the helium bath and determined from the vapour pressure.

For all the samples we find that the qualitative behaviour of the velocity with magnetization $<4\pi M>$ remains unchanged for the different temperatures. A comparison of these velocities, plotted as a function of $<4\pi M>$, indicates that the velocity is generally higher when the temperature is decreased. Since the velocity is not a unique function of $<4\pi M>$ at any given temperature there is overlap between the curves of velocities taken at different temperatures. The observed increase in velocity with decrease in temperature can be related to the role of the magnetic induction in the flux flow resistivity since flux jumps of a given $<4\pi M>$ were triggered in higher external fields at the lower bath temperatures.

II EXPERIMENTAL RESULTS

a) NbZr-1:

The longitudinal velocity of propagation of flux jumps was measured in the NbZr-1 sample for bath temperatures of $6^{\circ}K$ and $7.5^{\circ}K$. Velocities at $4.2^{\circ}K$ were presented earlier in chapter IX.

Figures 14.1 and 14.2 show respectively magnetization curves for bath temperatures of $6^{\circ}K$ and $7.5^{\circ}K$. The velocity of flux jumps triggered along the dashed parts of these curves are shown in figures 14.3 and 14.4. We note that for both temperatures the velocity increases with $<4\pi M>$ and depends strongly on magnetic field. This behaviour was also observed at $4.2^{\circ}K$ in the same sample (chapter IX).

Figure 14.5 compares the velocities obtained at these three temperatures ($4.2^{\circ}K$, $6^{\circ}K$ and $7.5^{\circ}K$) versus $<4\pi M>$. The data at $4.2^{\circ}K$ was taken for a greater variety of field profiles and external fields. Inspection of this data indicates that for a given $<4\pi M>$ the velocities obtained at higher temperatures usually lead to lower velocities. There is however a considerable overlap between the velocities at different temperatures due to the wide variations of velocity with magnetic

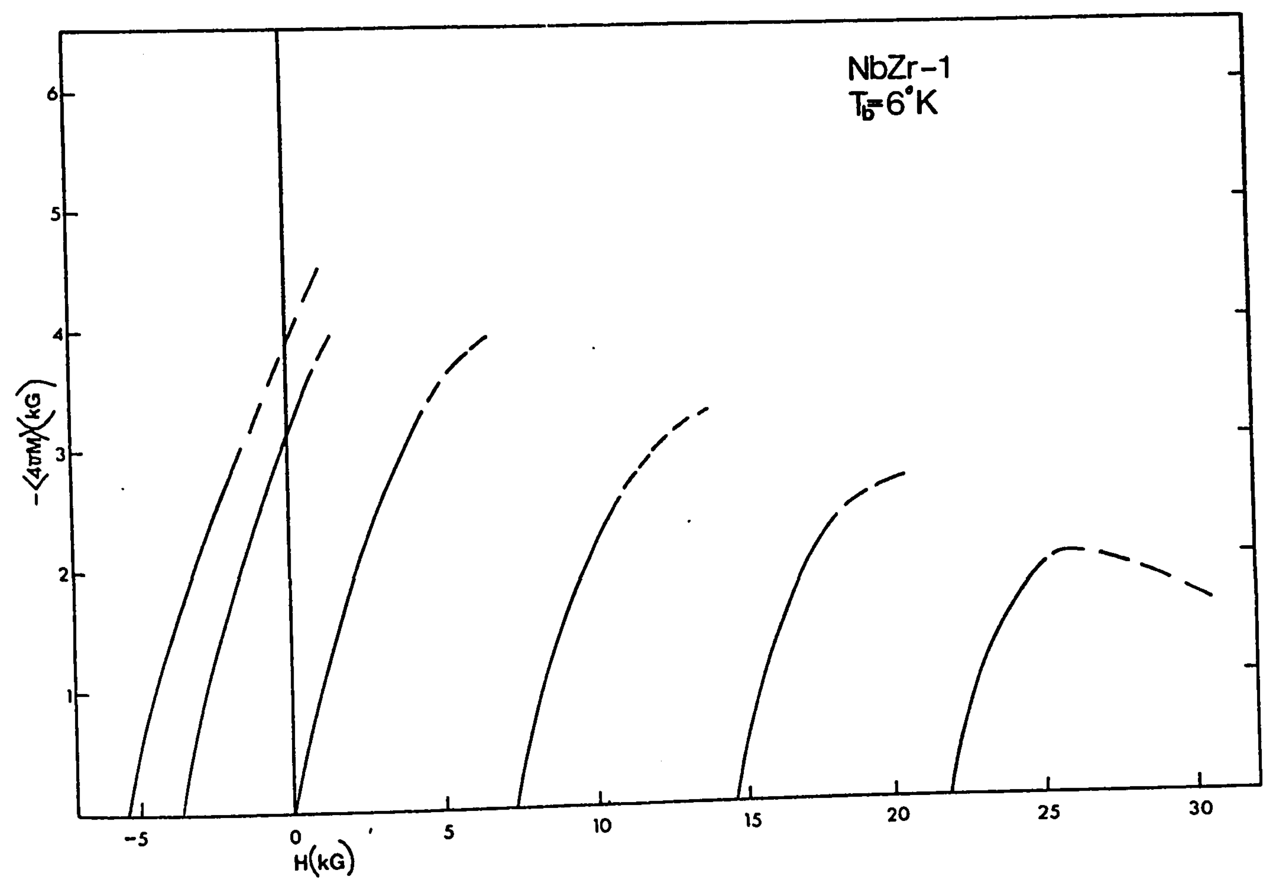

Fig. 14.1: Magnetization curves for NbZr-1 sample at T ∿ 6°K.

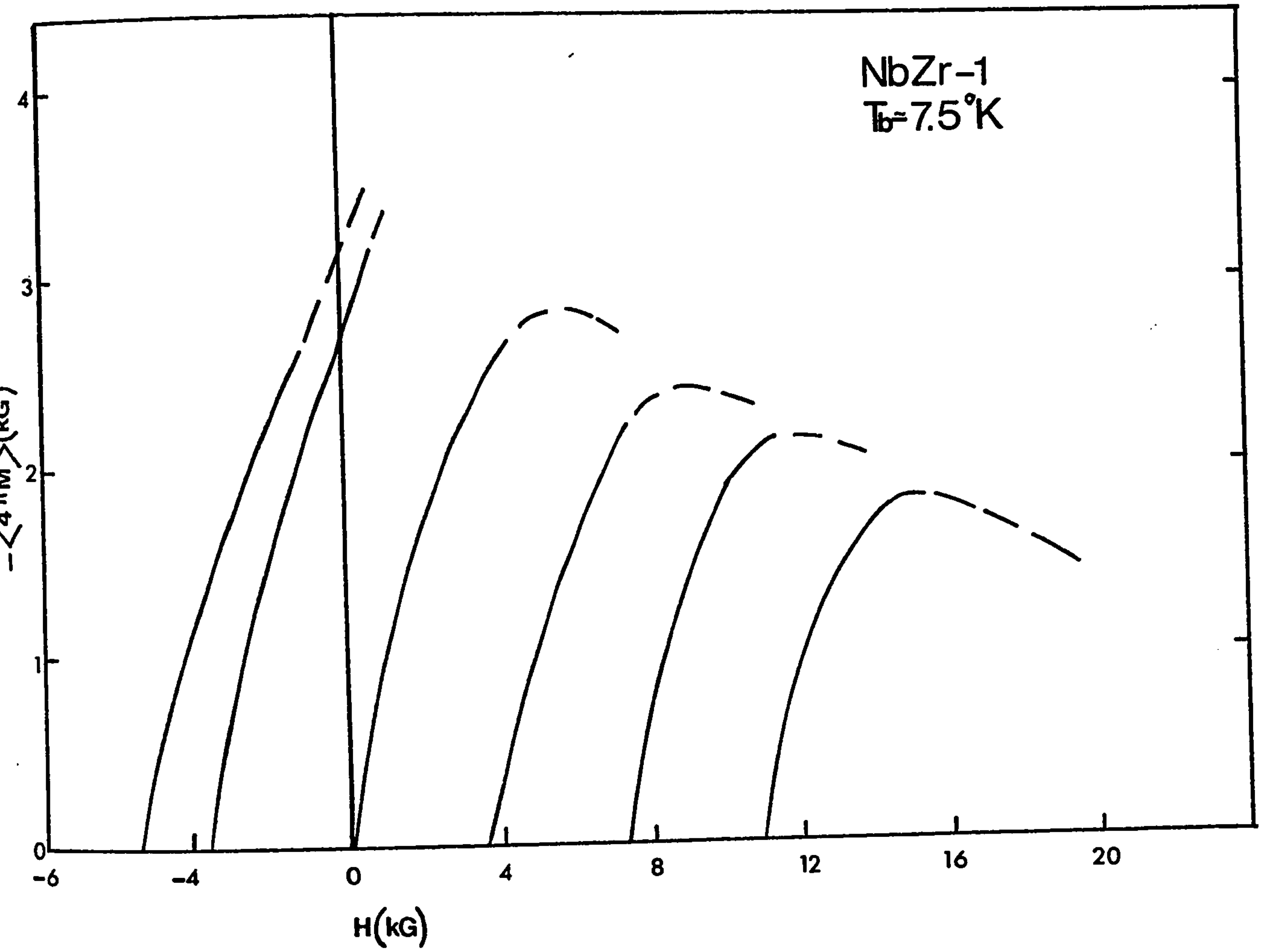

Fig. 14.2: Magnetization curves for NbZr-1 sample at T ∿ 7.5°K.

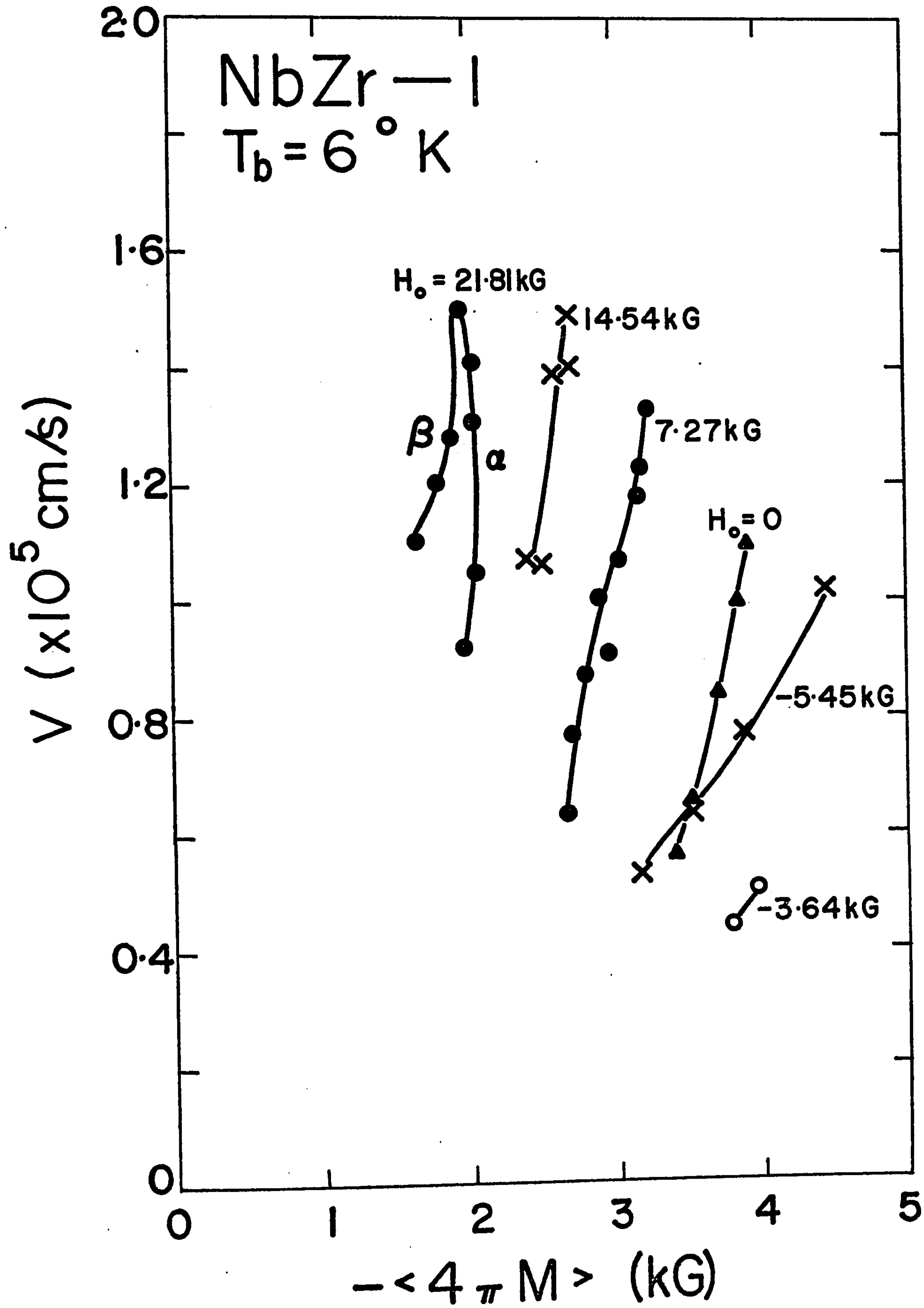

Fig. 14.3: Velocity vs. magnetization for NbZr-1 sample at $6^{\circ}K$ for flux jumps triggered along magnetization curve starting at field indicated.

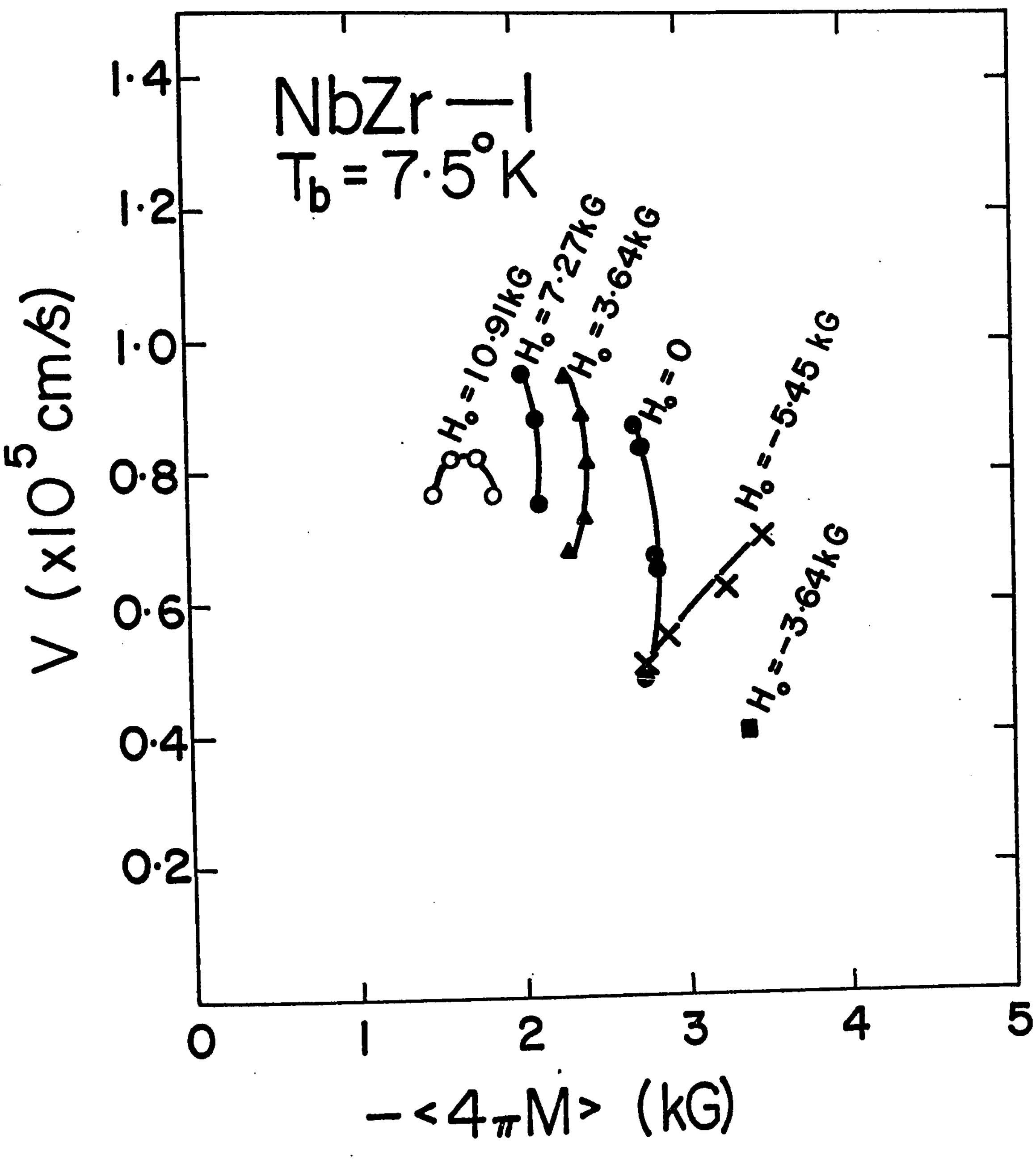

Fig. 14.4: Velocity vs magnetization for NbZr-1 sample at 7.3°K for flux jumps triggered along magnetization curve starting at field indicated. (see fig. 14.2).

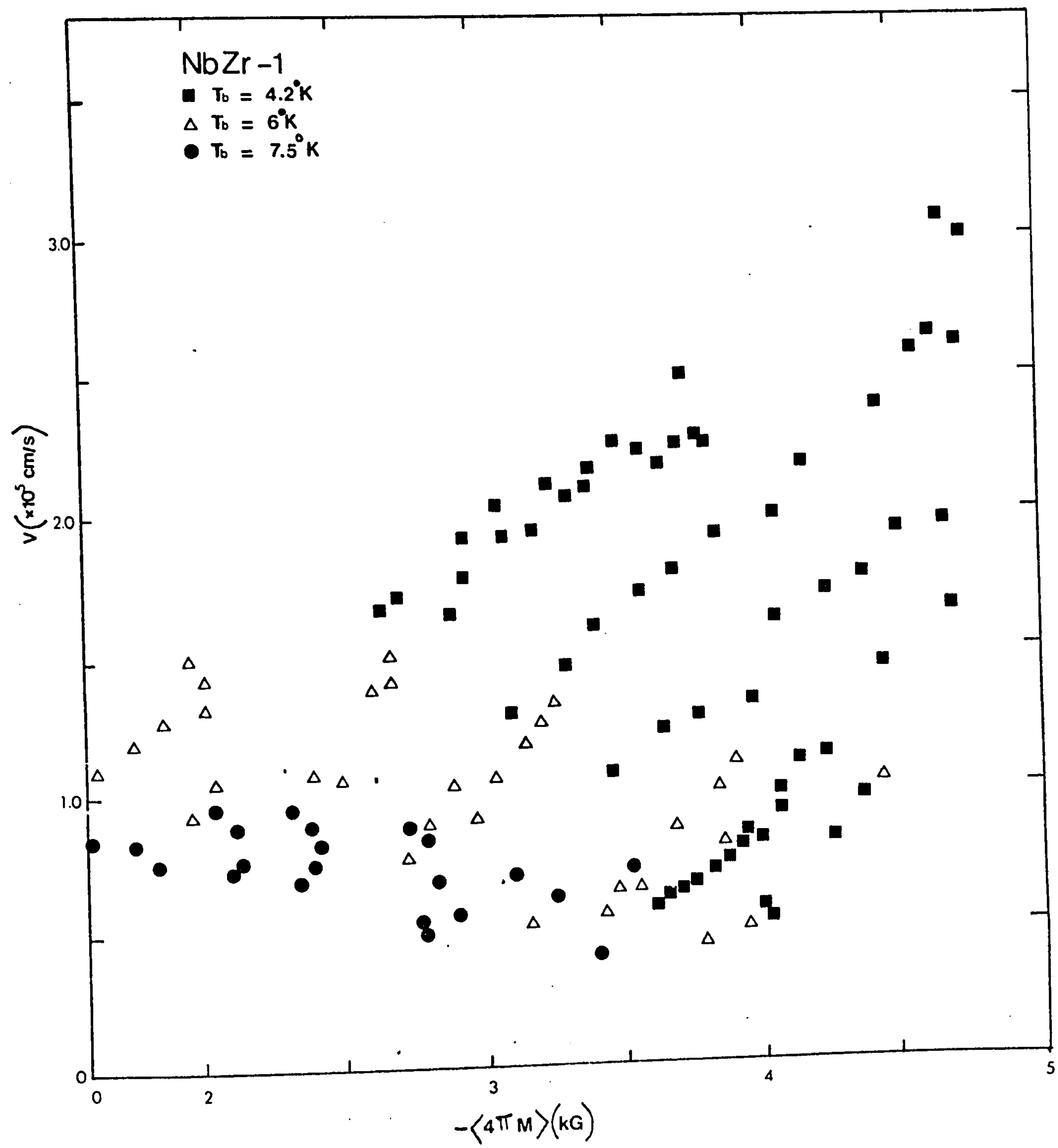

Fig. 14.5: Compilation of data on velocity vs magnetization for NbZr-1 sample at T = 4/2, 6 and 7/5°K.

field for a given temperature. We attribute the increase in velocity with decrease in temperature to the influence of the magnetic field in the phenomenon of propagation since, in our measurements, magnetic moments of a given size correspond to higher fields at lower temperatures. For example, a moment $<4\pi M>$ = 2 kG corresponds to a field of $\sim$ 28 kG at $6^{o}K$ (figure 14.1) and to a field of $\sim$ 14 kG at $7.5^{o}K$ (figure 14.2).

b) <u>NbTi-2</u>:

The velocity of propagation of flux jumps in the NbTi-2 sample was investigated at 2.18, 4.2, 6.0 and $7.9^{o}K$.

Figure 14.6 shows a series of magnetization curves taken at $2.18^{o}K$. In figure 14.7 we compare the velocities measured at this temperature with that observed at $4.2^{o}K$. We note that the behaviour of the velocity versus $<4\pi M>$ and their magnitudes are similar at the two temperatures.

Figures 14.8 and 14.9 show respectively magnetization curves at $6^{o}K$ and $7.9^{o}K$ for this specimen. The velocities measured along the dashed parts of these curves are shown respectively in figures 14.10 and 14.11 Again we note a general increase in velocity with $<4\pi M>$. We encounter less scatter in the data presented here because at these temperatures, flux jumps for only a small variety of field profiles and smaller range of fields were explored for a given $<4\pi M>$.

Figures 14.12 compares the velocities observed at $2.18^{o}K$, $6^{o}K$ and $7.9^{o}K$. As in the previous sample (NbZr) most of the scatter

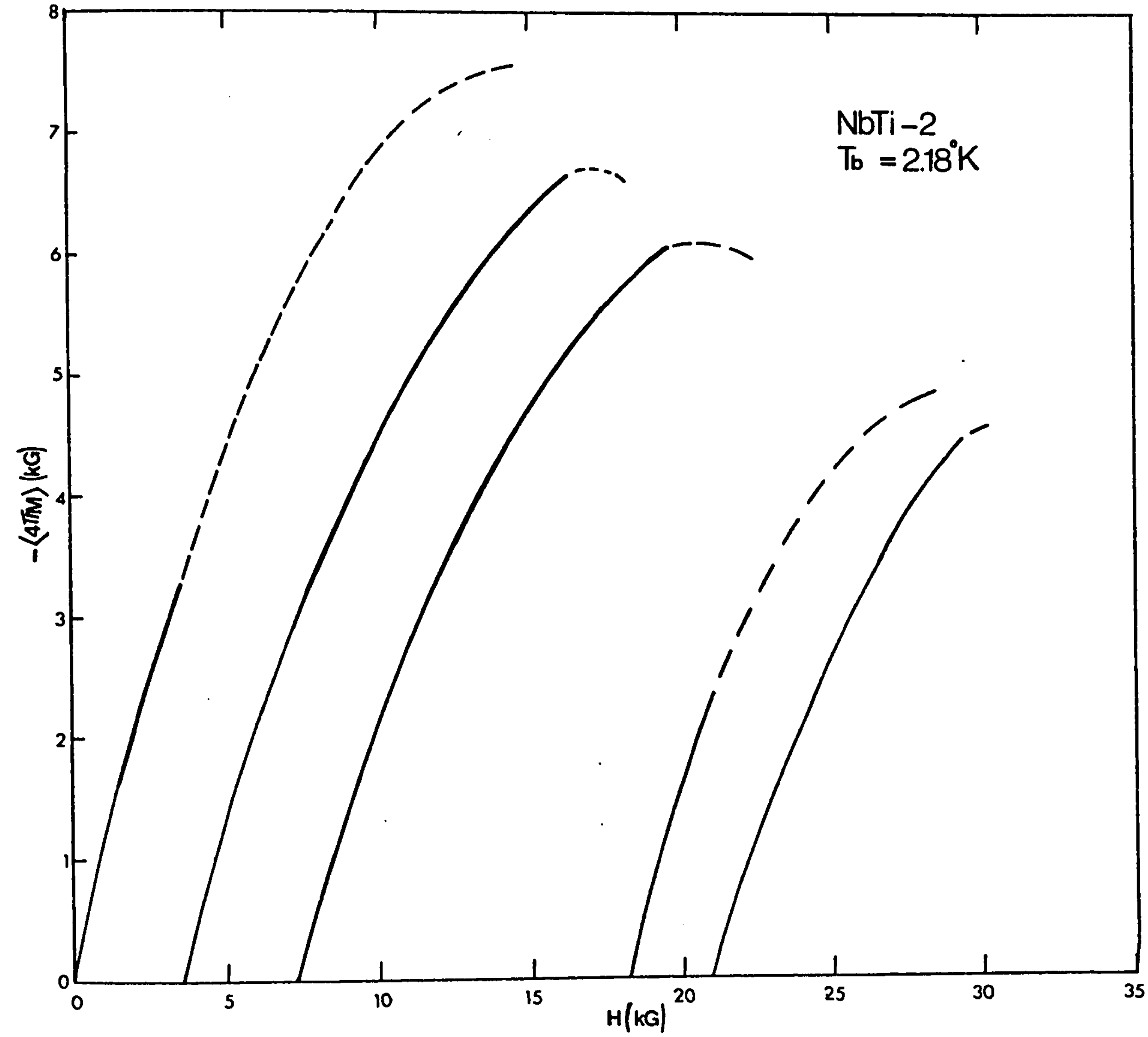

Fig. 14.6: Magnetization curves for NbTi-2 sample at T = 2.18°K.

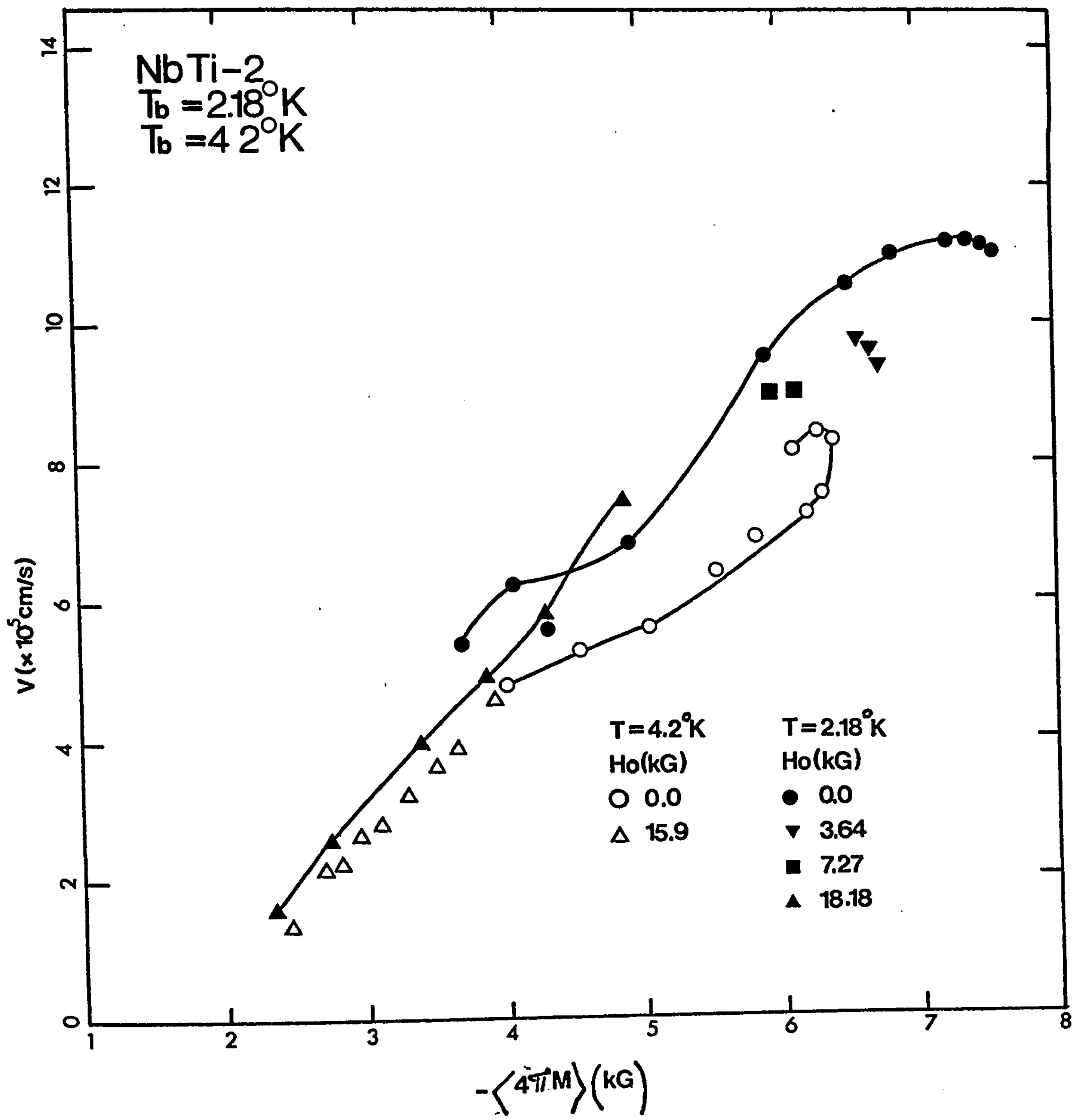

Fig. 14.7: Velocity vs. magnetization for NbTi-2 sample at T = 2.18 and $4.2^{\circ}K$ for flux jumps triggered along magnetization curves starting at fields indicated.

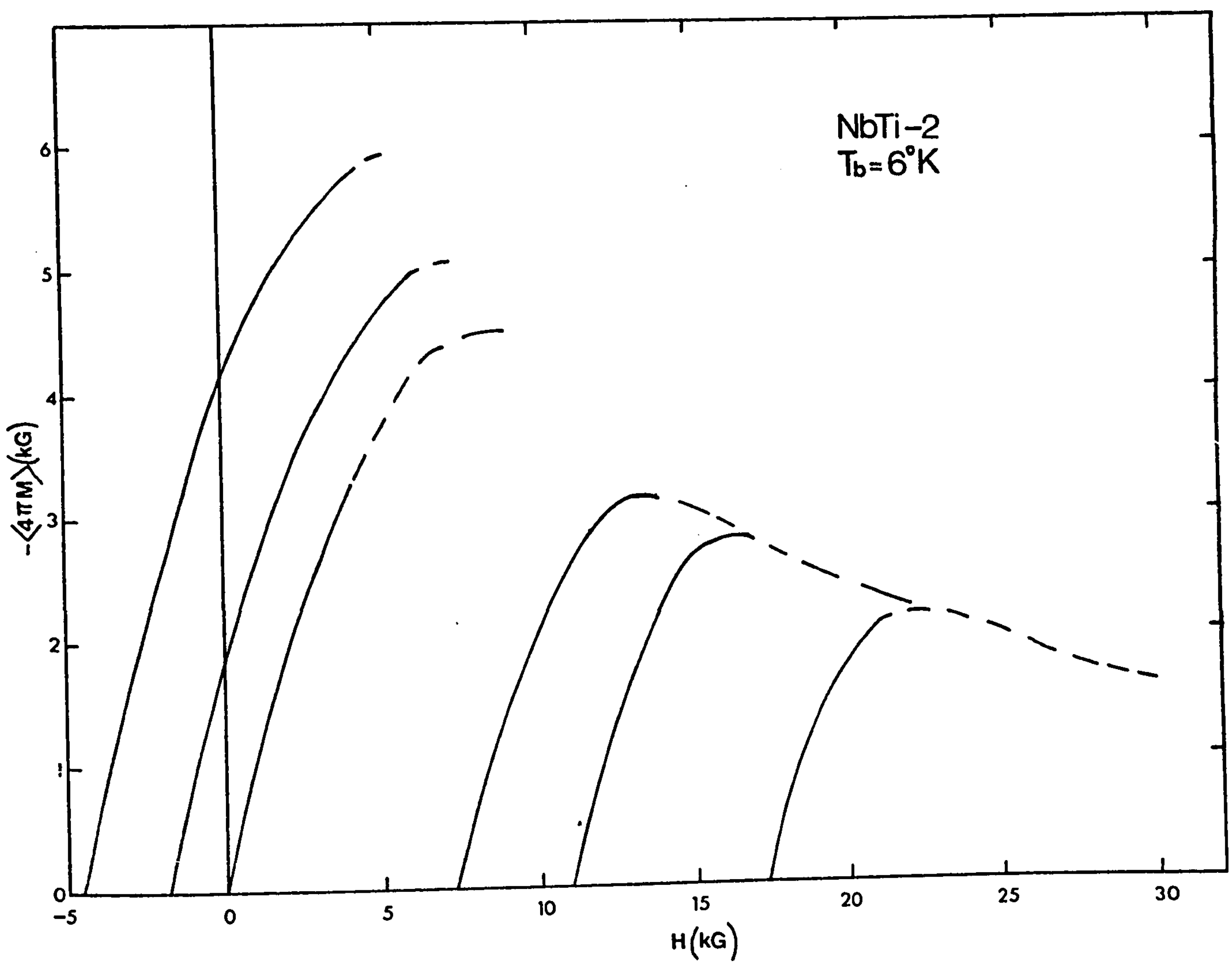

Fig. 14.8: Magnetization curves for NbTi-2 sample at T ∿ 6°K.

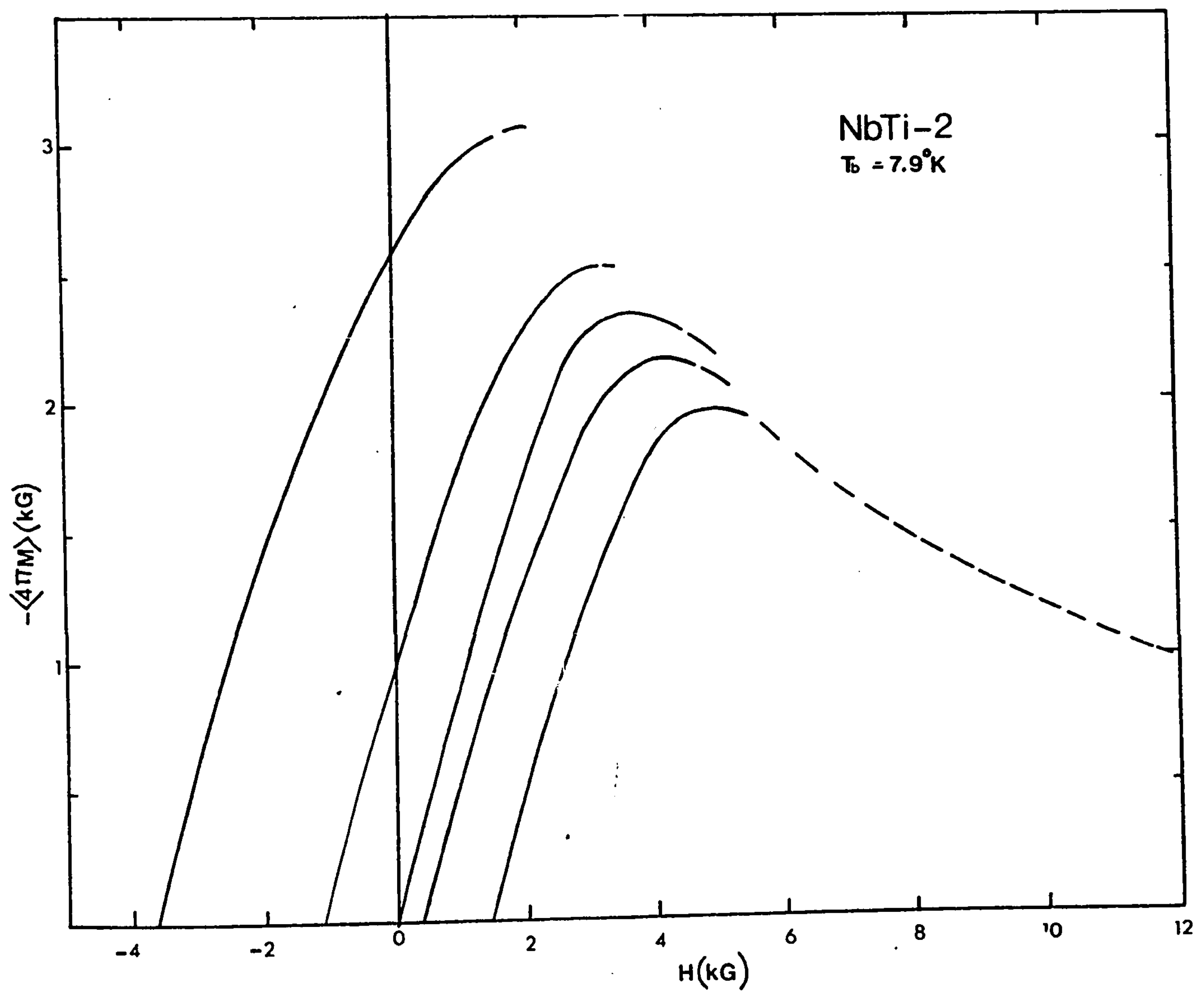

Fig. 14.9: Magnetization curves for NbTi-2 sample at T ∿ 7.9°K.

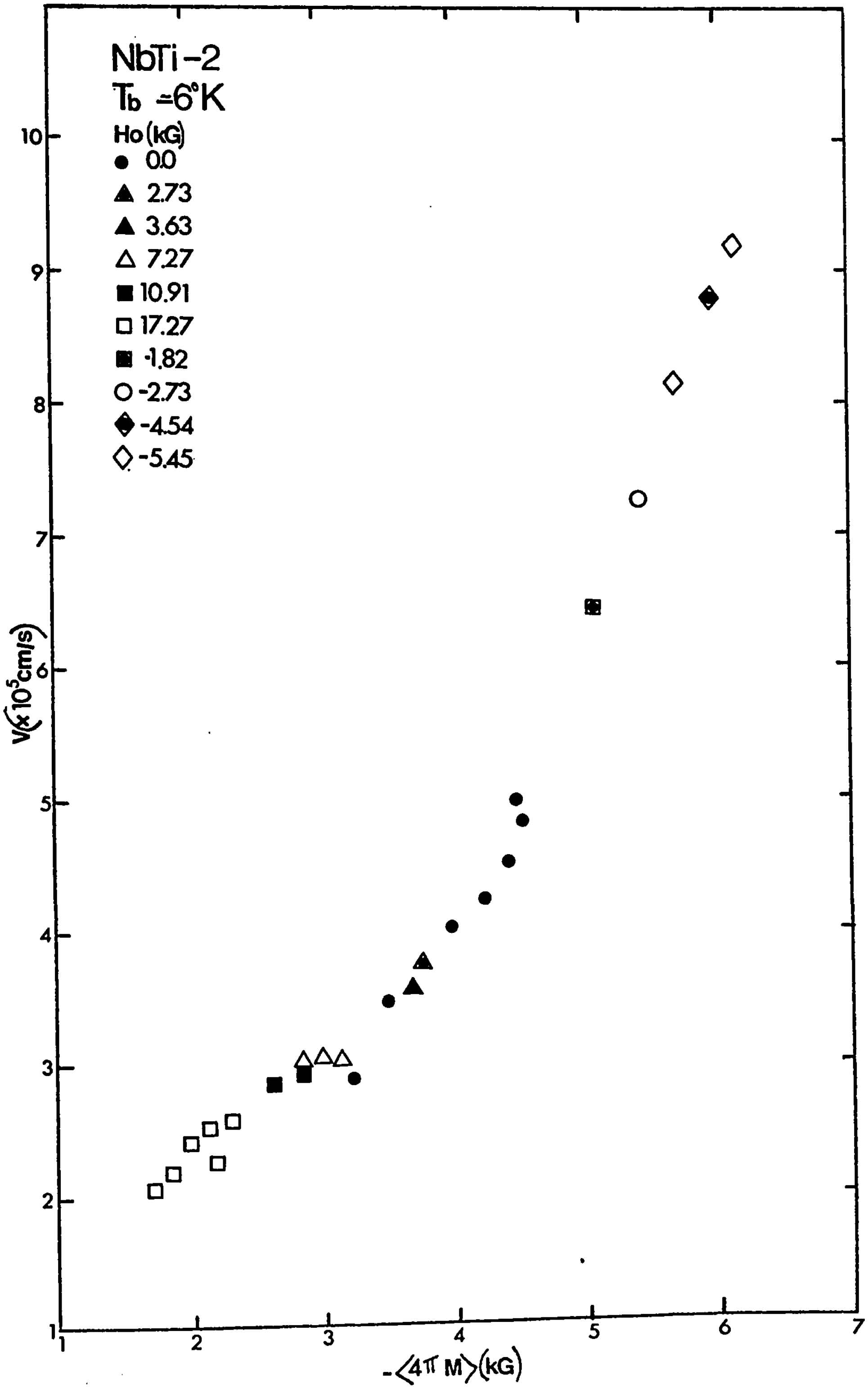

Fig. 14.10: Compilation of data on velocity vs. magnetization for flux jumps triggered along various magnetization curves at 6°K in NbTi-2 sample.

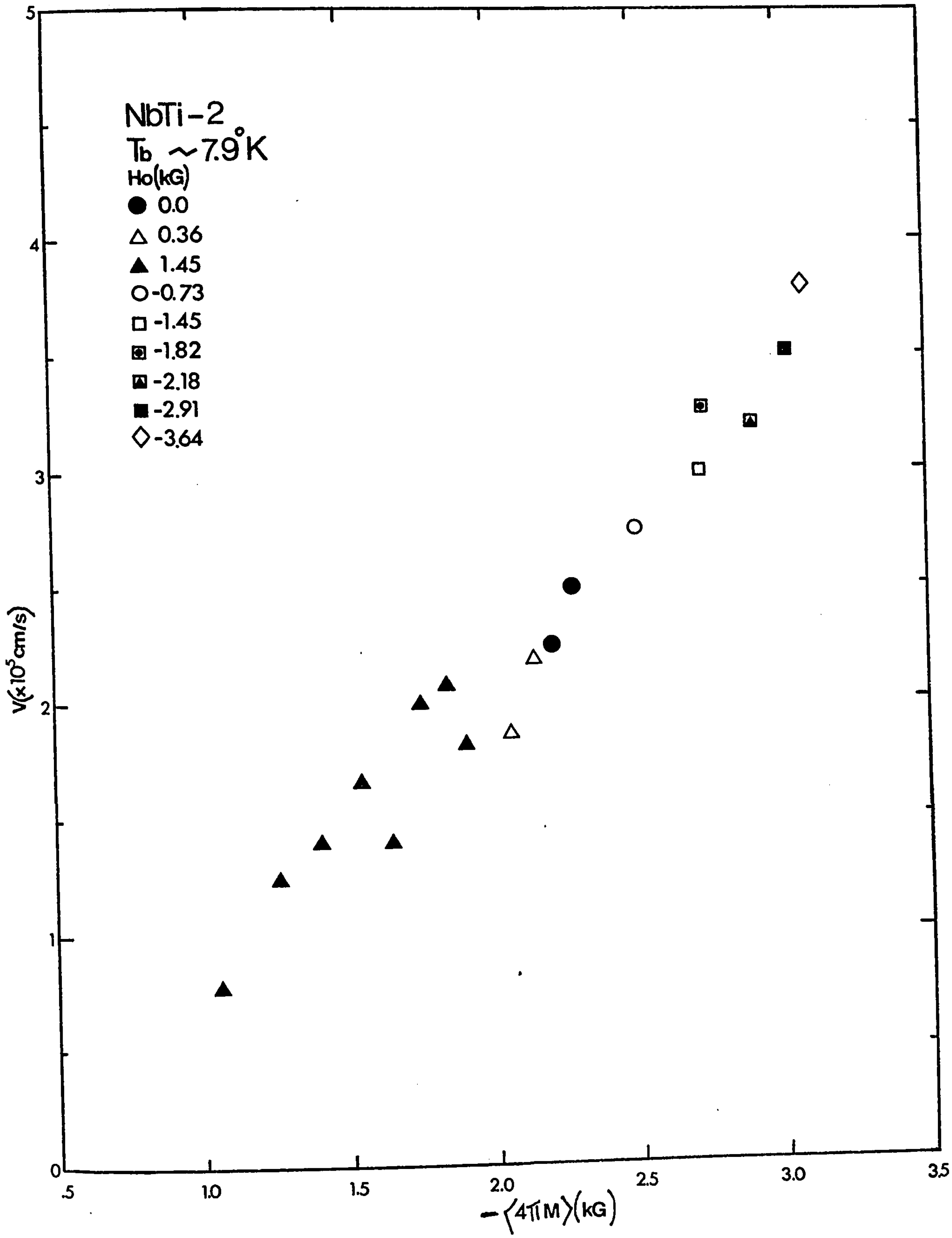

Fig. I4.11: Compilation of data on velocity vs. magnetization for flux jumps triggered along various magnetization curves at 7.9°K in NbTi-2 sample.

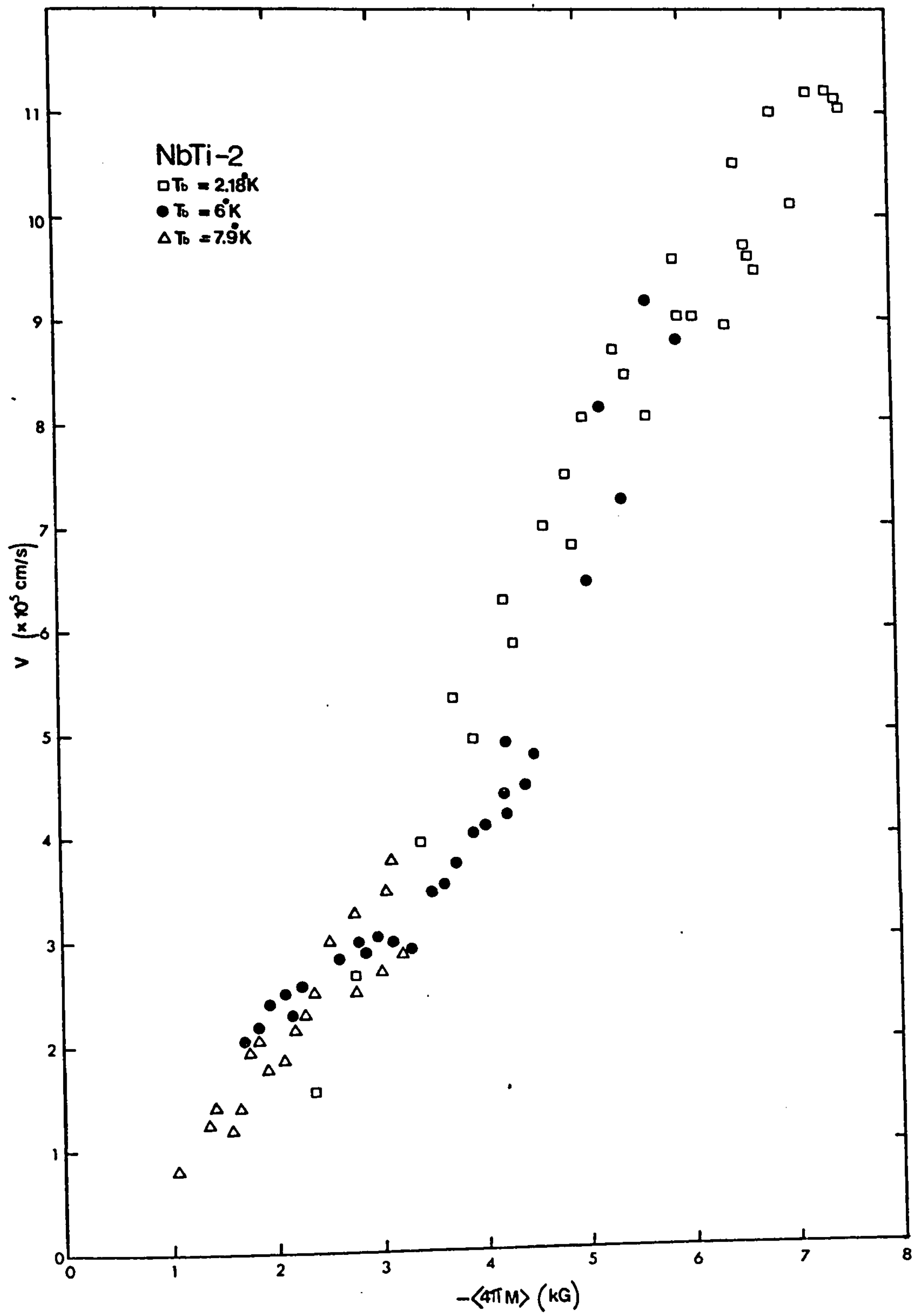

Fig. 14.12: Data of previous figures (14.10 and 14.11) compared with similar data taken at 2.18°K in same sample.

in the data for a given magnetization can be attributed to differences in the external magnetic field. A change in reduced bath temperature, T/T_c, does not appear in itself to lead to any significant changes in velocity.

c) V-1:

Figure 14.13 compares the velocities observed at different temperatures in a sample of Vanadium (V-1). The flux jumps were triggered along a large number of magnetization curves, the smaller values of $<4\pi M>$ corresponding to large fields. Although at a given temperature there is some scatter in the data due to variations of field profile and average magnetic induction, we note that for $<4\pi M>$ greater than $\sim$ 0.8 kG the velocity is larger for the lower bath temperatures. For the smaller moments ($<4\pi M> < 0.8$ kG) the velocity curves tend to overlap. At first glance, these curves appear to indicate that the temperature of the specimen plays an important role in determining the velocity. A careful examination of all of the pertinent aspects (H/H_{c2}, characteristics of the field profiles) for the group of flux jumps for individual curves reveals that these several contributions combine to yield curves which diverge strongly at large moments with decrease in temperature.

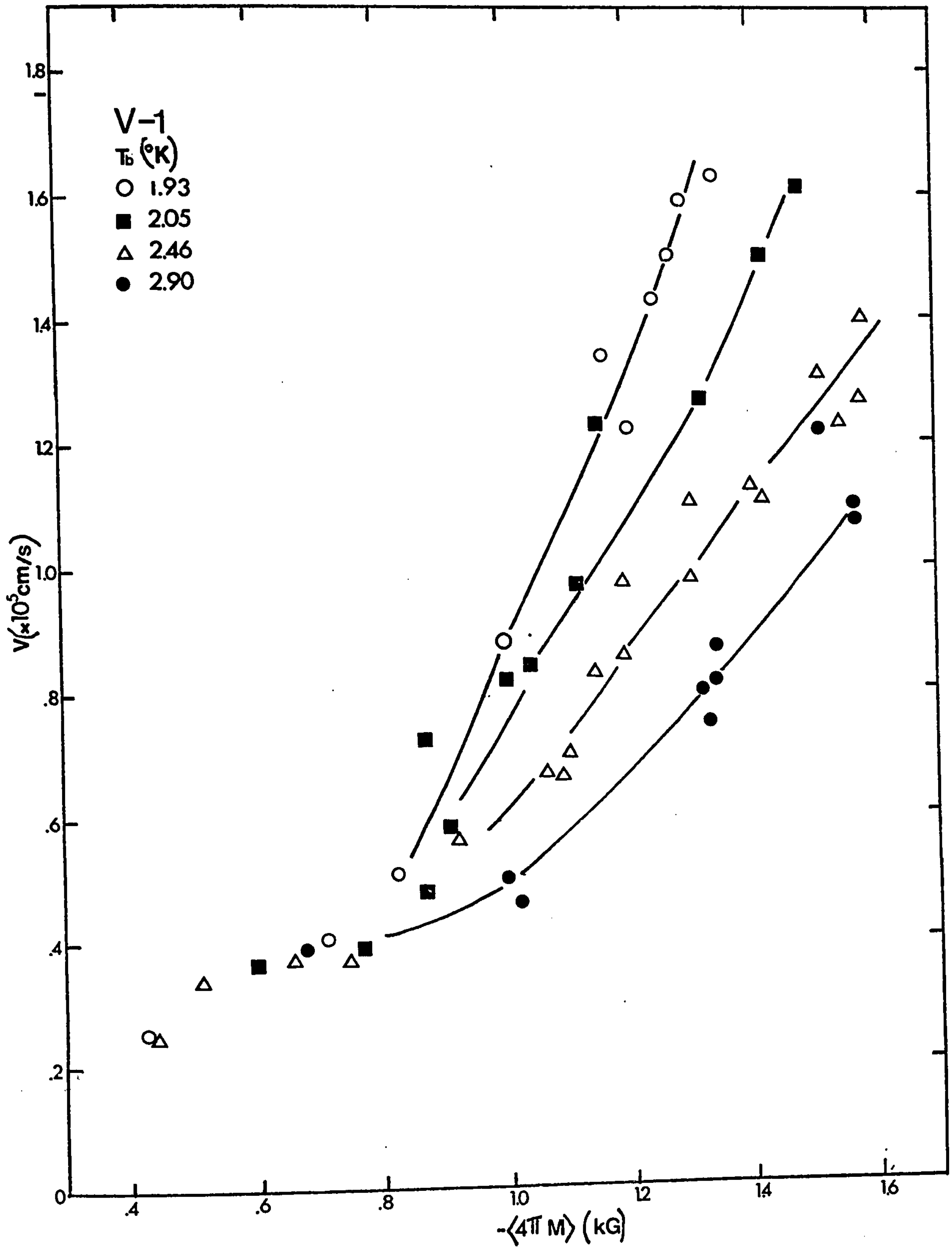

Fig. 14.13: Velocity vs. magnetization for Vanadium wire sample (V-1) measured at various temperatures indicated.

III DISCUSSION AND CONCLUSION

In this chapter we have reported on measurements of the velocity of propagation of flux jumps as a function of $\langle 4\pi M \rangle$ for samples of NbTi, NbZr and Vanadium at several bath temperatures. For all temperatures chosen for these samples the velocity is seen to increase with magnetization. From a comparison of the velocities at different temperatures we find that larger velocities usually occur when the temperature is lowered. This trend can however be attributed mainly to the effect of the magnetic field on the flux flow resistivity since flux jumps with a given $\langle 4\pi M \rangle$ correspond to higher fields at the lower temperatures in a given sample.

C H A P T E R XV

EFFECT OF DIAMETER ON LONGITUDINAL VELOCITY OF PROPAGATION OF FLUX JUMPS

I INTRODUCTION

In chapter IX we have presented measurements of the velocity of propagation of flux jumps in samples of NbTi, NbZr and Vanadium with different diameters. We noted that, for a given value of $<4\pi M>$, velocities are usually lower in samples of large diameter. In this chapter we explore the role of sample size in more detail. We also examine whether scaling laws applicable to the radial collapse of flux in cylinders of the same material with different diameters can account for the differences in longitudinal velocities. According to these scaling laws (chapter III) there is a quantitative correspondence in the size and duration of flux jumps for cylinders of the same material which have the same initial magnetization, identical field profiles and equal average magnetic inductions. In particular, under these circumstances, the magnitude, shape and duration of the voltage pulses will be identical for the cylinders, independently of diameter, provided the pulses are presented in terms of the reduced time t/τ_n, where τ_n is the normal state relaxation time. Since τ_n is proportional to the cross-section S of the cylinder, the rise time τ_{peak} and the relaxation time τ_R will also be proportional to S. As a consequence we expect the velocity to be inversely proportional to S since the longitudinal velocity is related to both τ_{peak} and τ_R (chapter XI).

II EXPERIMENTAL RESULTS

a) Vanadium:

Figure 15.1 compares velocities as a function of $<4\pi M>$ for two samples of Vanadium of different diameters at $2.5^{o}K$ (V-1 and V-2). We note that the velocities obtained for the sample of smaller diameter (V-1) are approximately a factor of two greater than the velocities obtained for sample V-2. In this case, the scaling laws for radial collapse are not completely applicable since the magnetization of the larger sample is greater in a given field than the magnetization of the sample of smaller diameter (see figures 9.30 and 9.34). Nevertheless it is encouraging to note that the ratio of the velocities ($\sim$ 2.4) compares approximately with the inverse ratio of the areas ($\sim$ 1.8)

b) NbTi:

Figure 15.2 compares the velocities encountered in two samples of NbTi of different diameter (NbTi-2 and NbTi-3). The corresponding magnetization curves are shown in figures 9.4 and 9.17. Unfortunately the scaling law is again not completely applicable to the raw data since equal magnetizations do not occur at comparable average fields. For a more meaningful comparison of velocities to be made we

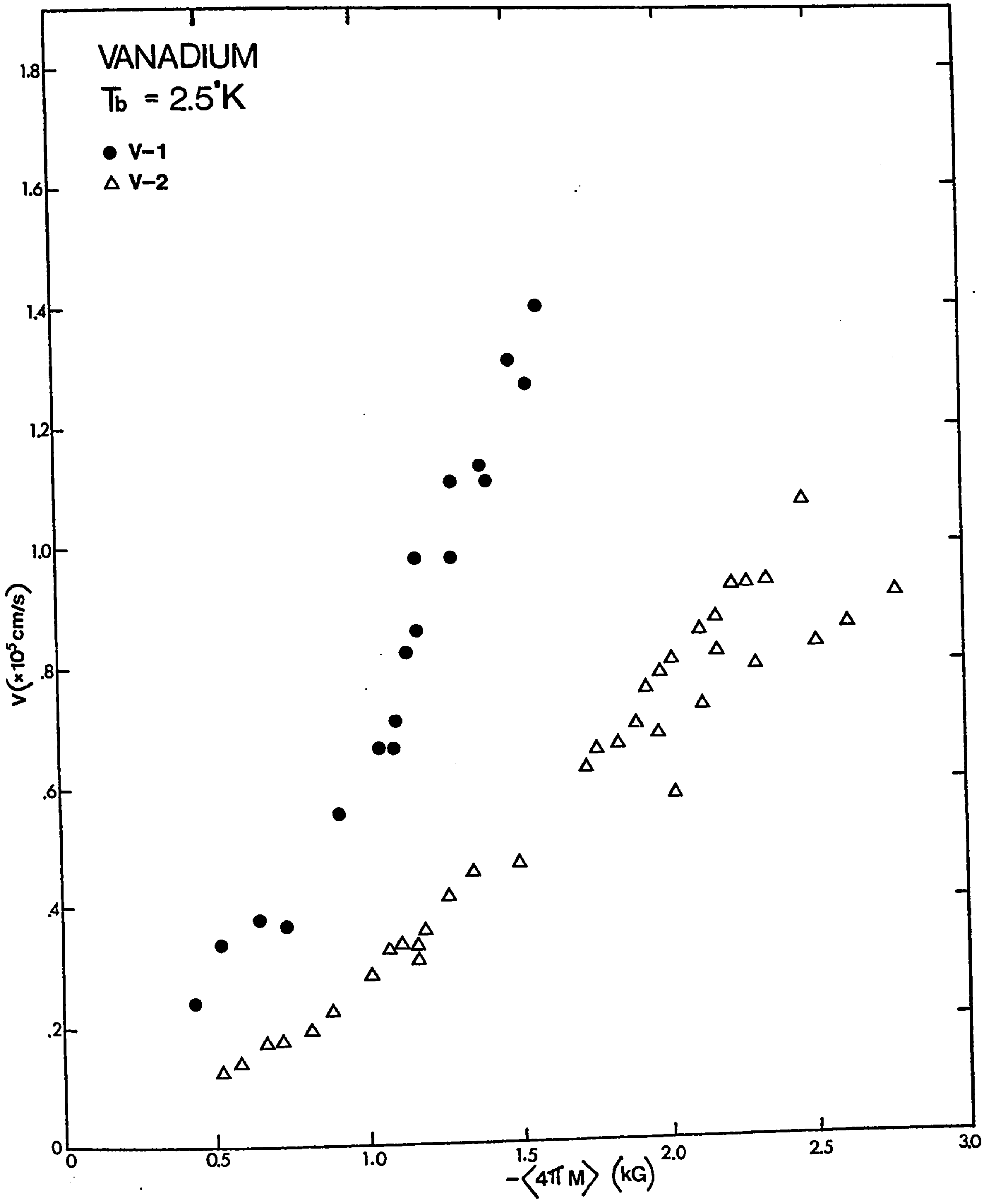

Fig. 15.1: Comparison of velocities in two Vanadium samples of different diameter (V-1 and V-2) at 2.5°K.

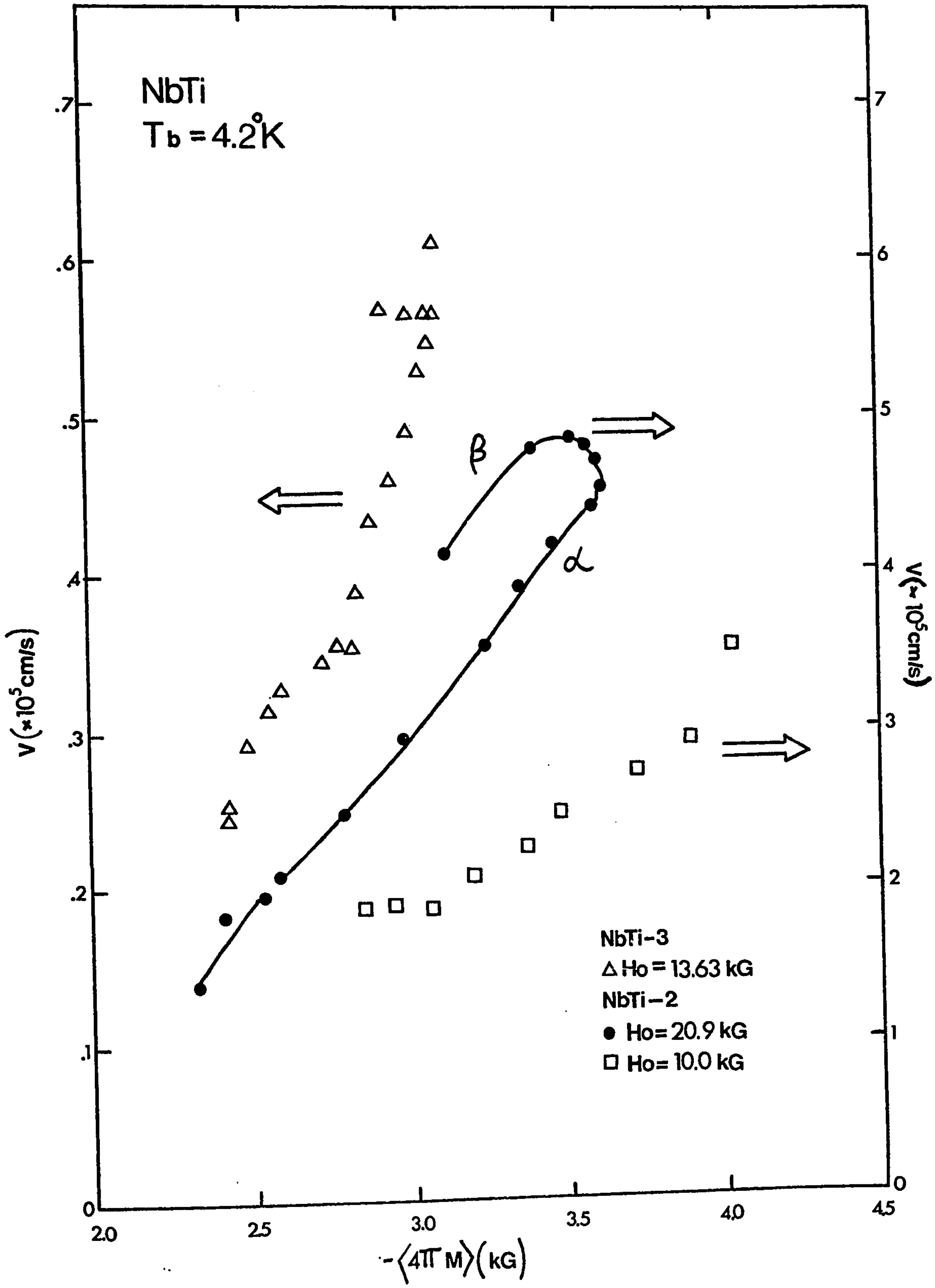

Fig. 15.2: Comparison of velocities obtained in the NbTi-2 and NbTi-3 samples at 4.2°K.

estimate an intermediate curve of velocity vs $<4\pi M>$ for the NbTi-2 sample by interpolation between the two measured curves. Using these interpolated values we find, for instance, that for $<4\pi M> \sim 3$ kG, $V \sim 2.4 \times 10^5$ cm/sec in NbTi-2. Comparing this value to the corresponding velocity $V \sim 0.35 \times 10^5$ cm/sec in NbTi-3 yields an observed ratio for the velocities of ~ 7, whereas the ratio of the inverse of the areas is ~ 14.

Figure 15.3 shows a comparison of velocities obtained in NbTi-1 and NbTi-2 for $H_o = 0$ (see figures 9.1 and 9.4 for the corresponding magnetization curves). In this case flux jumps of a given $<4\pi M>$ were produced in higher fields in NbTi-2. To partially and crudely take this feature into account in the comparison we take ratios of the higher field data (β branch) of the NbTi-1 sample with the lower field (α branch) data for the NbTi-2 sample. The observed ratio of velocities is ~ 1.5 whereas the ratio of the cross-sections is ~ 4.

c) NbZr:

Figure 15.4 compares the velocities obtained for the sample NbZr-1 ($H_o = 24.52$ kG) and sample NbZr-2 ($H_o = 27.27$ kG) for a bath temperature of 4.2^oK. We note again that the velocities are higher in the sample of smaller diameter (NbZr-1). The ratio of the velocities for a magnetization of 3.2 kG is ~ 3.2 whereas the ratio of the inverse of the areas is ~ 37. The large discrepancy between the two ratios for this material may be due to the following feature. The NbZr-2 sample had an extremely rough surface with several deep cracks extending to a

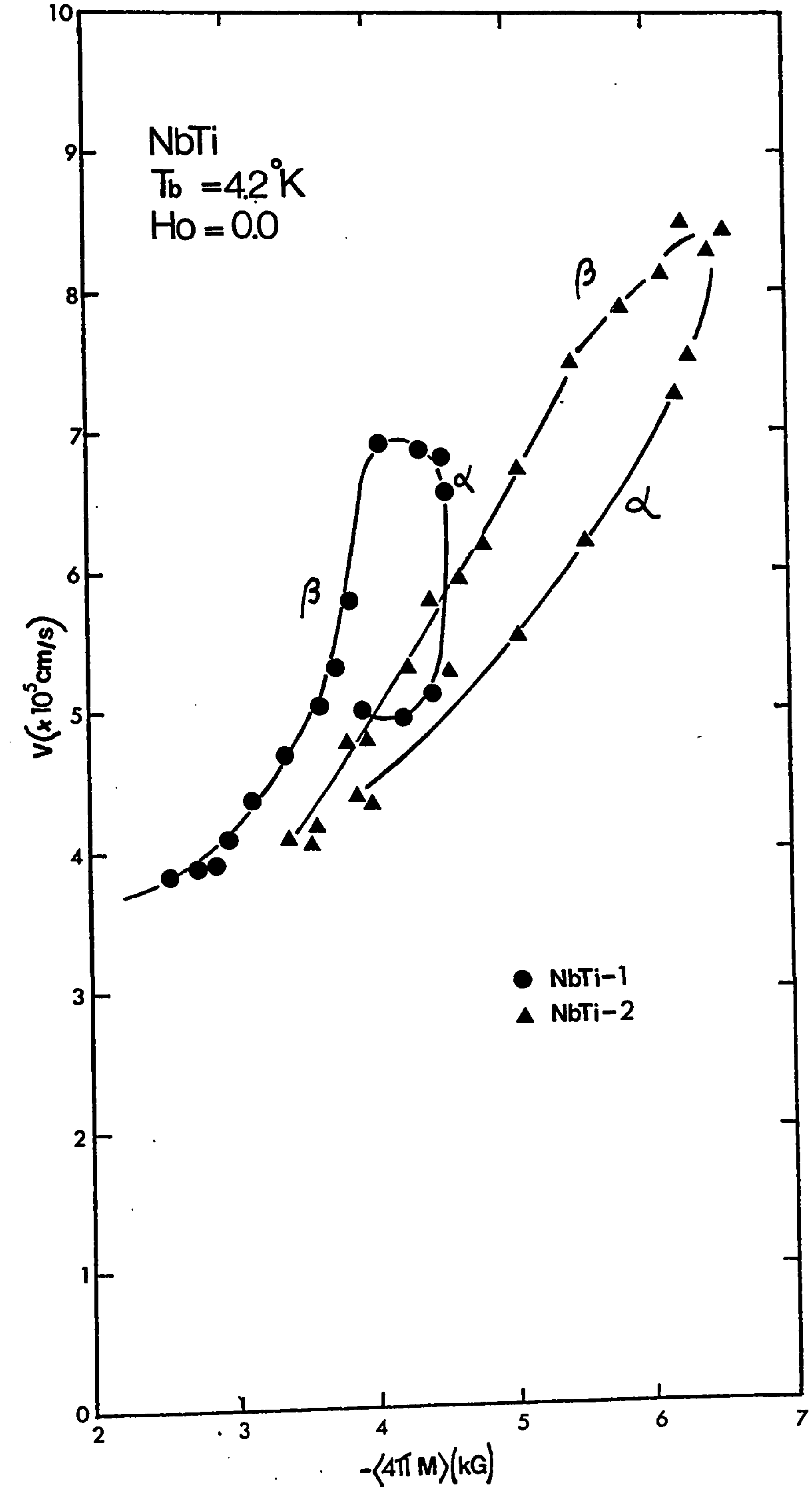

Fig. 15.3: Comparison of velocities obtained in the NbTi-1 and NbTi-2 samples at 4.2°K.

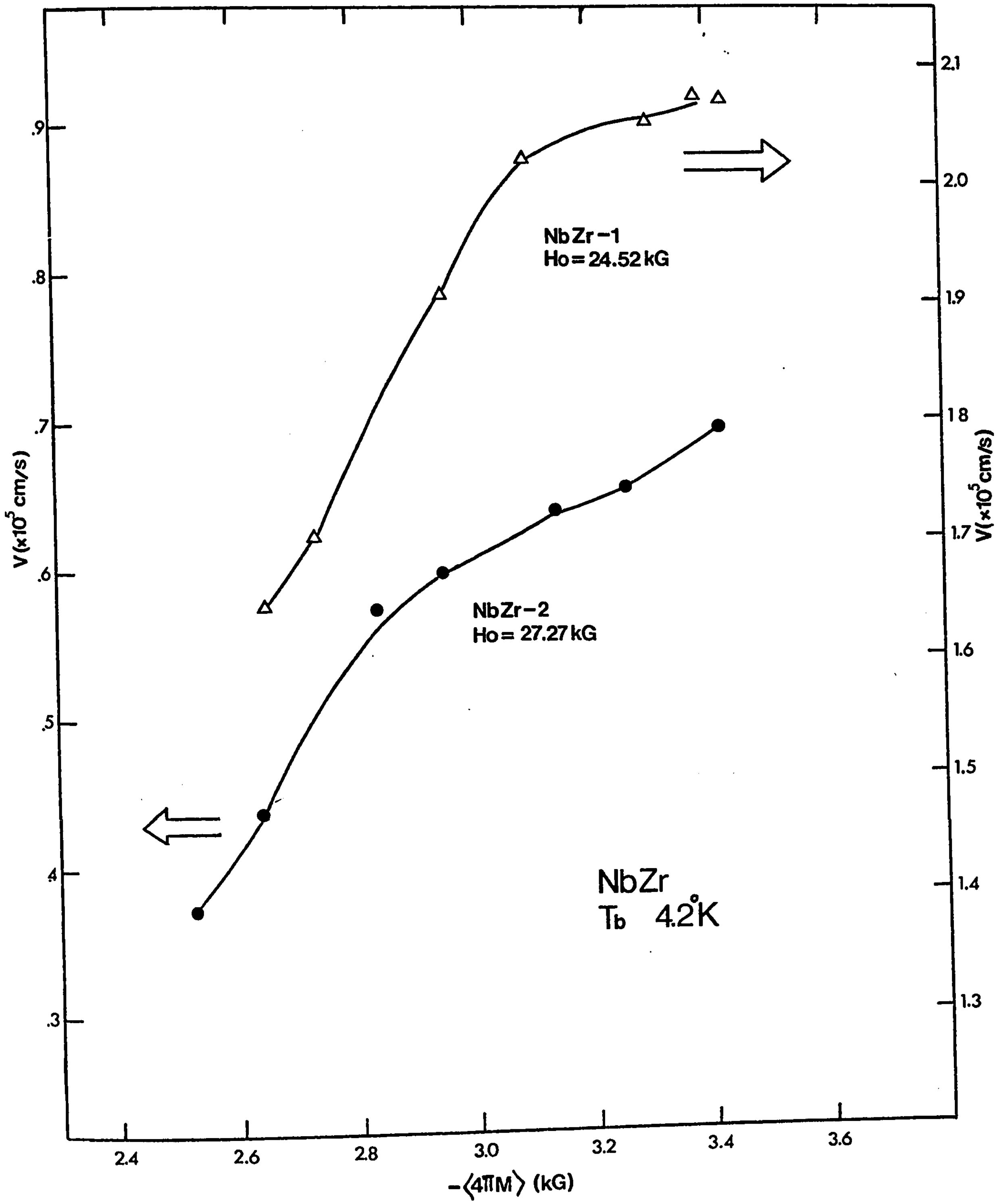

Fig. 15.4: Comparison of velocities in two NbZr samples of different diameter (NbZr-1 and NbZr-2) at 4.2°K.

depth of more than half its radius. The voltage pulses observed during longitudinal propagation of flux jumps in this sample exhibited considerable structure (see chapter X). We can then surmise that the flux penetration was very asymmetrical in this sample. If the flux collapse occurs in several separate regions and the disturbances propagate independently along the wire one can no longer expect the simple $V \propto 1/S$ law to apply. Under these circumstances we expect the velocity to be enhanced and to correspond to that for a specimen of diameter comparable to the distance between the fissures or cracks. This picture yields velocities in semi-quantitative agreement with our observations.

III DISCUSSION AND CONCLUSION

We have shown in this chapter that for a given value of $\langle 4\pi M \rangle$ the velocity of longitudinal propagation of flux jumps is smaller in cylinders of larger diameter. This behaviour can be understood qualitatively in terms of the characteristics of radial flux collapse for cylinders differing in diameter only. Our analysis of cylindrically symmetric flux penetration showed the time for radial flux collapse to be inversely proportional to the cylinder cross-section when the initial magnetizations, field profiles and average magnetic inductions are the same. We expect the longitudinal velocities to vary in the same manner since the speed of longitudinal propagation of flux jumps appears to be determined by the rate of radial collapse of flux. This scaling law is well obeyed for our vanadium samples. Although we encounter deviations from this scaling law in the NbTi samples, the results are encouraging. For the NbZr samples, we are confronted by a discrepancy of an order of magnitude. Nevertheless, in this case we can adequatenly reconcile our observations with expectations. The presence of several deep cracks along the length of the specimen of large diameter and the variegated structure of the voltage pulses seen during longitudinal propagation of the flux jumps in this sample both indicate that the radial flux collapse is irregular. We visualize that because of the cracks the specimen behaves as if it consisted of several parallel sections in each of which flux collapses and the disturbances propagate independently of the rest of the sample. As a consequence, the velocity of longitudinal propagation, in this situation, corresponds to that expected for a wire of diameter comparable to the spacing between the cracks and hence is much greater than anticipated for a homogeneous solid cylinder.

C O N C L U S I O N

In this thesis we have investigated two aspects of the kinetics of flux jumps in type II superconducting cylinders subjected to axial fields, the radial collapse of flux and the longitudinal propagation of this collapse.

We investigated both theoretically and experimentally the radial collapse of flux in type II superconducting cylinders perturbed initially over their entire surface. The theoretical analysis was based on a flux diffusion equation derived from Faraday's law of induction and the concept of flux flow resistivity. Numerical solutions of this equation and a coupled heat equation were presented for a large number of initial conditions for cylinders with physical characteristics corresponding to NbTi. Although in these calculations we assumed adiabatic conditions and the Bean critical state model, the calculations can easily be extended to more realistic situations.

The model gives a complete description of flux jumps, i.e. gives information on the limit of stability, the evolution and distribution of field, temperature and power dissipation density in the superconductor during flux jumps and, in particular, the final configuration of field and temperature.

To gain more insight on the role played by the initial magnetization $\langle 4\pi M \rangle$, the initial field profile, and average magnetic induction $\langle B \rangle$ we presented calculations of the rate of radial flux collapse, size of flux jumps, and evolution of field, temperature and power dissipation density profiles when each of these parameters is varied separately. These calculations indicate that the rate of radial flux collapse increases rapidly with $\langle 4\pi M \rangle$ and $\langle B \rangle$. For a constant $\langle 4\pi M \rangle$ the initial field profile is found to also play an important role. The size of the flux jumps decreases monotonically as the steepness of the field gradient is increased. The duration of flux jumps (pulse width) is a double-valued function of the initial depth of penetration of the field profile with the maximum occurring for an initial penetration of $\sim$ 20% of the radius. For very steep gradients the size of the flux jumps decreases rapidly and the rate of radial collapse increases very rapidly.

Experimental measurements of the relaxation time τ_R (pulse width) were presented for flux jumps triggered along a selected magnetization curve of a NbTi rod. This time was observed to be very large near the limit of stability, to decrease rapidly in this field region, and to vary slowly in fields distant from this region. This behaviour was reproduced qualitatively and quantitatively with our calculations.

We also carried out an experimental investigation of the longitudinal propagation of flux jumps in type II superconducting cylinders subjected to axial fields. We showed that when both a transport current and an axial magnetic moment are present in a superconducting wire the mechanism of propagation is either thermal or electromagnetic depending on whether the magnetic field profile is stable or unstable. When the wire is in an unstable critical state the mechanism of propagation changes from thermal to electromagnetic.

We also investigated the rate of propagation of instabilities in cylinders of NbTi, NbZr, Vanadium and Niobium carrying no transport current but for a large number of initial conditions. Velocities ranging between 10^4 and 10^6 cm/sec were encountered in these samples. The velocity was found to depend on the initial configuration of magnetic field before propagation. The role played by the initial average magnetization was investigated carefully. Velocities were found to generally increase with $<4\pi M>$ in all the samples. The initial magnetic profile and average magnetic induction were found to also play an important role. In all cases the changes in velocity could be qualitatively related to features emerging from the calculations for the radial flux collapse.

These results encouraged us to investigate more quantitatively the relation between the rate of radial flux collapse and the longitudinal velocity. Our observations show that the longitudinal velocity is entirely determined by the detailed characteristics of radial flux collapse. Consequently, a simple expression was proposed which satisfactorily predicts longitudinal velocities.

In some samples under certain circumstances the radial flux collapse is irregular and asymmetrical leading to the longitudinal propagation of several flux distributions travelling more or less independently along the cylinder. The occurrence of this type of phenomenon is deduced from structures in the voltage pulses observed during longitudinal propagation. To account for an initial diminution in longitudinal propagation velocity with level of conduction current in wires supporting axial trapped flux, we have postulated that local disturbances travel independently and helically following the lines of magnetic flux near the surface of the cylinder. The transport current density superimposed on the azimuthal magnetization currents leads to high rates of energy dissipation during the radial flux collapse and hence to large velocities of propagation along the lines of flux. At high conduction current levels this contribution dominates and leads to a nearly linear increase in the resultant velocity of propagation along the cylinder axis. A simple expression is developed in the perspective of this model which quantitatively describes our observations.

APPENDIX A

DIFFUSION OF MAGNETIC FIELD IN A NORMAL SLAB WHERE THE INITIAL FIELD PROFILE IS LINEAR: EXACT SOLUTION

The equation governing the penetration of field in a normal conductor is:

$$\frac{\partial^2 H}{\partial x^2} = \kappa^{-1} \frac{\partial H}{\partial t} \tag{A-1}$$

where $\kappa = 10^9 \rho_n / 4\pi$ is the magnetic diffusivity. In the case of a finite slab with the initial field profile given in figure 2.1, the solution to A-1 must satisfy the following boundary conditions:

a) At time $t = 0$:

$$H(x) = H_o \frac{|x|}{a} - H_o \tag{A-2}$$

b) At time $t \geqslant 0$:

$$H(a) = H(-a) = 0 \tag{A-3}$$

Each term in the series:

$$H(x,t) = \sum_{n=0}^{\infty} \ell^{-\kappa A_n^2 t} P_n \cos A_n x \quad , \tag{A-4}$$

where A_n and P_n are constants, satisfies equation A-1. The solution of A-4 which satisfies the boundary conditions A-2 and A-3 is therefore the solution we are looking for.

From A-3 we conclude that:

$$\cos A_n a = 0 \qquad \text{for all } n$$

and therefore:

$$A_n = \left(\frac{n\pi}{2a}\right) \qquad \text{for } n \text{ odd}$$

and:

$$P_n = 0 \qquad \text{for } n \text{ even.}$$

Using A-2 we obtain:

$$H(t=0,x) = H_o\left\{\frac{|x|}{a} - 1\right\} = P_o + \sum_{n\ \text{odd}} P_n \cos\left(\frac{n\pi}{2a}\right)x$$

Introducing $X = \frac{\pi x}{a}$:

$$H(X)_{t=0} = H_o\left\{\frac{2|X|}{\pi} - 1\right\} = P_o + \sum_{n\ \text{odd}} P_n \cos(nX) \qquad \text{A-5}$$

Equation A-5 is a Fourier series where the coefficients P_n can be easily evaluated:

$$P_o = \frac{2}{\pi} \int_{-\pi}^{\pi} H_o(\frac{2|x|}{\pi} - 1)\,dX = 0$$

$$P_n = \frac{H_o}{\pi} \int_{-\pi}^{\pi} [\frac{2|x|}{\pi} - 1] \cos nX \, dX$$

$$= \frac{4H_o}{n^2\pi^2} \quad [(-1)^n - 1]$$

Using these values of P_n in equation A-4 we obtain:

$$H(x,t) = \frac{-8H_o}{\pi^2} \sum_{n \text{ odd}} \frac{\cos (\frac{n\pi}{2a})x}{n^2} e^{-\kappa(\frac{n\pi}{2a})^2 t}$$

Integrating $H(x,t)$ over the whole slab yields the total flux $\phi(a,t)$ as a function of time:

$$\phi(a,t) = \int_{-a}^{+a} H(x)\,dx = 2\int_{o}^{a} H(x)\,dx$$

$$\phi(a,t) = \frac{-32H_o a}{\pi^3} \{e^{-\kappa(\frac{\pi}{2a})^2 t} - \frac{1}{3^3} e^{-\kappa(\frac{3\pi}{2a})^2 t} + \frac{1}{5^3} e^{-\kappa(\frac{5\pi}{2a})^2 t} - \ldots\}$$

After a short time compared to τ_n, the first term will dominate and we can neglect the other terms in the series, then:

$$\phi(a,t) \simeq \frac{-32H_o a}{\pi^3} e^{-t/\tau_n}$$

where

$$\tau_n = \frac{16a^2 \times 10^{-9}}{\pi\rho_n} \simeq \frac{5.093a^2 \times 10^{-9}}{\rho_n} \text{ sec.}$$

In a normal slab the decay of flux as a function of time can therefore be described as an infinite sum of exponentials where the time constants in the series of terms decrease rapidly.

For times large compared to the largest time constant τ_n, a good approximation is obtained by retaining only the first time in the series, characterized by time constant τ_n.

APPENDIX B

PENETRATION OF FLUX IN A SUPERCONDUCTING SLAB: NUMERICAL METHOD OF SOLUTION

The equations governing the penetration (or exit) of flux as a function of position and time in a superconducting slab have been derived in chapter III and are reproduced below:

$$\frac{\partial^2\phi}{\partial x^2} - \frac{4\pi}{10} J_c(T) = \frac{4\pi \times 10^{-9}}{\rho_f(H,T)} \frac{\partial\phi}{\partial t} \qquad \text{B-1}$$

$$C(T) \frac{\partial T}{\partial t} = \frac{10^{-7}}{4\pi} \left(\frac{\partial\phi}{\partial t}\right) \left(\frac{\partial^2\phi}{\partial x^2}\right) \qquad \text{B-2}$$

where

$$\phi(x) = \int_0^x H(x)\,dx, \qquad \text{B-3}$$

$C(T)$ is the specific heat per unit volume in Joules/cm^3.deg, ρ_f is the flux flow resistivity in Ω-cm, and J_c is the critical current density in A/cm^2. $H(x)$ is the local magnetic field in gauss.

The initial field profile which we consider is shown in figure 3.1 and is described by the following equations:

$$H(x) = \begin{cases} 0 & \text{for } x < x_z \\ \dfrac{H_{ex}}{(a - x_z)} (x - x_z) & \text{for } x_z \leqslant x \leqslant a \end{cases} \qquad \text{B-4}$$

The solution of B-1 and B-2 must therefore satisfy the following boundary conditions:

a) At time t = 0:

$$\phi(x) = \begin{cases} 0 & \text{for } x < x_z \\ \dfrac{H_{ex}}{(a - x_z)} \left(\dfrac{x^2}{x_z} - x_z x + \dfrac{x_z^2}{2}\right) & \text{for } x_z \leqslant x \leqslant a \end{cases} \qquad \text{B-5}$$

where $\phi(x)$ is obtained by integrating equation B-4.

The initial temperature is that of the bath, except for a perturbation which we introduce near the surface:

$$T(x) = \begin{cases} T_b & \text{for} \quad 0 < x < x_t \\ T_b + \delta T & \text{for} \quad x_t \leqslant x \leqslant a \end{cases} \qquad \text{B-6}$$

where x_t and δT are adjustable parameters.

b) At times $t \geqslant 0$:

$$\phi(x = 0) = 0 \qquad \text{B-7}$$

$$H(a) = H_{ex}$$

or B-8

$$\left(\frac{\partial \phi}{\partial x}\right)_{x=a} = H_{ex}$$

Before solving B-1 and B-2, we express these two equations in terms of dimensionless parameters:

$$\frac{\partial^2 \Phi}{\partial \eta^2} - K(1 - \theta) = L(\theta) \frac{\partial \Phi}{\partial \xi} \qquad \text{B-9}$$

$$\frac{\partial \theta}{\partial \xi} = \frac{1}{(G_1\theta + G_2\theta^n)} \left[\frac{\partial \Phi}{\partial \xi} \cdot \frac{\partial^2 \Phi}{\partial \eta^2} \right] \qquad \text{B-10}$$

where the following simple function was used to describe the dependence of the specific heat on magnetic field and temperature:

$$C(T) = \frac{H}{H_{c2}} \gamma T + \alpha T^n$$

The variables and coefficients appearing in B-9 and B-10 are defined as follows:

$$\Phi = \phi / \phi_o,$$

$\theta = T/T_{ch}$ where T_{ch} is the critical temperature in the applied field H

$$\xi = t/\tau_n$$

$$\eta = x/a$$

$$\phi_o = a.H_{ex}$$

$$\tau_n = \frac{5.09a^2 \times 10^{-9}}{\rho_n} \text{ sec} \qquad \text{B.11}$$

$$K = \frac{4\pi}{10} a^2 J_o/\phi_o$$

$$L(\theta) = \pi^2/ 4(\rho_f/\rho_n)$$

$$G_1 = \frac{4\pi H_o}{H_{c20}} \gamma T_{ch}^2 / (10^{-7} \phi_o^2/a^2)$$

$$G_2 = 4\pi\alpha T_{ch}^{n+1}/(10^{-7} \phi_o^2/a^2)$$

Using the value of $\frac{\partial \Phi}{\partial \eta}$ we can define a reduced field $\mathcal{H}(\eta)$ where:

$$\mathcal{H}(\eta) = \frac{H(x)}{H_{ex}}$$

Rewriting the boundary conditions in terms of the dimensionless parameters Φ and θ we obtain:

a) At time t = 0:

$$\Phi(\eta) = \begin{cases} 0 & \text{for } \eta < \eta_z \\ \frac{1}{(1-\eta_z)}\left\{\frac{\eta^2}{2} - \eta_z \eta + \frac{\eta_z^2}{2}\right\} & \text{for } \eta_z \leqslant \eta \leqslant 1 \end{cases} \qquad \text{B-12}$$

where $\eta_z = x_z/a$

$$\theta(\eta) = \begin{cases} \theta_b & \text{for } 0 < \eta < \eta_t \\ \theta_b + \delta\theta & \text{for } \eta_t \leqslant \eta \leqslant 1 \end{cases} \qquad \text{B-13}$$

where

$\theta_b = T_b/T_{ch}$ and $\eta_t = x_t/a$

b) at times $t \geqslant 0$:

$$\Phi(\eta=0) = 0 \qquad \text{B-14}$$

$$H(\eta=1) = 1$$

or $$\left(\frac{\partial\Phi}{\partial\eta}\right)_{\eta=1} = 1 \qquad \text{B-15}$$

To solve equations B-9 and B-10 numerically, the slab is divided into R intervals, each of length $\Delta\eta$, hence

$$\Delta\eta = 1/R$$

and the time is divided in equal intervals of normalized duration $\Delta\xi$. The position of the i^{th} grid point in the slab is therefore given by:

$$\eta_i = i\Delta\eta$$

and the time corresponding to the n^{th} interval given by:

$$\xi_n = n\Delta\xi$$

The method of solution consists in writing a finite difference analog to equation B-9 in which the values of Φ at time level $(n + 1)$ form a tridiagonal matrix whose coefficients are known at this time level. The values of Φ at time level $n + 1$ are then computed with the Thomas algorithm as described in appendix D. Using these values of Φ the temperatures $\theta_{i,\, n+1}$ are then computed using the analog of equation B-10; these temperatures are then used to evaluate Φ for the next time level.

Among the several possible analog equations we have chosen the Crank-Nicolson equation which is stable for a large range of ratios of $\Delta\eta^2/\Delta\xi$ and is second order correct both in η and in ξ (Rosenberg 69). In this equation all the finite differences are written about the point $(\eta_i,\ \xi_{n+\frac{1}{2}})$ which is halfway between the known (level n) and unknown (n + 1) time levels. In figure B.1 this point is shown as a cross. Values of the dependent variables Φ and θ are computed only for the points designated as circles.

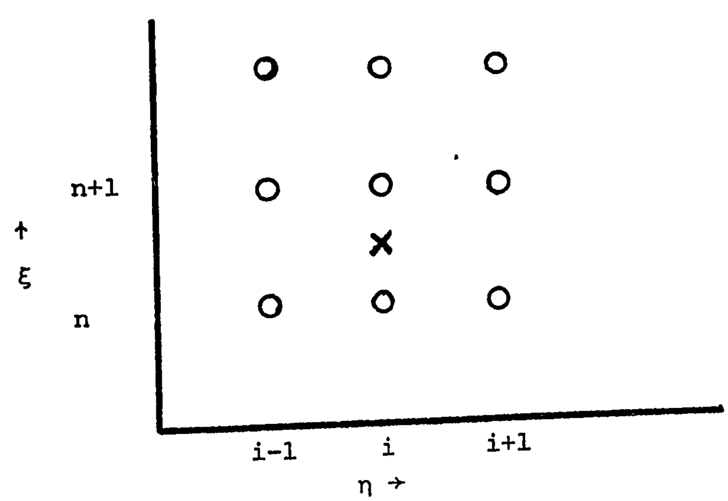

figure B.1

The second order correct analog for the time derivative of Φ at point $(\eta_i, \xi_{n+\frac{1}{2}})$ is:

$$\left(\frac{\partial\Phi}{\partial\xi}\right)_{i,\, n+\frac{1}{2}} \simeq \frac{\Phi_{i,\, n+1} - \Phi_{i,\, n}}{\Delta\xi} \qquad \text{B-16}$$

The derivative $\left(\frac{\partial^2\Phi}{\partial\eta^2}\right)_{i,\, n+\frac{1}{2}}$ is approximated by the arithmetic average of its finite difference analogs at points (η_i, ξ_n) and (η_i, ξ_{n+1}). The resulting analog is (Rosenberg 69):

$$\left(\frac{\partial\,\Phi}{\partial\eta}\right)_{i,\, n+\frac{1}{2}} \simeq \frac{1}{2}\left[\frac{\Phi_{i+1,\, n} - 2\Phi_{i,\, n} + \Phi_{i-1,\, n}}{(\Delta\eta)^2}\right.$$

$$\left. + \frac{\Phi_{i+1,\, n+1} - 2\Phi_{i,\, n+1} + \Phi_{i-1,\, n+1}}{(\Delta\eta)^2}\right] \qquad \text{B-17}$$

The Crank-Nicolson second-order correct analog to B-9 is obtained by replacing analogs B-16 and B-17 in B-9. In these analogs the value $\theta_{i,\, n+\frac{1}{2}}$ will appear. These values however are unknown and to obtain the values of Φ at time level n + 1 we make the following approximation:

$$\theta_{i,\, n+\frac{1}{2}} \simeq \theta_{i,\, n} \qquad \text{B-18}$$

A. Case Where the Field has Initially Penetrated to the Center of the Slab.

In the case where the field has initially penetrated to the center of the slab ($\eta_z = 0$) equation B-9 is valid throughout the entire slab at all times. Hence, we may obtain the following analog to B-9 at point $(\eta_i, \xi_{n+\frac{1}{2}})$. For $2 \leqslant i \leqslant R - 1$:

$$\Phi_{i-1,\, n+1} + \Phi_{i,\, n+1} \left\{ -2 - 2L(\theta_{i,\, n}) \frac{[\Delta\eta]^2}{\Delta\xi} \right\} + \Phi_{i+1,\, n+1}$$

$$= 2K(\Delta\eta)^2 \left[1 - \theta_{i,\, n}\right] - \delta^2\Phi_{i,n} - 2L(\theta_{i,\, n}) \frac{[\Delta\eta]^2}{\Delta\xi} \Phi_{i,\, n}$$

B-19

where

$$\delta^2 \Phi_{i,\, n} = \Phi_{i-1,\, n} - 2\Phi_{i,\, n} + \Phi_{i+1,\, n} \qquad \text{B-20}$$

To obtain the equations for $i = 1$ and $i = R$ we rewrite the boundary conditions B-20 as:

B-21a

$$\Phi_{i=0} = 0 \qquad \text{(all n)}$$

$$\frac{\Phi_{R+1,\, n} - \Phi_{R-1,\, n}}{2\Delta\eta} = 1 \qquad \text{(all n)}$$

or

$$\Phi_{R+1,\ n} = \Phi_{R-1,\ n} + 2\Delta\eta \qquad \text{B-21b}$$

Thus we obtain the analog equations for i = 1 and i = R:

For i = 1:

$$\Phi_{1,\ n+1} \{ -2 - 2\ L(\theta_{1,\ n}) \frac{[\Delta\eta]^2}{\Delta\xi} \} + \Phi_{2,\ n+1}$$

$$= 2K[\Delta\eta]^2 \ [1 - \theta_{i,\ n}] - \delta^2\Phi_{1,\ n} - 2L(\theta_{1,\ n}) \frac{[\Delta\eta]^2}{\Delta\xi} \Phi_{1,\ n}$$

B-22

where

$$\delta^2\Phi_{1,\ n} = \Phi_{2,\ n} - 2\Phi_{1,\ n}$$

and for i = R:

$$2\Phi_{R-1,\ n+1} + \Phi_{R,\ n+1}\{ - 2 - 2\ L(\theta_{R,n}) \frac{[\Delta\eta]^2}{\Delta\xi} \}$$

$$= -4\Delta\eta + 2K[\Delta\eta]^2 \ [1 - \theta_{R,n}] - \delta^2\Phi_{R,n} - 2L(\theta_{R,n}) \frac{\Delta\eta^2}{\Delta\xi} \Phi_{R,n}$$

B.24

where

B.25

$$\delta^2 \Phi_{R,n} = 2[\Phi_{R,n} + \Phi_{R-1,\ n}]$$

Equation B-19 is therefore the correct analog to B-9 for $2 \leq i \leq R-1$. For $i = 1$ and $i = R$, equations B-22 and B-24 are the corresponding correct analogs respectively.

Equations B-19, B-22 and B-24 form a tridiagonal matrix, the dependent variable being the value of Φ at time level $n + 1$, and can be solved with the Thomas algorithm (appendix D).

B. Case Where the Field Has Not Initially Penetrated to the Center of the Slab:

In the case where the magnetic field has not initially penetrated to the center of the slab (i.e. $\eta_z \neq 0$) equation B-9 is initially valid only for $\eta > \eta_z$. In this case we therefore use the technique of solution described in chapter III. We consider field profiles at time levels n and $n + 1$ (see figure B.2). At time level n the field penetrates the slab to a distance η_z which cannot in general be expressed as an integral number of intervals $\Delta\eta$. We therefore define the interval $\Delta\eta_1$ as the distance between the point η_z and the nearest grid point to the right of η_z, η_{iz+1}. The distance η_z is therefore given by:

$$\eta_z = (iz + 1)\Delta\eta - \Delta\eta_1 \qquad \text{B-26}$$

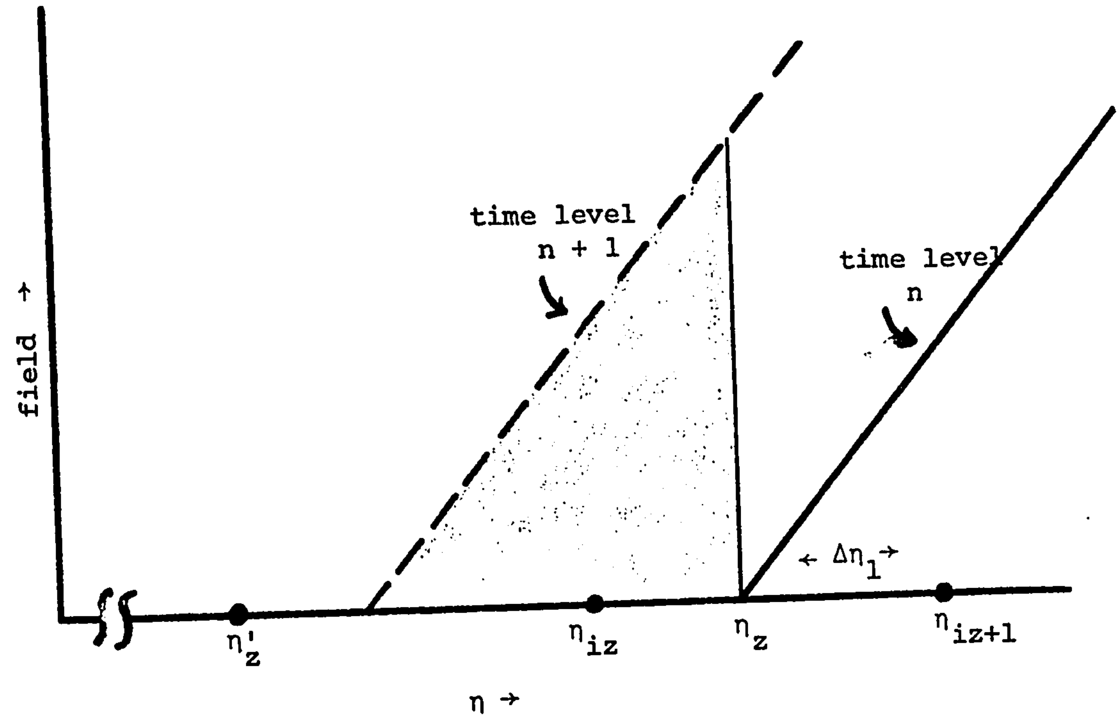

figure B.2

To calculate the field and flux at time level n + 1, we first impose the artifical boundary condition (see chapter III):

$$\Phi(\eta_z, \xi_n) \quad = \quad \Phi(\eta_z, \xi_{n+1}) \quad = \quad 0 \qquad \text{B-27}$$

We therefore assume that temporarily the flux at point η_z is zero at both time levels n and n + 1. We then proceed to write the analogs of B-9 for $iz + 1 \leq i \leq R$. These equations are unchanged for $i > iz + 1$ and are given in B-19 and B-24. Before writing the analog for i = iz + 1 we note that:

$$\left(\frac{\partial^2 \Phi}{\partial \eta^2}\right)_{iz+1,\ n} = \frac{\delta^2 \Phi_{iz+1,n}}{(\Delta\eta)^2} \qquad \text{B-28}$$

where

$$\delta^2 \Phi_{iz+1,\ n} = \frac{2}{\left[1 + \frac{\Delta\eta_1}{\Delta\eta}\right]} \left[\Phi_{iz+2,\ n} - \Phi_{iz+1,\ n} \left(\frac{\Delta\eta}{\Delta\eta_1} + 1\right)\right]$$

B-29

Again we use the Crank-Nisolson approximation:

$$\left(\frac{\partial^2 \Phi}{\partial \eta^2}\right)_{iz+1,\ n+\frac{1}{2}} \simeq \frac{1}{2} \left[\frac{\delta^2 \Phi_{iz+1,\ n+1}}{\Delta\eta^2} + \frac{\delta^2 \Phi_{iz+1,\ n}}{\Delta\eta^2} \right]$$

B-30

Using B-28 and B-30, we obtain the second order correct Crank-Nicolson analog to B-9 at point $(\eta_{iz+1},\ \xi_{n+\frac{1}{2}})$:

$$\Phi_{iz+2,\ n+1} + \Phi_{iz+1,\ n+1}\{[- (1 + \frac{\Delta\eta}{\Delta\eta_1}) - L(\theta_{iz+1,\ n})$$

$$[\frac{\Delta\eta^2}{\Delta\xi} (1 + \frac{\Delta\eta_1}{\Delta\eta})]\} = -\delta^2 \Phi_{iz+1,\ n} [1 + \frac{\Delta\eta_1}{\Delta\eta}]/2 +$$

$$+ \kappa [1 - \theta_{iz+1,\ n}] (\Delta\eta)^2 (1 + \frac{\Delta\eta_1}{\Delta\eta})$$

$$- \quad L(\theta_{iz+1,n}) [\frac{\Delta\eta^2}{\Delta\xi}][1 + \frac{\Delta\eta_1}{\Delta\eta}] \Phi_{iz+1,n} \qquad \text{B-31}$$

Equations B-19, B-24 and B-31 form a tridiagonal matrix and are solved with the Thomas algorithm, thus yielding values of Φ at time level n + 1 in the region $\eta \geq \eta_{iz+1}$. These values must however be corrected since they were obtained by assuming the artifical boundary condition B-27. To make this correction, we calculate the field $H(\eta)$ using the values of Φ for time level n + 1. This field profile is shown schematically in figure B.2. We then extrapolate this field profile to a distance η_z' where the field is equal to zero. To make this extrapolation we use the following approximation:

$$(\frac{\partial H}{\partial \eta})_{i < iz+1} = (\frac{\partial H}{\partial \eta})_{iz+1} = 2(\frac{\partial H}{\partial \eta})_{iz+2} - (\frac{\partial H}{\partial \eta})_{iz+3} \qquad \text{B-32}$$

which assumes that the slope $\partial H/ \partial \eta$ varies linearly from point iz + 3 to iz + 1 and then is constant for $i \leq iz + 1$. The corrected values of Φ are then given by:

$$\Phi'_{i \leq iz} = \delta\Phi(\eta_i - \eta_z')/(\eta'_z - \eta_z) \qquad \text{B-33}$$

$$\Phi'_{i > iz} = \Phi_{i > iz,\, n + 1} + \delta\Phi \qquad \text{B-34}$$

where

$$\delta\Phi = H_{iz + 1}[\Delta\eta'_1 - \Delta\eta_1]^2/2\, \Delta\eta'_1 \qquad \text{B-35}$$

and

$$\Delta\eta'_1 = \eta_{iz+1} - \eta'_z \quad .$$

The quantity $\delta\Phi$ is the cross-hatched area shown in figure B.2

Equation B-9 must however he solved simultaneously with equation B-10. As we mentioned earlier (eqn. B-18) the temperature at time level $n + \frac{1}{2}$ is taken to be equal to the temperature at time n. This approximation allows us to calculate the values of Φ for $iz + 1 \leqslant i \leqslant R$ at time $n + 1$ using the Thomas algorithm as shown above. Before the values of Φ at time level $n + 2$ are computed however we must calculate the temperature θ_i for $1 \leqslant i \leqslant R$ at time $n + 1$. This is done using the following analog to B-10:

$$\theta_{i,\, n+1} \approx \theta_{i,\, n} + \left(\frac{\partial\theta}{\partial\xi}\right)_{i,n} \Delta\xi \qquad \text{B-36}$$

Using the values of Φ and θ at time level $n + 1$ the flux and temperatures are computed fro the next time level. This is done by redefining the value of η_z as the new computed value η'_z and also using a new value for $\Delta\eta_1$.

A P P E N D I X   C

PENETRATION OF FLUX IN A SUPERCONDUCTING CYLINDER: METHOD OF SOLUTION

I ANALOG EQUATIONS

The equations governing the penetration (or exit) of flux and the temperature as a function of the position along the radius and time in a superconducting cylinder have been derived in chapter III and are reproduced below:

$$\frac{\partial^2\phi}{\partial r^2} - \frac{1}{r}\frac{\partial\phi}{\partial r} - \frac{8\pi^2}{10} r\, J_c(T) = \frac{4\pi \times 10^{-9}}{\rho_f} \frac{\partial\phi}{\partial t} \qquad \text{C-1}$$

$$C(T)\frac{\partial T}{\partial t} = \frac{10^{-7}}{8\pi^2} \frac{\partial\phi}{\partial t} \left[\frac{1}{r}\right] \left[\frac{\partial^2\phi}{\partial r^2} - \frac{1}{r}\frac{\partial\phi}{\partial r}\right] \qquad \text{C-2}$$

where the specific heat per cm^3 is given by

$$C(T) = \frac{H}{H_{c2}} \gamma T + \alpha T^n$$

and the magnetic flux

$$\phi(r) = 2\pi \int_o^r rH(r)\,dr. \qquad \text{C-4}$$

ρ_f is the flux flow resistivity, and J_c is the critical current density.

We consider the following initial triangular field profile:

$$H(r) = \begin{cases} 0 & \text{for} \quad r < r_z \\ \dfrac{H_{ex}}{(a-r_z)} (r - r_z) & \text{for } r_z \leqslant r \leqslant a \end{cases} \qquad \text{C-5}$$

The solution of B-1 and B-2 must therefore satisfy the following boundary conditions:

a) At time t = 0

$$\phi(r) = \begin{cases} 0 & \text{for } r < r_z \\ \dfrac{\pi H_{ex}}{3(a-r_z)} (2r^3 + r^3 z - 3r^2 r_z) & \\ & \text{for } r_z \leqslant r \leqslant a \end{cases} \qquad \text{C-6}$$

$$T(r) = \begin{cases} T_b & \text{for } 0 < r < r_t \\ T_b + \delta T & \text{for } r_t \leqslant r \leqslant a \end{cases} \qquad \text{C-7}$$

where r_t and δT are adjustable parameters.

b) At times $t \geq 0$

$$\phi(0) = 0 \qquad \text{C-8a}$$

$$H(a) = H_{ex}$$

or

$$\frac{1}{2\pi a}\left(\frac{\partial \phi}{\partial r}\right)_{r=a} = H_{ex} \qquad \text{C-8b}$$

In equation C-7 we have introduced a temperature perturbation δT which extends between radius r_t and the surface.

Before solving B-1 and B-2 we express these two equations in terms of dimensionless parameters:

$$\frac{\partial^2 \Phi}{\partial \eta^2} - \frac{1}{\eta}\frac{\partial \Phi}{\partial \eta} - \kappa\eta[1 - \theta] = L(\theta)\frac{\partial \Phi}{\partial \xi} \qquad \text{C-9}$$

$$\frac{\partial \theta}{\partial \xi} = \frac{1}{[G_1\theta + G_2\theta^n]} \left[\frac{\partial \Phi}{\partial \xi}\right]\left[\frac{1}{\eta}\right]\left[\frac{\partial \mathcal{H}}{\partial \eta}\right] \qquad \text{C-10}$$

where

$$\Phi = \phi/\phi_o, \qquad \phi_o = \pi a^2 H_{ex}$$

$$\eta = r/a, \qquad \xi = t/\tau_n$$

$$\tau_n = 2.17a^2 \times 10^{-9}/\rho_n$$

$$\mathcal{H}(\eta) = H(r)/H_{ex}$$

$$G_1 = \frac{H}{H_{c2}} \gamma T_c^2 / [\ 10^{-7} \phi_o H_{ex}/8\pi^2 a^2\ ]$$

$$G_2 = \alpha T_c^{n+1} / [\ 10^{-7} \phi_o H_{ex}/8\pi^2 a^2]$$

$$L(\theta) = 4\pi a^2 (1 - \theta) \times 10^{-9}/\rho_f \tau_n$$

$$K = (8\pi^2/10)(a^3) J_o/\phi_o$$

As in the case of the slab (appendix B) we divide the cylinder's radius into R intervals of equal length $\Delta\eta$. The radial position corresponding to the i^{th} interval is then given by:

$$\eta_i = i\Delta\eta$$

The analog of the first space derivative of Φ at point (η_i, ξ_n) then has the form:

$$\left(\frac{\partial\Phi}{\partial\eta}\right)_{i,n} = \frac{\Phi_{i+1,n} - \Phi_{i-1,n}}{2\Delta\eta} = \frac{\delta\Phi_{i,n}}{\Delta\eta}$$

where

$$\delta\Phi_{i,n} = (\Phi_{i+1,n} - \Phi_{i-1,n})/2$$

At time level $n + \frac{1}{2}$ we use the Crank-Nicolson approximation (Rosenberg 69):

$$\left(\frac{\partial\Phi}{\partial\eta}\right)_{i,\,n+\frac{1}{2}} = \frac{1}{2}\left[\frac{\delta\Phi_{i,n}}{\Delta\eta} + \frac{\delta\Phi_{i,n+1}}{\Delta\eta}\right] \qquad \text{C-11}$$

The analogs of $\frac{\partial \Phi}{\partial \eta}$ and $\frac{\partial \Phi}{\partial \xi}$ at point $(\eta_i, \xi_{n+\frac{1}{2}})$ are the same as those given in appendix B.

a) <u>Case where the Field has Initially Penetrated to the Center of the Cylinder</u>

In the case where the field has initially penetrated to the center of the cylinder equation C-9 is valid throughout the whole cylinder and the Crank-Nicolson analog to C-1 is for $2 \leqslant i \leqslant R-1$:

$$\Phi_{i-1,\ n+1}\left[1 + \frac{1}{2i}\right] + \Phi_{i,\ n+1}\left[-2 - 2\ L(\theta_{i,n})\ \frac{\Delta\eta^2}{\Delta\xi}\right]$$

$$+ \ \Phi_{i+1,\ n+1}\left[1 - \frac{1}{2i}\right] = -\delta^2\Phi_{i,\ n} + \delta\Phi_{i,\ n}/i$$

$$+ \ 2K[\Delta\eta]^3\ \left[1 - \theta_{i,\ n}\right] - 2L(\theta_{i,\ n})\ \Delta\eta^2\ \Phi_{i,\ n}/\Delta\xi \qquad \text{C-12}$$

For i = 1, we use the boundary condition C-8a which here takes the form:

$$\Phi_{o,\ n} = \Phi_{o,\ n+1} = 0$$

The analog to C-9 is therefore, for i = 1:

$$\Phi_{1,\, n+1} \left[-2 -2L(\theta_{1,\, n}) \frac{\Delta\eta^2}{\Delta\xi} \right] + \Phi_{2,\, n+1} \left[1 - \tfrac{1}{2}\right]$$

$$= -\delta^2\Phi_{1,\, n} + \delta\Phi_{1,\, n} + 2K \left[1 - \theta_{1,\, n}\right] \Delta\eta^3$$

$$- \quad 2L(\theta_{1,\, n})\Delta\eta^2 \quad \Phi_{1,n}/\Delta\xi \qquad \text{C-13}$$

For i = R, we use the boundary condition C-8b which here takes the form:

$$\left(\frac{\partial\Phi}{\partial\eta}\right)_{\eta_R} = 2$$

or

$$\Phi_{R+1,\, n} = \Phi_{R-1,\, n} + 4\Delta\eta \qquad \text{for all n.}$$

This yields the following analog to C-9 for i = R:

$$2\Phi_{R-1,\, n+1} + \Phi_{R,\, n+1} \left[-2 -2L(\theta_{R,n}) \frac{\Delta\eta^2}{\Delta\xi}\right]$$

$$= -4\Delta\eta \left[1 - \frac{1}{2R}\right] - \delta^2\Phi_{R,n} + \delta\Phi_{R,n}/R$$

$$+ \quad 2K \left[1 - \theta_{R,n}\right] R\, \Delta\eta^3 - 2L(\theta_{R,n})\Delta\eta^2\, \Phi_{R,n}/\Delta\xi \qquad \text{C-14}$$

b) <u>Case where the Field has not Initially Penetrated to the Centre of the Cylinder:</u>

In the case where the field has not initially penetrated to the center of the cylinder (i.e. $\eta_z \neq 0$) equation C-9 is valid initially only for $\eta > \eta_z$. We therefore use the technique described in chapter III and appendix B and introduce the boundary condition:

$$\Phi(\eta_z) = 0$$

at time levels n and n + 1.

Since this technique was described in detail for the slab in appendix B we will only outline the solution here.

Defining $\Delta\eta_1$ as the distance between the point η_z (for which the field $H(\eta_z)$ is zero) and the nearest grid point to the right of η_z we can obtain an analog to equation C-9 at point $(\eta_{iz+1}, \xi_{n+\frac{1}{2}})$ where η_{iz} is the largest grid point for which the flux Φ is zero. Equation C-9 is then solved only the region $\eta > \eta_z$. The first space derivative at point iz + 1 and time level n is:

$$\left(\frac{\partial\Phi}{\partial\eta}\right)_{iz+1,\ n} = \frac{\delta\Phi_{iz+1,\ n}}{\Delta\eta}$$

where

$$\delta\Phi_{iz+1,\,n} = \frac{\Phi_{iz+2,\,n}[\Delta\eta_1]^2 - \Phi_{iz+1,\,n}[\Delta\eta_1^2 - \Delta\eta^2]}{\Delta\eta_1\Delta\eta + \Delta\eta_1^2}$$

and the analog to C-9 for i = iz + 1 and time level n + ½ is:

$$\Phi_{iz+1,\,n+1}\Bigg\{-1 - \frac{\Delta\eta_1}{\Delta\eta} + \frac{1}{2[iz+1]\Delta\eta}\Big[\frac{\Delta\eta_1^2}{\Delta\eta} - \Delta\eta\Big]$$

$$- L(\theta_{iz+1,\,n})\frac{[\Delta\eta + \Delta\eta_1][\Delta\eta_1]}{\Delta\xi}\Bigg\}$$

$$+ \Phi_{iz+2,\,n+1}\left[\frac{\Delta\eta_1}{\Delta\eta} - \frac{\Delta\eta_1^2}{1[iz+1]\Delta\eta^2}\right]$$

$$= \frac{\Delta\eta_1[\Delta\eta_1 + \Delta\eta]}{2[iz+1]\Delta\eta}\;\frac{\delta\Phi_{iz+1,\,n}}{\Delta\eta} - \Delta\eta_1[\Delta\eta_1 + \Delta\eta]\frac{\delta^2\Phi_{iz+1,\,n}}{2[\Delta\eta]^2}$$

$$+ \Delta\eta_1[\Delta\eta + \Delta\eta_1]\; K[iz+1][\Delta\eta][1 - \theta_{iz+1,\,n}]$$

$$- L(\theta_{iz+1,n})[\Delta\eta + \Delta\eta_1]\,\Phi_{iz+1,\,n}/\Delta\xi \qquad \text{C-15}$$

Equations C-12 (for $iz + 1 < i < R$), C-14 and C-15 form a tridiagonal matrix which is solved with the Thomas algorithm (appendix D). This solution yields values of Φ at time level $n + 1$ for $i \geqslant iz + 1$. Since these values are obtained by initially assuming that the flux at point η_z (see figure B.2) is zero at both time levels n and $n + 1$ the values of Φ are corrected before they are used to compute the temperature distribution and flux configuration at the next time level. The method of correction is identical to the case of the slab and consists in first computing the field at each point $i > iz + 1$ in the cylinder using the uncorrected values of the flux and then extrapolating the field profile to a radius η'_z where $H(\eta'_z) = 0$. This extrapolation again assumes a linear variation of the slope $(\partial H/\partial\eta)$ between grid points $iz + 3$ and $iz + 1$ and a constant slope for all points between η'_z and η_{iz+1}:

$$\left(\frac{\partial H}{\partial \eta}\right)_{i < iz+1} = \left(\frac{\partial H}{\partial \eta}\right)_{iz+1} = 2\left(\frac{\partial H}{\partial \eta}\right)_{iz+2} - \left(\frac{\partial H}{\partial \eta}\right)_{iz+3}$$

The corrected values of Φ at time level $n + 1$ are thus given by (primed values):

$$\Phi'_{i \leq iz\ ,\ n+1} = \left(\frac{\partial H}{\partial \eta}\right)_{i,\ n+1} \{ \eta_i^2 \ [2\eta_i - 3\eta'_z] + \eta_z^3 \}/3$$

$$\Phi'_{i > iz} = \Phi_{i > iz,\ n+1} + \delta\Phi$$

where

$$\delta\Phi = \left(\frac{\partial H}{\partial \eta}\right)_{iz+1,\ n+1} \{\eta'_z \left[2\eta_z - 3\eta'_z\right] + \eta_z'^3\}/3$$

and

$$\Delta\eta'_1 = \eta_{iz+1} - \eta'_z$$

The temperatures at time level n + 1 are then computed using equation C-10.

II COMPUTER PROGRAM

a) Definition of symbols:

A	=	a (diameter of cylinder)
AA(I)	=	a_i (Thomas algorithm)
AIMF	=	magnetization <4πM> at time level n + 1
AIMZ	=	initial magnetization (t = 0)
AK	=	K

ALPHA	=	α
ATN	=	n (power appearing in specific heat)
B(I)	=	b_i (Thomas algorithm)
BT(I)	=	β_i (Thomas algorithm)
C(I)	=	c_i (Thomas algorithm)
D(I)	=	d_i (Thomas algorithm)
DELF(I)	=	$\delta^2\Phi_{i,\, n+1}$
DELFP(I)	=	$\delta^2\Phi_{i,\, n}$
DELTAF		$\delta\Phi$ (flux correction)
DHDR(I)	=	$(\partial H/\partial\eta)_i$
DIF(I)	=	$\delta\Phi_{i,\, n+1}$
DIFP(I)	=	$\delta\Phi_{i,\, n}$
DR	=	$\Delta\eta$
DR1	=	$\Delta\eta_1$
DRIN	=	$\Delta\eta_1'$
DT	=	time interval ($\Delta\xi$)
F(I)	=	$\Phi_{i,\, n+1}$
FP(I)	=	$\Phi_{i,\, n}$
FNORM	=	ϕ_o
G(I)	=	γ_i (Thomas algorithm)
GAMMA	=	γ (specific heat)
G1	=	G_1
G2	=	G_2
H(I)	=	H_i
HEX	=	$H_{ex} - H_o$

HTOT	=	$\langle B \rangle$
HZ	=	H_o
I	=	i
I*DR	=	η_i
IR	=	total number of space intervals
IRT*DR	=	η_t
IZ	=	iz
JCB	=	$J_c(T_b)$
JZ	=	J_o
K(I)	=	defined in the next section
L	=	$L(\theta)/(1 - \theta)$
P(I)	=	power at radius η_i in watts/cm^3
PERT	=	defined such that THZ = PERT * THB
RZ	=	η_z
TB	=	T_b
TC	=	T_c (H = 0)
TCH	=	$T_c(H)$
THB	=	T_b/T_{ch}
TH(I)	=	T_i/T_{ch}
THZ	=	$T_b + \delta T$
TIME	=	$10\ \tau_n$

b) Definition and Use of Parameter k(I):

Although the value of K appearing in equation C-9 is a constant we show in this section that it is useful to replace this constant by a variable K(I) which is independent of time and depends only on the radius given by the index I.

The diffusion equation C-1 was obtained from the following equation (see chapter III):

$$2\pi r\rho_f [J - J_c] = \frac{\partial\phi}{\partial t} \qquad (\text{for } J > J_c) \qquad \text{C-15}$$

The current density J was then expressed in terms of the flux ϕ,

$$J = \frac{10}{8\pi^2} \frac{1}{r} \left[\frac{\partial^2\phi}{\partial r^2} - \frac{1}{r} \frac{\partial\phi}{\partial r} \right] \qquad \text{C-16}$$

Since equations C-1 and C-15 essentially describe the difference between the current density J and the critical current density J_c and since this difference can be very small, problems can arise if J is calculated with the analog of equation C-16 and J_c is calculated analytically from:

$$J_c = J_o(1 - \theta) \qquad \text{C-17}$$

where J_o is a constant. These problems arise because of the inherent rounding off error which occurs when an analog equation is used.

Although the analog we have used is correct to second order we will show below that for small radii the analog of J gives an appreciable error in J when the initial field profile is triangular.

We consider the case where the field has initially penetrated to the center of the cylinder. In terms of dimensionless parameters the flux is given by

$$\Phi(\eta) = 2/3\ \eta^3 \qquad (\eta \leqslant 1) \qquad \text{C-18}$$

The value of the current density is then obtained from the following equation

$$J = \frac{10}{4\pi} \frac{H_{ex}}{a} \frac{\partial H}{\partial \eta} \qquad \text{C-19}$$

where:

$$\frac{\partial H}{\partial \eta} = \frac{1}{2\eta} \left[\frac{\partial^2 \Phi}{\partial \eta^2} - \frac{1}{\eta} \frac{\partial \Phi}{\partial \eta} \right] \qquad \text{C-20}$$

The analytical value of $\frac{\partial H}{\partial \eta}$ obtained from C-18 and C-20 is equal to 1. If If we compute however the value of $\frac{\partial H}{\partial \eta}$ at radius $i\Delta\eta$ using the analog of the right hand side of C-20 we obtain:

$$\left(\frac{\partial H}{\partial \eta}\right) = \frac{1}{3} \left[\frac{3i^2 - 1}{i^2} \right] \qquad \text{C-21}$$

In the limit of large i the value $(\frac{\partial H}{\partial \eta})_i$ tends towards the correct value of 1. For small values of i (and therefore for small radii), however, the analog of $(\partial H/\partial \eta)$ deviates from 1, and is equal to 2/3 for i = 1. If the analytical value of J_c (equation C-17) is used in equation C-1 (or C-15) the value of $J - J_c$ will therefore become negative for small values of i at the beginning of the computation. To eliminate this problem we compute the critical current density J_c at every point i using an analog equation:

$$J_{ci} = \frac{10H_{ex}}{4\pi a} (\frac{\partial H}{\partial \eta})_{i,t=0} \qquad \text{C-22}$$

where $(\partial H/\partial \eta)_{i,t=0}$ is computed from the initial field (or flux) profile with the analog of the right hand side of equation C-20.

In the program the value of J_c or J_o appears in the constant K (defined as AK in the program) where:

$$K = \frac{8\pi^2}{10} a^3 J_o/\phi_o \qquad \text{C-23}$$

In the regions where the field has initially penetrated the value of K can be rewritten as:

$$K = 2 (\frac{\partial H}{\partial \eta})_{t=0} /(1 - \theta_b) \qquad \text{for } \eta > \eta_z$$

We therefore define a local value of K at point i for $i \geqslant iz + 1$:

$$K_i = 2 (\frac{\partial H}{\partial \eta})_{i,t=0} /(1 - \theta_b)$$

In the regions where the field has not initially penetrated the cylinder ($\eta < \eta_z$) we introduce an "error" in K equal to the rounding off error occuring in the value of J (given in equation C-21):

For $i \leqslant iz$:

$$K_i = \frac{1}{3} \left(\frac{3i^2 - 1}{i^2}\right) \left(\frac{\partial H}{\partial \eta}\right)_{\eta > \eta_z,\ t=0}$$

where $\left(\frac{\partial H}{\partial \eta}\right)_{\eta > \eta_z, t=0}$ is the analytical value.

c) <u>Programme Listing:</u>

```
C PENETRATION OF FLUX IN A CYLINDER OF RADIUS=A UNDER ADIABATIC CONDITIONS
C A(CM),HEX(GAUSS),AIMAX(GAUSS),JZ(AMPS/CM2),JCB(AMPS/CM2),ALPHA(ERGS/CM3),
C  TC(DEG K),P(I)(WATTS/CM3),
C  TB=BATH TEMP , TC=CRIT TEMP , AIMZ=INITIAL MAGNETIZATION,
C  IP IS TOTAL NUMBER OF POINTS PRINTED
      IMPLICIT REAL*8 (A-H,J-L,O-Z)
      INTEGER J
      DIMENSION AA(900),B(900),BT(900),C(900),D(900),F(900),G(900),
     1DIF(900),DELF(900),DIFP(900),DELFP(900),DHDR(900),FP(900),TH(900),
     2THN(900),LRT(900),H(900),P(900),DC(900),K(900),HC2(900) ,THTC(900)
      READ(1,1) TC,A,ALPHA,ATN,RHO,HC20,HC20T
      READ(1,2) IR,NT,IRT
   66 CONTINUE
      READ(1,31) AIMZ,HZ,DT,IZ
      TB=4.2
      PERT=1.01
      IP=100
      WRITE(3,3)
      WRITE(3,4) TC,A,ALPHA,ATN,RHO,PERT,HZ
      WRITE(3,5)
      WRITE(3,2) IR,NT,IRT
C DEFINITION OF CONSTANTS
      DELTAF=0.0
      AIZ=IZ
      GAMMA=10480.
      PI=3.14159D0
      PI2=PI**2
```

```
      RZ=AIZ*A/IR
      A2=A*A
      HEX=AIMZ/(1.0D0-(2.0D0*A*A2+RZ**3-3.D0*A2*RZ)/(3.0D0*A2*(A-RZ)))
      JCB=HEX/(0.4*PI*(A-RZ))
       HTOT=HZ
      HR=HTOT/HC20
      TCH=TC*(1.-HTOT/HC20T)
      THB=TB/TCH
      THZ=THB*PERT
      JZ=JCB/(1.0D0-THB)
C  TIME IN MICROSECONDS=10X NORMAL STATE RELAXATION TIME
      TIME=21.7*1000.*A2/RHO
      WRITE (3,27)
      WRITE(3,4) TIME,HC20,HC20T
   27 FORMAT(1H0,6X,'TIME',10X,'HC20',13X,'HC20T')
      WRITE(3,32) TCH
   32 FORMAT(1X,'TCH',F10.5)
      L=4.0D3*PI*A2/(RHO*TIME)

      FNORM=HEX*A2*PI
      FNORM2=FNORM**2
      ATNP1=ATN+1.
      AK=0.8D0*PI2*A*JZ*A2/FNORM
      AG=FNORM*HEX/(8.*PI2*A2*ALPHA*TCH**ATNP1)
      AGG=FNORM*HEX/(8.*PI2*A2)
      AP=FNORM*HEX/(80.*PI2*A2*TIME)
      HC2B=HC20T*(1.-TB/TC)
      G1=HZ*GAMMA*TCH**2/(AGG*HC2B)
      G2=ALPHA*TCH**ATNP1/AGG
      RR=IR
      IRM1=IR-1
      DR=1.0D0/RR
      DR2=DR**2
      DR3=DR**3
      RR2=RR**2
      RR3=RR**3
      AIZ=RR*RZ/A
```

```
      IZ1=IZ+1
      IRT1=IRT+1
      AIMAX=HEX*A/(3.*(A-RZ))
      WRITE(3,17)
      WRITE(3,4) AIMZ,HEX,JCB,JZ,L,AG,AK,AIMAX
C  TIME ZERO IE INITIAL CONDITIONS
      T=0.0
      CN=0.0
      IF(IRT.EQ.0) GO TO 50
      DO 101 I=1,IRT
  101 TH(I)=THB
   50 CONTINUE
      DO 102 I=IRT1,IR
  102 TH(I)=THZ
      IF(AIZ.LT.1.0) GO TO 51
      DO 103 I=1,IZ
      DELF(I)=0.0
      DIF(I)=0.0
      DHDR(I)=0.0
  103 F(I)=0.0
   51 CONTINUE
      IZ2=IZ+2
      DO 104 I=IZ1,IR
  104 F(I)=(I*I*(2.*I-3.*AIZ)+   AIZ**3)/(3.*(RR-AIZ)*RR2)
      DR1DR=IZ+1.-AIZ
      DR1=DR1DR*DR
      DR1DRN=DR1DR
      DIF(IZ1)=(DR1*F(IZ2)-(DR1-DR/DR1DR)*F(IZ1))/(DR+DR1)

      DELF(IZ1)=(DR*F(IZ2)-(DR2/DR1+DR)*F(IZ1))/(DR+DR1)*2.0
      DIF(IR)=2.*DR
      DELF(IR)=2.*(F(IRM1)-F(IR))+4.*DR
      DO 105 I=IZ2,IRM1
      DIF(I)=(F(I+1)-F(I-1))/2.
  105 DELF(I)=F(I+1)-2.*F(I)+F(I-1)
      DO 115 I=IZ1,IR
```

```
      DHDR(I)=RR3*(DELF(I)-DIF(I)/I)/(2.*I)
  115 K(I)=2.*DHDR(I)/(1.-THB)
      DHDR(IZ1)=2.*DHDR(IZ2)-DHDR(IZ2+1)
      K(IZ1)=2.*DHDR(IZ1)/(1.-THB)
      DIF(IZ1)=2.*IZ1*DHDR(IZ1)/RR3
      DELF(IZ1)=2.*DHDR(IZ1)*(IZ+2)/RR3
      DO 117 I=1,IZ
  117 K(I)=AK*(3.*I*I-1.)/(3.*I*I)
      WRITE(3,7)
      WRITE(3,18) AIZ,IZ,DR1DR
      NN=0
      IZN=IZ
      IN=IR/IP
      WRITE(3,20) (F(IN*I),I=1,IP)
      WRITE(3,13) (DELF(I*IN),I=1,IP)
      WRITE(3,12) (DIF(I*IN),I=1,IP)
      WRITE(3,14) (DHDR(I*IN),I=1,IP)
      WRITE(3,15) (TH(I*IN),I=1,IP)
C
C     TIME GREATER THAN ZERO
C
      DO 199 N=1,NT
      NN=NN+1
      CN=CN+1.
      T=N*DT
      LRDT=2.*DR2*L/DT
      LRTIZ1=L*DR1*(DR+DR1)/DT
      DO 106 I=1,IR
      FP(I)=F(I)
      DIFP(I)=DIF(I)
      DELFP(I)=DELF(I)
      HC2(I)=HC20T*(1.-TH(I)*TCH/TC)
      LRT(I)=LRDT/(HR+(1.-HC2(I)/HC20)*DEXP((HTOT-HC2(I))/10000.)*HTOT
     1/HC2(I))
      IF(TH(I).GE.1.0) LRT(I)=LRDT
      DC(I)=0.5*K(I)*(1.-TH(I))
  106 THN(I)=TH(I)**ATN
      IZ1=IZ+1
      IZ2=IZ+2
```

```
      TIZ1=2.0D0*IZ1
      LRT(IZ1)=LRTIZ1/(HR+(1.-HC2(IZ1)/HC20)*DEXP((HTOT-HC2(IZ1)
     1)/10000.)*HTOT/HC2(IZ1))
      IF(TH(IZ1).GE.1.0) LRT(IZ1)=LRTIZ1
      DR1DR2=DR1DR**2
      DDR1=DR1*(DR1+DR)
      IF(TH(IZ1).GE.1.0) K(IZ1)=0.0
C
C    THOMAS ALGORITHM
C
      AA(IZ1)=0.0
      B(IZ1)=-1.-DR1DR+(DR1DR2-1.)/TIZ1-LRT(IZ1)
      C(IZ1)=DR1DR-DR1DR2/TIZ1
      D(IZ1)=DR1DR*(DR1DR+1.)*(DIFP(IZ1)/TIZ1-DELFP(IZ1)/2.)+DDR1*
     1(K(IZ1)*IZ1*DR*(1.-TH(IZ1)))-LRT(IZ1)*FP(IZ1)
      BT(IZ1)=B(IZ1)
      G(IZ1)=D(IZ1)/B(IZ1)
      DO 107 I=IZ2,IRM1
      DI=2.0D0*I
      IF(TH(I).GE.1.0) K(I)=0.0
      AA(I)=(DI+1.0D0)/DI
      B(I)=-2.0D0-LRT(I)
      C(I)=(DI-1.0D0)/DI
      D(I)=-DELFP(I)+DIFP(I)/I+2.*K(I)*DR3*I*(1.-TH(I))-LRT(I)*FP(I)
      BT(I)=B(I)-AA(I)*C(I-1)/BT(I-1)
  107 G(I)=(D(I)-AA(I)*G(I-1))/BT(I)
      IF(TH(IR).GE.1.0) K(IR)=0.0
      IF(TH(IR).GE.1.0) LRT(IR)=LRDT
      AA(IR)=2.0
      B(IR)=-2.-LRT(IR)
      C(IR)=0.0
      D(IR)=2.*DR2-4.*DR-DELFP(IR)+DIFP(IR)/IR+2.*K(IR)*DR2*(1.-TH(IR))
     1-LRT(IR)*FP(IR)
      BT(IR)=B(IR)-AA(IR)*C(IRM1)/BT(IRM1)
      G(IR)=(D(IR)-AA(IR)*G(IRM1))/BT(IR)
      F(IR)=G(IR)
      IRMIZ1=IR-IZ1
```

```
C
C  VALUE OF FLUX AT TIME N+1
C
      DO 108 J=1,IRMIZ1
      I=IR-J
      F(I)=G(I)-C(I)*F(I+1)/BT(I)
  108 CONTINUE
      DO 109 I=IZ2,IRM1
      DELF(I)=F(I+1)-2.*F(I)+F(I-1)
      DIF(I)=(F(I+1)-F(I-1))/2.
  109 DHDR(I)=(DELF(I)-DIF(I)/I)*RR3/(2.*I)
      DELF(IR)=2.*(F(IRM1)-F(IR))+4.*DR
      DIF(IR)=2.*DR
      DHDR(IR)=(DELF(IR)*RR2/2.-1.)
      DELF(IZ1)=F(2)-2.*F(1)
      DIF(IZ1)=F(2)/2.
      DIF(IZ1)=(DR1*F(IZ2)-(DR1-DR/DR1DR)*F(IZ1))/(DR+DR1)
      DELF(IZ1)=(DR*F(IZ2)-(DR2/DR1+DR)*F(IZ1))/(DR+DR1)*2.0
      DHDR(IZ1)=RR3*(DELF(IZ1)-DIF(IZ1)/IZ1)/(2.*IZ1)
      IZN=0
C VALUE OF MAGNETIC FIELD H(I)
C
      H(IR)=1.0
      DO 110 I=IZ1,IRM1
  110 H(I)=RR2*DIF(I)/(2.*I)
      IF(AIZ.LE.0.0) GO TO 58
C
C   CASE WHERE IZ NOT ZERO
C
      HIZD=RR2*(F(IZ2)-F(IZ1))/(2.*(IZ1+0.5))
      DHDR(IZ1)=2.*DHDR(IZ2)-DHDR(IZ2+1)
      DHDR(IZ1)=DC(IZ1)
      DRN=HIZD/DHDR(IZ1)-0.5*DR
      H(IZ1)=HIZD*DRN/(DRN+0.5*DR)
      AIZ=IZ1-DRN/DR
      IZN=AIZ
```

```
      IZN1=IZN+1
      IZN2=IZN+2
      IF(IZN.LT.1) GO TO 62
      DO 111 I=1,IZN
       H(I)=0.0
      AA(I)=0.0
      B(I)=0.0
      C(I)=0.0
      D(I)=0.0
      BT(I)=0.0
  111 G(I)=0.0
   62 CONTINUE
      ETA1=IZ1-DR1DR
      ETAZ=IZ1-DRN/DR
      DELTAF=DHDR(IZ1)*(ETA1**2*(2.*ETA1-3.*ETAZ)+ETAZ**3)/(3.*RR3)
      IF(IZN1.GT.IZ) GO TO 57
      DO 112 I=IZN1,IZ
      F(I)=DHDR(IZ1)*(I*I*(2.*I-3.*ETAZ)+ETAZ**3)/(3.*RR3)
  112 DHDR(I)=DHDR(IZ1)

   57 CONTINUE
      DR1N=DRN-(IZ-IZN)*DR
      IF(AIZ.LE.0.0) DR1N=DR
      DR1DRN=DR1N/DR
      DO 113 I=IZ1,IR
  113 F(I)=F(I)+DELTAF
      IF(DR1DRN.LE.0.001) GO TO 54
      DIF(IZN1)=2.*IZN1*DHDR(IZ1)/RR3
      DELF(IZN1)=2.*DHDR(IZ1)*(IZN+2)/RR3
      GO TO 55
   54 CONTINUE
      DIF(IZN1)=F(IZN2)/2.
      DELF(IZN1)=F(IZN2)-2.*F(IZN1)
   55 CONTINUE
      IF(IZN2.GT.IZ) GO TO 58
```

```
      DO 116 I=IZN2,IZ
      DIF(I)=(F(I+1)-F(I-1))/2.0
  116 DELF(I)=F(I+1)-2.*F(I)+F(I-1)
   58 CONTINUE
C  COMPUTATION OF TEMPERATURES
C
      DO 114 I=1,IR
      TH(I)=TH(I)+DHDR(I)*(F(I)-FP(I))*RR/(I*(G1*TH(I)+G2*THN(I)))
  114 P(I)=AP*(F(I)-FP(I))*DHDR(I)*RR/(DT*I)
      DR1DR=DR1DRN
      IF(NN.LT.5) GO TO 61
      DO 118 I=1,IR
  118 THTC(I)=TH(I)*TCH
      TUSEC=T*TIME
C DFDT=VOLTAGE SEEN BY 10 TURNS OF WIRE SURROUNDING CYLINDER
      DFDT=FNORM*(F(IR)-FP(IR))/(10.*DT*TIME)
      AIM=(1.0-F(IR))*HEX
      WRITE(3,8)
      WRITE(3,4) CN,T,DT,TUSEC,DFDT,AIM
      WRITE(3,9)
      WRITE(3,10) IZ,IZN,DR1DR,DELTAF
      WRITE(3,1) AIZ
      WRITE(3,20) (F(IN*I),I=1,IP)
      WRITE(3,11) (H(IN*I),I=1,IP)
      WRITE(3,16) (P(I*IN),I=1,IP)
      WRITE(3,15) (THTC(IN*I),I=1,IP)
      GO TO 60
   59 CONTINUE
      WRITE(3,14) (DHDR(IN*I),I=1,IP)
      WRITE(3,28) (DC(I*IN),I=1,IP)
      WRITE(3,12) (DIF(I*IN),I=1,IP)
      WRITE(3,13) (DELF(I*IN),I=1,IP)
      WRITE(3,21) (AA(I),I=1,IR)
      WRITE(3,22) (B(I),I=1,IR)
      WRITE(3,23) (C(I),I=1,IR)
      WRITE(3,24) (D(I),I=1,IR)
      WRITE(3,25) (BT(I),I=1,IR)
```

```
      WRITE(3,26) (G(I),I=1,IR)
   60 CONTINUE
    1 FORMAT(7F10.4)
    2 FORMAT(3I10)
    3 FORMAT(1H1,7X,'TC',14X,'A',11X,'ALPHA',11X,'ATN',12X,'RHO',11X,
     1'PERT',12X,'HZ'/)
    4 FORMAT(1X,8F15.5)
    5 FORMAT(1H0,8X,'IR',8X,'NT',7X,'IRT')
    6 FORMAT(1H0,6X,'AIMZ',10X,'FNORM',12X,'L',13X,'AK',13X,'AG',
     113X,'TIME',12X,'JZ',12X,'JCB')
    7 FORMAT(1H0,6X,'AIZ',13X,'IZ',12X,'DR1DR')
    8 FORMAT(1H0,7X,'CN',13X,'T',14X,'DT',11X,'TUSEC',14X,'DFDT',13X,
     1'AIM')
    9 FORMAT(1H0,2X,'IZ',3X,'IZN',12X,'DR1DR',12X,'DELTAF'/)
   10 FORMAT(1X,2I5,2F15.12)
   11 FORMAT(    2X,'H(I)',2X,10F12.8)
   12 FORMAT(    2X,'DIFT',2X,10F12.8)
   13 FORMAT(    2X,'DELF',2X,10F12.8)
   14 FORMAT(    2X,'DHDR',2X,10F12.5)
   15 FORMAT(    2X,'THI',2X,10F12.8)
   16 FORMAT(    2X,'P(I)',2X,10F12.3)
   17 FORMAT(1H0,6X,'AIMZ',12X,'HEX',11X,'JCB',13X,'JZ',14X,'L',13X,
     1 'AG',13X,'AK',11X,'AIMAX')
   18 FORMAT(1X,F15.5,5X,I10,F15.5)
   20 FORMAT(    2X,'F(I)',2X,10F12.8)
   21 FORMAT(1H0,2X,'A(I)',10F12.8)
   22 FORMAT(1H0,2X,'B(I)',10F12.8)
   23 FORMAT(1H0,2X,'C(I)',10F12.8)
   24 FORMAT(1H0,2X,'D(I)',10F12.8)
   25 FORMAT(1H0,2X,'BT(I)',10F12.8)
   26 FORMAT(1H0,2X,'G(I)',10F12.8)
   28 FORMAT(    2X,'DCI',10F12.8)
   29 FORMAT(1H0,2X,'DFLDIF',F12.8)
```

```
 30   FORMAT(1H0,7X,'THF',13X ,'TF',11X,'AIMFT',11X,'RZF',12X,'CN1',12X
   1  ,'CN2',12X,'CN3',14X,'Y'/)
 31   FORMAT(3F10.4,I10)
      NN=0
 61   CONTINUE
      DR1=DRN-(IZ-IZN)*DR
      IF(AIZ.LE.0.0) DR1=DR

      IF(AIZ.LE.0.0) AIZ=0.0
      DR1DR=DR1/DR
      IZ=IZN
      IF(IZN.LT.0) IZ=0
199   CONTINUE
      GO TO 66
300   CONTINUE
      RETURN
      END
```

APPENDIX D

THOMAS ALGORITHM FOR A TRIDIAGONAL MATRIX

In this appendix, we describe an algorithm due to Thomas by which the solution to a set of linear equations forming a tridiagonal matrix can be quickly solved with the aid of a digital computer (Rosenberg 69).

The set of equations is of the form:

$$
\begin{array}{ccccccccccccccccccc}
b_1\Phi_1 & + & c_2\Phi_2 & + & 0 & + & \cdots & + & \cdots & + & \cdots & + & \cdots & + & 0 & = & d_1 \\
a_2\Phi_1 & + & b_2\Phi_2 & + & c_2\Phi_3 & + & 0 & + & \cdots & + & \cdots & + & \cdots & + & 0 & = & d_2 \\
0 & + & \cdots & + & a_i\Phi_{i-1} & + & b_i\Phi_i & + & c_i\Phi_{i+1} & + & 0 & + & \cdots & + & 0 & = & d_i \\
0 & + & \cdots & + & 0 & + & \cdots & + & 0 & + & a_{R-1}\Phi_{R-2} & + & b_{R-1}\Phi_{R-1} & + & c_{R-1}\Phi_R & = & d_{R-1} \\
0 & + & \cdots & + & \cdots & + & \cdots & + & \cdots & + & 0 & + & a_R\Phi_{R-1} & + & b_R\Phi_R & = & d_R
\end{array}
$$

These R equations where $a_1 = c_R = 0$ form a tridiagonal matrix. The algorithm is as follows:

First compute

$$\beta_i = b_i - \frac{a_i c_{i-1}}{\beta_{i-1}} \qquad \text{with } \beta_1 = b_1$$

$$\gamma_i = \frac{d_i - a_i \gamma_{i-1}}{\beta_i} \qquad \text{with } \gamma_1 = \frac{d_1}{b_1}$$

The values of the dependent variable Φ are then computed from:

$$\Phi_R = \gamma_R \quad \text{and}$$

$$\Phi_i = \gamma_i - \frac{c_i \Phi_{i+1}}{\beta_i}$$

APPENDIX E

VALIDITY OF CORRECTION $\delta\Phi$ USED FOR THE NUMERICAL SOLUTION OF THE FLUX DIFFUSION EQUATION

In chapter III and appendix B we have described a technique by which the equation:

$$\frac{\partial^2 \Phi}{\partial \eta^2} - \kappa[1 - \theta] = L(\theta) \frac{\partial \Phi}{\partial \xi} \qquad \text{E-1}$$

could be solved even when the field has not initially penetrated to the center of the slab. In this appendix we will show that if we consider two linear profiles of field at time ξ and $\xi + \delta\xi$ (see figure D.1) the contribution $\delta\Phi$ (equal to the shaded area in figure D.1) to the flux at any point other than η_z tends to zero as $\delta\xi$ tends to zero.

Our technique of solution of equation D.1 assumes that the change in flux at a given point $\eta > \eta_z$ between time ξ and $\xi + \delta\xi$ is given by:

$$\Delta\Phi = \Phi\,(\eta,\ \xi + \delta\xi) - \Phi\,(\eta,\xi) + \delta\Phi \qquad \text{E-2}$$

where $\Phi(\eta,\ \xi + \delta\xi)$ is calculated by assuming initially that the flux

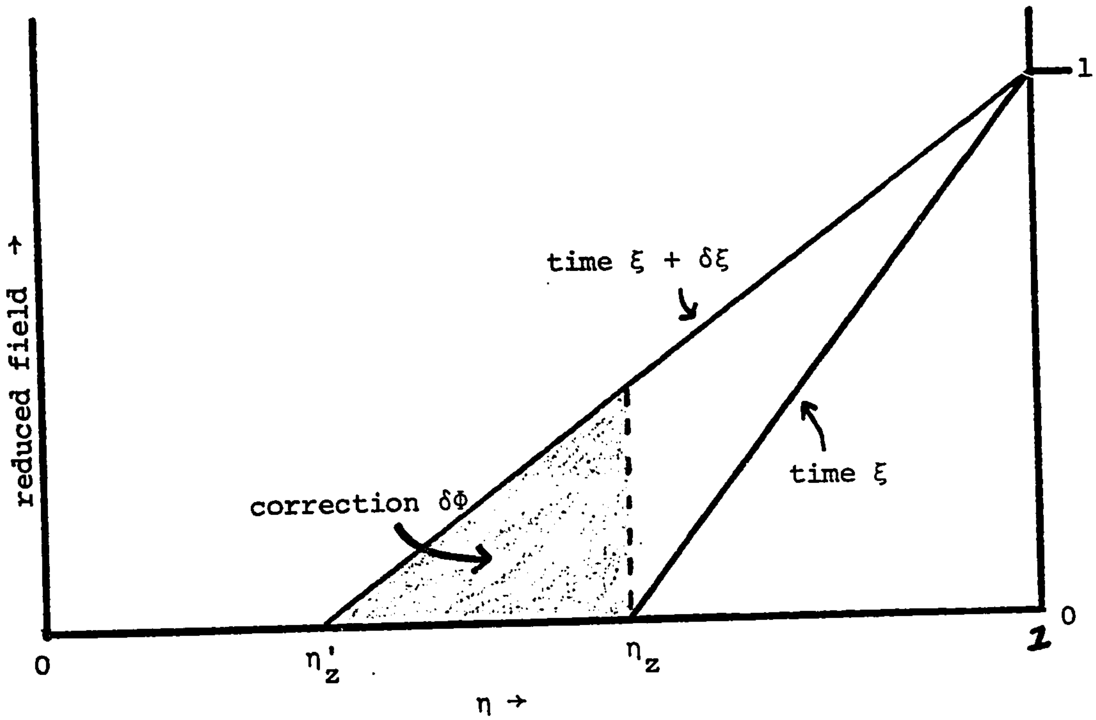

figure D.1

at point η_z is zero at time levels ξ and $\xi + \delta\xi$, and $\delta\Phi$ is a correction corresponding to the shaded area of figure D.1

The purpose of this appendix is to show that for $\delta\xi \to 0$ the contribution $\delta\Phi$ to the change in flux $\Delta\Phi$ (equation D.2) tends to zero. In other words, we want to show that:

$$\lim_{\delta\xi \to 0} \Delta\Phi = \Phi(\eta, \xi + \delta\xi) - \Phi(\eta,\xi) \tag{E.3}$$

We will prove this limit to be valid for the two linear profiles of field shown in figure D.1. In practice the field profiles are concave downwards and therefore using linear profiles will over-estimate the effect of the correction $\delta\Phi$.

Instead of demonstrating limit D-3 to be valid we will prove the following equivalent limit:

$$R = \lim_{\delta\xi \to 0} \frac{\delta\Phi}{\Phi(\eta, \xi + \delta\xi) - \Phi(\eta, \xi)} = 0 \qquad \text{E-4}$$

Since the field profiles are assumed to be linear at times ξ and $\xi + \delta\xi$ the flux Φ at these times is obtained by simple integration:

$$\Phi(\eta, \xi) = m \left[\frac{\eta^2}{2} - \eta_z \eta + \frac{\eta_z^2}{2} \right] \qquad \text{E-5}$$

$$\Phi(\eta, \xi + \delta\xi) = m' \left[\frac{\eta^2}{2} - \eta_z' \eta + \frac{\eta_z}{2} \right] - \delta\Phi \qquad \text{E-6}$$

where $m = \dfrac{1}{(1 - \eta_z)}$

$m' = \dfrac{1}{(1 - \eta_z')}$

and $\delta\Phi = \dfrac{m'[\eta_z - \eta_z']^2}{2}$

The value of Φ at time $\xi + \delta\xi$ in equation D-6 is the "uncorrected" value since we have subtracted the correction $\delta\Phi$.

Using equations D-5 and D-6 we can rewrite limit D-4:

$$R = \frac{\dfrac{m'[\eta - \eta']^2}{2}}{m'\left[\dfrac{\eta^2}{2} - \eta_z'\eta + \dfrac{\eta_z'^2}{2}\right] - m\left[\dfrac{\eta^2}{2} - \eta_z\eta + \dfrac{\eta_z^2}{2}\right] - \dfrac{m'[\eta - \eta_z']^2}{2}}$$

Using the fact that $\lim\limits_{\delta\xi\to 0} \dfrac{m}{m'} = 1$ we obtain:

$$R = \frac{\eta_z - \eta_z'}{2(\eta - \eta_z) - [\eta_z - \eta_z']^2}$$

$$= 0 \qquad \text{for } \eta \neq \eta_z \qquad \text{since} \quad \lim_{\delta\xi \to 0} \eta_z - \eta_z' = 0$$

Therefore for all points $\eta > \eta_z$ the contribution of the correction $\delta\Phi$ tends to zero.

REFERENCES

ABRIKOSOV, A.A.

57 Soviet Physics - JETP 5, 1174 (1957)

ANDERSON, P.W.

64 and Y.B. KIM, Rev. Mod. Phys. 36, 39 (1964)

BABISKIN, J

62 and P. G. SIEBENMANN, Report of NRL Progress, April 1962

BAIRD, D.C.

64 Can. J. Phys. 42, 1682 (1964)

BEAN, C.P.

59 and R.W. DEBLOIS and L.B. NESBITT, J. Appl. Phys. 30, 1976 (1959)

64 Rev. Mod. Phys. 36, 31 (1964)

BOYER, L

72 and G. FOURNET, A. MAILFERT and J.L. NOEL, Proceedings of the Thirteenth International Conference on Low Temperature Physics, Boulder, Colorado August 1972, (to be published).

BROOM, R.F.

60 and E.H. RHODERICK, Brit. J. Appl. Phys. 11 292 (1960)

BUSSIERE, J.F.

72a and M.A.R. LEBLANC, Proceedings of the 1972 Applied Superconducting Conference, IEEE Pub. No. 72CH0682-5-TABSc, (1972), p. 452.

72b and M.A.R. LEBLANC, Proceedings of the Thirteenth International Conference on Low Temperature Physics held in Boulder, Colorado August 1972 (to be published).

CARSLAW, H.S.

59 and J.C. JAEGER The Conduction of Heat in Solids, 2nd edition, Oxford University Press, 1959

CHERRY, W.H.

60 and J.I. GITTLEMAN, Solid-State Electronics, Pergamon Press 1, 287 (1960).

CHIKABA, J.

70 Cryogenics 10, 306 (1970).

CHOPRA, K.L.

59 and T.S. HUTCHISON, Can. J. Phys. 37 614 (1959)

CROW, J.E.

72 and M. SUENAGA, Proceedings of the 1972 Applied Superconductivity Conference, IEEE Pub.No. 72CHO682-5-TABSC (1972), p. 472

DESORBO, W.

64 and W.A. HEALY, Cryogenics, 4, 257 (1964)

65 Phil. Mag. 112, 853 (1965)

DUIJVESTINJN, A.J.W.

59 IBM J. Research Develop. 3, 132 (1959)

EL BINDARI, A.

63 and M.M. LITVAK, J. Appl. Phys. 34, 2913 (1963)

FABER, T.E.

53 Proc. Roy. Soc. (London) A219 75 (1953)

55 and A.B. PIPPARD, Progress in Low Temperature Physics, Vol. 1 (C.J. Gorter, ed.) Wiley (Interscience) New York, 1955 p. 159

58 Proc. Roy. Soc. (London) A248, 460 (1958)

FARRELL, D.E.

66 and I. DINEWITZ and B.S. CHANDRASEKAR, Phys. Rev. Letters, 16, 91 (1966).

FERREIRA DA SILVA, J.

66 and N.W.J. VAN DUYKEREN, and Z. DOKOUPIL, Physica, 32, 1253 (1966)

GILCHRIST, J. le G.

70 and P. MONCEAU, J. Phys. C, 3, 1399 (1970)

HAMPSHIRE, R. G.

69 and J. SUTTON and M.T. TAYLOR, Supplément au Bulletin de L'institut International du Froid, 1969-1 (251)

HANCOX, R,

65 Appl. Phys. Letters 7, 138 (1965).

HARRISON, R.B.

72 and L. S. WRIGHT and M.R. WERTHEIMER, Proceedings of the Thirteenth International Conference in Low Temperature Physics, held in Boulder Colorado August 1972 (to be published)

73 to be published in Phys. Rev. B, February 1973

HART, H. R. Jr

68 Technical Report of General Electric Research and Development Center, No. 68-C-297 (1968)

HUEBENER, R. P.

72 and L. G. STAFFORD and F.E. ASPEN Phys. Rev. B, 5, 3581 (1972)

ITTNER, W.B.

58 Phys. Rev. 111, 1483 (1958)

IWASA, Y.

68 and J.E.C. WILLIAMS, J. Appl. Phys. 39, 2547 (1968)

69 and C. WEGGEL, D.B. MONTGOMERY, R. WEGGEL, and J. R. HALE, J. Appl. Phys. 40, 2006 (1969)

JONES, A.R.

67 and E. H. RHODERICK and A. C. ROSE-INNES, Phys. Letters 24A, 318 (1967).

KIM, Y.B.

65 and C. F. HEMPSTEAD and A.R. STRNAD, Phys. Rev. 139, A1163 (1965)

69 and M.J. STEPHEN, "Flux Flow and Irreversible Effects" in Superconductivity Vol. II (R.D. Parks, ed.) Marcel Dekker Inc., New York 1969, p. 1107.

LAENG, G.

71 and F. HAENSSLER and L. RINDERER, J. Low Temp. Physics, 4, 533 (1971)

LEBLANC, M.A.R.

66 and D.J. GRIFFITHS, Appl. Phys. Letters 9, 131 (1966)

LEUPOLD, H.A.

64 and H.A. BOORSE, Phys. Rev. 134, A1322 (1964)

LIFSHITZ, E.M.

50 J. Exptl and Theoret. Phys. (USSR) 9, 834 (1950)

LUBELL, M.S.

69 Oak Ridge Research Report ORNL-TM-2771 (1969)

72 Cryogenics 12, 340 (1972)

NEURINGER, C.J.

66 and Y. SHAPIRA, Phys. Rev. 148, 231 (1966)

OGASAWARA, T.

70 and K. YASUKOCHI, and T. AKACHI, Proceedings of the 12th Inter-

national Conference on Low Temperature Physics (1970), p. 385

OVERTON, W.C. Jr.

71 J. Low Temp. Physics, 5, 397 (1971)

PIPPARD, A.B.

50 Phil. Mag. 41, 243 (1950)

RADEBAUGH, R.

66a and P.H. KEESOM, Phys. Rev. 149, 209 (1966)

66b and P.H. KEESOM, Phys. Rev. 149, 217 (1966)

ROSENBERG, D.V.

69 "Methods for the Numerical Solution of Partial Differential Equations", American Elvesier Publishing Co., New York 1969

SWARTZ, P.S.

68 and C.P. BEAN, J. Appl. Phys. 39, 4991 (1968)

SWIHART, J.C.

63 J. Appl. Phys. 34, 851 (1963)

TAKEO, M.

71 J. Phys. Soc. Japan 30, 697 (1971)

TRAUBLE, H.

68 and U. ESSMANN, Phys. Stat. Sol. 25, 373 (1968); J. Appl. Phys. 39, 4052 (1968).

WALKER, M.S.

65 and J.K. HULM, Appl. Phys. Letters 7, 114 (1965)

66 and J.K. HULM, J. Appl. Phys. 37, 1015 (1966)

72 and J.K. HULM, Proceedings of the 1972 Applied Superconductivity Conference, IEEE Pub.No. 72CHO682-5-TABSC (1972), p. 446

WERTHEIMER, M.R.

67 and J. le G. GILCHRIST, J. Phys. Chem. Solids 28, 2509 (1967)

WHETSTONE, C.N.

65 and C.E. ROOS, J. Appl. Phys. 36, 783 (1965)

WIPF, S.L.

67 Phys. Rev. 161, 404 (1967)

YAMAFUJI, K.

69 and M. TAKEO, J. CHIKABA, N. YANO, and F. IRIE, J. Phys. Soc. Japan, 26, 315 (1969)

YASUKOCHI, K.

72 and T. ANDO and T. OGASAWARA, Proceedings of the 4th International Cryogenic Engineering Conference, Eindhoven, May 1972 (to be published by Cryogenics)

ZBASNIK, J.

69 private communication see also (Y. IWASA 69)